Atmospheric Convection and Gravity Waves

Oliver John Halliday

Institute for Climate and Atmospheric Science

University of Leeds

A thesis submitted for the degree of

Doctor of Philosophy

30th November 2018

To my old man, my life supervisor.

Acknowledgements

First and foremost, I would like to thank my supervisors Prof. Doug Parker and Dr. Stephen Griffiths for their continuous support, wisdom, enthusiasm and patience. Without their insight and encouragement this thesis, which feels their influence throughout, would not have been possible. I would like to also thank Prof. Doug Parker for facilitating my involvement in the INCOMPASS field campaign, which is an experience I will never forget.

Further thanks go to my CASE supervisors Dr Simon Vosper and Dr Alison Stirling at the UK Met Office, who provided timely, contextualising feedback during my sporadic visits to Exeter. I must also thank Dr Rachel Stratton, whose simulations helped improve this thesis.

From the first moment, I was welcomed into the Atmospheric Dynamics research group, and for that I am grateful. I particularly owe Steef Boeing, for continued interest and input in my work, and Declan Finney, for assisting with the collection of data used in this thesis.

I thank my wonderful friends and family, who, when my head was in the clouds never failed to bring me back down to earth. Special thanks go to the members of my PhD cohort Mike, Ilkka, Hana and Lauren, who were always there to remind me I was not alone, and my loving, selfless parents, without whom, none of this would have been possible.

Thank you to the Faversham and the Union's Old Bar for their great selection of ales and for being open at 5pm on Fridays, and to anyone who joined me for a pint over the better part of the last decade.

Finally, and most importantly, I thank my beautiful wife Bryony for her unconditional support and endless love.

Contents

List of Figures

Chapter 1

Introduction

1.1 Atmospheric Convection

Earth's atmosphere is constantly convecting. From large cells, providing teleconnections between the tropics and poles, to single isolated clouds, a rich variety of convective events span a range of scales. Often visibly manifest in clouds, convection plays an intricate, not to say leading role in the dynamics of the Earth's weather and climate. Few would argue that the most striking meteorological features encountered on Earth are hurricanes, tornados and tropical storms (all of which invariably involve cumulonimbus convection) and all would recognise that forecasting these systems is a social and economic necessity, as their high wind speeds and potential flash flooding can cause large destruction of infrastructure and, indeed, direct loss of human life.

This thesis will focus, in part, on cumulonimbus convection, which occurs due to highly buoyant, localised regions (O(10 kms)) of air punching rapidly upwards, through the troposphere. Strong vertical motions result in phase changes in the water vapour in moist air, which help the observer to notice dramatic, bubbling clouds which can precipitate intensely. Since thermally-driven mixing moves air parcels from the lower to the upper troposphere, meteorologists often refer to cumulonimbus as "deep" convection. But while some aspects of deep convection are well understood, others continue to challenge our understanding.

1.1.1 The Physics of Moist Convection

The stratification of the atmosphere and its base temperature distribution arise out of the competition between incoming short-wave (solar) radiation, which heats the surface, and emitted outgoing long-wave radiation, which cools the troposphere. Broadly, the resulting stratification of the troposphere, with its negative temperature lapse rate (the rate at which temperature reduces with height, see e.g. Holton & Hakim (2012)) permits convective processes.

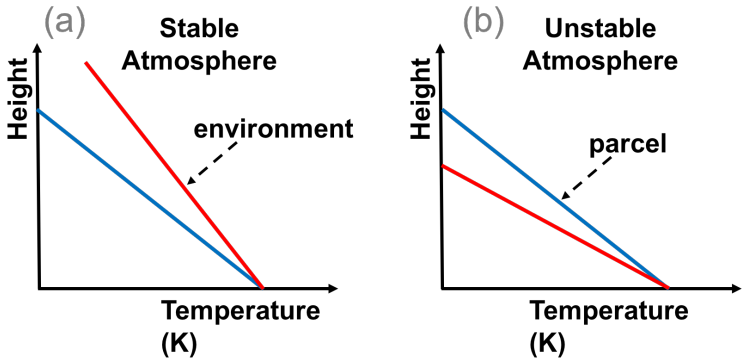

Figure 1.1: Stable (non-convective) vs. non-stable (convective) atmospheric conditions. In (a) the parcel is cooler than the environment and is therefore not buoyant. In (b) the parcel is warmer than the environment and is therefore buoyant.

The work of this thesis relies heavily on the concept of buoyancy forcing, which may be conveniently connected to convection. This is perhaps best illustrated initially considering dry air, using a Boussinesq vertical momentum equation, which, at its simplest (see Chapter 7 of Houze Jr (2014)) may be written

$$\frac{Dw}{Dt} \approx b, \quad b \equiv g\frac{\theta}{\theta_0(z)} \approx -g\frac{\rho}{\rho_0(z)} \tag{1.1}$$

in which b is a buoyancy term, which creates vertical acceleration, θ is potential temperature perturbation, $\theta_0(z)$ is a reference potential temperature and all other symbols have their usual meaning. θ is the temperature which a *dry* parcel of air at pressure p would have, were it brought adiabatically to pressure $p_s = 1000\,\text{hPa}$. From the first law of thermodynamics

$$\theta \equiv T\left(\frac{p_s}{p}\right)^{R/c_p}. \tag{1.2}$$

Here, R is the universal gas constant and c_p the specific heat at constant pressure. Note that in our formulations in Chapters 2..4, an equivalent regime of approximations will be used to couple-in induced buoyancy perturbations, instead using a thermodynamic equation. It is immediate from equation 1.1 that the root, physical cause of buoyancy forcing is is the action of strong, terrestrial gravity on density perturbations which, in turn, are determined by potential temperature, θ.

Consider now moist air. As well as direct heating, the potential temperature and buoyancy of a parcel may also arise from internal microphysics. Most relevant here is the phase change of water vapour. As the water vapour content of a parcel condenses, latent heat of condensation is released and the parcel heats (or cools less rapidly). Conversely,

evaporation of liquid within the parcel requires a source of latent heat of evaporation, which is drawn from the substance of the parcel, cooling it. The *equivalent* potential temperature, θ_e is defined as the potential temperature which a parcel of air would have, were all its water vapour content condensed and the resulting latent heat of condensation used to warm the parcel. One approximate expression is $\theta_e \approx \theta \exp\left(\frac{Lcq_s}{c_pT}\right)$, where L_c is the latent heat of condensation and q_s is the mass of water vapour per unit mass of dry air. Importantly, θ_e is conserved during changes of a parcel's pressure (say during vertical motion) even if the water vapour condenses whereas θ is only conserved for vertical motions whilst unsaturated (Holton & Hakim, 2012). To capture the effects of e.g. latent heat forcing necessarily associated with convection, in a description based upon θ, it is therefore essential to include in the basic set of Chapter 2..4 an explicit buoyancy forcing (in the thermodynamic equation), which, note, might also be interpreted as diabatic or sensible heating, if convenient.

Atmospheric convection is the result of a temperature difference between a parcel of air which has been lifted and its environment. Should a parcel of air at a certain height have a temperature different to its environment, there is a parcel-environment instability, leading to buoyancy-driven movement of the parcel, or convection, which mixes the parcel with the environment. Figure 1.1 is a schematic of the atmospheric conditions convection requires. An air parcel cooler and therefore denser than its environment will not have upward buoyancy, meaning it is stable within the atmosphere i.e. it will not be upwardly displaced readily, rather it will tend to subside and return to its position of mechanical equilibrium. Conversely, a parcel warmer than its environment will have upward buoyancy, meaning it is unstable within the atmosphere i.e. it will be easily displaced upwards, away from its position of mechanical equilibrium, and convect.

More quantitatively now, the development of convective storms depends on such predisposition in the environment. Several scalar indices exist, to measure susceptibility of given temperature and moisture fields to deep convection. Meteorologists quantify rate of and propensity to deep convection perhaps most widely using the parcel and environmental lapse rates and the convectively available potential energy (CAPE hereafter). To understand CAPE, consider a parcel whose temperature is greater than that of the environment it is within. Such a parcel is less dense than the surrounding air i.e. it is buoyant and will rise aloft, from the level of free convection (LFC hereafter), as shown in figure 1.2. As the parcel rises, it is subject to reduced pressure, it expands (we presume adiabatically, since air is an insulator), and thus its temperature will fall, according to the conservation of its potential temperature (equation 1.2). If the temperature of the surroundings decreases more quickly than the parcel's, it remains buoyant, instability and convection are maintained (see figure 1.1). Convection will continue until the parcel inevitably is no

longer warmer than its environment- which must happen in an environment of finite depth (due e.g. to the troposphere-stratosphere boundary i.e. the tropopause lid). The parcel is therefore no longer buoyant. At this equilibrium level (EL hereafter), convection ceases. Note, the parcel's momentum will usually cause it to overshoot and oscillate about the EL (see figure 1.2 below). Integrating the buoyancy force over the parcel's vertical displacement yields the CAPE measure, with units $\mathrm{J\,kg^{-1}}$ of potentially buoyant air. CAPE is an upper limit for an ideal, undiluted parcel. Equation 1.3, which is equation (8.1) of Houze (2014), gives the integral used to calculate CAPE

$$CAPE = g \int_{Z_{LFC}}^{Z_E L} \left(\frac{\theta(z) - \bar{\theta}(z)}{\bar{\theta}(z)} \right) dz, \tag{1.3}$$

where $\bar{\theta}$ is the potential temperature of the environment, g is the acceleration due to gravity, Z_{LFC} is the level of free convection and Z_T is the cloud top, assumed to be the level where $\theta = \bar{\theta}$, i.e. the equilibrium level. Apparently CAPE is a functional of θ. In figure 1.2, the amount of CAPE is represented by the shaded region between the saturated adiabat and the sounding, above the LFC.

Now, how does a parcel reach the LFC? Consider the situation in which there is a layer of warmer environmental air above the surface (say) preventing the cooler parcels at the surface from rising into the atmosphere. Here, convection is inhibited unless something other than a temperature difference can cause the parcel to rise. The amount of energy required for our parcel to overcome this inhibition, and reach the LFC, is know as convective inhibition (CIN hereafter). CIN, conceptually, is the opposite to CAPE in that it indicates the amount of energy available to prevent an air parcel from rising from the surface to the level of free convection. It is, again, measured with a vertical integral similar to that of 1.3, covering our hypothetical, inhibiting layer from the surface to the level of free convection or, more generally, form the bottom to the top of the inhibiting layer

$$CIN = g \int_{Z_{bottom}}^{Z_{top}} \left(\frac{\theta(z) - \bar{\theta}(z)}{\bar{\theta}(z)} \right) dz. \tag{1.4}$$

The above is a simplified account. In real convection, as a parcel rises, drag provides a counter force to buoyancy, and entrainment of environmental air alters the parcel's lapse rate. Moisture vapour in the parcel plays an appreciable role, as it changes phase in response the parcel cooling and releases latent heat of fusion (Reif, 2009), which, through enthalpy exchange (Kittel & Kroemer, 1970), is a major contributor to the positive buoyancy driving updrafts. These phase changes are nonlinear processes, and entrainment of dry air affects them in complex ways which we cannot go into here.

Interpretation of CAPE and CIN data is often counter-intuitive. For instance, one might expect minimal, or no CIN to be favourable for thunderstorms, but it is actually the case that large amounts of CIN provide

a lid on convection, allowing warm, humid air to accumulate at low levels, so that the CAPE increases and when storms finally occur, they are more intense (Colby Jr, 1984). Here, we are concerned most with gravity wave coupling to convection, for which CAPE and CIN can provide a useful tool. In chapters 2..4, we will formulate a model of gravity wave adjustment to buoyancy forcing. Most obviously, our gravity waves communicate potential temperature adjustments in θ (and hence T), thus modifying the environmental CAPE and CIN, via equations 1.3 and 1.4. This mathematical fact may be refined into more physical statements as we see in Chapter 2, where we argue that gravity waves transport momentum, which over time can erode CIN, which assists in lifting parcels to the level of free convection. Figure 1.2 is a skew-T diagram graphically demonstrates a convecting parcel's journey through CIN and CAPE and in the process depicts the convective state of a given atmosphere.

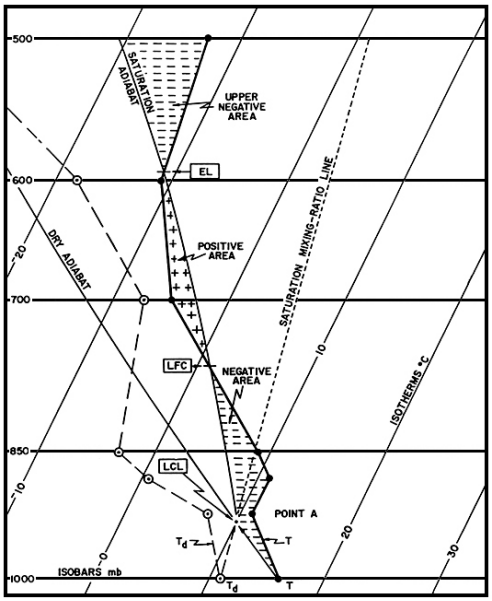

Figure 1.2: A skew-T diagram to demonstrate computed CAPE, CIN and LFC. Note, the dry adiabat connecting the point labelled T close to the mid-abscissa to the 600mb isobar on the right ordinate, and also saturated adiabat. This extends from the foot of the sounding. When the saturated adiabat, which we consider to represent a parcel, lies to the left of the sounding, for $z < z_{LFC}$ here, CIN will be negative (see equation 1.4). When the saturated adiabat lies to the right of the sounding, for $z_{LFC} < z < z_{EL}$, CAPE will be positive (see equation 1.3).

For convection to initiate, or "trigger", some other physical process must be present to overcome CIN. We give some known examples. At the surface, changes in the Earth's topography or spatial temperature variations (e.g. land/sea gradients) can trigger vertical motions which, under favourable conditions, can trigger coherent cloud patterns (Kir-

shbaum & Durran, 2005; Nastrom & Fritts, 1992). Further, the land surface use can play a role, as e.g. moisture stored in soil evaporates and injects latent heat into the system, creating a feedback loop (Koster *et al.*, 2004; Walker & Rowntree, 1977). Cold pools, a density current caused by condensation and precipitation, can also provide dynamical lifting in the low levels (Schlemmer & Hohenegger, 2014; Tompkins, 2001), and atmospheric waves have also been observed to trigger convection as the momentum they transport acts to erode CIN (Birch *et al.*, 2013; Lane *et al.*, 2001; Mapes, 2000).

1.1.2 The Role of Tropical Convection in the Weather and Climate System

Tropical convection generates kinetic energy in the atmosphere. Thermally driven, turbulent vertical mixing leads to ascent of warm, moist air and, ultimately, precipitation, which releases further heat into the atmosphere. The atmosphere compensates via fast gravity waves with characteristic phase speeds of roughly 30ms^{-1}), which communicate adjustment into the environment. We reserve a qualitative description of the adjustment process for later in this chapter and quantitative descriptions for Chapters 2, 3 and 4. The horizontal spatial range of influence over which the adjustment occurs, conventionally quantified by the Rossby radius

$$L_R = \frac{NH}{f}, \tag{1.5}$$

where N is the Brunt-Vaisala frequency, H is the height of the tropopause and f is Coriolis' parameter, is heavily influenced by latitude. In the tropics, where f tends to zero, L_R approaches infinity and, in some sense, perturbations in the tropics affect the whole tropical belt, for example via the equatorial waveguide effect, to be discussed shortly. In the mid-latitudes, where f is non-zero, the adjustment to convection is restricted, and is characterised by a Rossby radius which is of the order of a few thousand kilometres (f 10^{-4}s^{-1}, $H = 8 - 15\text{km}$, N 0.01s^{-1}, $g = 9.81\text{ms}^{-2}$).

Unfortunately, too little is known about the interaction of convective perturbations with the larger-scale circulations (the chicken and egg problem), even after modern, high-resolution large-domain numerical simulations of tropical convection, together with spectral analysis methods, have been applied.

Another, important way in which the tropics is dynamically interesting is in its capacity to host a spectrum of waves which are trapped about the equator. Theoretically predicted by Matsuno (1966) and Gill (1980), who worked from the primitive equations, the change in sign of Coriolis parameter at the equator acts as a waveguide for a set of Matsuno modes, which are propagating modes which may be classified as Kelvin, Rossby, gravity and mixed Rossby gravity waves. These phenomena, which are

particular significance to the present work, are now widely accepted to interact with, organise and even force convection. See e.g. Wheeler & Kiladis (1999). We defer further discussion of these phenomena until chapter 5.

1.1.3 Modelling and Forecasting

Numerical modelling is clearly a valuable resource which, nevertheless, provides hurdles to overcome. Despite huge increases in computing speed and memory in recent years, deep convection is still a sub-grid processes in general circulation models (GCMs hereafter) and thus it needs to be parameterised. It is safe to say that convection parameterisations remain imperfect. In current GCMs deep convection is designated a sub-grid process in that a convection scheme -essentially an algorithmic extension- adjusts the temperature, moisture and cloud fields within a mesh-resolved grid column, leaving the resolved, mesh-based dynamics to propagate this adjustment more remotely, and thereby influence, for instance, the convective available potential energy (CAPE) of the wider environment (Stensrud, 2009). Therefore, the dynamical response to convection is highly dependent upon the model convection scheme, which itself is sensitive to the closures and assumptions placed upon the underlying parameterisations.

There are several types of deep convective parametrisation scheme in operational use (Stensrud, 2009). Typically, a convection scheme attempts to represent an ensemble of clouds within a given gridbox, through a bulk formulation. For instance, the Gregory and Rowntree mass-flux scheme used in the MetUM (Gregory & Rowntree, 1990; Walters *et al.*, 2017) models the effects of entrainment and detrainment on the ensemble convective-cloud mass flux by analogy with a single, model plume in the gridbox. The resulting heating tendencies are applied at the grid scale, and it is assumed that all compensating subsidence occurs within that gridbox, whereas, in reality, it has long been known that gravity waves propagate laterally, to move the zones of subsidence away from the location of the forcing (e.g. Yanai *et al.* (1973)). While gravity-wave modes are themselves represented only by the resolved grid, representation of the drag caused by gravity-wave breaking and initiated by sub-grid orography (and sometimes precipitating convection) is parametrised separately (e.g. Bushell *et al.* (2015); Walters *et al.* (2017)). Some sub-grid statistics of the cloud field are diagnosed in GCMs (via e.g. the Prognostic Cloud Scheme), but these are principally used to interact with the radiation scheme and do not, at present, feedback onto the dynamic, thermodynamic and cloud fields.

From the above discussion, we conclude that convection schemes need to provide a physically realistic forcing and response on the resolved model scales. The basic ingredients necessary to achieve this in a parameterisation are (i) a method to trigger the convection, (ii) a cloud

model and (iii) a closure assumption. Further, they need to force the correct dynamical response, part of which is the spectrum of gravity waves. While current convection schemes hold some information about the sub-grid cloud field, they do not use any sub-grid cloud information in the excitation of gravity waves, which are only forced by the grid-resolved tendencies imposed by the convection scheme. This leads to a possible mis-match between the true field of gravity waves excited by sub-grid convection, on the kilometre scale, and the gravity waves forced on the grid-scale, by the convection scheme. It is still an open question whether such effects need to be handled explicitly, within convection schemes, or whether the model grid will handle them satisfactorily.

1.2 Gravity Waves

Gravity waves are common in Earth's atmosphere as they can be produced by a variety of sources. A key property of all waves is their ability to transport energy away from the disturbances that generate them. Gravity waves are said to communicate the atmospheric adjustment to some disturbance. In the present context, the causal disturbance is convection. However, it is well known that many other gravity wave sources, including mountains and wind shear also have meteorological significance.

1.2.1 Introduction

A fluid is said to be stably stratified if the density of a lifted parcel is greater than that of its environment. Such a fluid is host to wave motions able to propagate horizontally and vertically. Since the Earth's atmosphere is almost always stably stratified, common sense alone suggests that it is safe to assume atmospheric waves exist and, indeed, no formal assumption is, however, necessary for an overwhelming body of evidence for atmospheric gravity waves has accumulated over the past half a century. Moreover, on occasion, even the amateur meteorologist can observe the normally invisible wave field as it interacts with the visible cloud field (an important concept for this work, note) as illustrated in figure 1.3.

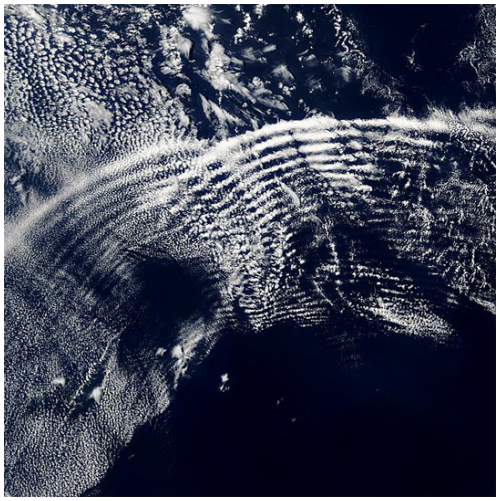

Figure 1.3: Satellite image of patterned cloud above the Indian Ocean. The cloud or water vapour 'ripples' make gravity waves visible, Photograph by NASA.

Were all atmospheric waves visible, and were it possible to accelerate their motion, one would see a rich tapestry of propagating waves of many shapes, sizes and speeds. Figure 1.4, reproduced from Hines (1974), is a surreal representation of an imagined scene. Here, we see waves propagating in all directions. Some extend through the whole image, others are localised and are intended to appear stationary, some have a frequency and amplitude which grows with height and some even break or change direction. Currently, it is clear that gravity waves are not present only in the isolated or bounded layers of the atmosphere (its boundary layer, troposphere or stratosphere), but instead transcend layers, as they do so becoming subject to well-known, generic wave phenomena such as reflection, refraction and breaking- a complex picture in which the level of the complexity is just beginning to be appreciated. In the present context, the question is how, and to what extent do gravity waves impact the weather and climate system as a result of coupling to convection?

Figure 1.4: A surrealist representation of samples from the range of atmospheric gravity waves. Taken from 'The Upper Atmosphere in Motion', Hines (1974).

Atmospheric waves add a significant contribution to circulation and mixing in the Earth system. Like ripples in a pond, gravity waves transport energy and momentum, providing telecommunications down field from their source and are thus an essential part of atmospheric dynamics, on all meteorological scales. Calculations of the atmospheric budgets, whether at the largest scales of general circulation, or the smaller scales of surface turbulence, routinely include contributions from wave transport and mixing. On the synoptic scale, for example, Lindzen (1981) and Holton (1982) investigate the effect of gravity waves on the general circulation (see Fritts (1984) for a review). On the mesoscale, Uccellinni (1987), Koch et al. (1988), Fritts (1992), Lane and Reeder (2001) and Wei and Zhang (2014), to name a few, study the interaction between convective storms and gravity waves. Mountain-generated gravity waves have been studied by e.g. Clark and Peltier (1977), Smith (2007). Chimonas (1972) has shown that, even on micro-scales, gravity waves interact with turbulence in a stable boundary layer. There is a continuing interest in the meteorology of atmospheric gravity waves, supported by periodic field campaigns, such as TOGA-COARE (Webster & Lukas, 1992) and DEEPWAVE (Fritts *et al.*, 2016), with devoted resources for their observation. Indeed, evaluating the role of waves in each dynamical situation is now accepted as necessary.

It is appropriate to remark that any real, physical process is made unique (for instance, by its initial conditions) and that what are represented in Fig 1.4 are samples from a continuous spectrum. Accordingly, a full review of gravity waves is beyond the scope of this thesis and even the state of the computational art and observational methodology. The object here is to select a few smoother pebbles from the vast atmosphere of truth (only slightly to mis-quote): that is to extract qualitative understanding from simple analytical models based upon linear theory, better to understand the role of gravity waves in atmospheric convection. It is therefore also appropriate to sound a cautionary note. The basis for

most theoretical studies (including this) is linear theory. Broadly, this removes wave-wave interactions, and splits variables into a sum of a base state, which is unaffected by waves, and a small, first-order perturbation, which is attributed to waves effects. These approximations are not without cost, as in the physical atmosphere, waves do interact with other waves and turbulence, which are now neglected. However, linear theory provides a tractable tool for an analysis which is a good estimate for wave phenomena at first order. In Chapter 2 of this thesis, we will touch further upon the extent to which we can trust linear gravity wave theory. At this stage, we simply seek to reassure the reader that analysis with linear theory is a worthwhile where qualitative understanding is at issue, for -rhetorically- is it even possible to think in terms of a nonlinear world?

1.2.2 Gravity Wave Modelling

In the stably stratified atmosphere of Earth, the potential temperature, θ, increases with height. Imagine, then, adiabatically displacing a parcel of air aloft. The parcel will then be negatively buoyant and the force of gravity acting on its anomalous density will restore the parcel back to a neutral level. In doing so, the parcel will gather momentum and overshoot its level of neutral buoyancy and become positively buoyant and so forth. Clearly, a stratified atmosphere is conducive to parcels oscillating vertically about their equilibrium altitude. Put more succinctly, the presence of buoyancy as a restoring force in a fluid leads to the occurrence of oscillations and hence waves.

Modelling the above-described process mathematically, by constructing a mechanical force balance on a buoyant parcel, the ideal gas equation of state, which is suitable for air, and the hydrostatic approximation (Holton & Hakim, 2012), one can quite straightforwardly determine an expression for a characteristic frequency of buoyancy-driven oscillations as

$$N(z) = \sqrt{\frac{\theta}{g}\frac{\partial \theta}{\partial z}}, \tag{1.6}$$

which is known as the Brunt-Vaisala frequency. For stably stratified fluid, $\frac{\partial \theta}{\partial z} > 0$, so $N > 0$. A typical value of N in the troposphere is 0.012s^{-1}, (Holton & Hakim, 2012), giving a buoyancy period of roughly 8 minutes. Note that this above expression for $N(z)$ is not unique.

Evidently, the atmosphere is prone to oscillatory motion and little imagination is required to see that once the parcel moves, adjacent parcels will be induced to move also. To model buoyancy-driven, gravity wave effects (indeed, any wave motion) one typically seeks, within some regime of mathematical approximations, the dynamics i.e. an equation of motion (or wave equation) governing some field variable. Subject to the initial assumptions, its solutions describe some phenomenon- for present purposes, internal, linear gravity waves.

Gravity waves rely on the physics of buoyancy (Gill, 1982; Vallis, 2006) the understanding of which is facilitated by the Boussinesq approximation. This assumes (i) changes in density caused by the motion are primarily the result of temperature, rather than pressure changes and (ii) in the equations expressing the conservation of momentum (the Euler equation) and mass (the continuity equation), density changes may be neglected except where they are coupled to the gravitational acceleration, i.e. in the Euler equation, in its buoyancy force term. Assumptions (i) and (ii) are referred to as the Boussinesq approximation (Spiegel & Veronis, 1960). We remark that acoustic waves, which propagate by density variations, are effectively filtered from a description which uses the Boussinesq approximation. Within the Boussinesq approximation, which we shall use in this introduction, the continuity equation is replaced by two statements

$$\frac{D\rho}{Dt} = 0, \quad \underline{\nabla} \cdot \underline{u} = 0. \tag{1.7}$$

Note, here we are approximating $\frac{d\theta}{\theta}$ by $\frac{d\rho}{\rho}$ (allowable under the Boussinesq approximation) in order to use density as the state variable. Further discussion of this important point is reserved for Chapters 2, 3.

For a rotating, 2D system in the x, z plane, without variation in the y direction (our foundation geometry), we consider the following Boussinesq formulation of linear theory, in the usual notation

$$\begin{aligned}
\frac{\partial u}{\partial t} - fv &= -\frac{1}{\bar{\rho}}\frac{\partial p}{\partial x}, \\
\frac{\partial v}{\partial t} + fu &= 0, \\
\frac{\partial w}{\partial t} + \frac{g}{\bar{\rho}}\rho &= -\frac{1}{\bar{\rho}}\frac{\partial p}{\partial z}, \\
\frac{\partial u}{\partial x} + \frac{\partial w}{\partial z} &= 0, \\
\frac{\partial \rho}{\partial t} + w\frac{d\rho_0}{dz} &= 0.
\end{aligned} \tag{1.8}$$

Here, the base state is rest, $\bar{\rho}$ is an average density, $\rho_0(z)$ is the base state of density and the last two equations represent a linearisation of equation 1.7. In equations 1.8, it is implicit that Rossby number, R_o (see section 1.4.4) is large, note.

Typically, it is easiest to apply physical boundary or matching conditions to field variable w. We therefore eliminate variables from basic set 1.8 in favour of w

$$\nabla_H^2 \frac{\partial^2 w}{\partial t^2} + f^2 \frac{\partial^2 w}{\partial z^2} + N^2(z)\frac{\partial^2 w}{\partial x^2} = 0. \tag{1.9}$$

Here, the buoyancy frequency is

$$N^2(z) \equiv -\frac{g}{\bar{\rho}}\frac{d\rho_0}{dz}. \tag{1.10}$$

Since we have used linear theory, all solutions to equation 1.9 above are superposable.

The basic set in equations 1.8 and the field variables chosen are suitable for this introduction. However, they are not used everywhere in this thesis. For instance, in Chapter 2, we shall replace the last equation with a thermodynamic equation (Gill, 1982; Vallis, 2006) (to investigate gravity waves which are forced by heating), remove the second (by initially neglecting rotation, which is reinstated in Chapter 3) and take a hydrostatic approximation in the third equation. Moreover, the vertical variation in base state density $\rho_0(z)$ and the physics briefly discussed in section 1.1.1 cause $N(z)$ (equation 2.17) to change value at the tropopause, producing a complicated stratification, which influences gravity wave propagation. The influence of stratification on gravity wave mediated atmospheric adjustment to heating, both dynamic and steady-state, is our central concern. Hence, we reserve for Chapters 2..4 treatments of gravity wave propagation in the presence of stratification. In this introduction, we shall consider certain, relatively simple scenarios which serve as limiting cases for work of later chapters, where we shall be particularly concerned with trapped and radiating dynamics. Accordingly, we consider here trapped and unbounded gravity wave propagation, with rotation but without stratification.

1.3 Reference Gravity Wave Problems

In this and the next section, we consider reference cases which will provide a "orthogonal" framework in which the results of chapters 2,3 and 5 may be understood. We start with more straightforward phenomena and reserve for the next section the more problematic gravity wave interactions which are, probably most relevant.

1.3.1 Trapped Gravity Waves with Rotation

First consider trapped gravity waves in $z \in [0, H]$ with physical boundary conditions representative of a lid

$$w(x, 0, t) = w(x, H, t) = 0, \quad \forall x, t, \tag{1.11}$$

and N constant but $f \neq 0$. Note that the boundary conditions here and throughout are the kinematic boundary conditions of inviscid fluid dynamics (Landau & Lifshitz, 1959). Substituting a x-propagating solution

$$w(x, z, t) = \Re\left(W(z)\mathrm{e}^{i(kx-\omega t)}\right), \quad k = \frac{2\pi}{\lambda} \tag{1.12}$$

which is adapted to the physical domain, note, into equation 1.9, it is straightforward to obtain the following

$$\frac{d^2W}{dz^2} + \kappa^2 W = 0, \quad \kappa^2 \equiv k^2\left(\frac{N^2-\omega^2}{\omega^2-f^2}\right), \quad W(0) = W(H) = 0. \tag{1.13}$$

Above, λ is the horizontal wavelength of the motion, hence $k \in [0, \infty)$. Non-trivial solutions only exist for the system in equations 1.13 for the following conditions

$$\kappa H = n\pi, \quad n \in \mathrm{Z}^+, \quad \omega = \pm\sqrt{\frac{N^2k^2 + \frac{n^2\pi^2}{H^2}f^2}{k^2 + \frac{n^2\pi^2}{H^2}}}, \quad W(z) = \sin\left(\frac{n\pi z}{H}\right). \tag{1.14}$$

Various choices of n produce different physical patterns of wave motion but propagation is by assumption in the x direction, with a point on wave of constant phase (e.g. a crest or trough) moving with phase speed

$$c_p \equiv \frac{\omega}{k} = \pm\sqrt{\frac{N^2 + \frac{n^2\pi^2}{H^2k^2}f^2}{k^2 + \frac{n^2\pi^2}{H^2}}}, \tag{1.15}$$

where we have used the second of equations 1.14, which relates $\omega - k$ and as such is a dispersion relation. Gravity waves are dispersive i.e. have a range of phase speeds. Moreover, it appears that increasing rotation, $f \to \infty$, will tend to make a trapped gravity wave mode (i.e. a choice of n) of given k propagate faster.

A group of superposing waves, or wave packet, may be formed from an integral superposition of modes over a localised range of k i.e. a range of Fourier components. In light of the above, initially coherent, superposing waves will propagate at different speeds, c_p, and change relative phase. However, if the superposition weight function peaks sharply at $k = k_0$ (say) the propagating disturbance can be characterised by a time-evolving envelope function with slow spreading, which allows one to introduce a group speed, which characterises the speed at which the envelope moves and is given by $\frac{d\omega}{dk}$ (Arfken, 1966). For gravity waves, this group speed, from the second of equations 1.14 is

$$c_g \equiv \frac{d\omega}{dk} = \frac{\frac{n^2\pi^2}{H^2}(N^2 - f^2)}{\left(N^2 + \frac{n^2\pi^2}{H^2k^2}f^2\right)^{1/2}\left(k^2 + \frac{\pi^2n^2}{H^2}\right)^{3/2}}. \tag{1.16}$$

The derivative in the above is typically evaluated at $k = k_0$. For $f = 0$ it is easy to show that $c_p > c_g$ and so, in that limit, peaks always move forwards through the envelope- as can be observed in gravity waves, or ripples, propagating on the air-water interface of pond.

1.3.2 Gravity Waves in Unbounded Media with Rotation

Return to equation 1.9 and substitute a trial solution consistent with a 2D system with no variation in the y direction, which is vertically unbounded i.e. a wave which can propagate in both the x and z directions

$$w(x, z, t) = \Re\left(W\mathrm{e}^{i(kx+mz-\omega t)}\right) = \Re\left(W\mathrm{e}^{i(\underline{k}\cdot\underline{r}-\omega t)}\right), \tag{1.17}$$

where, we have

$$\underline{r} \equiv (x, 0, z), \quad \underline{k} \equiv (k, 0, m), \tag{1.18}$$

where $\underline{k}$ is now the wave vector. W is now constant, note.

We now obtain, by simple algebra, the following dispersion relation for gravity waves in an unbounded system

$$\omega = \pm \frac{\sqrt{m^2 f^2 + N^2 k^2}}{\sqrt{k^2 + m^2}}. \tag{1.19}$$

Positions (x, z) in physical space with $kx + mz = c$ (c is a constant) have, at a given instant, t, the same phase. Hence, positions such that ($\underline{k} \cdot \underline{r} = c$ correspond to 2D wavefronts. Let $\delta\underline{r} \equiv (\delta x, \delta z)$ be a displacement perpendicular to $\underline{k}$. Then $\underline{k} \cdot (\underline{r} + \delta\underline{r}) = \underline{k} \cdot \underline{r} = c$ with $k = |\underline{k}|$. Put another way, all points in a plane perpendicular to wave vector $\underline{k}$ have the same phase and comprise a wavefront. Let s denote displacement parallel to $\underline{k}$, perpendicular to a wavefront. Now our gravity wave adjustment may be written $w(x, z, t) = \Re\left(W e^{i(ks - \omega t)}\right)$ implying, a phase speed $c_p = \omega/k$ and in the direction $\hat{k}$, that is a phase velocity

$$\underline{c}_p = \frac{\omega}{k}\hat{k} = \pm \frac{\sqrt{\frac{m^2 f^2}{k^2} + N^2}}{k^2 + m^2}(k, 0, m). \tag{1.20}$$

The velocity of a group of waves is also generalised as follows

$$\underline{c}_g = \underline{\nabla}_{\underline{k}}\omega \equiv \left(\frac{\partial\omega}{\partial k}, 0, \frac{\partial\omega}{\partial m}\right), \tag{1.21}$$

which, on appeal to dispersion relation, equation 1.19, yields

$$\underline{c}_g = \frac{mk(N^2 - f^2)}{(k^2 + m^2)^{3/2}\left(m^2 f^2 + N^2 k^2\right)^{1/2}}(m, 0, -k). \tag{1.22}$$

Several remarks are in order now. First, it is immediate from equations 1.20 and 1.22 that $\underline{c}_p \cdot \underline{c}_g = 0$: that is, the group and phase velocities are perpendicular.

1.3.3 Gravity Waves Reflection and Transmission

Waves reflect and transmit where there are discontinuities in the propagation medium properties. For example, light (electromagnetic) waves as they pass from air to water, or long wavelength gravity waves in the ocean surface change direction as the ocean depth changes. The process can be understood as a consequence of physical change in plane wave propagation velocity and modelled by matching two infinite medium solutions, using appropriate physical constraints at the boundary e.g. w conditions.

For the 2D plane gravity waves considered in the previous sub-section, a change in buoyancy frequency, N, will cause such a change in the propagation speed. It follows that in a discontinuously stratified medium, in

which N changes from one value to another at the tropopause (with $\rho_0(z)$ still continuous, note), there will be gravity wave reflection back into the troposphere and refraction, or transmission into the stratosphere. This physical process has significant impact on our approach to the dynamics of adjustment in Chapters 2 and 3 and so is treated in context, in section 2.5.3.

1.3.4 Taylor-Goldstein Equation

In this section, we set Coriolis parameter $f = 0$. To provide further context for the work of Chapters 2, 3 we consider here the Taylor-Goldstein equation (Holton & Hakim, 2012), named after G. I. Taylor and S. Goldstein, who derived it independently in 1931. It is a differential equation which governs the behaviour of gravity wave perturbations in a flow with a vertically stratified base state, again derived from the two-dimensional Euler and continuity equations, using the Boussinesq approximation, elimination of variables and, importantly, an assumption of horizontally propagating solutions for density, pressure and the stream-function of the perturbation flow

$$[\rho, p, \psi] = \left[\hat{\rho}(z), \hat{p}(z), \hat{\psi}(z)\right] \exp(ik(x - ct)). \tag{1.23}$$

In equation 1.23 above, k is a wavenumber and $c \in \mathbb{C}$ is a phase speed, or eigenvalue. The Taylor-Goldstein equation is

$$(U - c)\left(\frac{d^2}{dz^2} - k^2\right)\hat{\psi} - \frac{\partial^2 U}{\partial z^2}\hat{\psi} + \frac{N^2}{U - c}\hat{\psi} = 0. \tag{1.24}$$

Here, $U(z)$ is the assumed base state of steady shear. For an imaginary c, the flow is unstable. We shall consider the process of solving equations similar to equation 1.24 in Chapters 2 and 3, using a modal expansion approach, where we shall derive an equivalent equation for an increased number of field variables and thermodynamic and fluid dynamic physics.

Returning to the discursive test-bench of the Taylor-Goldstein equation, we note that, for given k, if ψ is a solution for wave speed c, then ψ^* is a solution for wave speed c^*, that is, for every stable solution there is an unstable solution of the Taylor-Goldstein equation (Gill, 1982; Vallis, 2006). One could find solutions to equation 1.24 by applying boundary conditions from a physical boundary condition that $w = 0$ at the Earth's surface and on some effective lid a distance H aloft

$$\hat{\psi}(0) = \hat{\psi}(H) = 0. \tag{1.25}$$

We shall see in Chapters 2 an 3 that it is such boundary conditions as 1.25 above that facilitate the determination of the wave speeds, c, as eigenvalues which then allow the solutions of equation 1.24. (Note, this is not the only boundary conditions to yield solutions. For example, over

a sinusoidal hill a radiative upper boundary condition would also yield solutions).

Our test-bench discussions regarding atmospheric gravity waves in this section could be designated 'textbook'. However, Chapter 2 considers domain and physical stratification which is, essentially, a combination of the cases outlined in this introduction. Not surprisingly, therefore, the mathematical treatment there uses discrete, superposing spatially separable solutions, each with the essential character of a solution for trapped gravity waves. Their interpretation in the context of meteorology will rely on understanding of infinite media gravity waves and their interaction with a material discontinuity.

In the next two sections we delve deeper into the science, to consider further example cases which are still the focus of much research, which illustrate the *interaction*, or coupling between atmospheric convection and, among other things, gravity waves.

1.4 The Influence of Gravity Waves on the Weather and Climate System

As we have discussed, gravity waves influence the general circulation of the atmosphere through their transport and deposition of momentum. The equations which govern the atmosphere, under statically stable conditions, permit a further range of wave solutions and gravity waves can be generated by airflow over mountains, vertical shear or the penetration of stable layer by convection, to name a few. As they propagate, these gravity waves make adjustments to mass and momentum fields, moving and manoeuvring the atmosphere towards a balanced state.

In this section, in order to give context to our subsequent results chapters, particularly Chapter 5, we discuss some well-known, relatively simple examples of gravity waves' influence on the weather and climate system, reserving for the next section an introduction to the problem of gravity wave coupling to convection.

1.4.1 Ducted Gravity Waves

Typically, waves generated in the lower atmosphere will transfer much of their energy upward, thus losing much of their energy by the time they have travelled a few wavelength horizontally from their source. However, if some mechanism, such as a change in wind shear, alters the static stability with height, upward propagating waves can be reflected, channelling the waves to propagate large horizontal distances from their source. An example recipe for wave ducting is low stability air (which implies evanescent waves) overlying a stable layer, which is often found near the ground at night in arid regions. Strong curvature in a jet flow can also cause trapping. The mathematics of such ducted, or trapped,

gravity wave was discussed in section 1.3.1.

Ducted gravity waves can impact the weather by producing bands of clouds and precipitation remote from their source, or even contribute to convection initiation. For an extensive case study, see Ralph *et al.* (1993), who measured ducted gravity waves over Southern France. For further reading, see, e.g., Francis (1975), Lindzen & Tung (1976), Fritts & Alexander (2003).

1.4.2 Mountain Gravity Waves

Varying orography beneath an airflow provides a mechanism of vertical displacement, and as such, gravity wave generation. Wave energy originating from the terrain can propagate upward to the top of the troposphere, and relatively small mountains may affect airflow a considerable distance above the ground. Under other atmospheric conditions, such as those responsible for ducted gravity waves, most of the wave energy can be trapped in a layer near the surface extending downstream from a mountain. These are known as trapped lee waves, the mathematics of which is described by the Taylor-Goldstein equation (see section 1.3.4 above). A well known solution of the Taylor-Goldstein equation was first found by Scorer (1949), who wrote a modified version of equation 1.24 for perturbation vertical velocity, which reads

$$\frac{d^2\hat{w}}{dz^2} + (l^2 - k^2)\hat{w} = 0, \tag{1.26}$$

where

$$l = \sqrt{\frac{N^2}{U^2} - \frac{1}{U}\frac{d^2U}{dz^2}}, \tag{1.27}$$

where $U = U(z)$ is the vertical profile of horizontal wind. Here l is known as the *Scorer parameter*. Whether the Scorer parameter is bigger or smaller than k^2, we obtain fundamentally different solutions to 1.26, which relate to the nature of lee wave vertical propagation or trapping. Trapping conditions are favoured when $l^2(z)$ decreases strongly with height (especially if the Scorer parameter drops suddenly in the mid-troposphere which then separates into a lower layer with high stability (l^2 large) and an upper layer with low stability (l^2 small)). As such, the Scorer parameter is often used by meteorologists who wish to determine if gravity waves will develop or not. In practice, it is derived from vertical soundings or wind and temperature upstream of a mountain chain to forecast the probability of lee wave development.

If sufficient moisture is present, orographic gravity waves can lead to the formation of beautiful lenticular clouds, as shown in figure 1.5.

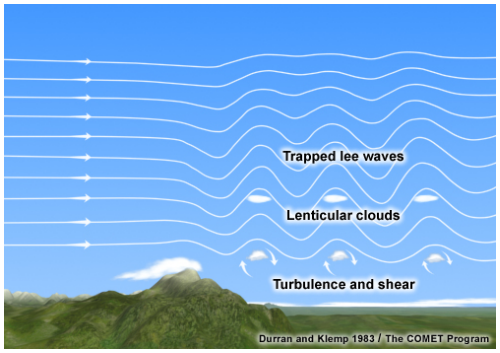

Figure 1.5: Schematic of clouds related to trapped lee waves. From the Cooperative Program for Operational Meteorology, Education, and Training (COMET), adapted from (Durran & Klemp, 1983).

For an overview on mountain-generated gravity waves, see e.g. Fritts & Alexander (2003); Nappo (2013); Scorer (1949); Smith (1979).

1.4.3 Stratospheric Gravity Waves

Gravity waves forced by disturbance in the troposphere, such as orography or convection can propagate to large altitudes high up in the stratosphere and mesosphere. As the air thins, the amplitude of the waves increases, and eventually non-linear effects lead to wave breaking, which transfers their momentum to the mean flow. As such, stratospheric gravity waves can play a role in interesting meteorological features such as the Quasi-Biennial Oscillation (Baldwin *et al.*, 2001). It is beyond the scope of this thesis for a detailed discussion on stratospheric gravity waves, but one could read Fritts & Alexander (2003) for a review.

1.4.4 Atmospheric Rossby Adjustment

The ratio of the horizontal, non-linear term in the fluid momentum equations to the Coriolis term defines Rossby number

$$R_o \equiv \frac{\text{non-linear horizontal acceleration}}{\text{Coriolis acceleration}} = \frac{U^2/L}{fU} = \frac{U}{fL}. \qquad (1.28)$$

Here U is a chosen, reference horizontal velocity, and L is a reference horizontal distance. In Chapter 4 we shall choose for L the horizontal length scale of the applied heat forcing. It is sometimes convenient use the Rossby radius of deformation as an alternative to R_o to characterise the response of the atmosphere to forcing. This is the distance, L_R, over which rotational effects become as important as gravity wave effects. We can conveniently approximate this distance for present purposes as follows. Again return to equation 1.9, for gravity waves, and observe that this balance is reached when its term in f compares to the other

terms i.e. $f^2\frac{\partial^2 w}{\partial z^2} \approx N^2(z)\frac{\partial^2 w}{\partial x^2}$. Applying simple scaling arguments and considering the nth mode (so that z derivatives scale as H/n), we have $\frac{f^2 w}{n^2 H^2} = \frac{N^2 w}{L_{R,n}^2}$ that is

$$L_{R,n} = \frac{NH}{nf}. \tag{1.29}$$

For quasi-steady, large-scale, bulk motions in the atmosphere (or ocean) an often acceptable approximation is $R_o \ll 1$, which simplifies the steady, horizontal momentum equations 1.8 to a *geostrophic balance* between Coriolis' force and the pressure gradient: $-fv = \frac{1}{\rho_0(z)}\frac{\partial p}{\partial x}$, $fu = \frac{1}{\rho_0(z)}\frac{\partial p}{\partial y}$. p serves as the horizontal velocity stream-function to the horizontal velocity adjustment, which defines a *geostrophic equilibrium*. Specifically, a geostrophic equilibrium in non-viscous geophysical fluid dynamics is a motion with Coriolis force balancing horizontal pressure forces.

The approach of perturbed, rotating fluids to steady-state, geostrophic equilibria (if they exist) is a classic problem in several branches of geophysical fluid dynamics, widely dubbed the *Rossby adjustment process*. On synoptic scales, rotation in fluids couples to planetary rotation, so the determination of a geostrophic equilibrium and the formulation of the Rossby adjustment dynamics commonly is based upon potential vorticity Gill (1982), which is a conserved quantity for many systems. We shall return to this matter in Chapter 4.

In terms of recent history, the dynamics of Rossby adjustment is most transparently addressed in the context of rotating shallow layers of incompressible liquid with mechanical perturbations, for example with initial surface discontinuities (Gill *et al.*, 1986), with surface discontinuities and boundaries (Gill, 1976) and with atmospheric storm-induced stresses stirring the mixing layer (Gill, 1984). This is because shallow water formulation may be reduced to three field variables. Typically, the final state of the system, after all transients have propagated off, has a structure which is controlled by L_R. For example, Gill (1976) has shown that final state currents parallel to a left boundary (for the Northern Hemisphere) represent a geostrophic adjustment to flow in a long, rotating channel when L_R is small compared with channel width. A compact, self-contained account of the prediction of a final state of surface deformation, after Rossby adjustment, may be found in section 7.2 of Gill (1982). This steady solution (equation (7.2.22)) for an initial surface discontinuity contains only one length scale- that of the Rossby radius of deformation, L_R. For further reading, see Bannon (1995) and Chagnon & Bannon (2005).

Gill's solution, despite neatly having only one length scale, does not take account for the upward dispersion of energy as we see in the real atmosphere. In Chapter 4 we address this by considering a deep atmosphere, subject to a thermodynamic perturbation i.e. a finite interval of heat forcing. To investigate the effects of rotation on the systems of

Chapters 2,3, we shall formulate a Rossby adjustment problem analogous to the those outlined above, but with the steady-state thermal wind and a pressure fields used to define an analog of geostrophic adjustment. We consider what effect upward radiation of wave energy has on L_R. The steady solution presented in Chapter 4 will be shown to contain two effective length scales: the Rossby radius and a scale determined by the scale of the applied buoyancy forcing.

1.5 Interaction Between Atmospheric Gravity Waves and Convection

Various sources of gravity wave generation have long been identified. These include the waves generated, or forced, by orography and wind shear, considered in the last section and, of most interest in this thesis, convection. The mechanisms for the generation of gravity waves by topography and wind shear have been studied extensively, but convective generation mechanisms are less well understood, probably because the case of convectively forced gravity waves is not simple.

Convection modifies its environment primarily through gravity waves, and the rapid onset of deep convection (order of minutes) typically leads to a wave-front which communicates compensating subsidence into the environment (Bretherton & Smolarkiewicz, 1989). Figure 1.6, taken from Fovell et al. (1992) graphically illustrates this process.

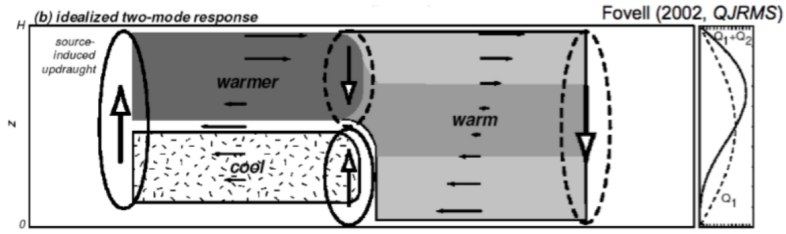

Figure 1.6: Schematic of convective adjustment mediated by gravity waves. Taken from Fovell et al. (1992).

1.5.1 Convectively Forced Gravity Waves

Convection can be triggered, or suppressed, by gravity waves. Further, convection and waves occur in concert- it is difficult to deduce cause and effect from either alone.

Although it has been known for some time that convection can excite gravity waves, only more recently have observations and models begun to characterise the source mechanisms and dynamics of convectively forced waves. This is in large part due to the lack of single characteristic phase speed or frequency- convection generates waves throughout a range of

phase speeds, frequencies and vertical and horizontal scales. We shall see this clearly, in our work in chapters 2, 3.

Numerical Models have greatly enhanced our understanding of waves generated by convection, but there remain many open questions. Possibly most significant, moist convection provides a time-dependent thermal forcing (due to latent heat release) that can interact with overlaying stable layers and shear in complex ways that are not fully understood. Three mechanisms have been proposed to describe convective generation. In simplified form

1. Gravity waves are forced by temporal variations of the diabatic heating within the cloud. Studies based on numerical simulations and models have shown that, in this mechanism, the dominant vertical wavelength of the excited tropospheric gravity waves is approximately twice the depth of the heating (e.g. Alexander *et al.* (1995); Bretherton (1988); Lane & Reeder (2001); Piani *et al.* (2000)).

2. "Obstacle effect": an up-draught develops in shear and blocks the flow, producing cloud-relative flow across the top of the cloud (e.g Clark et al. 1986). Thus, waves are generated in a similar way to the mountain waves discussed above.

3. A "mechanical oscillator" individual up-draught decelerates rapidly at the tropopause, and oscillates about the level of neutral buoyancy (Fovell et al. 1992).

In reality, the three mechanisms are not distinct, but coupled. This thesis will focus on the dynamics of thermally forced gravity waves in chapters 2 and 3, on their environmental legacy in chapter 4 and their signature in chapter 5.

1.5.2 Convectively Coupled Waves

Tropical deep convection is observed to be organised on the synoptic and mesoscale (Tulich *et al.*, 2007; Wheeler & Kiladis, 1999), and it is argued that gravity waves provide a mechanism for the aggregation of cumulonimbus storms (Tulich *et al.*, 2011) as they communicate the necessary atmospheric adjustment to the neighbouring troposphere through subsidence or lifting. The "gregarious" nature of mesoscale tropical convection cells is thought to be driven (at least in part) by a low-level rising mode in the vicinity of a convecting storm, which increases the depth of moisture at low-levels, making conditions more favourable for new convective events (Fovell *et al.*, 1992; Mapes, 1993). Momentum and temperature changes, communicated through the propagation of convectively generated gravity waves may also condition the remote troposphere to convection triggering or suppression (Bretherton & Smolarkiewicz, 1989; Pandya *et al.*, 2000; Shige & Satomura, 2000).

Gravity waves modify the troposphere through vertical motion. If the vertical motion at low levels is strong, of the order of metres per second as may occur in a trapped gravity wave or bore, then this may directly trigger deep convection (Emanuel *et al.*, 1994). However, even relatively weak vertical motion on the order of centimetres per second will induce adiabatic warming and cooling that modifies the stability of the atmospheric profile, through its CAPE and convective inhibition (CIN). A number of case studies focus upon tropospheric gravity waves' initiation and/or control of the initiation of convection at locations remote from the parent storm (Hankinson *et al.*, 2014; Lac *et al.*, 2002; Zhang *et al.*, 2001). In particular, gravity waves have been observed to suppress the second initiation of convection through waves of subsidence for up to six hours after initial forcing, until waves of low-level ascent remove the inhibition and allow the convection to occur (Birch *et al.*, 2013; Marsham & Parker, 2006).

In any such study, there is an open question of whether the strength of the gravity wave signal in the far field from the source is dependent on trapping of the waves within the troposphere. For example Lindzen and Tung (1976) showed that a change in stability at the tropopause plays a part in the formation of deep tropospheric gravity wave modes as waves will be partially reflected due to the sudden change in stability. The trapping conditions can be non-trivial to diagnose on a case by case basis. Conditions of trapping could be met for certain ranges of horizontal wavenumber if there are suitable patterns of wind profile and stratification (Birch *et al.*, 2013), and when trapping occurs, a rigid lid model may be suitable to analyse the wave field. More generally a radiative boundary condition located at the tropopause is, physically, more realistic than a rigid lid but it is mathematically disruptive (Edman & Romps, 2017). Certainly, such a condition does not lend itself to an analytical treatment of forced convection. However, previous theoretical studies have shown that one can circumvent this difficulty with a high rigid lid (Holton *et al.*, 2002; Mapes, 1998; Nicholls *et al.*, 1991) and still retain wave-like structures in the troposphere. Nicholls et al. constructed a restricted, idealised semi-analytical model using a Dirichlet rigid lid condition, the location of which is raised aloft, to address the influence of gravity waves in adjusting the neighbouring cloud-free troposphere. The importance of mode 1 and 2 gravity waves is apparent in their results and confirmed by Lane and Reeder (2011), who show that the mode 3 gravity wave also plays a significant role in modifying convective inhibition in the neighbourhood of deep convection.

The Earth's rotation also affects the tropospheric response to deep convection: the gravity waves are part of a Rossby adjustment to the convection, and their propagation establishes a larger-scale balanced response to the potential vorticity field created by the convective sources. Inclusion of planetary rotation also significantly increases the complexity of the problem, by perturbing the gravity wave dispersion relation, mak-

ing mathematically tractable gravity wave modes elusive . Numerical studies that have examined isolated clouds in rotating frames (Andersen & Kuang, 2008; Shutts & Gray, 1994) and indicate that the Coriolis force is important in reducing the radius of influence of the wave modes (Liu & Moncrieff, 2004).

1.6 Motivation and Previous Studies

As we have seen, it has been known for some decades that deep convection interacts with gravity waves. Convection is known to force a spectrum of gravity waves, which communicate the adjustment to convection into the environment (Bretherton & Smolarkiewicz, 1989). These waves have been observed to feed back onto convection (Fritts, 1984; Tulich & Kiladis, 2012), and can even be responsible for further convection (Birch *et al.*, 2013; Marsham & Parker, 2006). However, observations have proved difficult, and have not yet provided a complete description of the convection-wave relationship due to poor coverage (e.g. Alexander *et al.* (2008)).

Most of our knowledge of convectively coupled waves has relied on numerical models. Successful studies have clarified the dynamics of wave generation (Clark *et al.*, 1986; Fritts & Nastrom, 1992; Lane & Reeder, 2001; Lane *et al.*, 2001; Zhang, 2004), determined the role of wind shear (Beres *et al.*, 2002), examined the effects of rotation (Liu & Moncrieff, 2004; Shutts & Gray, 1994), interrogated the wave field forced by a realistic cloud (Alexander *et al.*, 1995; Beres, 2004) and found evidence for convection-wave coupling (Lane & Zhang, 2011; Tulich *et al.*, 2007).

Whilst models are extremely useful, they are not perfect. Large-scale GCMs are extremely complex and contain many interacting processes, meaning convection-wave relationships are difficult to untangle. Further, in the case of GCMs, whose resolution is on the order of 100 km, convection and gravity waves are not fully resolved, leading to incorrect convectively coupled gravity wave spectra. In order to obtain accurate predictions, modelers apply a gravity wave drag parameterisation scheme (e.g. Lindzen (1981)). Whilst current convection schemes hold some information about the subgrid cloud field, they do not use any subgrid cloud information in the excitation of gravity waves: waves are only forced by the grid-resolved tendencies imposed by the convection scheme. This leads to a possible mis-match between the true field of gravity waves excited by subgrid convection on the kilometre scale and the gravity waves forced on the grid scale by the convection scheme.

In order to develop accurate parameterisation schemes, it is important to understand the mechanisms that generate gravity waves. However, the convective generation mechanisms are not well understood. Existent parameterisation schemes do not satisfactorily capture of the spatial and temporal distribution of cumulonimbus storms- a clear indicator that current understanding is deficient (Stephens *et al.*, 2010). Whilst this

may be attributable to other, omitted physical processes and feedbacks, an improved representation of gravity wave-convection interactions also provides a candidate process worthy of deeper investigation.

A mathematical study with relatively few parameters allows a more straightforward investigation. Most mathematical studies have been based on linear theory, in which waves can be considered perturbation to the base state. Idealised studies have interrogated the interaction and self-organisation between tropospheric gravity waves and deep convection (Emanuel, 1986; Lindzen, 1974; Raymond, 1983). More fundamental models based on simple equations have also been useful in , for example, unveiling the "gregarious" nature of convection (Mapes, 1993), predicting the dynamics of convectively forced gravity waves (Nicholls *et al.*, 1991; Parker & Burton, 2002) and quantifying the effect of the tropopause boundary (Edman & Romps, 2017).

In summary, we need to study convective-gravity wave interactions as they play an important role in the weather and climate. Observations have not provided concrete descriptions, and therefore numerical modelling is needed. Since convection and some wave activity is not resolved in complicated GCMs, a parameterisation scheme is required in order to provide accurate predictions of convection-wave interactions. In order to apply an accurate, successful parameterisation, we need to understand the fundamental physics. Mathematical models simplify the problem, and allow quantitive estimates of the characteristics of convection and gravity wave interactions.

We now outline the problems addressed in this thesis, which is largely (but not exclusively) based on mathematical models.

1.7 Thesis Outline

The bulk of this thesis (Chapters 2, 3, 4) is organised around the mathematics and meteorology of three, related, essentially analytical models, all of which address buoyancy-forced, gravity-wave mediated adjustment to convection, in a stratified atmosphere, with a potentially radiating tropopause. These models only capture one part of the problem: the forcing of gravity waves by convection, without feedback of gravity waves onto convection. However, Chapter 5 does attempt to assess gravity wave coupling to predominantly equatorial convection, by examining cutting-edge, high resolution, convection-permitting Unified Model data. The guiding ethos of all the work (other than that of Chapter 5) is the development of analytical models and qualitative understanding.

In Chapter 2 we use a prescribed tropospheric heat source to model convective heating to investigate: (1) What is the gravity wave response, and (2) how does the response depend upon (i) the lengthscale of the forcing? and (ii) the upward radiation of energy at the tropopause? The latter is a key question, and the solution can depend upon whether the troposphere is bounded by a rigid lid, or instead has some model

stratosphere. To facilitate our investigations, we develop a transient, non-rotating model of buoyancy forcing, in a 2D stratified atmosphere, with a radiating tropopause and a variable base state of density, after Nichols et al. 1991 and Edman and Romps 2017. This model is predominantly analytical (except for a reliance on a numerical solution of its eigenvalue equation). Notably, it separates horizontal and vertical variation, the latter being based upon a modal decomposition, it derives from a closed description, in linear theory, based upon field variables u, w, b and p with prescribed $\rho_0(z)$ variation (necessitated by the deep nature of the convection we aim to address) and heat or buoyancy forcing, S (mainly the first baroclinic mode). After suitable assessment, the 2D model of Chapter 2 is used to examine the effects of radiation at the tropopause from a fundamental perspective, to assess its impacts in the context of numerical models' parametrisation and to assess secondary convection triggering. A pleasing mathematical feature of the 2D model of Chapter 2 is that its predicted adjustments all emerge from superposed modes, each with a propagation speed equal to the eigenvalue which enters the vertical problem.

Having established the credentials of our essential approach to upward gravity wave radiation, a compellingly simple question arises from the work of Chapter 2, namely: what is the impact of the third, spatial dimension? In Chapter 3 we develop an axially symmetric 3D model with, we stress, an otherwise equivalent physical and mathematical composition as that in Chapter 2. In cylindrical geometry, a key difference is that the forced gravity waves decay as they move outward due to geometrical constraints (to conserve energy), and studies of gravity waves show concentric wave bands being emitted from a central storm (e.g. Lane & Reeder (2001); Piani *et al.* (2000)). What might be the knock-on effects for the triggering of further convection? In Chapter 3, we modify the model of Chapter 2 to an extended basic set which includes v and, based upon more general Sturm-Liouville theory (Arfken, 1966). Here, Hankel-Laplace (rather than Fourier-Laplace) transform techniques become necessary to address a modified horizontal variation. Moreover, the inversion from reciprocal space must be performed numerically.

Another simple question arises: what is the influence of rotation? Without background rotation, a period of transient forcing does not lead to a local response at large time (with the large time response taking the form of radiating gravity waves, which may decay in amplitude as they radiate upwards and outwards). With background rotation, there is a completely different possibility: the generation of a local pressure anomaly (with associated buoyancy anomaly), that is in geostrophic balance with a transverse wind. We regard the study of this ultimate balanced vortex state as being a fundamental question. In particular, how does the horizontal lengthscale of the balanced state depend upon that of the forcing and the underlying system (i.e., the deformation radius)? What is the vertical structure of the response? We do this by consid-

ering the changes to the potential vorticity via the prescribed heating, in what may be regarded as a Rossby adjustment problem. Chapter 4 deals with the post-convection steady state, but again, we stress, with otherwise equivalent physical and mathematical composition as that in Chapter 2. A more substantial generalisation of the mathematical framework will be required, as we now include a transverse wind component. Furthermore, limiting cases must be considered analytically, using a non-dimensionalisation approach, fully to interpret our meteorologically relevant data.

Chapter 2...4 have dealt with analysing the gravity wave response to prescribed thermal forcing. However, what is often seen in the real world is the outcome of a fully-coupled system, in which the convection forces gravity waves and the gravity waves force convection. In Chapter 5, we examine the nature of this fully coupled response. In particular, we use high-resolution, convection permitting Met Office Unified Model simulations of the sub-Saharan African climate to analyse the frequency-wavenumber spectra of moisture and dynamical fields (OLR, rainfall, vertical velocity and potential temperature) for gravity wave-like response. Tulich and Kiladis (2012) found evidence of coupling between convection and gravity waves in analysis of TRMM data. TRMM, however, has the limitation of being relatively low resolution. Here, we are using a dynamical model at much higher resolution, and thus see the outcome of a fully coupled grave wave-convective system. In such systems, what are the typical speeds of (coupled) gravity waves? Do these couple to equatorial modes? How is the spectrum the result of many individual storm events? Chapter 5 characterises the structure and properties of convectively coupled gravity and e.g. Matsuno (1966) wave modes, now based upon a numerical approach. Our methodology is adapted from that of Wheeler and Kiladis (1999) and involves a latitudinal compression of physical fields which are suitable proxies for convection and then filtration and subsequent Fourier inversion of data in reciprocal space.

The pursuit of relatively simple (semi-)analytical models has been fruitful and has illuminated some non-trivial aspects of convective adjustment, and has opened many avenues for further research. Analysis of high-resolution, fully coupled convection gives insight into the nature of real system and provides some context for our analytical results. We finish in Chapter 6 with a discussion of our results, and reflect on further research questions that arise.

Chapter 2

Forced Gravity Waves and the Tropospheric Response to Convection

2.1 Introduction

In this chapter we will present theoretical work directed toward improving our understanding of the mesoscale influence of deep convection on its tropospheric environment through forced gravity wave effects. From a simple set of linear, hydrostatic, non-rotating, incompressible equations, we find a two-dimensional analytical solution to prescribed heating in a stratified atmosphere, which is upwardly radiating when the domain lid is sufficiently high. We interrogate the spatial and temporal sensitivity of both the vertical velocity and potential temperature to different heating functions, considering both the near-field and remote responses to steady and pulsed heating. We find that the mesoscale tropospheric response to convection is significantly dependent on the upward radiation characteristics of the gravity waves, which are in turn dependent upon the temporal and spatial structure of the source, and the assumed stratification. Finally, we will make comparisons with an idealised Met Office Unified Model simulation. The majority of this chapter has (at the time of writing) recently been published in the Quarterly Journal of the Royal Meteorological Society.

2.2 Background

Here, based on an analytical description of a deep atmosphere which is thermally forced via a prescribed heating function, we build a model capable of addressing two questions:

1. What is the effect of the conditions of upward wave radiation on the spatial and temporal distribution of convective adjustment, over the timescales of a few hours, relevant to mesoscale dynamics?

2. What is the influence of spatial and temporal structure of thermal forcing on gravity wave characteristics? In particular, do changes in the thermal forcing function, on a scale unresolved by a GCM, lead to significant differences in the tropospheric response to that forcing?

In this Chapter, we extend the analytical work of Nicholls et al. (1991), Holton et al. (2002) and Edman and Romps (2017) to address the above questions, assessing the mesoscale effect of horizontal and vertical variation in the pattern of convective forcing, with special attention paid to the sensitivity of the remote horizontal response, as well as atmospheric stratification. Specifically, we develop and apply a suitable analytical model that accommodates variation in both the spatial and temporal patterning of thermal forcing. To facilitate an analytical study, we will found our model on idealised, linear equations for a deep atmosphere and generalise a technique due to Nicholls et al. (1991) in which the upper boundary or lid of the domain is many times higher aloft than the tropopause, so that the solution asymptotes to what can be considered a pseudo-radiating regime. As in those previous studies, we choose two-dimensional planar geometry in an environment without vertical shear. The importance of shear in squall line development has been shown by Thorpe et al. 1982, Rotunno et al. 1988 and Schmidt et al. 1990, but studies have confirmed it is not necessary in all cases (Barnes & Sieckman, 1984), and a symmetrical response can even be found in simulations with complicated environmental wind (Nicholls, 1987). Furthermore, real deep convection also occurs in more complex geometries, and there are a number of interesting studies tackling aspects of this problem by utilising fully 3D numerical simulations with complex physics. In such simulations, more realistic physical features, such as typhoon generated gravity waves (Kim *et al.*, 2014; Kim & Chun, 2011; Ong *et al.*, 2017), mesoscale circulation around squall lines (Pandya *et al.*, 2000), and gravity waves generated by deep convection (Lane & Reeder, 2001; Piani *et al.*, 2000) can be understood. Two-dimensional planar geometry in the absence of shear (which achieves wave reflection/refraction through a change in stratification) is chosen here as the simplest model with which we can confront the above questions.

Before we begin, it is pertinent to cast a closer eye over two publications which contain a similar content to that of this chapter.

2.2.1 Previous Work

Whilst this Chapter will consist of original work, we will on occasion make reference to a couple of similar studies, namely Nicholls et al. (1991) and Edman and Romps (2017). Both previous studies have sought analytical solutions to a forced, 2D, hydrostatic deep atmosphere. Here, we will address different problems to those considered by Nicholls et al. (1991)

and Edman et al. (2017), but it is still useful to take care in comparing models. Table 2.2.1 details the differences.

	Model Composition		
	Halliday et al. 2018	Nicholls et al. 1991	Edman et al. 2017
Horizontal Forcing Structure	$\exp\left(-\frac{x^2}{2L}\right)$	$\frac{L^2}{(x^2+L^2)}$	$\delta(x)$
Vertical Forcing Structure	$\sin(\frac{n\pi z}{H})$	$\sin(\frac{n\pi z}{H})$	$\delta(z)$
Heating rate ($\mathrm{K\,s^{-1}}$)	0.01	0.02	0.01
Method	Modal Expansion	Modal Expansion	Green's Function
Tropopause Height (km)	10	10	17
Trapped cases	yes	yes	no
Piecewise N(z)	yes	no	yes
N_t	0.01	0.01	0.01
N_s/N_t	2	1	2.5

Table 2.1: Differences in the analytical models of Halliday et al. (2018) Nicholls et al. (1991) and Edman et al. (2017)

We will now detail the derivation of our analytical model.

2.3 Mathematical Model

2.3.1 Governing equations

We consider small disturbances about a state of rest, in a two-dimensional incompressible fluid. The governing equations for hydrostatic flow are

$$\begin{aligned} \frac{\partial u}{\partial t} &= -\frac{1}{\rho_0(z)}\frac{\partial p'}{\partial x}, \quad \frac{1}{\rho_0(z)}\frac{\partial p'}{\partial z} = b, \\ \frac{\partial b}{\partial t} + N^2 w &= S, \quad \frac{\partial u}{\partial x} + \frac{\partial w}{\partial z} = 0, \end{aligned} \tag{2.1}$$

where (u, w) is the wind vector, p' is the perturbation pressure, $\rho_0(z)$ is the basic state density, $b = -g\rho'/\rho_0(z)$ is the buoyancy (where ρ' is the perturbation density), $S(x, z, t)$ is a prescribed buoyancy forcing, and $N(z)$ is the buoyancy frequency, defined by

$$N^2(z) = -\frac{g}{\rho_0(z)}\frac{\mathrm{d}\rho_0(z)}{\mathrm{d}z}. \tag{2.2}$$

We do not make the Boussinesq approximation, i.e., ρ_0 is not taken to be constant in the horizontal momentum equation, so that the effects of a deep (albeit incompressible) atmosphere are included. (e.g., see §6.4 of Gill (1982). This is a widely-used system of equations in dynamical meterology (e.g., Lindzen (1974), Chumakova et al. (2013))

The buoyancy forcing S, with units of $\mathrm{m\,s^{-3}}$, arises due to a thermal forcing Q, with units of $\mathrm{K\,s^{-1}}$, which in a more complete description would appear in the potential temperature equation $D\theta/Dt = Q$. We use a Boussinesq-like correspondence between the two, with

$$S = \frac{gQ}{\theta_0}, \tag{2.3}$$

where θ_0 is a reference potential temperature (taken to be 273 K). Later on, we will also evaluate a potential temperature perturbation θ' from b, again using a Boussinesq-like correspondence

$$b = \frac{g\theta'}{\theta_0}. \tag{2.4}$$

Eliminating variables in (2.1), a single equation for the vertical velocity w may be obtained in terms of S:

$$\frac{\partial}{\partial z}\left(\rho_0(z)\frac{\partial}{\partial z}\frac{\partial^2 w}{\partial t^2}\right) + \rho_0(z)N^2(z)\frac{\partial^2 w}{\partial x^2} = \rho_0(z)\frac{\partial^2 S}{\partial x^2}. \tag{2.5}$$

This is to be solved between rigid lower and upper boundaries at $z = 0$ and $z = H$:

$$w(z=0) = 0, \quad w(z=H) = 0. \tag{2.6}$$

2.3.2 Modal Expansion

Free modes of the form $w = A(x - c_n t)\phi_n(z)$ (where A is any given function) with horizontal wave speed c_n, satisfy (2.5) and (2.6) provided

$$\begin{aligned} \frac{\mathrm{d}}{\mathrm{d}z}\left(\rho_0\frac{\mathrm{d}\phi_n}{\mathrm{d}z}\right) + \frac{\rho_0 N^2}{c_n^2}\phi_n = 0, \\ \phi_n(0) = \phi_n(H) = 0, \end{aligned} \tag{2.7}$$

where $\rho_0(z)$ and $N(z)$ are linked via (2.2). From (2.7), it follows that the eigenvalues c_n are real, and that the eigenfunctions $\phi_n(z)$ satisfy an orthonormality condition:

$$\int_0^H \rho_0 N^2 \phi_n \phi_m \,\mathrm{d}z = \delta_{nm}. \tag{2.8}$$

Since the eigenfunctions, $\phi_n(z)$, are complete, the vertical structure

of $w(x,z,t)$ and $S(x,z,t)$ can be written as

$$\begin{aligned} w(x,z,t) &= \sum_{j=1}^{\infty} w_j(x,t)\phi_j(z), \\ S(x,z,t) &= N^2(z)\sum_{j=1}^{\infty} S_j(x,t)\phi_j(z). \end{aligned} \tag{2.9}$$

The inclusion of the pre-factor $N^2(z)$ in S is for mathematical convenience, so that when multiplied by $\rho_0\phi_n$ and integrated over $0 < z < H$ we obtain

$$S_n(x,t) = \int_0^H \rho_0(z)\phi_n(z)S(x,z,t)\,\mathrm{d}z, \tag{2.10}$$

i.e. $S_n(x,t)$ is completely determined by the given buoyancy forcing $S(x,z,t)$. However, the modal expansion coefficients $w_n(x,t)$ must be found from evolution equations, which are obtained by multiplying (2.5) by ϕ_n and integrating over $0 < z < H$ yielding

$$-\frac{1}{c_n^2}\int_0^H \rho_0 N^2\phi_n\frac{\partial^2 w}{\partial t^2}\,\mathrm{d}z + \int_0^H \rho_0 N^2\phi_n\frac{\partial^2 w}{\partial x^2}\,\mathrm{d}z = \int_0^H \rho_0\phi_n\frac{\partial^2 S}{\partial x^2}\,\mathrm{d}z, \tag{2.11}$$

where the first term has been twice integrated by parts, and we have used (2.7). Substituting the modal expansions (2.9) and using (2.8) we obtain

$$\frac{\partial^2}{\partial x^2}w_n(x,t) - \frac{1}{c_n^2}\frac{\partial^2}{\partial t^2}w_n(x,t) = \frac{\partial^2}{\partial x^2}S_n(x,t), \tag{2.12}$$

which, for $S = 0$ simplifies to the second order wave equation, for free modes of horizontal speed c_n.

Equation (2.12) is the basis for the rest of this study. Once solved, we shall find the full solutions for $w(x,z,t)$ from (2.9) and for $b(x,z,t)$ by integrating $\partial b/\partial t = S - N^2 w$.

2.3.3 Buoyancy forcing: temporal structure

We assume a separable buoyancy forcing of finite duration, T

$$S(x,z,t) = S_0 X(x)Z(z)\left(\Theta(t) - \Theta(t-T)\right), \qquad T > 0. \tag{2.13}$$

Here $Z(z)$ and $X(x)$ are vertical and horizontal structure functions with maximum amplitude unity, $\Theta(t)$ is the Heaviside function, and S_0 is the maximum value of the buoyancy forcing. Then (2.12) becomes

$$\frac{\partial^2 w_n}{\partial x^2} - \frac{1}{c_n^2}\frac{\partial^2 w_n}{\partial t^2} = S_0\sigma_n\frac{\partial^2 X}{\partial x^2}\left(\Theta(t) - \Theta(t-T)\right),$$

where

$$\sigma_n = \int_0^H \rho_0(z)\phi_n(z)Z(z)\,\mathrm{d}z. \tag{2.14}$$

This may be solved, for arbitrary $X(x)$, using a Fourier transform in x (with conjugate variable k) and a Laplace transform in t (with conjugate variable p), following Nicholls *et al.* (1991). Using standard transform relations (e.g., Arfken, 1966) we obtain

$$\tilde{\tilde{w}}_n(k,p) = \frac{S_0 c_n^2 \sigma_n k^2 \tilde{X}(k)}{p\,(p+ic_nk)\,(p-ic_nk)}\left(1-e^{-pT}\right). \tag{2.15}$$

Here $\tilde{X}$ denotes the Fourier transform of $X(x)$, and $\tilde{\tilde{w}}$ the Fourier and Laplace transform of w. The above result assumes quiescent initial conditions, and that $w \to 0$ as $|x| \to \infty$ sufficiently quickly for the Fourier transform to exist.

Using the delay theorem of Laplace transforms (e.g., Arfken, 1966) on the partial fraction expansion of (2.15), taking inverse Laplace and Fourier transforms yields

$$\begin{aligned} w_n(x,t) &= S_0\left(1-\Theta(t-T)\right)X(x)\sigma_n \\ &- \frac{S_0}{2}\left(X(x+c_nt)+X(x-c_nt)\right)\sigma_n \\ &+ \frac{S_0}{2}\Theta(t-T)\left(X(x-c_n(t-T))\right)\sigma_n \\ &+ \frac{S_0}{2}\Theta(t-T)\left(X(x+c_n(t-T))\right)\sigma_n. \end{aligned} \tag{2.16}$$

A few remarks are now appropriate. As in Nicholls et al. (1991) and Parker and Burton (2002), the modal solution contains non-dispersive waves moving leftwards and rightwards with speed c_n. Also note (2.16) holds for any buoyancy forcing for which the horizontal and vertical structure is separable, and for any stratification; the response to steady buoyancy forcing may be obtained on setting $T \to \infty$, when terms with factor $\Theta(t-T)$ disappear.

The full vertical velocity, $w(x,z,t)$, can be determined from (2.16) when used with (2.9). The corresponding buoyancy response, $b(x,z,t)$, is obtained by substituting (2.16) and (2.9) into (2.1), to give

$$\begin{aligned} \frac{\partial}{\partial t}\left(\frac{b}{S_0}\right) &= \frac{N^2}{2}\Theta(t)\sum_n \sigma_n\left(X(x+c_nt)+X(x-c_nt)\right)\phi_n(z) \\ &-\frac{N^2}{2}\Theta(t-T)\sum_n \sigma_n\left(X(\xi-c_nt)+X(\xi'+c_nt)\right)\phi_n(z), \end{aligned} \tag{2.17}$$

where, for convenience, we have defined $\xi = x + c_nT$, $\xi' = x - c_nT$. Note that the buoyancy frequency, N, appears as a factor in the above. Since eigenfunction $\phi_n(z)$ is continuous (see section 2.3.5) equation 2.17 implies that the z-variation of b will be discontinuous at the tropopause, if N is discontinuous there.

2.3.4 Buoyancy forcing: spatial structure

To obtain quantitative predictions of w and b (and hence θ) a horizontal variation $X(x)$ and a vertical variation $Z(z)$ must be chosen. For $X(x)$ we choose a Gaussian function of horizontal width L:

$$X(x) = \exp\left(-\frac{x^2}{2L^2}\right), \tag{2.18}$$

since in localised deep convection the horizontal variation of buoyancy peaks at the hot-tower centre and weakens, due to, e.g., turbulent mixing with distance. The choice of $Z(z)$ is informed by observed heating profiles, which peak in the mid troposphere and are small at the surface and tropopause due to low-level cooling and the cessation of convective instability respectively. As in Nicholls et al. (1991), a suitable first approximation is

$$Z(z) = \sin\left(\frac{\pi z}{H_t}\right)(\Theta(z) - \Theta(z - H_t)), \tag{2.19}$$

which is continuous and has a single peak at $z = H_t/2$, where H_t is the height of the tropopause. Note, the tropopause now coincides with the top of the buoyancy forcing used throughout this chapter, i.e., $Z(z) = 0$ when $z > H_t$. Figure 2.1 is a schematic representation of the horizontal and vertical variation of the buoyancy forcing function we use throughout, except for section 2.6.2 (which we shall address at that time).

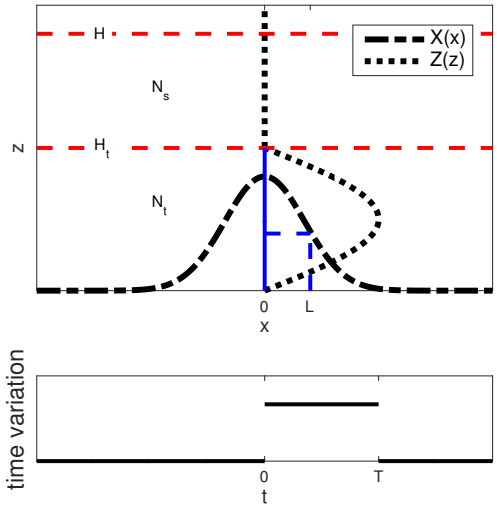

Figure 2.1: Schematic of the horizontal and vertical variation of our buoyancy forcing function. The top panel shows the vertical and horizontal variation described by $Z(z)$, $X(x)$, respectively. The characteristic width of the forcing is L. The bottom panel shows the time dependence. The vertical variation chosen corresponds to the first baroclinic mode of heating in the troposphere, between the ground and the tropopause (broken red line).

With this assumed form for X, the vertical velocity may be determined straightforwardly from (2.9) and (2.16). We may also now integrate (2.17), using the initial condition $b = 0$, to obtain

$$\begin{aligned} b = S_0 \frac{N^2 L}{2} \sqrt{\frac{\pi}{2}} \sum_j \frac{\sigma_j}{c_j} \phi_j(z) \\ \times \{\Theta(t) G(c_j, L, x, t) + \Theta(t-T) G(c_j, L, x, t-T)\}, \end{aligned} \tag{2.20}$$

where we have defined

$$G(c_j, L, x, t) = \operatorname{erf}\left(\frac{c_j t - x}{\sqrt{2}L}\right) + \operatorname{erf}\left(\frac{c_j t + x}{\sqrt{2}L}\right). \tag{2.21}$$

The potential temperature immediately follows from (2.4).

2.3.5 Model Stratification

The simplest possible representation of the tropospheric and stratospheric stratification is

$$N(z) = \begin{cases} N_t, & z \leq H_t, \\ N_s, & H > z > H_t, \end{cases} \tag{2.22}$$

where N_t and N_s are constants, which corresponds to a basic state of density of

$$\rho_0(z) = \begin{cases} \rho_s e^{-\frac{z}{D_t}}, & z \leq H_t, \\ \rho_s e^{-\frac{H_t}{D_t}} e^{-\frac{(z-H_t)}{D_s}}, & H > z > H_t. \end{cases} \tag{2.23}$$

For definiteness, let $N_s \geqslant N_t$. The tropospheric and stratospheric scale heights are given by

$$D_t = \frac{g}{N_t^2}, \quad D_s = \frac{g}{N_s^2}. \tag{2.24}$$

We seek the corresponding free modes $\phi_n(z)$ and wavespeeds c_n from (2.7), which yields a solution

$$\phi_n(z) = A_n \sin(k_n z)\, e^{\frac{z}{2D_t}}, \qquad z < H_t, \tag{2.25}$$

$$\phi_n(z) = A'_n \sin(k'_n (z - H))\, e^{\frac{z}{2D_s}}, \quad H_t \leq z < H, \tag{2.26}$$

where we have defined

$$k_n = \sqrt{\frac{N_t^2}{c_n^2} - \frac{1}{4D_t^2}}, \quad k'_n = \sqrt{\frac{N_s^2}{c_n^2} - \frac{1}{4D_s^2}}. \tag{2.27}$$

The solutions (2.25) and (2.26) must be matched at the tropopause, $z = H_t$, by applying continuity of ϕ_n and $d\phi_n/dz$, yielding an equation for c_n:

$$\begin{aligned} \frac{k_n}{k'_n} + \left(\frac{1}{D_t} - \frac{1}{D_s}\right) \frac{\tan(k_n H_t)}{k'_n} \\ - \tan(k_n H_t) \cot(k'_n (H_t - H)) = 0. \end{aligned} \tag{2.28}$$

We solved (2.28) numerically, using a bisector method, to determine seeding values of c_n which were then refined using a Newton-Raphson method. Recall that the wave speeds, c_n, are real.

We pause to consider the continuity conditions imposed upon eigenfunctions $\phi_n(z)$ above. These may be derived as follows. From equations (2.9) it is immediate for w continuous $\phi_n(z)$ must be continuous. Integrating equation (2.7) on a narrow range of z across the tropopause

$$\left[\rho_0 \frac{\mathrm{d}\phi_n}{\mathrm{dz}}\right]_{H_t-\delta}^{H_t+\delta} + \frac{1}{c_n^2}\int_{H_t-\delta}^{H_t+\delta} \rho_0 N^2 \phi_n(z')dz' = 0. \tag{2.29}$$

Setting $\delta \to 0$ in the above, the integral limits converge, the integral vanishes and we are left with the condition $\left[\frac{\mathrm{d}\phi_n}{\mathrm{dz}}\right]_{H_t-\delta} = \left[\frac{\mathrm{d}\phi_n}{\mathrm{dz}}\right]_{H_t+\delta}$ i.e $\frac{\mathrm{d}\phi_n}{\mathrm{dz}}$ and $\phi_n(z)$ are both continuous at $z = H_t$.

Return to considering limiting cases of equation (2.28). If $N_t = N_s \equiv N$, then $k_n = k_n'$ and(2.28) becomes $1 = \tan(k_n H_t)\cot(k(H_t - H)) \implies \tan(k_n H)\left(1 + \tan^2(k_n H_t)\right) = 0$, which gives $Hk_n = n\pi$, and from (2.27) we obtain for the wave speeds

$$c_n = \frac{NH}{\sqrt{n^2\pi^2 + \frac{H^2}{4D_t^2}}}. \tag{2.30}$$

The wavespeeds of Nicholls et al. (1991) are recovered in the Boussinesq limit, $H \ll D_t$, with $c_n \to NH/n\pi$, corresponding to Fourier modes $\phi_n(z) \to A_n \sin(n\pi z/H)$. The wavespeeds of Parker and Burton (2002) are recovered by further setting $H = H_t$. Returning to $N_t \neq N_s$, from (2.8) the normalization coefficients in (2.25) and (2.26) are

$$\begin{aligned} A_n = &\left(\frac{N_t^2\rho_s}{2}\left(H_t - \frac{\sin(2k_nH_t)}{2k_n}\right)\right. \\ &+ \frac{N_s^2\rho_s}{2}\left(\frac{\sin^2(k_nH_t)}{\sin^2(k_n'(H_t-H))}\right) \\ &\left.\times\left(H - H_t + \frac{\sin(2k_n'(H_t-H))}{2k_n'}\right)\right)^{1/2}, \\ A_n' = &\left(\frac{\sin(k_nH_t)}{\sin(k_n'(H_t-H))}\right) \\ &\times \exp\left(\left(\frac{1}{2D_t} - \frac{1}{2D_s}\right)H_t\right)A_n. \end{aligned} \tag{2.31}$$

From (2.32), with our choice $Z(z) = \sin(\pi z/H_t)\left(\Theta(z) - \Theta(z - H_t)\right)$ we now find

$$\begin{aligned} \sigma_n = \frac{\rho_s A_n}{2} Re\Bigg(&\frac{\exp\left(ik_nH_t - H_t/2H\right) + 1}{ik_n + i\frac{\pi}{H_t} - \frac{1}{2D_t}} \\ &- \frac{\exp\left(ik_nH_t - H_t/2H\right) + 1}{ik_n - i\frac{\pi}{H_t} - \frac{1}{2D_s}}\Bigg), \end{aligned} \tag{2.32}$$

with the A_n determined from (2.31), and the c_n and k_n via a numerical solution of (2.28).

2.4 Numerical Implementation and Convergence

2.4.1 Computation of the Wave Speeds, c_n

We return to the matter of the numerical solution of equation 2.28 for the wave speeds, c_n. It is convenient to consider the solutions as particular values, c_n, of the continuous variable x, $x \in \mathbb{R}^+$, with $c = \frac{H}{x}$, and to seek the solution of

$$f(x) = 0, \tag{2.33}$$

where

$$\begin{aligned} f(x) &\equiv \frac{K_n(x)}{K_n'(x)} + \left(\frac{1}{R_t} - \frac{1}{R_s}\right)\frac{\tan(R_0 K_n(x))}{K_n'(x)} \\ &+ \tan(R_0 K_n(x))\cot((1-R_0)K_n'(x)). \end{aligned} \tag{2.34}$$

In the above we have defined

$$K_n(x) \equiv \sqrt{N_t^2 x^2 - \frac{1}{4R_t^2}}, \quad K_n'(x) \equiv \sqrt{N_s^2 x^2 - \frac{1}{4R_s^2}}, \tag{2.35}$$

using the following dimensionless ratios

$$R_t \equiv \frac{D_t}{H}, \quad R_s \equiv \frac{D_s}{H}, \quad R_0 \equiv \frac{H_t}{H}. \tag{2.36}$$

Note that R_t, R_s and R_0 change value with lid height, H. Note also that, from the first term of equation (2.34), for real solutions, x, it is clearly necessary to restrict the domain of x, such that $x \geq x_{min}$ with

$$x_{min} \equiv \max\left(\frac{1}{2N_s R_s}, \frac{1}{2N_t R_t}\right) = \frac{1}{2N_s R_s}. \tag{2.37}$$

The solid blue line in figure 2.2, was obtained as discussed below. It shows typical variation of $f(xH)$ for $xH \in [x_{min}H, x_{min}H + 2000]$, with $H = 10H_t$ i.e. $R_0 = 0.1$ (which is a large value of R_0). This choice of data produces, in a convenient range of scaled variable xH, all the features of function $f(xH)$, discussed in the following three paragraphs, which must be considered to produce numerical solutions.

Since $N_s > N_t$ and, in general, $R_0 \ll 1$, it is clear that $(1-R_0)K_n'(x)$ will always increase more rapidly with x than $R_0 K_n(x)$. Consequently, the same cotangent term in equation 2.34 varies most rapidly, with the term in $\tan(R_0 K_n(x))$ responsible for the "reversal" visible in figure 2.2, after 9 cycles. In figure 2.2, the position x_{min} is indicated by the black

asterisk. The period of the $f(x)$ quickly attains a constant value. The smaller period for small x visible in figure 2.2 may be understood by noting that the rate of increase with x of the argument of the cotangent term

$$\frac{dK_n'}{dx} = \frac{N_s^2 x}{\sqrt{N_s^2 x^2 - \frac{1}{R_s^2}}}, \tag{2.38}$$

is very large for x close to $x_{min} = \frac{1}{2N_s R_s}$. For $x \gg x_{min}$, the range in x, δx, corresponding to a single cycle of the variation of the cotangent term in equation 2.34 is bounded : $(1 - R_0)N_s\delta x < \pi$. Accordingly, we can approximate the period of the great majority the oscillations of $f(x)$ as follows

$$\delta x \approx \frac{\pi}{(1 - R_0)N_s}, \tag{2.39}$$

which, for given R_0, is an upper bound, note. Note also that δx is relatively insensitive to the height of the lid, since $R_0 \leq 0.1$ for the range of H studied in the sequel.

For purposes of a numerical solution, the most rapid variation in equation (2.34) (for small x) must be adequately resolved. For the range of H values to be studied, the requisite level of resolution was deemed to correspond to

$$\Delta x = \frac{\delta x}{200}, \quad R_0 = 0.1. \tag{2.40}$$

Since the tangent and cotangent functions have an infinite number of zeros, it is clear that equation 2.34 will have an infinite number of real solutions. Of course, we shall truncate the sequence, x_n, for some finite, large n. However, $M = \max(n)$ must increase with H, since relatively sharp diabatic heating profiles require more modal terms to achieve consistent resolution and we have

$$M = m_0 \frac{H}{H_t}. \tag{2.41}$$

In the sequel we will choose a value of the proportionality constant of $m_0 = 20$.

We may now state the problem of finding the c_n numerically as follows. For a given lid height H, we seek the $x_n = \frac{H}{c_n}$ from a numerical solution of the problem:

$$f(x) = 0, \quad x \in [x_{min}, k\delta x], \quad \delta x = \frac{\pi}{(1 - R_0)N_s}, \quad \Delta x = \frac{\delta x}{200}. \tag{2.42}$$

In practice, the number of solutions of $f(x)$ obtained in the chosen interval will slightly exceed the value of $M = m_0 \frac{H}{H_t}$, and the set was truncated.

For a given value of parameter H, the range of x in equation 2.42 was defined as a Matlab vector, with components x_i. The Matlab vector $f_i(x_i)$, which is plotted against vector x_i in figure 2.2, was determined

from equation 2.34, using Matlab mesh operations. Initial seeds, x_n^*, were determined for further refinement (see below) by a synchronised search of the Matlab vectors f_i and x_i, using the following algorithm, which simply records abscissa crossing points

$$
\begin{aligned}
&n = 1 \\
&\text{for } i = 1 : \text{length}(f) \\
&\quad \text{if } (f_i f_{i+1} < 0) \wedge ((|f_i| < 5) \vee (|f_{i+1}| < 5)) \\
&\quad\quad x_n^* = x_i \\
&\quad\quad n := (n+1) \\
&\quad \text{end if} \\
&\text{end for}
\end{aligned}
\tag{2.43}
$$

The location of the converged seeds are displayed as red asterisks in figure 2.2. Note, the extra conditions above are required to avoid seeding the fictitious " fly-back" crossing points on the abscissa, corresponding to the vertical connection between one cycle of the cotangent graph and the next, the threshold values of 5 being determined by trial and error. Seeds x_n^* were converged using a maximum of 20 cycles of Newton-Raphson iteration, using the convergence criterion:

$$
\left| \frac{x_n^{*(p+1)} - x_n^{*(p)}}{x_n^{*(p)}} \right| < 10^{-5}, \tag{2.44}
$$

where $x_n^{*(p)}$ denotes the pth estimate of the n^{th} root.

Converged values of x_n were all converted to the corresponding wave speed using the relationship:

$$
c_n = \frac{1}{x_n}. \tag{2.45}
$$

A specimen set of converged wave speeds are plotted along with the corresponding heating expansion coefficients, σ_n, in figure 2.5, which are considered in the next section.

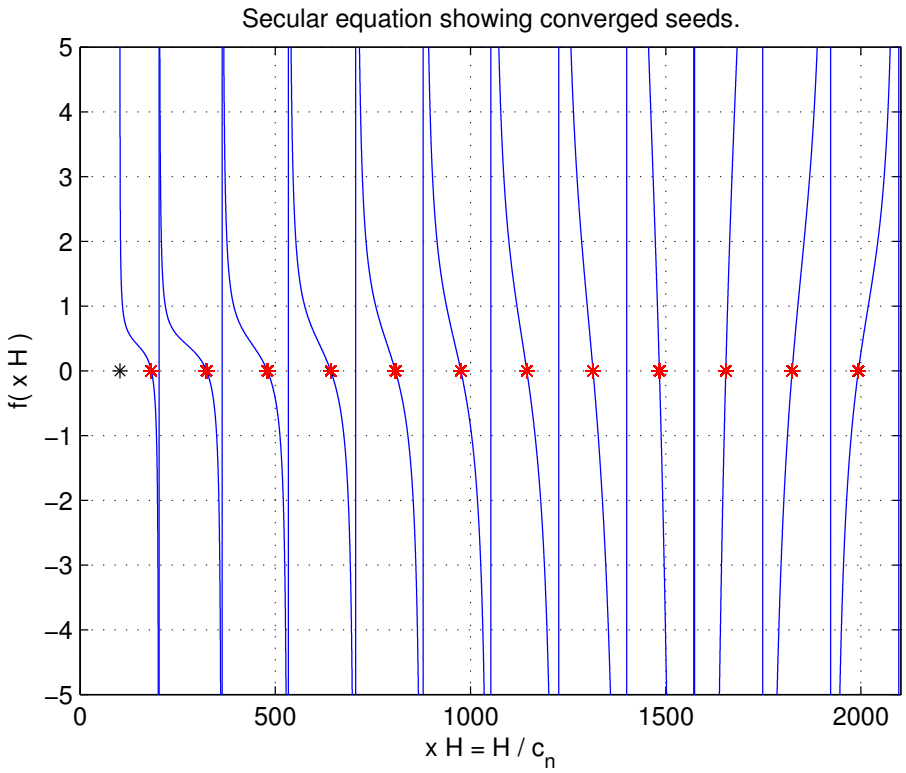

Figure 2.2: The solid blue line shows the variation of the left hand side of the secular equation 2.28 for $H = 10H_t$ i.e. ratio $R_0 = 0.1$ using a restricted range of independent variable $Hx = \frac{H}{c}$. The cotangent term in equation 2.34 varies most rapidly, the term in $\tan(R_0 K_n(x))$ being responsible for the "reversal" occurring after 9 cycles. The position of x_{min} is indicated by the black asterisk. The position of converged solutions, Hx_n, are indicated by red asterisks.

2.4.2 Convergence of the Heating Profile

It is appropriate to verify the expansion coefficients, σ_n, in equation 2.31. Moreover, given the reliance of our solution on the numerical calculation detailed in section 2.4.1, it is necessary to verify that a complete set of wave speeds have been extracted, for a given lid height, H. Accordingly, for all the data presented in the sequel, the vertical variation of our defined, diabiatic heating profile was recovered, from its modal expansion in equation (2.9) and compared with the target form, $Z(z)$, defined in equation (2.19) and illustrated in schematic figure 2.1. Figure 2.3, below, shows the vertical variation of the applied buoyancy forcing, recovered from its modal expansion

$$Z_r(z) \equiv \sum_{n=0}^{M} \sigma_n \phi_n(z). \tag{2.46}$$

Figure 2.4, below, shows the vertical variations of the associated absolute error:

$$\epsilon(z) \equiv (Z_r(z) - Z(z)) \,, \tag{2.47}$$

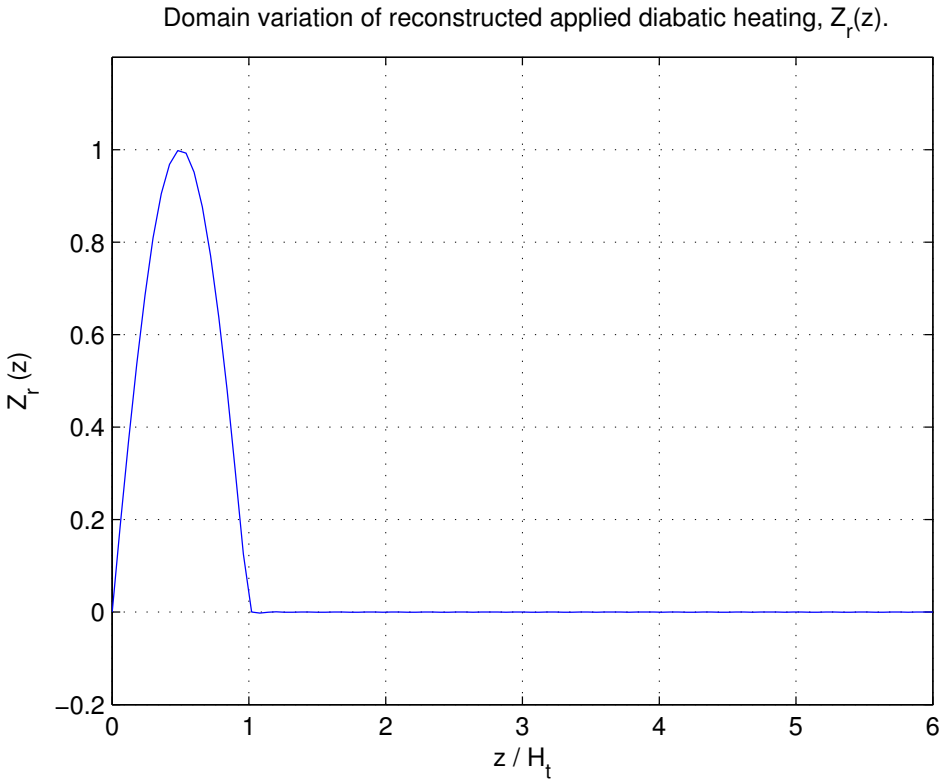

Figure 2.3: Checking the modal expansion. A domain plot of the reconstructed vertical variation of assumed diabatic heating, $Z_r(z)$ (see equation 2.46), plotted over a range of vertical coordinate, to confirm correct behaviour. For this data $H_t = 1$, $H = 50H_t$, $m = 50$.

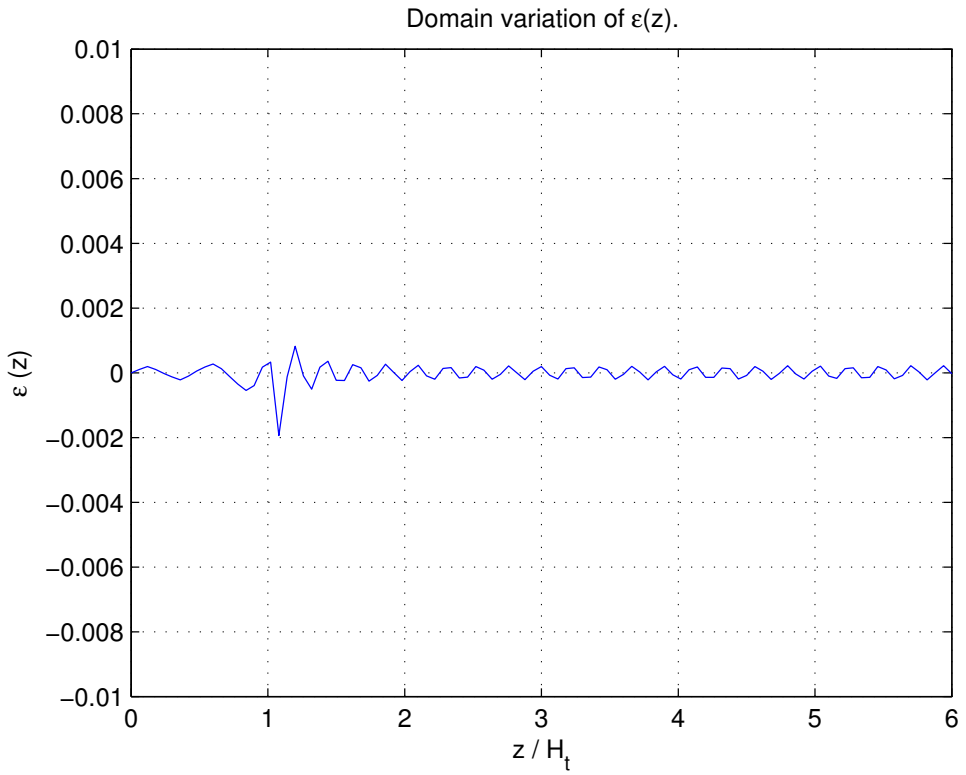

Figure 2.4: A domain plot of the absolute error, between the target diabatic heating profile and that recovered by its modal expansion, equation 2.46. As for the previous figure, for this data $H_t = 1$, $H = 50H_t$, $m_0 = 50$. The maximum absolute error occurs at the model tropopause.

Note that a sensible relative error cannot be defined, given $Z(z) = 0$, $z > H_t$. The data in figures 2.3 and 2.4 was compiled for $H_t = 1$, $H = 50H_y$, $k = 50$ (see next section). However, the visualised region is reduced to $z \in [1, 6H_t]$. As expected, the relative error in the heating profile and, by extension, the whole atmospheric adjustment, is greatest at the location of the model tropopause. This data is indicative of a non-uniform convergence in the modal expansion. However, convergence is seen to be satisfactory over the domain.

For the data shown in figures 2.3 and 2.4, we show, in figure 2.5, the variation with n, mode number, of the heating expansion coefficients, σ_n and the associated wave speeds, c_n.

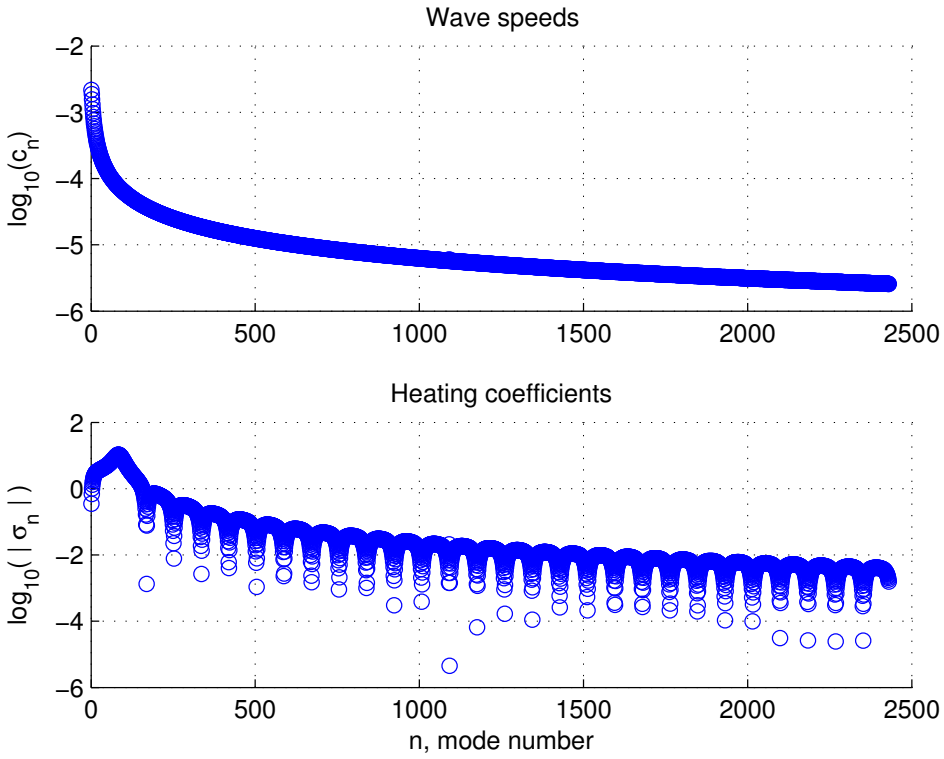

Figure 2.5: Converged wave speeds and corresponding heating expansion coefficients plotted against mode number, for the data used produce figures 2.3 and 2.4.

2.4.3 Convergence to a Radiating Solution

The existence of a model lid at $z = H$ means that upwards propagating waves are inevitably reflected downwards, and will thus return to disrupt the tropospheric response in $0 < z < H_t$, in which we are most interested. This aphysical effect could perhaps be eliminated by taking $H \approx 50\,\mathrm{km}$ and introducing a sponge layer at the top of the domain. However, a neater solution - and one which is compatible with our mathematical formulation - is simply to take $H \gg H_t$, so that upwards propagating waves do not have time to reflect and return to disrupt the tropospheric response, which can then be considered as quasi-radiating. The values of H that are required to achieve this may themselves be aphysical (e.g., hundreds of km), in which case the response only makes sense physically in the troposphere and stratosphere (say). The response far above that, where our equations are motion are not valid, is ignored: this part of the domain simply serves to implement a radiating boundary condition for the lower atmosphere.

But how large need H be for such a quasi-radiating response? We probe the convergence of the tropospheric response as H increases for

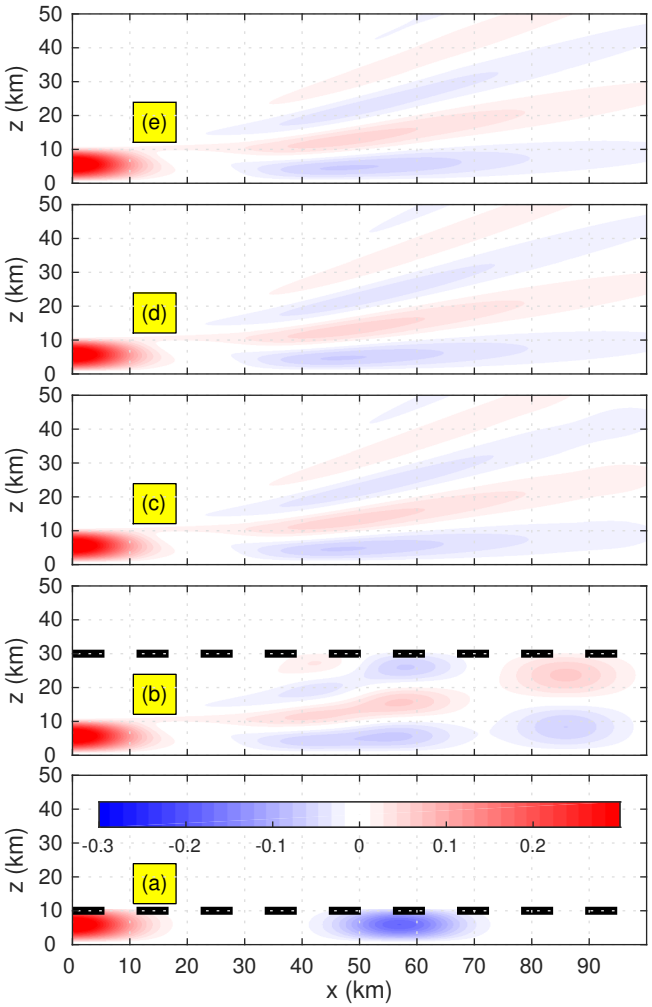

Figure 2.6: The transition to a radiating solution with increasing lid altitude $H \gg H_t = 10\,\mathrm{km}$. Shown is the w response for $x > 0$ in $\mathrm{m\,s^{-1}}$, 30 mins after onset of forcing. $L = 10\,\mathrm{km}$, $N = 0.01\,\mathrm{s^{-1}}$, $H_t = 10\,\mathrm{km}$. (a) $H = 10\,\mathrm{km}$, (b) $H = 30\,\mathrm{km}$, (c) H =100 km, (d) $H = 640\,\mathrm{km}$, (e) H =3000 km.

the case of a uniformly stratified atmosphere $N(z) = N = 0.01\,\mathrm{s^{-1}}$ and with steady forcing such that $L = 10\,\mathrm{km}$, $H_t = 10\,\mathrm{km}$, which shall be the standard choice throughout. Figure 2.6 shows the w response for $x > 0$, 30 mins after forcing onset, for a lid at 10 km (tropopause), 30 km, 100 km, 640 km, 3000 km. We are thus moving from the trapped mode ($H = H_t$) of Parker and Burton (2002), to a model with $H = 30\,\mathrm{km}$ and limited upward radiation (Nicholls *et al.*, 1991), and then eventually converging to radiating solution when $H \gg H_t$. In particular, we see large differences as H increases from 10 to 100 km (a to b): higher order modes (with larger horizontal phase speeds) are excited and propagate more rapidly into the environment, and an upwardly radiating gravity wave field develops aloft. However, increasing lid height above 100 km has almost no effect on tropospheric response, although the stratospheric

response changes somewhat. Indeed, figure 2.6(d, e) are indistinguishable, which indicates a converged solution. This convergence is quantified using an absolute difference

$$\Delta w(x,z,t,H,L) = w(x,z,t,H,L) - w_\infty(x,z,t,L), \tag{2.48}$$

where w_∞ is the converged solution with $H = 3000\,\text{km}$ (figure 2.6(e)). We calculate the tropospheric relative error

$$\begin{aligned} \epsilon(H,L) &= \frac{\Delta w_{rms}(x,z,t,H)}{(w_\infty)_{rms}}, \\ f_{rms} &\equiv \sqrt{\frac{\sum_x \sum_z \left(f(x,z,t)\right)^2}{N_x N_z}}, \end{aligned} \tag{2.49}$$

where the uniform grid on which a response f is evaluated contains $N_x \times N_z$ points, in the domain $0 < x < 300\,\text{km}$, $0 < z < 10\,\text{km}$. In figure 2.6, the calculated values of ϵ are, reading upwards, 1.06, 0.12, 8.5×10^{-4}, 2.3×10^{-12} (panel (e) is w_∞). Arbitrarily, we deem that a value of $\epsilon \leq 10^{-3}$ corresponds to a converged solution, and therefore figure 2.6(c,d) can be considered converged.

It is also important to consider how ϵ depends upon L. Figure 2.7 shows the convergence for a range of horizontal forcing widths $1\,\text{km} < L < 100\,\text{km}$. We observe that, generally, when L is smaller, ϵ is larger. For the range of L used in this study, $10\,\text{km} \leq L \leq 100\,\text{km}$, taking $H_t = 640\,\text{km}$ we are guaranteed $\epsilon \leq 10^{-3}$ (for this choice of parameter space). We therefore take this value of H for rest of this study.

We can understand the dependence of ϵ on L by considering hydrostatic gravity waves $\sim \exp\{i(kx+mz-\omega t)\}$ in an unbounded atmosphere with uniform N, taken here in the Boussinesq limit for simplicity. Taking this limit in (2.5), we obtain the usual gravity wave dispersion relation, $\omega = Nk/m$, and hence a group velocity

$$\underline{c}_g = \left(\frac{\partial\omega}{\partial k}, 0, \frac{\partial\omega}{\partial m}\right) = \frac{N}{m}\left(1, 0, -\frac{k}{m}\right). \tag{2.50}$$

The time taken for wave energy to reflect from the lid and return

$$t_r = \frac{2H}{c_{g_z}} = \frac{2H}{Nk/m^2} = \frac{2Hm^2}{Nk}. \tag{2.51}$$

Such unphysical reflections can then be avoided be taking $t < t_r$, or equivalently, $H > Nkt/2m^2$. Since we expect the gravity wave response to have the same characteristic scales as the forcing, i.e. $k \approx L^{-1}$ and $m \approx {H_t}^{-1}$, we require

$$H > \frac{N{H_t}^2 t}{2L}. \tag{2.52}$$

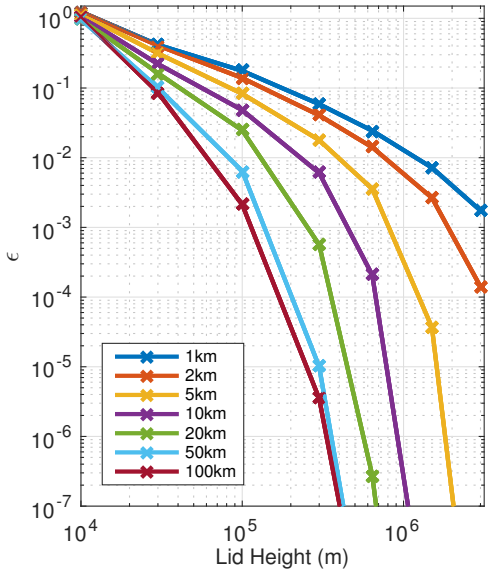

Figure 2.7: Convergence with H of the simplified (constant N) model. Plots of the relative error in the w-response, ϵ, with lid height, H, compiled for $t = 30\,\text{mins}$ after the onset of forcing, $0 < x < 300\,\text{km}$ and a range of forcing widths L: $1\,\text{km} < L < 100\,\text{km}$ (see key) with the same total heat input. As expected, horizontally narrower forcing profiles converge more slowly with H.

So, for a quasi-radiating solution at large t, we would need a large H. For our convergence tests with $t = 30\,\text{mins}$, $N = 0.01\,\text{s}^{-1}$, $L = 10\,\text{km}$ and $H_t = 10\,\text{km}$, we thus expect a converged solution with $H > 250\,\text{km}$.

The number of modes M retained in the modal expansion also need to vary with H to ensure a consistent resolution of both the forcing and the response. We achieve this by taking $M = 20H/H_t$.

2.5 The Dynamics of Convective Adjustment

We now test the sensitivity of the gravity wave response to different model configurations (e.g., constant versus varying N) and to the temporal and spatial structure of the thermal forcing. Of particular interest is the speed and magnitude of the resulting dominant tropospheric response, and how this may pre-condition the troposphere to further convection. We also identify aspects of the tropospheric response that may be absent in low-resolution atmospheric models. Throughout we analyse the vertical velocity w and the potential temperature perturbation θ, since both are influential in the organisation of deep convection.

We use results from three different model configurations: (i) a trapped regime with a rigid lid at the tropopause (TRAP hereafter), (ii) a radiating regime with a high model lid and constant N (RAD1 hereafter),

(iii) a radiating regime with a high model lid but different values of N in the troposphere and stratosphere (RAD2 hereafter). For cases (ii) and (iii) we follow §2.4.3 and take the model lid at $H = 64H_t = 640\,\mathrm{km}$. We choose the maximum buoyancy forcing to be $S_0 = 3.6 \times 10^{-5}\,\mathrm{m\,s^{-3}}$, which, using equation (3.8), corresponds to a maximum heating rate $Q_{\max} = 0.001\,\mathrm{K\,s^{-1}}$, and a maximum rainfall rate of $14\,\mathrm{mm\,hr^{-1}}$, typical of a cumulonimbus storm. Note, our heating rate is half of that used by Nicholls et al. (1991). Note also that, since our system is linear, any other choice of S_0 will scale the solution accordingly.

2.5.1 Response to Steady Heating: Trapping and Radiation

In order to characterise the effects of upward radiation, we compare the response from TRAP and RAD1 (both with uniform $N = 0.01\,\mathrm{s^{-1}}$) to steady heating with horizontal lengthscale $L = 10\,\mathrm{km}$. In TRAP, the w response takes the form shown in figure 2.6a, with a single non-dispersive pulse of subsidence emanating from the heating at $x = 0$, which travels uniformly at the speed c_t of the first gravity wave mode (i.e. $c_t = NH_t/\pi \approx 30\,\mathrm{m\,s^{-1}}$ in the Boussinesq limit). The response is more complex in RAD1, as illustrated in figure 2.8, where the time evolution of both the w and θ responses are shown. (Note that, as in §2.4.3, the solutions are symmetric about $x = 0$, and are only shown for $x > 0$). In the deep atmosphere, an entire spectrum of deeper gravity wave modes is excited, which travel at a range of horizontal speeds, each of which exceeds c_t. So, (i) the adjustment is communicated more rapidly into the neighbourhood of the forcing relative to TRAP, (ii) the dominant tropospheric response now inevitably disperses, leading to a reduction in the magnitude of the tropospheric response in w relative to TRAP.

This reduction is quantified in figure 2.9, which shows the maximum tropospheric value of $|w|$ for $|x| > 100\,\mathrm{km}$. This automatically excludes the steady w response around $x = 0$, and instead focusses on the outwardly propagating subsidence pulse. For TRAP, $|w|_{\max} \approx 0$ until $t \approx 50\,\mathrm{mins}$ (i.e., $t \approx 100\,\mathrm{km}/c_t$, when the single gravity wave appears), after which it rises and then quickly settles to a constant value, since this pulse is non-dispersive. For RAD1, there is a signature in $|w|_{\max}$ for smaller times (due to the spectrum of deeper and faster gravity wave modes), and then decay at large times. For these parameters, the implied maximum in $|w|$ is only 20% of that in TRAP: the remote response with upward radiation is significantly less than with a lid. We return to this issue in §2.5.3, where the case RAD2 is discussed. We will also use figure 2.9 as the basis for comparisons in Chapter 3.

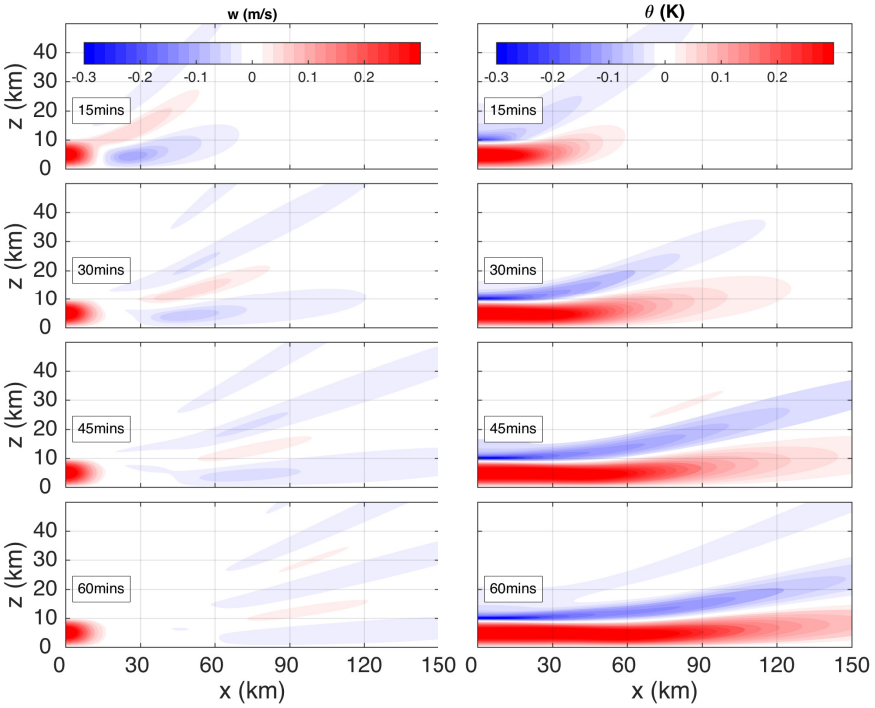

Figure 2.8: The time evolution of the response for w (left) and θ (right) to steady heating with $L = 10\,\text{km}$, uniform $N = 0.01\,\text{s}^{-1}$, $H = 640\,\text{km}$ in RAD1. Note that t increases down each column.

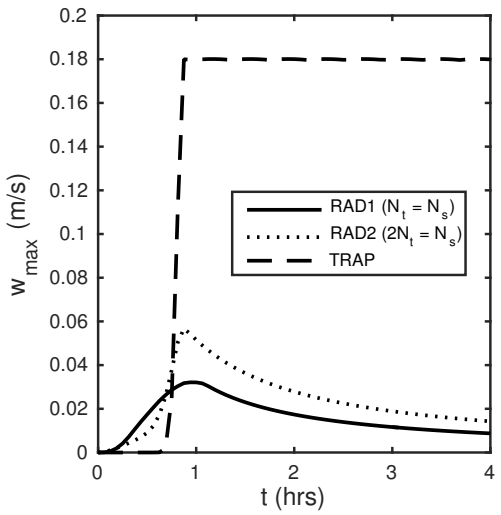

Figure 2.9: Time series of maximum tropospheric values of $|w|$ for $|x| > 100\,\text{km}$ when forced with a steady heating of width $L = 10\,\text{km}$.

2.5.2 Steady versus Transient Heating

We now consider differences between the response for steady heating (applied for all $t > 0$), and pulsed heating (applied only for $0 < t < T$, as in equation (2.13)). Figure 2.10 shows the response in w and θ at

$t = 60$ mins, for each of TRAP, RAD1 and RAD2 with $T = 30$ mins. In all cases, the remote tropospheric response consists of a pulse of negative w, followed by an elongated pulse of positive θ, then a pulse of positive w, after which the response dies out.

Figure 2.11 provides a more detailed comparison between steady heating and a (different) case with $T = 60$ min. Shown is the time-evolution of the horizontal variation of the vertically-averaged tropospheric w (broken) and θ (solid) responses. Since heating is steady for the initial 60 mins in both cases, the responses are identical, as shown in panels (a) and (b). Panels (c) and (d) show results from a simulation where heating is steady for all time, whilst (e) and (f) show results from a simulation where heating is terminated at 60 mins. In the pulsed case, note the regions of ascent, which propagate away from $x = 0$ immediately after heating terminates. The maximum values of w decrease with time, in exactly the same way as shown in figure 2.9 for the preceding subsidence pulse. However, the regions of vertically-averaged ascent give values of w that remain significant for the initiation of convection (in the sense to be discussed in §2.5.4) for up to 4 hrs after initiation of heating.

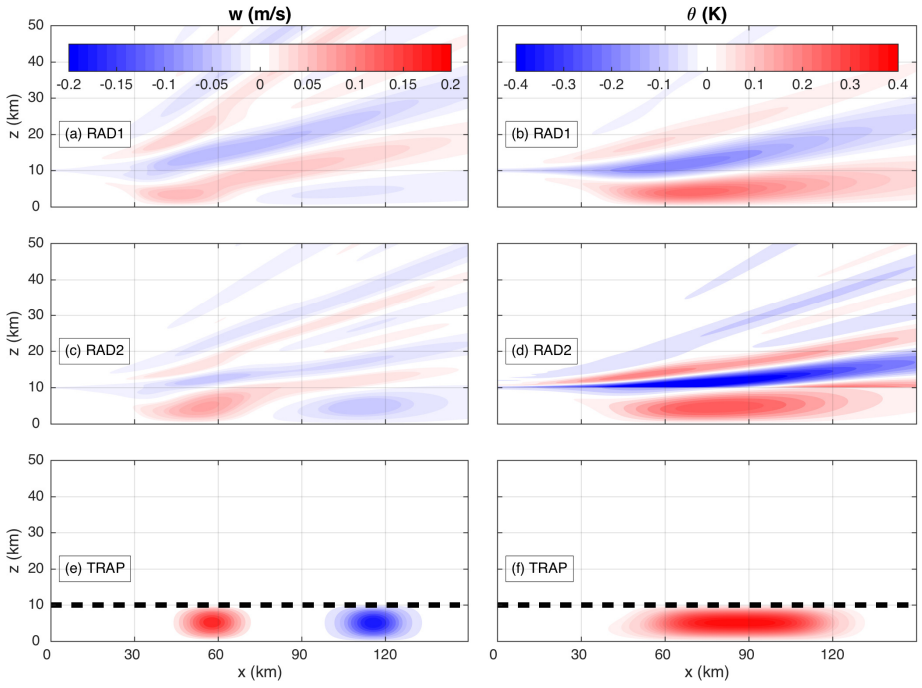

Figure 2.10: Response at $t = 60$ mins to a pulsed heating of length $T = 30$ mins, with $L = 10$ km, $N_t = 0.01\,\mathrm{s}^{-1}$, $N_s = 0.02\,\mathrm{s}^{-1}$ (RAD2 only), and $H = 640$ km (RAD1, RAD2).

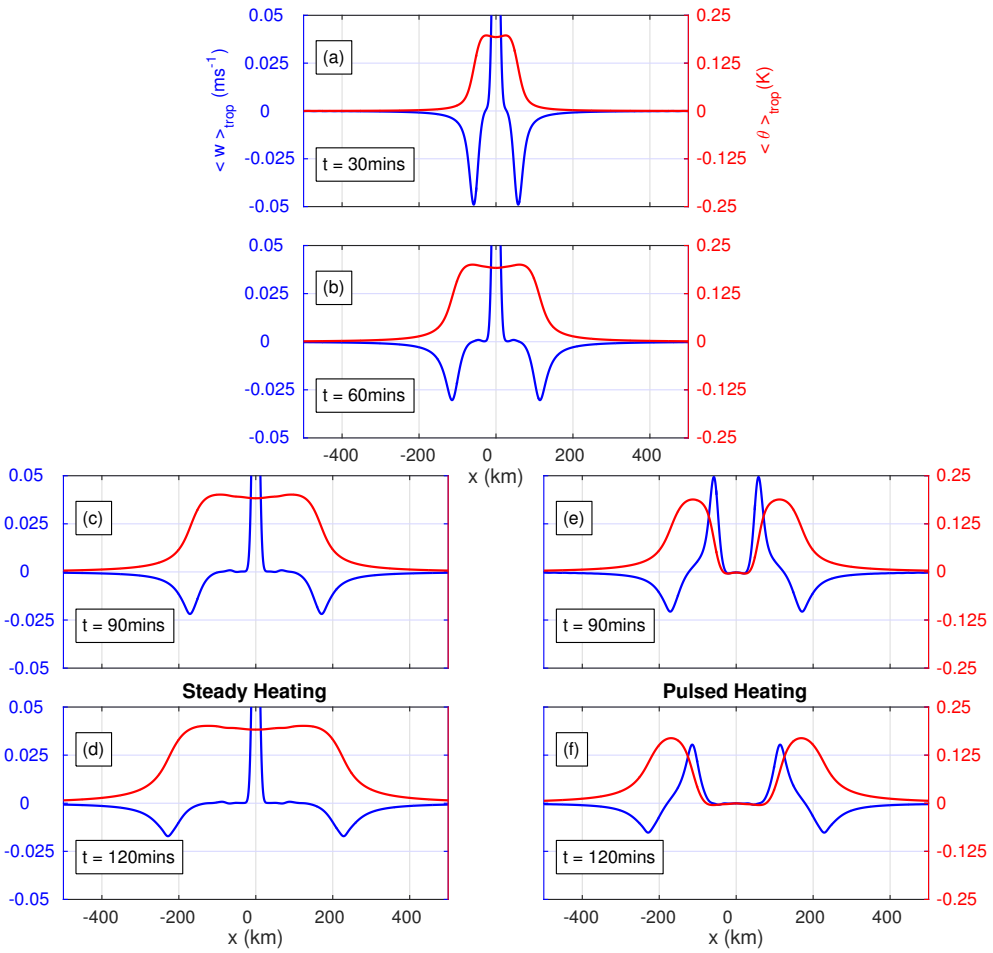

Figure 2.11: Vertically averaged response for steady heating (left) and a 60 min pulse of heating (right), in RAD1. Shown are vertical averages over the troposphere for w (blue lines) and θ (red lines), with $L = 10\,\text{km}$, uniform $N = 0.01\,\text{s}^{-1}$, and $H = 640\,\text{km}$. Panels (a,b) show the response to heating over $0 < t < T = 60\,\text{mins}$ (same for both steady and pulsed heating). Panels (c, d) show the response for a further 60 mins of (steady) heating. Panels (e, f) show the response when the heating is terminated after 60 mins (pulsed heating).

2.5.3 Effects of a Model Stratosphere

Whilst interrogation of RAD1 has been informative on the tropospheric response, in reality N varies with height. We model this using a piecewise constant $N(z)$, with $N_t = 0.01\,\text{s}^{-1}$ in the troposphere, and $N_s = 0.02\,\text{s}^{-1}$ in the stratosphere (RAD2). Since the jump in N at the tropopause leads to partial reflection of upwardly propagating waves (e.g. Sutherland 1996), RAD2 is expected to be an intermediate case between TRAP (total wave reflection at rigid lid) and RAD1 (no tropopause, so no wave reflection). Note that in RAD2 the choice $N_s = 2N_t$, $N_t = 0.01\,\text{s}^{-1}$ is physically representative.

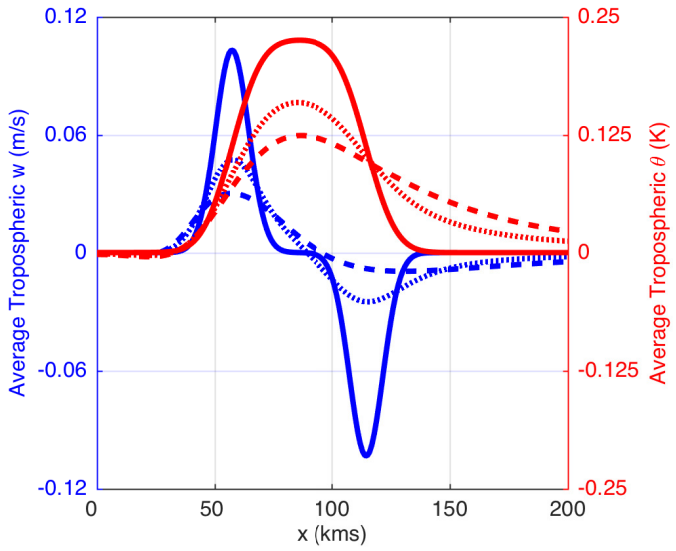

Figure 2.12: Vertically-averaged response for the results of figure 2.10. Shown are the vertical averages over the troposphere for w (blue lines) and θ (red lines) at $t = 60$ mins, to a 30 min heat pulse. Solid lines: TRAP. Dashed lines: RAD1. Dotted lines: RAD2 ($N_t = 0.01\,\mathrm{s}^{-1}$, $N_s = 0.02\,\mathrm{s}^{-1}$)

.

Figure 2.10(c,d) shows the response after 60 mins in RAD2 to a pulsed heating of length 30 mins. The response in RAD2 has the same general form as that in RAD1, although in RAD2 the dominant tropospheric response propagates slightly faster (consistent with the larger average values of N in RAD2), and is more intense (consistent with the anticipated wave reflection at the tropopause). Of course, the tropospheric response in TRAP is stronger still. This is confirmed in figure 2.12 which shows the horizontal variation of the vertically-averaged tropospheric responses shown in figure 2.10. The peak values of $|w|$ in RAD1 and RAD2 are 50% and 30% of those in TRAP, whilst the peak values of $|\theta|$ are 70% and 60% of those in TRAP. Apparent is the increased dispersion of the dominant response in RAD1 and RAD2 (as higher order modes of varying speed contribute to the adjustment), although the timing of the peak responses remains constant across all configurations. The time evolutions of the corresponding first subsidence pulses are shown in figure 2.9, for the simpler case of steady heating (i.e. where there is no trailing pulse of ascent). Note how the (remote) response in RAD2 is consistently 50-100% higher than in RAD1 over $1\,\mathrm{h} < t < 4\,\mathrm{h}$.

Although the above choice $N_s = 2N_t$ for RAD2 is physically realistic, it is interesting to examine how the response depends upon the ratio N_s/N_t (with $N_s/N_t = 1$ corresponding to RAD1). To do so, we first consider reflection and transmission of gravity waves at the tropopause. From equation (2.1), applied to our chosen stratification, we have, for

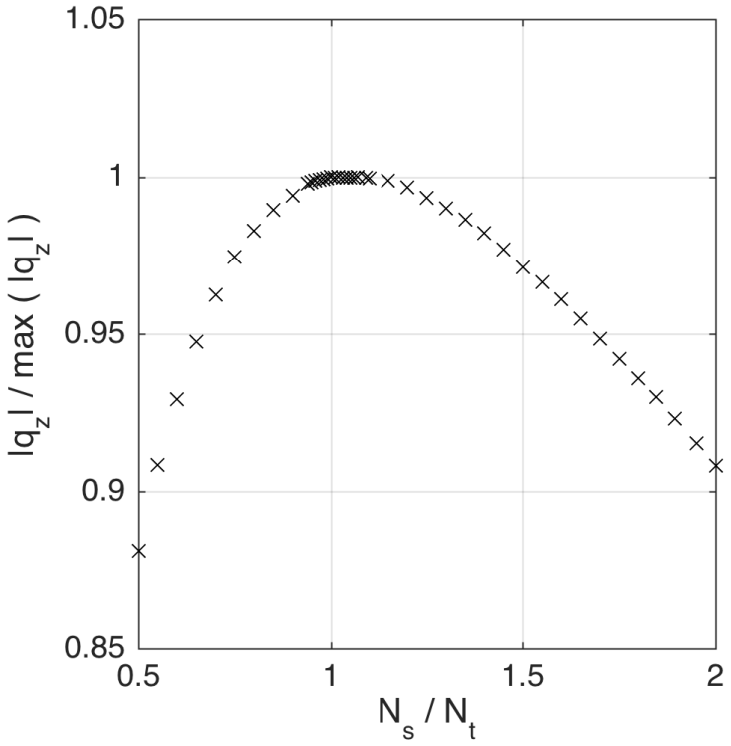

Figure 2.13: Horizontally-averaged vertical energy flux $|q_z| = |pw|$, at a fixed time $t = 60\,\text{min}$, plotted as a function of ratio N_s/N_t, measured with our model RAD2 in response to a 60 min pulse of heating with $L = 10\,\text{km}$, $N_t = 0.01\,\text{s}^{-1}$. The horizontal averaging is done over $0 < x < 100\,\text{km}$. Values have been normalised by the maximum value of q_z across all values of N_s/N_t.

the two regions

$$\frac{\partial^2 p'}{\partial x^2} + \frac{1}{N_t^2}\frac{\partial^2}{\partial t^2}\frac{\partial^2 p'}{\partial z^2} = 0, \quad z < H_t, \quad \frac{\partial^2 p'}{\partial x^2} + \frac{1}{N_s^2}\frac{\partial^2}{\partial t^2}\frac{\partial^2 p'}{\partial z^2} = 0, \quad z > H_t, \tag{2.53}$$

where we have neglected density variation in the vicinity of the tropopause. Plane wave solutions with dispersion relations $\omega = \frac{N_d k}{m}$, $N_d \in [N_t, N_s]$, are easily verified, so we have, for the pressure adjustment of a gravity wave

$$p'(x,z,t) = \begin{cases} p_{0(t)} e^{i(k_t x + m_t z - \omega_t t)}, & z \le H_t, \\ p_{0(s)} e^{i(k_s x + m_s z - \omega_s t)}, & z > H_t, \end{cases}$$

with $\omega_t = \frac{N_t k_t}{m_t}$ etc. Note, for the present discussion subscript t refers to tropospheric value, not the usual time derivative. Pressure (and w) is continuous at the troposphere, at all x, t. Hence $k_t = k_s \equiv k$ and $\omega_t = \omega_s \equiv \omega$. Now, the pressure adjustments, dispersion relations and

velocity adjustments (obtained from equations 2.1) are

$$p'_t = p_{0(t)}e^{i(kx+m_t z-\omega t)}, \quad u_t = \frac{kp'_t}{\rho_0(z)\omega}, \quad w_t = \frac{k^2 p'_t}{\rho_0(z)\omega m_t}, \quad m_t = \frac{N_t k}{\omega}, \tag{2.54}$$

$$p'_s = p_{0(s)}e^{i(kx+m_s z-\omega t)}, \quad u_s = \frac{kp'_s}{\rho_0(z)\omega}, \quad w_s = \frac{k^2 p_s}{\rho_0(z)\omega m_s}, \quad m_s = \frac{N_s k}{\omega}. \tag{2.55}$$

We further obtain from the dispersion relation

$$\frac{N_t}{m_t} = \frac{N_s}{m_s}. \tag{2.56}$$

Consider an upward propagating, incident pressure wave $A_I e^{i(kx+m_t z-\omega t)}$ and reflected pressure wave $A_R e^{i(kx-m_t z-\omega t)}$ both in the tropopause and upward propagating, transmitted wave $A_T e^{i(kx+m_s z-\omega t)}$. Continuity of pressure, p', at the tropopause, which is temporarily located at $z = z_t$, yields

$$A_I e^{im_t z_t} + A_R e^{-im_t z_t} = A_T e^{im_s z_t}, \tag{2.57}$$

whilst continuity of w and equation 2.56 yield

$$A_I e^{im_t z_t} - A_R e^{-im_t z_t} = A_T \frac{N_t}{N_s} e^{im_s z_t}. \tag{2.58}$$

It is convenient to set $z_t = 0$ before adding equations 3.1 and 3.3, producing an expression for the ratio of wave amplitudes

$$\frac{A_T}{A_I} = \frac{2}{\left(1 + \frac{N_t}{N_s}\right)}. \tag{2.59}$$

Adjacent to the tropopause, the vertical component of the energy flux vector $p'(x,t)w'(x,t)$ is given by expressions $\frac{A_T^2 k^2}{\omega\rho_0(z)m_t}e^{i(kx-\omega t)}$ $(z \leq 0)$ and $\frac{A_I^2 k^2}{\omega\rho_0(z)m_s}e^{i(kx-\omega t)}$ $(z > 0)$ from which it is immediate that the ratio of transmitted energy flux, in the stratosphere, to incident energy flux, in the troposphere, is

$$R = \frac{A_T^2}{A_I^2}\frac{m_t}{m_s} = \frac{4}{\left(1 + \frac{N_t}{N_s}\right)^2}\frac{N_t}{N_s}, \tag{2.60}$$

where we have used equations 2.56 and 2.59. It is straightforward to show that a maximum of R occurs for $N_t = N_s$.

For a 60 min pulse of heating, with $L = 10\,\text{km}$, $N_t = 0.01\,\text{s}^{-1}$ and a range of values of N_s, we have computed the upward energy flux, $p'w$, at the tropopause at a fixed time of $t = 60\,\text{mins}$. We denote the horizontal average over 100 km by q_z. This is shown in figure 2.13, where, as predicted by the above model, the upwards radiation is maximised when

$N_s = N_t$, i.e., when there is no wave reflection at the tropopause, consistent with the results of Sutherland (1996; 2010), who considered the simple case of Boussinesq monochromatic waves in an unbounded atmosphere. When $N_s \neq N_t$, figure 2.13 shows that the upwards radiation (in energy) is reduced by up to 12% over $0.5 < N_s/N_t < 2$. This reduction is consistent with the results shown in figure 2.10.

2.5.4 Triggering of Convection

The triggering of convection can be controlled by boundary-layer thermals having enough kinetic energy to overcome convective inhibition (CIN) at the top of the boundary layer (e.g. Mapes 2000), and one process that can erode the CIN is low-level ascent. This acts to raise the height of any inversion at the top of the boundary layer, and can also induce convergence that enhances low-level moisture (Mapes, 1993). Meanwhile, upper level subsidence acts to stabilise the troposphere, reducing the amount of CAPE.

After a localised convection event of the type modelled here by the prescribed heating, radiating gravity waves provide the necessary local dynamical adjustment (Bretherton & Smolarkiewicz, 1989), which involves periods of both tropospheric descent and ascent (figure 2.10). The initial subsidence pulse with deep tropospheric warming provides an ambient atmosphere with reduced CAPE (i.e., less favourable for further convection), but this disappears in the following pulse, which also has low-level ascent (to erode CIN, and is thus favourable for further convection). Case studies have shown these processes to be influential in controlling the triggering of further convection close to a parent storm (e.g., Marsham and Parker 2006, Birch et al. 2013), even when w is only of the order of centimetres per second, and is thus too small to act as a direct trigger for convection.

We now use our model to identify zones where the radiating gravity waves provide an ambient atmosphere favourable for triggering of convection, in the above sense. Figure 2.14 shows results from RAD2 following a 1 h pulse of heating. We consider θ in the middle troposphere (shown as coloured contours) as a measure of reduced CAPE, and positive w at 1 km as a measure of CIN erosion (shown as shaded regions). Immediately after the termination of heating at 1 h, a series of zones appear with small or negative mid-tropospheric θ and positive low-level w, each of which moves away from the parent storm and is favourable for further convection. The first such zone is highlighted within the dashed contour; this moves outwards from the parent storm at approximately $20\,\mathrm{m\,s^{-1}}$.

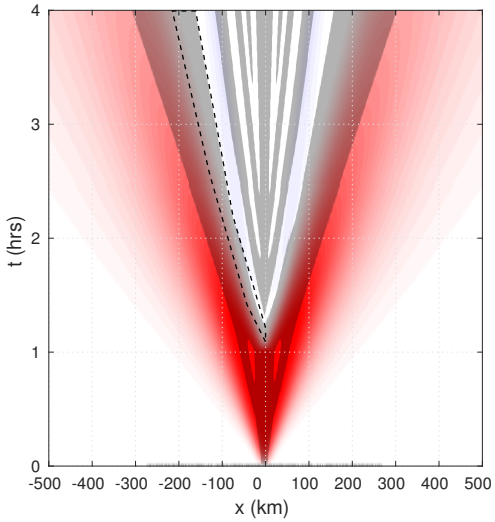

Figure 2.14: Hovmöller plot showing the response to a 1 hr pulse of heating in RAD2, with $L = 10\,\mathrm{km}$, $N_t = 0.01\,\mathrm{s}^{-1}$, $N_s = 0.02\,\mathrm{s}^{-1}$. The coloured contours show mid-tropospheric θ; red regions, in which the atmosphere is warmed, will have reduced CAPE. The shaded region shows where $w > 0$ at 1 km, which will act to erode CIN. The dashed contour encloses one of several bands that may thus be preferential for triggering of subsequent storms.

2.6 Implications for Convection Parameterisation Schemes and GCMs

In §2.5 we quantified the dynamical response to buoyancy forcing representing a single convection event with a width of about 10 km. We now investigate how the dynamical response to such an event would appear in a coarse model (e.g., a GCM) in which convection is not resolved, and is instead parametrised by applying heating over a grid cell with width of about 100 km. We consider how the local and remote responses are then altered, and the implied changes in the heating tendency.

Note that we are not considering the alternative scenario in which a population of sub-grid clouds (each of width 10 km, say) is spread over a grid cell of width 100 km (say). In that case, the differences between the exact dynamical response (excited by a population of small-scale heatings) and that due to a single smeared-out heating (perhaps corresponding to a convection scheme) might be smaller. Our experiment, involving a single isolated sub-grid cloud, might be regarded as a "worst case scenario" for a convection scheme.

2.6.1 Sensitivity of Gravity Wave Response to Horizontal Length Scale of Heating

Under conditions of identical total (x-integrated) heat input, our model shows that variation in the horizontal length scale of the heating, L, induces significant changes in the timing and magnitude of the immediate and remote atmospheric adjustment. We now quantify these differences for the response to pulsed heating of duration 1 h, between cases with $L = 10\,\text{km}$, and $L = 100\,\text{km}$. The former is representative of single, isolated convective hot towers, whilst the latter is representative of parameterised convection in a GCM, where small length scales cannot be resolved and the heating must be imposed at the grid scale (or larger). To ensure the same total heat input in both cases, the maximum buoyancy forcing, S_0 satisfies $S_0(L = 10\,\text{km}) = 10\,S_0(L = 100\,\text{km})$.

Figure 2.15 shows the responses in w and θ. The response is averaged both vertically over the troposphere $0 \le z \le 10\,\text{km}$, and horizontally over $|x - x_0| \le 50\,\text{km}$ for each of $x_0 = 0$ (panel a: local response directly over heating) and $x_0 = 100\,\text{km}$ (panel b: remote response). The horizontal averaging means we are comparing the response to "real" convection ($L = 10\,\text{km}$) when smeared over a GCM grid cell of width 100 km, with the response to parameterised convection ($L = 100\,\text{km}$) over the same grid cell. That is, we compare how the response *should* appear on the model grid, with how it *will* appear when convection is parameterised (ignoring any additional degradation due to the numerical scheme of the GCM, since the response here is calculated exactly via (2.16) and (2.17)).

We first discuss the local response shown in figure 2.15(a). When $L = 10\,\text{km}$, the w response quickly reaches a steady-state value, but this "correct" value is never attained when $L = 100\,\text{km}$, with w remaining smaller. It is a similar story for the θ response, but θ does eventually reach the "correct" steady-state value. When the heating is terminated at 1 hr, both w and θ decay in about 30 mins when $L = 10\,\text{km}$; but the decay takes twice as long (circa 1 h) when $L = 100\,\text{km}$.

The remote response is shown in figure 2.15(b). Here the magnitude of the response is smaller when $L = 100\,\text{km}$ than when $L = 10\,\text{km}$, for both w and θ. There is also a non-trivial change in the timing of the peak warming, which occurs too soon (by about 15 mins) when $L = 100\,\text{km}$. However, the eventual decay (for $t > 2\,\text{h}$) is similar in both cases.

There are implications for the accuracy of the entire dynamical adjustment in GCMs when small-scale convective heating ($L = 10\,\text{km}$) is replaced by smeared-out parametrised heating on the grid scale ($L = 100\,\text{km}$). In particular, this induces errors of about 20% in magnitude in both w and θ, for both the local and remote responses. Any dynamical processes sensitive to w and θ will be correspondingly compromised. For example, the suppression and initiation of further convection will be modified, via the CAPE and CIN mechanisms discussed in §2.5.4. We stress that such modifications are possible even though the absolute dif-

ferences in w are only $1-2\,\mathrm{cm\,s^{-1}}$: these differences would be insignificant for direct triggering of convection, but they will imply 20% differences in quantities such as CAPE and CIN.

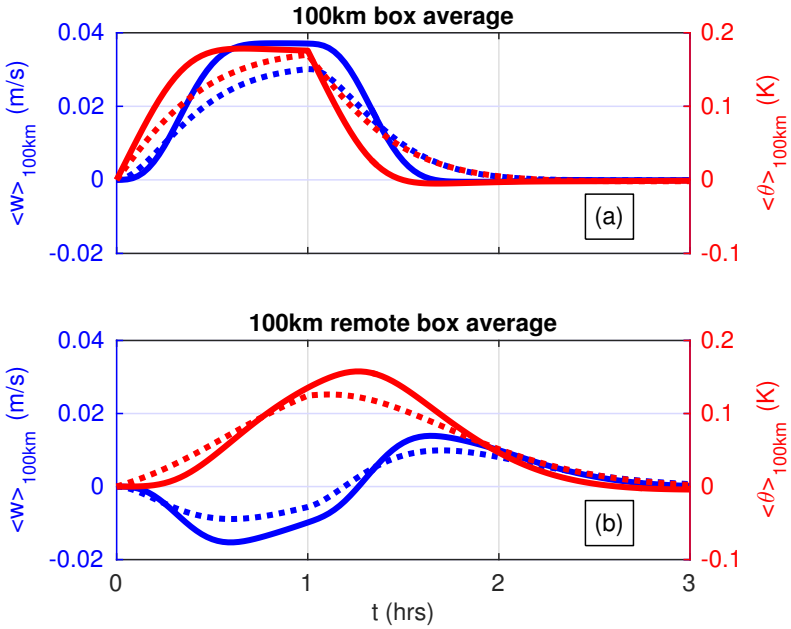

Figure 2.15: Time evolution of the averaged tropospheric responses in RAD2 when $L = 10\,\mathrm{km}$ (solid lines) and $L = 100\,\mathrm{km}$ (dotted lines). Shown are w (blue) and θ (red), with additional horizontal averaging over (a) $-50\,\mathrm{km} < x < 50\,\mathrm{km}$ (local response) and (b) $50\,\mathrm{km} < x < 150\,\mathrm{km}$ (remote response).

Looking at figure 2.15, one might conclude that, despite differences in the first few hours after initiation, both cases of heating are in some agreement by around 3 hours. However, figure 2.16, which is an instantaneous vertical cross section of the corresponding fields at $t = 4\,\mathrm{hours}$, reveals anomalies in the vertical structure. Here, $\Delta w \equiv (w(L = 100\,\mathrm{km}) - w(L = 10\,\mathrm{km}))$ and $\Delta\theta \equiv (\theta(L = 100\,\mathrm{km}) - \theta(L = 10\,\mathrm{km}))$.

In summary, from figures 2.15 and 2.16 we conclude that narrow, intense heating, representing a convective hot tower, induces the largest velocities and warming. Less intuitive is the observation that the differences in behaviour persist for several hours. Coarse GCM models with parameterised heating will fail to resolve some of the variation in responses and, hence, fail to simulate modification of the convective environment.

Note that the results of this section can also be interpreted in a completely different way, in which we are comparing the dynamical responses induced by two fundamentally different kinds of convection. Then, the narrow intense heating ($L = 10\,\mathrm{km}$) models a single isolated hot tower, whilst the wider less intense heating ($L = 100\,\mathrm{km}$) models a mesoscale convective system.

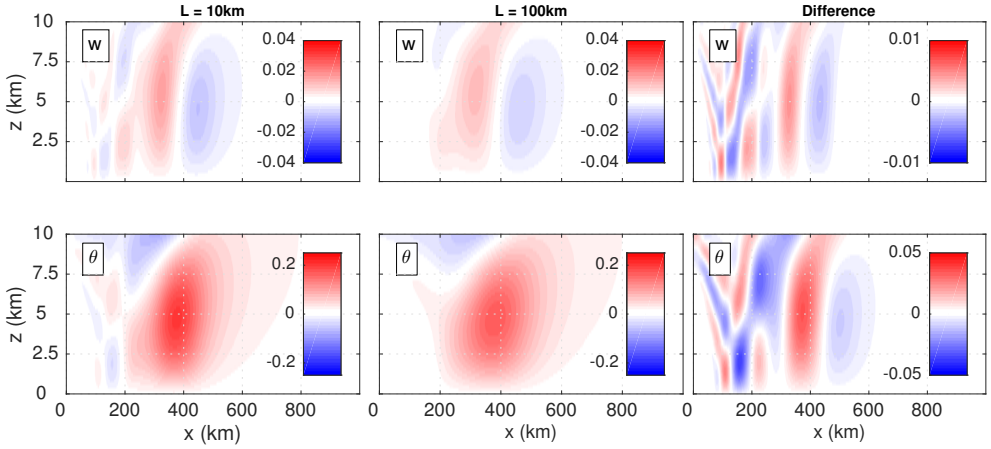

Figure 2.16: Vertical cross sections of w (ms^{-1}) and θ (K) response to forcing of horizontal lengths $L = 10\,\mathrm{km}$ (top) and $L = 100\,\mathrm{km}$ (bottom), which is pulsed for $t = 1\,\mathrm{hr}$. The response at $t = 4\,\mathrm{hrs}$ is shown. The right hand column is the difference. Total heating is the same in both cases.

2.6.2 Redistribution of heating

GCM parameterisation schemes generally make the assumption that all subsidence happens within the convecting grid box (Arakawa & Schubert, 1974) . In this section we estimate the error associated with the spatial homogenisation (or smoothing-out) of the grid-box heating (implicit in a GCM) by comparing adjustments with more realistic heating distributions. Once again, we will consider the "worst case scenario" where convective heating in the grid box is confined to a single hot tower.

An appreciation of the error associated with GCM-like smoothing of heating can be achieved through analysis of the heating tendency field, $\frac{\partial b}{\partial t}$. From (2.1), recall

$$\frac{\partial b}{\partial t} = S - N^2(z)w. \tag{2.61}$$

For steady heating (which allows a constant value of b to develop at all positions in the domain), in the long-time limit, a steady-state $\frac{\partial b}{\partial t} = 0$ develops, when there is a balance between heating and w response fields, with $S(x,z,t) - N^2(z)w(x,z,t) = 0$.

To consider the dynamics of tendency, $\frac{\partial b}{\partial t}$, in the context of GCMs, it is first necessary to ensure that all heating is contained within the spatial domain of our model. For the purposes of this section (alone) we therefore re-define the x-dependence in our buoyancy forcing function, $S(x,z,t)$, to be a simple box function

$$X(x) = \Theta\left(x + \frac{L}{2}\right) - \Theta\left(x - \frac{L}{2}\right), \tag{2.62}$$

where, recall Θ is the Heaviside function. Whilst the Gaussian x-dependence used elsewhere in this study is more realistic, a box function has no

tail, and therefore all heating is contained within the domain which, for present purposes, we regard equivalent to a parent grid box. We shall consider two cases. The horizontal heating variation, $X(x)$, is taken to have i) a realistic horizontal scale with $L = 10\,\mathrm{km}$, representative of a single cloud, and ii) a GCM-like smoothed scale with $L = 100\,\mathrm{km}$. In both cases, the total heating is ensured to be the same by setting $S_0(L = 10\,\mathrm{km}) = 10S_0(L = 100\,\mathrm{km})$. This choice of $X(x)$ may be straightforwardly implemented in (2.16) for w, and then in (2.20) for b, with G taken as

$$\begin{aligned} G(c_j, L, x, t) &= \Theta(ct - x + L)(ct - x + L)/L \\ &- \Theta(ct - x - L)(ct - x - L)/L \\ &- \Theta(-ct - x + L)(-ct - x + L)/L \\ &+ \Theta(-ct - x - L)(-ct - x - L)/L. \end{aligned} \tag{2.63}$$

Figure 2.17 compares the instantaneous spatial integral (in x and z) of tropospheric heating tendency over a 100 km box (centred on $x = 0$) for our chosen cases (i) and (ii) above. The differences between the red and blue lines represents the error introduced when there is smoothing of heating. Shown also is the heating tendency time series of a scaled heating (black line), which we shall discuss later in this section.

In the $L = 10\,\mathrm{km}$ heating case, the propagating modes of subsidence take time to propagate outside the 100 km box. Thus for a small time almost all the subsidence is within the box, and the average tendency, $< \partial b/\partial t >$, is almost constant. As the descending modes move through the edges of the 100 km box, subsidence transfers to neighbouring regions and the tendency within the box falls. In contrast, when the heating is artificially smoothed over the 100 km box (red line), the subsidence immediately occurs outside the box and tendency is immediately reduced inside the parent box, as the vertical motion begins to compensate the heating term. However, at around 25 mins, the blue line sinks below the red, and it approaches equilibrium faster than its smooth counterpart thereafter. This behaviour is consistent with the longer tendency modes in the smoothed heating taking more time to separate-out and to leave the parent box.

A further comparison is made in figure 2.18, which shows Hovmöller plots of the difference between tropospheric heating tendency for the cases (i) and (ii) described above. Shown is a high-resolution solution, in which heating is considered to be structured within the GCM box, and the same solution coarsened to GCM-like resolution ($\Delta x = 100\,\mathrm{km}$, $\Delta t = 15\,\mathrm{mins}$) via spatial and temporal box averaging. Again we observe subsidence modes warming neighbouring grid boxes immediately in the smooth case, and the heating tendency persisting in the parent grid box for longer. The parent grid box is therefore too cold for the first 30 mins and too warm for the subsequent 30 mins, with errors of the order of 10% apparent. The adjacent grid boxes mirror these differences for the first hour. Differences in the following hour are attributed to the longer modes

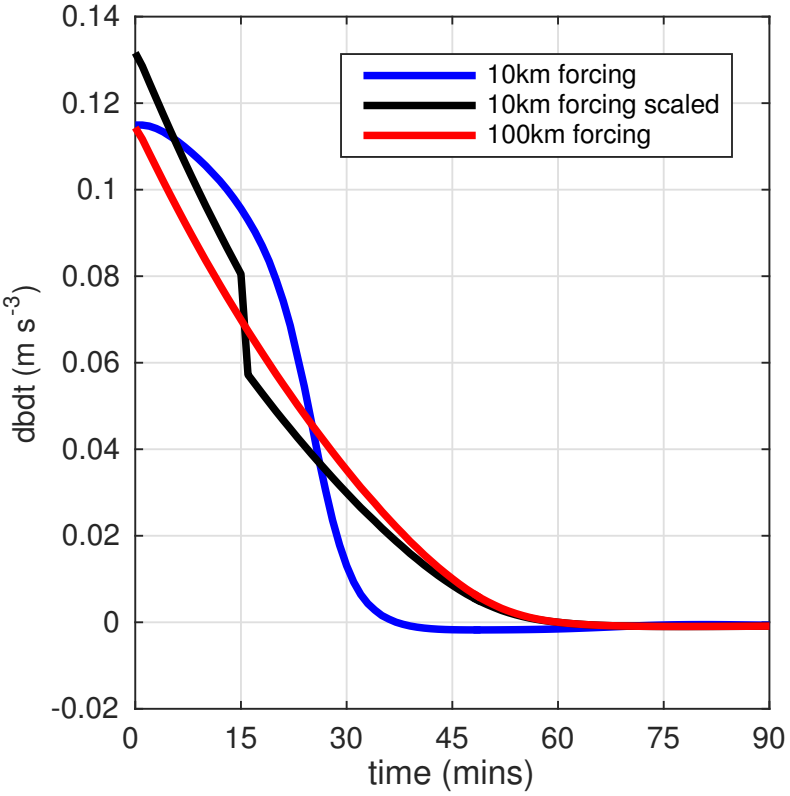

Figure 2.17: Time series of 100 km spatially integrated heating tendencies for a 10 km realistic heating (blue), a 100 km smoothed GCM-like heating (red) and a scaled 100 km heating (black). Total heating is the same in both cases. The difference between the red and blue lines represents a time-local error in heating tendency which arises as a consequence of spatial smoothing of heating, over the domain (GCM box). The black line shows a scaled heating (see text) which has a reduced error in the parent grid box.

generated from the smooth heating dispersing the envelope of dominant response (the narrow heating has a tighter envelope). Differences in the parent and adjacent grid box after 2hours are minimal (this fact is also visible in figure 2.17). The domain far-field response shows minimal difference throughout the simulation.

The errors apparent in figures 2.17 and 2.18 suggest a calibration might fruitfully be applied to GCM heating parameterisation schemes, to compensate for the thermodynamic errors associated with incorrect propagation of the subsidence response away from heating. We postulate a simple multiplicative scaling to the smoothed GCM-like heating, designed to produce a response closer to that observed in a calculation forced with a more realistic (i.e. narrow) horizontal variation of heating. Put another way, we propose to scale the time-dependence of the forcing in such a way that the red line in figure 2.17 moves closer to the blue line. Accordingly, comparing the smoothed heating with the narrow, it

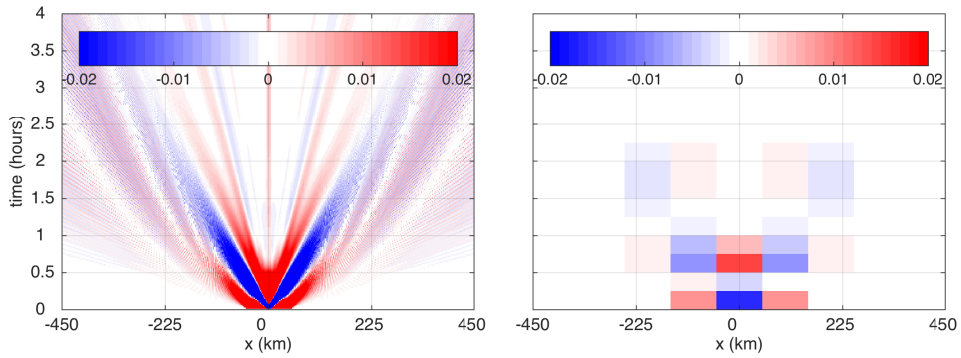

Figure 2.18: Hovmöller plot of differences in tropospheric heating tendency ($\mathrm{m\,s^{-3}}$) between the non-scaled cases considered in figure 2.17. Panel (a) shows a fully resolved solution, panel (b) shows a solution which has been coarsened to 100 km grid box and 15 min time step (representative of a GCM). In the parent grid box, the smoothed heating is too cold at 30 mins, then too warm for 30 mins, before reconciling with the realistic case.

is apparent that the smoothed heating requires an increased amplitude for some time, followed by a decreased amplitude, before returning back to its original amplitude for later times, when the responses to smooth and narrow forcing have reconciled. Denote the first time at which the lines in figure 2.17 cross by T_1 and that at which both reach equilibrium by T_2. For $0 < t < T_1$, we scale the heat-forcing by factor $\alpha_1 > 1$, for $T_1 < t < T_2$ we scale it by $\alpha_2 < 1$, and for $t > T_2$ no scaling is applied i.e. we return the buoyancy forcing to its nominal value.

We now seek to minimise the area between the red and blue curves of figure 2.17. We apply the following practical constraints:

1. T_1, T_2 are chosen to be multiples of 15 minute blocks. From inspection of figures (2.17) and (2.18), we choose $T_1 = 30$ mins, $T_2 = 60$ mins.

2. $(\alpha_1 - 1)T_1 = (1 - \alpha_2)T_2 \implies \alpha_2 = \frac{T_1 + T_2 - \alpha_1 T_1}{T_2}$.

Constraint 2 is chosen to ensure that total heat input is the same in both the scaled and non-scaled cases for $t > T_2$.

Using an overall cost parameter, ξ, defined as

$$\xi = \left\langle \left| \left\langle \frac{\partial b^{(1)}}{\partial t} \right\rangle_{x,z} - \left\langle \frac{\partial b^{(2)}}{\partial t} \right\rangle_{x,z} \right| \right\rangle_t , \tag{2.64}$$

where $b^{(1)}$ is the buoyancy response to a $L = 10$ km forcing and $b^{(2)}$ is the buoyancy response to a $L = 100$ km forcing, and the averaging is done over the troposphere in the central 100 km box. We measure the error, and minimise it over $1 < \alpha_2 < 1.5$. We find an initial forcing amplification

of $\alpha_1 = 1.15$ and then a forcing suppression of $\alpha_2 = 0.85$. The black line in figure 2.17 shows data from our time-variant scaled smooth heating, which is now closer to the blue in the parent grid box. However, whilst our scaling *ansatz* may improve the response in the parent grid box, the response in the adjacent field shows the expected increase in error, as shown in figure 2.19.

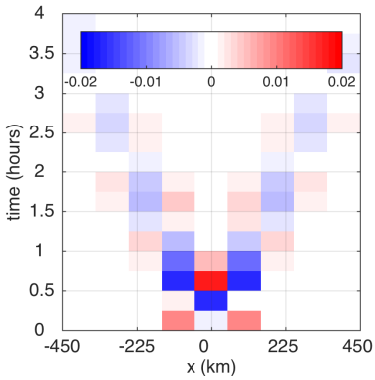

Figure 2.19: Hovmöller plot of differences in buoyancy tendency ($\mathrm{m\,s^{-3}}$) between a 10km forcing and a 100km forcing which has been scaled in order to reduce error (see text). The parent box now has a reduced error to begin, but the far field has an increased error.

In this section, we have quantified error associated with the smoothing-out of convective heating in a manner similar to that performed in GCMs. We have proposed a mechanism to improve the grid-box response, with a simple time-dependent heating parameterisation. Whilst this parameterisation led to error reduction in the parent grid box, the adjacent and neighbouring grid boxes experience increased error. Whether it is possible to improve the parameterisation with more sophisticated time-dependent heating remains an open question not addressed here. Certainly, one place to start would be with a more rigorous analysis of the parameter space influencing the error, together with consideration of a global error.

2.7 Comparison with a Unified Model Simulation

2.7.1 Introduction

We compare an idealised two-dimensional version of the Met Office Unified Model (iUM hereafter), with a prescribed heating, to the linear analytic model constructed by Halliday et al. (2017) and described in this Chapter. We evaluate forced gravity wave dynamics, with particular interest in quantifying the extent to which convective adjustment can be captured with linear dynamics, and supplying a benchmark study for

Table 2.2: Details of model grid and time step

Model setting	
Number of model levels	70
number of model rows	6
number of model columns	600
Horizontal gridlength (km)	1.0
Model top (km)	38.5
time step (s)	10.0

further comparisons. iUM runs were performed by Rachel Stratton at the UK Met Office.

2.7.2 Model Configuration

The Met Office Unified Model (UM) (Cullen, 1993) is a full 3D latitude-longitude model which can be run in an idealised mode. In idealised mode the UM can be configured to run on a Cartesian grid with a small number of rows in the y-direction and a large number of columns in the x-direction so that it resembles a "2D like" configuration. The UM configuration uses the ENDGame (Even Newer Dynamics for General atmospheric modelling of the environment) dynamics (Wood *et al.*, 2014). The dynamics is semi-Lagrangian which means that a longer time step can be used and the model will still remain stable but this will tend to damp gravity waves. For this simulation a shorter time step of 10 seconds is being used. The UM is not formulated to ensure energy conservation. The UM horizontal grid has an Arakawa C-grid staggering. The vertical grid in idealised mode with a flat surface has a height coordinate with a Charney-Phillips staggering. A uniform vertical grid could be used for idealised experiments but we chose to used a vertical grid with more levels near the surface increasing spacing with height, similar to that used for numerical weather prediction and climate. The UM idealised simulation is run in dry mode. At the upper and lower model boundaries the mass flux is constrained to be zero. All moist processes in the model are switched off. The radiation scheme is off, so for this simulation the only physics and diffusion being used is the boundary layer turbulence scheme which at high resolution is run with 3D turbulent mixing scheme based on Smagorinsky (1963). The model was initialised to have a similar potential temperature profile to the theoretical model, with a surface temperature of 300K and a surface pressure of 1000hPa. Initially the model is at rest with no winds. The simulation is forced with a heating in the troposphere identical to that described for the theoretical model and applied for the first hour of the model simulation. The model is run for two hours. Note as the UM idealised model is setup with bicyclic boundary conditions gravity waves can travel out of one end of the grid back round into the opposite end of the grid.

2.7.3 Theoretical Model Configuration

We run our 2D model in two configurations: (i) with a rigid lid at 38.5 km to match that of the iUM (TLow hereafter), and (ii) with a very high rigid lid so that the solution can be considered fully radiating in the spatial and temporal domains of interest here (TRad hereafter). We can therefore test the model structure of the forced waves.

In all runs the prescribed heating has the same spatial and temporal structure as before, has an aspect ratio of 1, and a maximum heating rate of $864\,\mathrm{K\,day^{-1}}$ (note, this is different to what is previously used in this chapter, but matches the iUM runs). The heating is a one hour pulse, which is on for the opening hour of the simulation, and then turned off. Total simulation time is two hours.

2.7.4 Mesoscale Features

We perform a qualitative comparison of the w response in the iUM, TLow and TRad in figure 2.20. At first order, we recognise consistent features in all models: (i) agreement in spatial and temporal wave patterns, and (ii) a tropospheric subsidence mode whilst heating is on, followed by a propagating "rebound" mode when the heating is turned off. Note also the width of the mode is proportional to that of the forcing. We conclude that linear theory captures the main mesoscale features of convective adjustment.

However, we also observe differences in the amplitude of response. Indeed in panel (c) of figure 2.20, we see growing differences in the amplitude of the waves as they reach the iUM damping layer.

After the first hour of the simulation, from the wave packet, a modal structure emerges in the iUM and TLow runs (clearly visible in panel (f) of figure 2.20). TRad does not have this feature, which we speculate is an artefact of lid height. This detail is not so prevalent in the iUM (panels b, c of figure 2.20). However, at longer times, after the modes have had time to separate out, a modal structure (discrete wave pattern) does emerge in the iUM (also visible in panel (c) of figure 2.21, discussed below).

2.7.5 Dispersion of Wave Modes

Panels (a,...,c) of figure 2.21 show the time series of mean tropospheric vertical velocity ($< w >_{\mathrm{trop}}\,\mathrm{m\,s^{-1}}$) at remote points 50 km, 150 km and 250 km from the heat forcing, respectively. Black lines indicate iUM data, red indicate TLow and blue lines indicate TRad. The resolution of TLow and TRad is $\Delta x, \Delta z = 100\,\mathrm{m}$ $\Delta t = 0.5\,\mathrm{mins}$.

In panel (a), each model captures a consistent, smooth subsidence gravity wave mode, followed by the rebound mode when the heating is turned off. At this point we see no modal dispersion. The iUM has

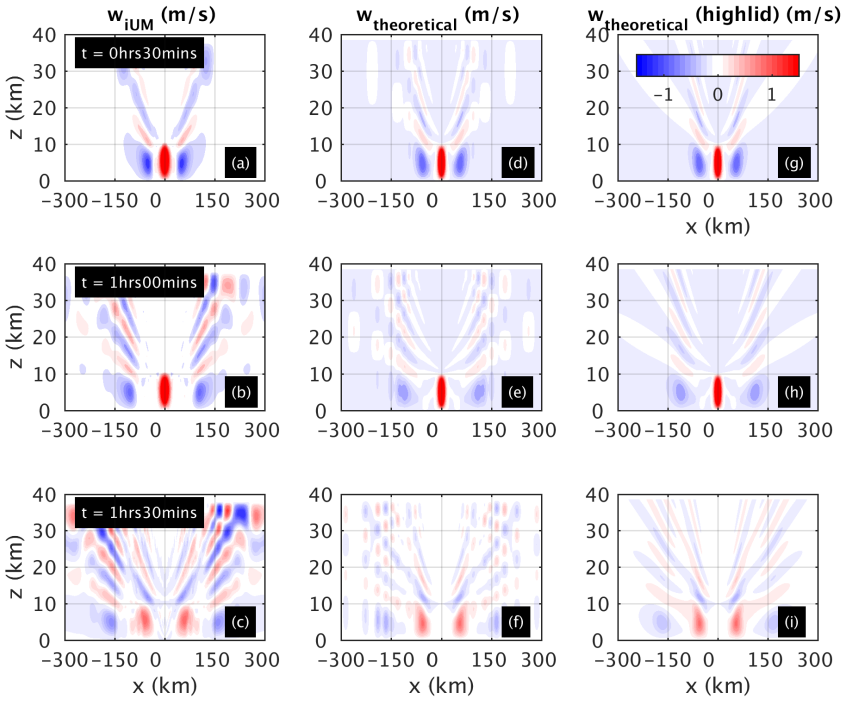

Figure 2.20: Vertical cross sections of vertical velocity, $w\,\mathrm{m\,s^{-1}}$. Panels (a,...,c) show iUM data with a lid at 38.5 km, (d,...,f) show theoretical data with a lid at 38.5 km, and (g,...,i) show theoretical data with a very high lid. Time advances down the panels in 30 min steps. In all cases, the heat forcing is 10 km deep, aspect ratio 1 and pulsed for the initial hour of simulation.

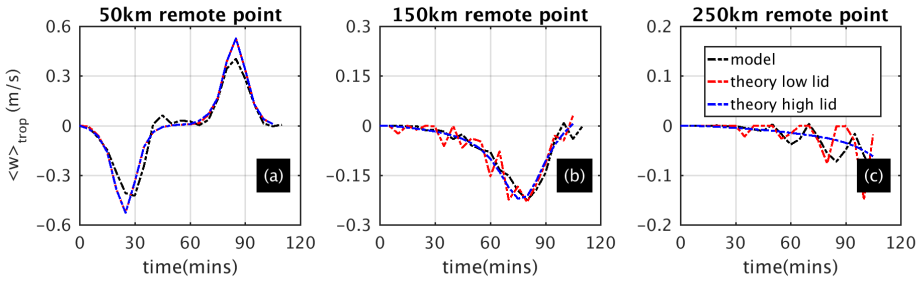

Figure 2.21: Time series of mean tropospheric $w\,\mathrm{m\,s^{-1}}$ for points 50 km, 150 km and 250 km respectively, Note the varying range of y-axis. Black lines indicate iUM data, red indicate TLow and blue indicate TRad.

a reduced amplitude of tropospheric mean w (roughly 80% that of the theoretical models).

In panel (b) we clearly see certain gravity wave frequency in the TLow w, which oscillates about the model and TRad response with time period roughly 10 mins. A quick calculation suggests this is due to the location of lid, since

$$T = \frac{2\pi L}{NH}, \tag{2.65}$$

where T is the time period, L is the width of heat forcing, N buoyancy frequency, and H height of heat forcing. In our case, $L = H = 10\,\mathrm{km}$, $N = 0.01\,\mathrm{s^{-1}}$ in the troposphere and therefore $T = 2\pi/N \approx 10\,\mathrm{mins}$. Note also, at this location, the time series is long enough only for the initial subsidence mode to pass.

In panel (c) of figure 2.21, the iUM too develops this periodicity, which has an amplitude growing with time.

2.8 Conclusion

Using an analytical solution to a 2D thermally-forced, deep atmosphere, we have constructed an idealised model of convective adjustment. We have expressed vertical velocity and potential temperature response in terms of convectively-forced gravity wave modes and, hence, we have illuminated the role of these modes in conditioning the troposphere for further convection. We find that the characteristics of our forced gravity waves are influenced by the spatial and temporal dependence of the forcing function, the nature of the upper boundary condition applied to the domain, and upon model stratification.

We tested the influence of the upper boundary condition and found that a trapped solution with rigid lid at the tropopause (allowing no wave radiation into the stratosphere), yields a single gravity mode, communicating high intensity downward motion and warming, which propagates into the neighbouring troposphere and inhibits the chance of further con-

vection. Raising the altitude of the upper lid high into the mesosphere and beyond (to approximate the semi-infinite solution) allows a range of higher-order gravity wave modes to be excited, with much deeper and faster modes acquiring importance. The convective adjustment is therefore communicated into the immediate environment faster than in the trapped case. We note also that allowing waves to radiate upward sees a reduction in the magnitude and intensity of the tropospheric response, as expected.

Investigating the temporal dependence of gravity wave characteristics through a pulsed forcing function, we find that when the pulse of forcing is truncated, a rebound mode of upward motion propagates away from the initially heated region, and the potential temperature response returns to base state. Further, using figure 2.14, we identify propagating zones where the radiating gravity waves provide an ambient atmosphere favourable for further convection. In such zones, there is no longer tropospheric subsidence (which reduces CAPE), and there is low-level ascent which will erode CIN.

The inclusion of a model stratosphere, with $N_s = 2N_t$ increases the intensity of the tropospheric response, due to wave reflection at the tropopause (compared with $N_s = N_t$). We also notice a slight increase in the propagation speed of the mode of dominant response. We find a maximum of energy radiated into the stratosphere (communicated by gravity waves) for $N_t = N_s$, as there is no interface and therefore no reflection. With this in mind, we consider our trapped model (TRAP) and optimally-radiating model (RAD1) as respective lower and upper bounds on radiation at the tropopause. The most realistic intermediate model (RAD2, with $N_t = 2N_s$), which has partial trapping and radiation, has upward radiation between the two bounds.

We quantify the error associated with smoothing out convective heating from a subgrid, single convective hot tower onto a coarse GCM grid. Performing "worst case scenario" experiments, in which a convection scheme spreads heating from a cloud of width 10 km over a full model grid box of width 100 km, we find that the timing and magnitude of the adjustment is dependent on the heating distribution. Perturbations in potential temperature and vertical velocity will be distributed faster and over a larger region in the parameterised case. Furthermore, an isolated cloud has a strong response on a sub-GCM-grid scale, which has implications for the forcing of neighbouring grid cells in current numerical models, since the timing and magnitude of the response, communicated by gravity waves, is sensitive to the horizontal length scale of the forcing function. Further, analysis of the heating tendency reveals errors of the order of 20% and correspond to a grid-box heating tendency which falls too quickly when heating is spatially smoothed (parameterised), due to a failure to account for the finite time taken by small-scale responses to propagate out of the grid-box. We propose a simple time-varying scaling to the heating to minimise these errors. Such a scaling decreases the

error in the grid box that is the parent to convection, but increases error in adjacent boxes. We propose ways in which to potentially improve this scaling, but leave this for another study.

The analytical model developed in this work allows us to draw conclusions on the role of convectively forced gravity waves. Notably, even with maximum upward energy radiation, we observe a significant tropospheric response to prescribed thermal forcing. Further, the gravity wave characteristics associated with the convective adjustment are highly sensitive to the upper boundary condition at the tropopause, heating function and model stratosphere.

We compare the convectively forced gravity wave dynamics in our 2D model with a 2D idealised version of the Met Office Unified Model (iUM). The iUM runs were performed by Rachel Stratton at the UK Met Office. The iUM has a lid at 38.5 km. We configure the analytic model in two different ways: (i) with a lid at 38.5 km, to match that of the iUM, (TLow), and (ii) a very high lid, so that the response can be considered radiating in the spatial and temporal domain of interest here (TRad).

We find qualitative agreement in the mesoscale adjustment to convective forcing, with all simulations capturing a tropospheric subsidence and "rebound" mode generated by a 1 hour forcing. These modes have horizontal and vertical length scale proportional to that of the forcing function. However, as time advances we notice a growing discrepancy in the wave amplitude in the upper stratosphere, which may be worth further investigation.

In the TLow runs, a modal structure appears as an artefact of lid height. The iUM response has a more subtle version of this structure, but is closer to the response of TRad.

An oscillation in the mean tropospheric w, with time period ≈ 10 mins emerges in the time series of a point 150 kms from forcing in the theoretical runs due to a relationship with the forcing aspect ratio and lid height.

We consider our theoretical tool a benchmark for any further model comparison work. One place to start would be testing iUM resolution, coarsening from the 1 km runs used here toward global circulation model (GCM) resolution (O(10 km)). We speculate that as the numerical model reaches coarser resolution, it will capture only part of the gravity wave spectrum. Another potentially fruitful study might diagnose wave fluxes in the stratosphere, and quantify the errors in the iUM against our TRad.

2.9 Summary

We have quantified the effect of upward radiation on the tropospheric response to convection, using a two-dimensional, linear, hydrostatic model after Nicholls et al. (1991) and Edman and Romps (2017). Our model is directly applicable to certain atmospheric processes (e.g. squall lines),

furnishes simple, informative, analytic solutions, and provides insight into numerical models.

However, a 2D model is not without obvious limitations. In reality, the volume available to a horizontally propagating disturbance increases linearly with horizontal coordinate - the further the wave propagates, the more it can spread. Our two dimensional model overlooks this fact, which we judge to be its most significant limitation. The opportunity to extend our base model to three dimensions is hard to resist on the basis of completeness alone. However, there are better, physical, reasons to found a three dimensional model, suitable for further study, as many atmospheric phenomena are intrinsically three-dimensional in character, e.g. MCSs and typhoons (which have some axial symmetry).

In the next Chapter, we will extended our model to the case of axial symmetry, again seeking semi-analytic solutions to a buoyancy forcing and investigate the dynamics of convective adjustment in a trapped and pseudo-radiating atmosphere. We will also make comparisons to the 2D results presented in this Chapter.

Chapter 3

Three Dimensional Forced Gravity Waves

3.1 Introduction

In Chapter 2 we reported on linear analytical solutions for the flow and thermodynamic response to pulsed buoyancy forcing, within a deep, two-dimensional atmosphere. These solutions are good approximations for certain convecting atmospheric features, such as squall lines, and illuminate the fundamental mechanisms of convective adjustment. However, real convection is often observed in three dimensions which thus implies *radial* adjustment and emission into the environment. Example systems include MCSs or isolated convective hot towers- see section 3.2.

Motivated mainly by a wish to quantify the difference between 2D and 3D properties, we here extend our previous, 2D forced gravity wave model into a cylindrical, axisymmetric geometry. The 2D treatment of Chapter 2 neglected the Coriolis force on grounds of scaling. Had this been included, it would not have been possible to obtain solutions for general horizontal variation of heating, which provided an additional, mathematical motive for setting $f = 0$. In 3D, it is not possible to write fully analytical solutions, even for $f = 0$. In the 3D treatment of this chapter, we therefore include Coriolis' parameter in the mathematical treatment, for completeness, since removing it is no longer advantageous. However all results have $f = 0$.

The goal for this Chapter is to develop a cylindrically-symmetric, pseudo-radiating forced gravity wave model, after Chapter 2, and then to use it to make selective comparisons with our 2D model. Since it is possible to retain all the key physical features of the 2D model of Chapter 2, (heating structure, stratification etc.), differences between the data from the models of Chapters 2 and 3 may be attributed to the role of the third spatial dimension. Put another way, an axially symmetric, 3D model facilitates an understanding of the effect of 3D under controlled circumstances, since the vertical variation and stratification may be "transplanted" from the corresponding 2D problem. One can

therefore attribute changes to geometrical effects i.e. more realistic domain properties and the presence of a fifth field variable- the tangential velocity component.

We organise as follows. In section 3.2, we consider the background to the problem. In section 3.3, we will develop the companion mathematical model, which will be based upon a Hankel transform, for predicting the w and b adjustments. In 3.4 we consider its numerical implementation and in section 3.5 we discuss 3D output and quantify key differences relative to the 2D case.

Throughout, our treatment will emphasise horizontal variation, since the vertical stratification and modal expansion is identical to that of Chapter 2 Furthermore, our notation and use of symbols is identical with those used in Chapter 2 with the following caveats: (i) k is retained as the variable conjugate to horizontal position, r (which replaces x) even though the corresponding transfrom space cannot, rightly, be designated Fourier space, and (ii) a velocity component perpendicular to the $r - z$ plane will now be admitted.

3.2 Background

As we saw in Chapter 2, thermally forced gravity waves play in important role in convective adjustment, and linear theory allows us to accurately predict wave dynamics. However, whilst Chapter 2 illuminates the nature of two-dimensional forced gravity waves, gravity waves are predominately three-dimensional in reality, and propagate in horizontally circular patterns away from their source (Dewan *et al.*, 1998).

Studies characterising the three-dimensional aspect of convectively forces gravity waves have largely been based on high resolution numerical models (Beres, 2004; Beres *et al.*, 2002; Hauf & Clark, 1989; Horinouchi *et al.*, 2002; Lane & Reeder, 2001; Piani *et al.*, 2000) and emphasise how the wave field is largely determined by response to local forcing, i.e. individual convective updraughts rather than an ensemble.

Of course, studying a 3D problem begs the question of the influence of rotation, and the geostrophic adjustment to a 3D forcing is well studied (e.g. Fritts & Luo (1992) Zhu & Holton (1987)). However, since we will have $f = 0$ until Chapter 4, we defer discussion on geostrophic adjustment until then.

Here, again based on an analytical description of a deep atmosphere which is thermally forced via a prescribed heating function, we build a model capable of addressing the question

- What is the effect of the conditions of upward radiation on the spatial and temporal distribution of convective adjustment over the timescale of a few hours, relevant to mesoscale dynamics?

Note, this is an identical question to that of Chapter 2, with the focus in this Chapter being on how the inclusion of a third dimension influences

the adjustment. Naturally, we will also make comparisons to the 2D model.

We will found our model on idealised, linear equations for a deep atmosphere (in which the model lid is many times higher than the tropopause). For a standard set of equations, see e.g. Holton 2002. We apply a projection method to decompose into eigenmodes, which we can solve using Fourier and Laplace techniques for solutions to w and θ (recall, this is a slightly more generalised method than that of Nicholls (1991)). As we shall see in §3.3 this process is more complicated than in Chapter 2, as extra terms in the master equation for, say, w mean that the integral which inverts the spatial Fourier coordinate can no longer be evaluated analytically. Instead, we apply a Hankel transformation and evaluate the integral numerically.

3.3 Mathematical Model

We shall formulate a description in three dimensions, using cylindrical polar coordinates, which is as consistent as possible with our previous, two-dimensional model. Accordingly, our assumed stratification is identical to that in Chapter 2, as is the temporal and vertical structure of the assumed heat or buoyancy forcing. The horizontal variation is re-defined as follows. We place the vertical, z-axis at the centre of the domain, assume axial symmetry i.e. partial derivatives of all adjustments with θ all vanish and we centre heating on $r = 0$. Physically, our domain transformation means that we must allow an additional field variable, the tangential velocity, u_θ, which introduces an additional equation in the basic set. The domain, spatial-temporal distribution of heating and stratification is very similar to that used in Chapter 2. The modified heating distribution is summarised in figure 3.1.

3.3.1 Governing Equations

We continue to use the hydrostatic approximation in the vertical equation. The basic set of flow equations, now expressed within cylindrical polars contain an axial flow and now read:

$$\frac{\partial u_r}{\partial t} - f u_\theta = -\frac{1}{\rho_0(z)}\frac{\partial p}{\partial r}, \tag{3.1}$$

$$\frac{\partial u_\theta}{\partial t} + f u_r = 0, \tag{3.2}$$

$$b = \frac{1}{\rho_0(z)}\frac{\partial p}{\partial z}, \tag{3.3}$$

$$\frac{\partial b}{\partial t} + N(z)^2 w = S, \tag{3.4}$$

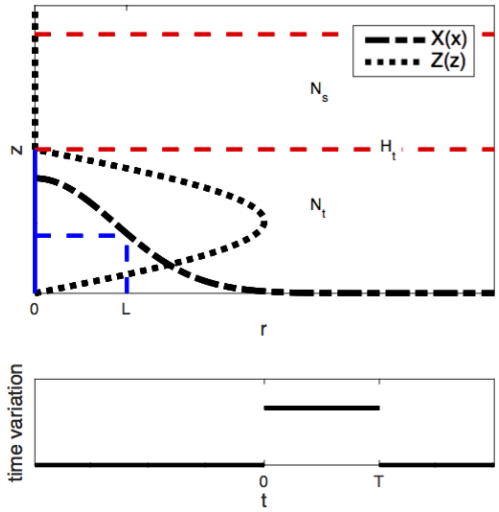

Figure 3.1: Schematic representation of the heating and stratification used for the three-dimensional model. All symbols and notation are identical with those used in Figure 2.1 of Chapter 2. The top panel shows the vertical and horizontal variation of heating, described by $Z(z)$ and $X(r)$ respectively. The characteristic width of heating is L. The bottom panel shows the time dependance. As in Chapter 2, the vertical variation of heating corresponds to the first baroclinic mode.

$$\frac{1}{r}\frac{\partial}{\partial r}(ru_r) + \frac{\partial w}{\partial z} = 0. \tag{3.5}$$

Above, $\underline{u} = u_r\hat{e}_r + u_\theta\hat{e}_\theta + w\hat{e}_z$ is the perturbation wind vector, p is the perturbation pressure, $\rho_0(z)$ is the basic state density, $b = -g\rho'/\rho_0(z)$ is the buoyancy (where ρ' is the perturbation density), $S(r,z)$ is a prescribed buoyancy forcing, and $N(z)$ is the buoyancy frequency

$$N^2(z) = -\frac{g}{\rho_0(z)}\frac{d\rho_0(z)}{dz}. \tag{3.6}$$

Certain remarks are in order before proceeding. We assume above no axial variation in any adjustment

$$\frac{\partial g}{\partial \phi} = 0, \quad \forall g. \tag{3.7}$$

Equation 3.5 may be written $\frac{\partial u_r}{\partial r} + \frac{u_r}{r} + \frac{\partial w}{\partial z} = 0$. The momentum and thermodynamic equations are mathematically unchanged from 2D (use of the r variable notwithstanding). The spatial influence of the third dimension will be communicated into our analysis solely from the continuity equation. In the horizontal momentum equations 3.1 and 3.2 of our basic equation set, the Coriolis acceleration $f\hat{e}_z \times \underline{v}$ has been expressed

in cylindrical polar coordinates as follows

$$\underline{a} = \frac{1}{r}\begin{vmatrix} \hat{e}_r & r\hat{e}_\theta & \hat{e}_z \\ 0 & 0 & f \\ u_r & ru_\theta & 0 \end{vmatrix} = -fu_\theta\hat{e}_r + fu_r\hat{e}_\theta.$$

Now, following our 2D treatment of Chapter 2, we do not make the Boussinesq approximation, i.e., ρ_0 is not taken to be constant in the horizontal momentum equation, so that the effects of a deep (albeit incompressible) atmosphere are again included. The buoyancy forcing S, with units of $\mathrm{m\,s^{-3}}$, again arises due to a thermal forcing Q, with units of $\mathrm{K\,s^{-1}}$, which in a more complete description would appear in the potential temperature equation $D\theta/Dt = Q$. We use a Boussinesq-like correspondence between the two, with

$$S = \frac{gQ}{\theta_0}, \tag{3.8}$$

where θ_0 is a reference potential temperature (taken to be 273 K). Later on, we will also evaluate a potential temperature perturbation θ' from b, again using a Boussinesq-like correspondence

$$b = \frac{g\theta'}{\theta_0}. \tag{3.9}$$

We again obtain an equation for w by eliminating variables from our basic set, which now reads as follows

$$\begin{aligned} \frac{\partial}{\partial z}\left(\rho_0(z)\frac{\partial^2}{\partial t^2}\frac{\partial w}{\partial z}\right) &+ f^2\frac{\partial}{\partial z}\left(\rho_0(z)\frac{\partial w}{\partial z}\right) \\ &+ \rho_0(z)N(z)^2\frac{1}{r}\frac{\partial}{\partial r}\left(r\frac{\partial w}{\partial r}\right) = \rho_0(z)\frac{1}{r}\frac{\partial}{\partial r}\left(r\frac{\partial S}{\partial r}\right). \end{aligned} \tag{3.10}$$

By setting $f = 0$, equation 3.10 is seen to differ from its 2D counterpart, equation 2.5, in the structure of its two terms of horizontal variation. These terms generate additional contributions $\rho_0(z)N(z)^2\frac{1}{r}\frac{\partial w}{\partial r}$ and $\rho_0(z)\frac{1}{r}\frac{\partial S}{\partial r}$, which will vanish at large r, as a 2D description re-emerges. In fact, for $f = 0$ both equations 3.10 and 2.5 may be written

$$\frac{\partial}{\partial z}\left(\rho_0(z)\frac{\partial^2}{\partial t^2}\frac{\partial w}{\partial z}\right) + \rho_0(x)N^2(z)\nabla_H^2 w = \rho_0(z)\nabla_H^2 w, \tag{3.11}$$

in which the horizontal Laplacian ∇_H^2 (without vertical, z, derivatives) is adapted to the symmetry to the 2D or 3D problem respectively

$$\begin{aligned} \nabla_H^2 &\equiv \frac{\partial^2}{\partial x^2} + \frac{\partial^2}{\partial y^2} \to \frac{\partial^2}{\partial x^2}, \\ \nabla_H^2 &\equiv \frac{\partial^2}{\partial r^2} + \frac{1}{r}\frac{\partial}{\partial r} + \frac{1}{r^2}\frac{\partial^2}{\partial \phi^2} \to \frac{\partial}{\partial r}\left(r\frac{\partial}{\partial r}\right). \end{aligned} \tag{3.12}$$

Mathematically, handling the 3D horizontal (radial) variation will necessitate the use of a Hankel transform, in place of the Fourier transforms used previously. We return to this matter in sections 3.3.5 and 3.3.6 below.

For completeness, we note that for the present case of $f \neq 0$, the energy equation corresponding to our basic set of equations in 3D is still given by

$$\frac{\partial}{\partial t}\left(\bar{E}+\bar{V}\right)+\underline{\nabla}\cdot(p\underline{v})=\frac{\rho_0 sb}{N^2}, \tag{3.13}$$

again with

$$\bar{E}=\frac{\rho_0}{2}\underline{v}\cdot\underline{v}, \quad \bar{V}=\frac{\rho_0 b^2}{2N^2}. \tag{3.14}$$

3.3.2 Model Stratification

We maintain equivalence with the model of Chapter 2 by again assuming the simplest possible, non-trivial representation of the tropospheric and stratospheric stratification, namely

$$N(z)=\begin{cases}N_t, & z\leq H_t,\\ N_s, & H>z>H_t,\end{cases} \tag{3.15}$$

which, again, corresponds to a basic state of density of

$$\rho_0(z)=\begin{cases}\rho_s e^{-\frac{z}{D_t}}, & z\leq H_t,\\ \rho_s e^{-\frac{H_t}{D_t}}e^{-\frac{(z-H_t)}{D_s}}, & H>z>H_t.\end{cases} \tag{3.16}$$

For definiteness, let $N_s \geqslant N_t$. The tropospheric and stratospheric scale heights are given by

$$D_t=\frac{g}{N_t^2}, \quad D_s=\frac{g}{N_s^2}. \tag{3.17}$$

With this stratification, equation 3.10 can be solved, formally, by employing the modal expansion developed in Chapter 2, notwithstanding issues of interpretation, discussed in section 3.3.4.

3.3.3 Modal Expansion

The modal expansion applied to the two-dimensional case is formally applied to equation 3.10. Adopting this procedure requires us to revisit the physical interpretation of the eigenvalues c_n, below, which, in the two-dimensional case, without rotation, could be understood as free wave speeds. With that proviso, it will be shown in this section that the modal expansion employed in Chapter 2 successfully decomposes the three-dimensional, extended problem. Write

$$w(r,z,t)=\sum_j w_j(r,t)\phi_j(z), \quad s(r,z,t)=N(z)^2\sum_j s_j(r,t)\phi_j(z), \tag{3.18}$$

with the same equation and vertical boundary conditions for the orthonormal functions $\phi_j(z)$ as in Chapter 2, namely

$$\frac{d}{dz}\left(\rho_0(z)\frac{d\phi_n}{dz}\right)+\frac{\rho_0(z)N(z)^2}{c_n^2}\phi_n=0,\quad \phi_n(0)=\phi_n(H)=0. \tag{3.19}$$

We also employ the same matching conditions on the $\phi_j(z)$ at the tropopause, $z=H_t$ i.e. continuity of the eigenfunction, $\phi_n(z)$, and its first derivative and the corresponding eigenvalues, c_n, were computed using the same numerical procedure as in Chapter 2, section 2.4.1. Note that assuming the vertical variation satisfies equation 3.19 does not restrict the stratification- equation 3.19 applies to any $N(z)$.

We now re-write the governing equation 3.10 using the modal expansions in equations 3.18 . The first term in equation (3.10) will transform as in the 2D case of Chapter 2, when integration by parts and the boundary conditions are used

$$\begin{aligned}&-\frac{1}{c_n^2}\int_0^H\rho_0(z)N(z)^2\phi_n\frac{\partial^2 w}{\partial t^2}dz-\frac{f^2}{c_n^2}\int_0^H\rho_0(z)N(z)^2\phi_n w dz+\\&+\int_0^h\rho_0(z)N(z)^2\phi_n\frac{1}{r}\frac{\partial}{\partial r}\left(r\frac{\partial w}{\partial r}\right)dz=\int_0^H\rho_0(z)N(z)^2\phi_n\frac{1}{r}\frac{\partial}{\partial r}\left(r\frac{\partial s}{\partial r}\right)dz.\end{aligned} \tag{3.20}$$

We now substitute the expansions in equations (3.18) and appeal to the orthogonality of the $\phi_n(z)$ to separate the horizontal part of the problem as

$$-\frac{1}{c_n^2}\frac{\partial^2 w_n(r,t)}{\partial t^2}-\frac{f^2}{c_n^2}w_n(r,t)+\frac{1}{r}\frac{\partial}{\partial r}\left(r\frac{\partial w_n(r,t)}{\partial r}\right)=\frac{1}{r}\frac{\partial}{\partial r}\left(r\frac{\partial s_n(r,t)}{\partial r}\right). \tag{3.21}$$

It will be recognised that the formal decomposition of the 3D problem, using equation 3.20, succeeds in effecting a separation between the horizontal and vertical part of the problem, the solution of which is our main current concern. The vertical variation is unchanged from that derived in section 2.3.5, note.

3.3.4 Free Modes

Before proceeding further, we pause to consider the physics of the eigenvalues, c_n. Free modes are solutions for $f=S=0$. In this limit, the 2D convection dynamics equivalent to equation 3.10, above, is expressed in equation 2.5 (with S=0). It is straightforward to verify the 2D dynamics then consists of free modes $w(x,z,t)=A(x-ct)\phi(z)$ with A as any function. Phase speeds, c, and functions $\phi(z)$ are identified with eigenvalues, c_n, and eigenfunctions, $\phi_n(z)$, of the Sturm-Liouville problem in equation 3.19.

Consider now the 3D trial solution

$$w(r,z,t)=A(r,t)\phi(z), \tag{3.22}$$

which does not necessarily have the structure of a horizontally traveling wave, note. Substitute into equation 3.10 (having set $f = S = 0$). After some algebra, equation 3.22 yields a less straightforward, separable problem

$$\frac{\frac{1}{r}\frac{\partial}{\partial r}\left(r\frac{\partial A}{\partial r}\right)}{\frac{\partial^2 A}{\partial t^2}} = -\frac{\frac{d}{dz}\left(\rho_0(z)\frac{d}{dz}\phi(z)\right)}{\rho_0(z)N(z)^2\phi(z)} \equiv \frac{1}{\kappa^2}. \tag{3.23}$$

From equation 3.23, the vertical part of the problem may be reduced to that expressed in equation 3.19: clearly, we can identify $\phi(z)$ with eigenfunction $\phi_n(z)$ and separation constant κ with c_n. Hence, eigenvalue, c_n, enters a partial differential equation for A

$$\frac{\partial^2 A}{\partial r^2} + \frac{1}{r}\frac{\partial A}{\partial r} = \frac{1}{c_n^2}\frac{\partial^2 A}{\partial t^2}. \tag{3.24}$$

No travelling wave solutions to equation 3.24 are obvious. However, we expect a cylindrical spreading of energy, and so write

$$A(r,t) = B(r,t)r^{-1/2} \tag{3.25}$$

which, when substituted into equation (3.24), yields

$$\frac{\partial^2 B}{\partial r^2} + \frac{B}{r^2} = \frac{1}{c_n^2}\frac{\partial^2 B}{\partial t^2}, \tag{3.26}$$

which, for large r, reduces to the Cartesian form of the second order wave equations. Appealing to d'Alembert's solution $B(r,t) = B(r - c_n t)$, we find

$$\lim_{r\to\infty}\left(A(r,t)\right) = \frac{B(r-c_n t)}{r^{1/2}}, \tag{3.27}$$

which is an outwards travelling wave, with speed c_n, having an amplitude damping corresponding to the expected cylindrical wavefront. Physically, the factor $r^{-1/2}$ allows for conservation of energy flux through a squat cylinder of fixed height and circumference $2\pi r$.

Reverting to function $A(r,t)$, we note that seeking a separable solution $A(r,t) = R(r)T(t)$ to equation (3.24) leads to Bessel's equation with $n = 0$, for $R(r)$ (see equation (3.33) below).

In the two-dimensional case, the existence of the Fourier inversion "shift" theorem leads to superposable solutions in equation 2.16, for $w_n(x,t)$. Each has the form of a horizontally traveling wave. As we shall see, the three-dimensional model requires a Hankel transform (see 3.3.6), rather than a Fourier transform. No equivalent "shift" theorem exists for a Hankel inversion and solutions, for $w_n(r,t)$, determined via equation 3.21 cannot be written as horizontally traveling waves. This fact is consistent with the observation that no simple traveling wave solution to equation 3.24 is obvious. It is apparent that, in three dimensions, we lose physical connection between free modes' phase speeds and the eigenvalues, c_n (except at large r). The c_n are formally taken to parameterise the solutions $w_n(r,t)$ of equation 3.21, which we now continue to seek.

3.3.5 The Hankel transform and Bessel's Equation

In this section, we attempt to explain the role, in the present context, of the Hankel transform. Our intention is not an exhaustive treatment: rather, we wish to indicate common concepts between 2D treatment and the present 3D extension. A coherent but succinct account of Bessel's equation and the Hankel transform may found in Chapter 3 of Jackson's Electrodynamics (Jackson, 1999).

We note from equation 3.11 that the horizontal variation of our problem is determined by the appropriate horizontal Laplacian operator. Chapter 2 essentially used Fourier transform techniques to solve a Cartesian form of the Laplacian. In 3D, the equivalent methodology, adapted to the cylindrical polar form of Laplacian, uses Bessel functions which, like sine and cosine, have suitably useful orthonormality properties. Based upon Jackson (Jackson, 1999), we relate the salient aspects of Bessel's equation and its solution briefly, now.

Bessel functions arise as the solution of the radial part of the cylindrical polar form of the full Laplace equation,

$$\nabla^2\Phi = \frac{\partial^2\Phi}{\partial r^2} + \frac{1}{r}\frac{\partial\Phi}{\partial r} + \frac{1}{r^2}\frac{\partial^2\Phi}{\partial\phi^2} + \frac{\partial^2\Phi}{\partial z^2} = 0, \tag{3.28}$$

when a separable solution $\Phi(r,\phi,z) = R(r)Q(\phi)Z(z)$ is sought as follows. Substitute into equation 3.28 to obtain $R''/R + R'/(rR) + Q''/(r^2Q) + Z''/Z = 0, \forall r,\phi,z$. Since Z''/Z is only a function of z, by assumption, it follows $Z''/Z = k^2$, a constant. Then, multiplying the remaining equation by r^2 one obtains $r^2R''/R + rR'/R + k^2r^2 + Q''/Q = 0, \forall r,\phi$ and again Q''/Q is seen to be only function of cylindrical angular variable ϕ, hence $Q''/Q = -n^2$, a constant integer (see below). Hence, it follows for the radial equation $R''/R + R'/(rR) + k^2 - n^2/r^2 = 0$, which we multiply by R. In summary, we have straightforwardly separated equation 3.28 into three ODEs, related by their parameters

$$\begin{aligned} \frac{d^2Z}{dz^2} - k^2Z &= 0, \\ \frac{d^2Q}{d\phi^2} + n^2Q &= 0, \\ \frac{d^2R}{dr^2} + \frac{1}{r}\frac{dR}{dr} + \left(k^2 - \frac{n^2}{r^2}\right)R &= 0. \end{aligned} \tag{3.29}$$

Setting aside boundary conditions and superposition, the solutions for $Z(z)$ and $\Phi(\phi)$ are essentially straightforward

$$Z(z) = \mathrm{e}^{\pm kz}, \quad Q(\phi) = \mathrm{e}^{\pm in\phi}, \tag{3.30}$$

for $n \in \mathbb{Z}^+$. The physical constraint $Q(\phi) = Q(\phi + 2\pi)$ is responsible for the restriction $n \in \mathbb{Z}^+$ but k is, currently, arbitrary. Note that $n \in \mathbb{R}$ is

possible. Make the variable change $x = kr$ in the third of equations 3.29 to yield the radial, nth order Bessel equation:

$$\frac{d^2R}{dx^2} + \frac{1}{r}\frac{dR}{dx} + \left(1 - \frac{n^2}{x^2}\right) R = 0. \tag{3.31}$$

An indicial solution is assumed, leading to two linearly independent possibilities: Bessel functions $J_n(x)$ and $Y_n(x)$ of the order $\pm n$. $J_n(x)$ (relevant here) is bounded as $x \to 0$

$$J_n(x) \;=\; \left(\frac{x}{2}\right)^n \sum_{j=1} \frac{(-1)^j}{j!\Gamma(j+n+1)} \left(\frac{x}{2}\right)^{2j}, \tag{3.32}$$

whereas $Y_n(x)$ is not. For integer arguments, $\Gamma(N) = (N-1)!$. We note, then, that zero-order Bessel function $J_0(x)$ satisfies Bessel's equation with $n = 0$

$$x\frac{d^2J_0}{dx^2} + \frac{dJ_0}{dx} + xJ_0 = 0 \iff \frac{d}{dx}\left(x\frac{dJ_0}{dx}\right) = -xJ_0. \tag{3.33}$$

Now, the Fourier transform used in 2D in Chapter 2 (and assumed there to exist, recall)

$$\mathbf{F}\left(f(x)\right) \equiv \hat{f}(k) \equiv \frac{1}{\sqrt{2\pi}} \int_{-\infty}^{\infty} f(x) e^{ikx} dx, \tag{3.34}$$

was used essentially for its ability to transform partial derivative expressions characteristic of the Cartesian, horizontal Laplacian

$$\mathbf{F}\left(\nabla_H^2 f\right) = \mathbf{F}\left(\frac{d^2 f}{dx^2}\right) = (-ik)^2 \hat{f}(k) = \text{constant}\hat{f}(k). \tag{3.35}$$

Here we need only have $\frac{df}{dx} \to 0$, $f \to 0$, $x \to \infty$. This above property is responsible from generating an algebraic equation in transform space, which may be solved for the transform quantity. Equation (3.35) corresponds to the so-called Fourier transform of derivatives theorem (Arfken, 1966).

To solve the equivalent 3D problem, we seek a transformation with properties after equation 3.35, but which will work on the cylindrical polar coordinate form of horizontal Laplacian. Such a transform is the Hankel transform, $\mathbf{Ha}_n\left(f(x)\right) \equiv \int_0^\infty x f(x) J_n(kx) dx$. We shall require the zero-order ($n = 0$) case as we are investigating axisymmetric motion, which may be suitably defined and written

$$\mathbf{Ha}_0(f(r)) = \hat{f}(k) \equiv \int_0^\infty r f(r) J_0(kr) dr. \tag{3.36}$$

Note, like the Fourier transform, the Hankel transform has an inverse

$$f(r) = \mathbf{Ha}_0^{-1}(\hat{f}(k)) \equiv \int_0^\infty k\hat{f}(k) J_0(kr) dk. \tag{3.37}$$

For present purposes, the essential property of zero-order Hankel transform, equation 3.36, which is analogous the properties of the Fourier transform expressed in equation 3.35 is

$$\mathbf{Ha}_0\left(\nabla_H^2 f(r)\right) = \mathbf{Ha}_0\left(\frac{1}{r}\frac{\partial}{\partial r}\left(r\frac{\partial f}{\partial r}\right)\right) = -k^2\mathbf{Ha}\left(f(r)\right). \tag{3.38}$$

where, note, it is the cylindrical polar form the horizontal Laplacian in use. In fact, equation 3.38 relies on conditions regarding the boundary properties of transformed function, f, and transformation kernel, $rJ_0(r)$, which we shall set-out in detail, in the next section. We conclude this section by stating key properties of $J_0(kr)$ and the zero order Hankel transform.

$J_0(kr)$ may be conveniently defined

$$J_0(kr) \equiv \frac{1}{2\pi}\int_0^{2\pi} e^{ikr\cos(\theta)}d\theta = \frac{1}{2\pi}\int_0^{2\pi}\cos(kr\cos(\theta))d\theta, \tag{3.39}$$

since $J_0(kr)$ must be real. It is immediate from equation (3.39) that

$$J_0(kr) = J_0(-kr). \tag{3.40}$$

$J_0(kr)$ has an orthogonality property, or closure function (Arfken, 1966)

$$\int_0^\infty J_0(kr)J_0(k'r)rdr = \frac{1}{k}\delta(k-k'), \tag{3.41}$$

where $\delta(k-k')$ is the Dirac delta function, which is analogous to the following property for the Fourier transfrom kernel function, note

$$\frac{1}{2\pi}\int_{-\infty}^{\infty}\mathrm{e}^{i(k-k')x}dx = \delta(k-k'). \tag{3.42}$$

3.3.6 Transformation of the w Equation

We seek $w_n(r,t)$ by solving 3D equation (3.21) using a Laplace-Hankel Transform approach analogous to the Fourier-Laplace approach applied in Chapter 2. Our analysis makes use of integration by parts and the results of the previous section to transform integrals. We shall assume that evaluated terms vanish and indicate where we make this assumption. Broadly, it is possible to follow our approach in Chapter 2 of making $\hat{\bar{w}}_n$ subject in the transformed equation, then performing a Laplace and Hankel inversion. The Hankel inversion, to find an expression for $w_n(r,t)$, must be performed numerically, as no Hankel inversion theorem exists analogous to the shift theorem used in our 2D treatment in Chapter 2. (Recall, in Chapter 2, $w_n(x,t)$ was written directly, in terms of translating and possibly time-shifted, but otherwise general horizontal variation of the applied heating or buoyancy forcing).

We first apply the Laplace transform in equation 3.21

$$-\left(\frac{p^2+f^2}{c_n^2}\right)\bar{w}_n+\frac{1}{r}\frac{\partial}{\partial r}\left(r\frac{\partial \bar{w}_n}{\partial r}\right)=\frac{1}{r}\frac{\partial}{\partial r}\left(r\frac{\partial \bar{s}_n}{\partial r}\right). \tag{3.43}$$

Later we will consider the form for $\bar{s}_n$ for pulsed heating. Next, apply the Hankel transform (to the r variable) by multiplying by $rJ_0(kr)$, then integrating over $r \in [0,\infty)$

$$-\left(\frac{p^2+f^2}{c_n^2}\right)\int_0^\infty r\bar{w}_n(r,t)J_0(kr)dr+\int_0^\infty J_0(kr)\frac{\partial}{\partial r}\left(r\frac{\partial \bar{w}_n}{\partial r}\right)dr = \int_0^\infty J_0(kr)\frac{\partial}{\partial r}\left(r\frac{\partial \bar{s}_n}{\partial r}\right)dr. \tag{3.44}$$

Integrate by parts to obtain

$$\left(\frac{p^2+f^2}{c_n^2}\right)\mathbf{Ha}_0(\bar{w}_n)+\int_0^\infty r\frac{\partial \bar{w}_n}{\partial r}\frac{\partial J_0(kr)}{\partial r}=\int_0^\infty r\frac{\partial \bar{s}_n}{\partial r}\frac{\partial J_0(kr)}{\partial r}dr, \tag{3.45}$$

where we have assumed that w and $\bar{s}$ decay sufficiently quickly for terms at infinity to vanish. Integrate by parts again, taking $u = r\frac{\partial J_0}{\partial r}$ and $\frac{\partial v}{\partial r} = \frac{\partial \bar{w}_n}{\partial r}$ or $\frac{\partial v}{\partial r} = \frac{\partial \bar{s}_n}{\partial r}$, with the same assumptions on w and $\bar{s}$, to eliminate the evaluated terms

$$\begin{aligned} &-\left(\frac{p^2+f^2}{c_n^2}\right)\mathbf{Ha}_0(\bar{w}_n)+\int_0^\infty \bar{w}_n\frac{\partial}{k\partial r}\left(kr\frac{\partial J_0(kr)}{k\partial r}\right)kdr \\ &=\int_0^\infty \bar{s}_n\left(\frac{\partial}{k\partial r}\left(kr\frac{\partial J_0(kr)}{k\partial r}\right)\right)kdr. \end{aligned} \tag{3.46}$$

It is convenient to change variable, $x \equiv kr$ in the integrands above

$$-\left(\frac{p^2+f^2}{c_n^2}\right)\mathbf{Ha}_0(\bar{w}_n)+\int_0^\infty \bar{w}_n\frac{d}{dx}\left(x\frac{dJ_0}{dx}\right)dx=\int_0^\infty \bar{s}_n\frac{d}{dx}\left(x\frac{dJ_0}{dx}\right)dx. \tag{3.47}$$

We may now use Bessel's equation (3.33) to substitute $\frac{d}{dx}\left(x\frac{dJ_0}{dx}\right) = -xJ_0$

$$-\left(\frac{p^2+f^2}{c_n^2}\right)\mathbf{Ha}_0(\bar{w}_n)+\int_0^\infty -xJ_0\bar{w}_n dx=\int_0^\infty -xJ_0\bar{s}_n dx. \tag{3.48}$$

Resetting $x = kr$ we find

$$-\left(\frac{p^2+f^2}{c_n^2}\right)\mathbf{Ha}_0(\bar{w}_n)-k^2\int_0^\infty \bar{w}_n rJ_0(kr)dr=-k^2\int_0^\infty \bar{s}_n rJ_0(kr)dr, \tag{3.49}$$

which, we note, may be written

$$\left(\frac{p^2+f^2}{c_n^2}\right)\mathbf{Ha}_0(\bar{w}_n)+k^2\mathbf{Ha}_0(\bar{w}_n)=k^2\mathbf{Ha}_0(\bar{s}_n). \tag{3.50}$$

We can now solve for Laplace-Hankel transform $\hat{\bar{w}}_n$

$$\hat{\bar{w}}_n(k,p) = \frac{c_n^2 k^2}{(p+ig_n(k))(p-ig_n(k))}\hat{\bar{s}}_n(k,p), \tag{3.51}$$

where we have defined

$$g_n(k) \equiv \sqrt{f^2 + k^2 c_n^2}. \tag{3.52}$$

and $\hat{\bar{s}}_n(k,p)$ is the Hankel-Laplace transform of the horizontal variation of heating, to be considered in the next section. It will be recognised that the analytic result in equation 3.51 is the 3D analogue of the Fourier-Laplace transform for the 2D problem, given in equation 2.15. As such it has equivalent dependancy on the heating expansion coefficients, $\hat{\bar{s}}_n(k,p)$.

3.3.7 Buoyancy Forcing: Temporal and Spatial Structure

Following Chapter 2, we assume the following form for a pulsed, applied heating

$$s(r,z,t) = s(r,t)Z(z) = S_0 F(r)\left(\Theta(t) - \Theta(t-T)\right)\sum_j \sigma_j \phi_j(z), \tag{3.53}$$

implicit in which is the following definiton for the heating expansion coefficients

$$s_j(r,t) = S_0 F(r)\left(\Theta(t) - \Theta(t-T)\right)\sigma_j, \qquad \forall j. \tag{3.54}$$

Recall, the σ_j are determined by the defined vertical variation of the heating as

$$\sigma_j = \int_0^{H_t} \rho_0(z) N(z)^2 \phi_n(z) Z(z) dz. \tag{3.55}$$

The horizontal spatial structure of heating is treated below. Figure 3.1 is a schematic of the heating, or buoyancy forcing assumed here, together with the assumed stratification, for reference. The vertical variation, $Z(z)$ is that in equation (2.19) for the 2D case. The σ_j are again given by equation (3.55).

In our previous, 2D treatment, one could invert the equivalent of equation (3.51) for all functions $\hat{F}(k)$, using general properties of Fourier transforms. Hankel functions do not possess equivalent properties. It is therefore necessary to define a horizontal variation for our heating function, $s(r,z,t)$. We choose a horizontal variation of heat forcing which is analogous to that used in Chapter 2, namely

$$F(r) \equiv \frac{1}{2\pi L^2}\exp\left(-\frac{r^2}{2L^2}\right), \quad r \in [0,\infty). \tag{3.56}$$

The factor $\frac{1}{2\pi L^2}$ again ensures that the domain-integrated heating is independent of L.

3.3.8 Solutions for w and b

With our assumed heating structure and stratification, we find straightforwardly, for the Laplace-Hankel transform of heating coefficient implicitly defined by equations 3.54 and 3.56

$$\hat{\bar{s}}_j = \sigma_j S_0 \left(\frac{1 - e^{-pT}}{p} \right) \hat{F}(k). \tag{3.57}$$

Substituting into equation (3.51) and assuming quiescent initial conditions, we therefore find the Laplace-Hankel transform of $w_n(r,t)$ as

$$\frac{\hat{\bar{w}}_n(k,p)}{S_0} = \sigma_n \frac{c_n^2 k^2 \hat{F}(k)(1 - e^{-pT})}{p(p + ig_n(k))(p - ig_n(k))}. \tag{3.58}$$

Recall, $g(k)$ is defined in equation 3.52 and $\hat{F}(k)$ is the Hankel transform of $F(r)$, which will be assigned shortly. On using partial fractions and the delay property of Laplace transforms we perform the Laplace inversion in the 3D case much as in the 2D case

$$\begin{aligned}
\frac{\hat{w}_n(k,t)}{S_0} &= \frac{k^2 \hat{F}(k) c_n^2 \sigma_n}{g_n(k)^2} \Theta(t) \\
&- \frac{k^2 \hat{F}(k) c_n^2 \sigma_n}{2g_n(k)^2} \Theta(t) e^{ig_n(k)t} \\
&- \frac{k^2 \hat{F}(k) c_n^2 \sigma_n}{2g_n(k)^2} \Theta(t) e^{-ig_n(k)t} \\
&- \frac{k^2 \hat{F}(k) c_n^2 \sigma_n}{g_n(k)^2} \Theta(t-T) \\
&+ \frac{k^2 \hat{F}(k) c_n^2 \sigma_n}{2g_n(k)^2} \Theta(t-T) e^{ig_n(k)(t-T)} \\
&+ \frac{k^2 \hat{F}(k) c_n^2 \sigma_n}{2g_n(k)^2} \Theta(t-T) e^{-ig_n(k)(t-T)}.
\end{aligned} \tag{3.59}$$

In the sequel, we maintain the order of terms in the right hand side of equation 3.59: we do not factorise the right hand side of the above for reasons which will emerge.

We now proceed to the Hankel inversion of equation 3.59, which will be comprised of integrals to be evaluated numerically. We use the following notation for the inverse Hankel transform of a term from equation 3.59 above

$$F'(r,t:m,g_n(k)) = \mathbf{Ha}_0^{-1} \left(\frac{k^2 e^{img_n(k)t} \hat{F}(k)}{g_n(k)^2} \right), \tag{3.60}$$

that is, we define

$$F'(r,t:m,g_n(k)) \equiv \int_0^\infty \left(\frac{k^3 e^{mig_n(k)t} \hat{F}(k)}{g_n(k)^2} \right) J_0(kr)dk, \quad m \in [-1,0,1]. \tag{3.61}$$

Clearly $F'(r,t:m,g_n(k))$ will be complex-valued in general, even if $\hat{F}(k)$ is real. However, the structure of equation (3.59) ensures that the imaginary parts of the right hand side always cancel. In contradistinction to the 2D case, the integral in equation 3.61 cannot be performed for general $\hat{F}(k)$. The consequence of this mathematical fact is that the physical structure of 2D equation 2.16 (of superposed, time-shifted, uniformly propagating modes) is lost in the 3D case.

To perform a numerical Hankel inverse transformation of equation 3.59 it will be necessary to assume a particular form for the horizontal variation of heating, $F(r)$. We maintain parity with our 2D case and take for the horizontal variation of our buoyancy forcing a Gaussian variation in r which is normalised, so as to conserve the total heat input into the model atmosphere. It is possible to establish the following correspondence between this $F(r)$ and its Hankel transform (Bracewell & Bracewell, 1986).

$$F(r) \equiv \frac{1}{2\pi L^2} e^{\left(-\frac{r^2}{2L^2}\right)} \iff \hat{F}(k) = \frac{1}{2\pi} e^{\left(-\frac{L^2k^2}{2}\right)}. \tag{3.62}$$

In terms of $F'(r,t:m,g_n(k))$, equation 3.59 may be written

$$\begin{aligned}
\frac{w_n(r,t)}{S_0} &= c_n^2\sigma_n\Theta(t)F'(r,t:0,g_n(k)) \\
&- \frac{c_n^2\sigma_n}{2}\Theta(t)F'(r,t:1,g_n(k)) \\
&- \frac{c_n^2\sigma_n}{2}\Theta(t)F'(r,t:-1,g_n(k)) \\
&- c_n^2\sigma_n\Theta(t-T)F'(r,t:0,g_n(k)) \\
&+ \frac{c_n^2\sigma_n}{2}\Theta(t-T)F'(r,t-T:1,g_n(k)) \\
&+ \frac{c_n^2\sigma_n}{2}\Theta(t-T)F'(r,t-T:-1,g_n(k)).
\end{aligned} \tag{3.63}$$

where we can now write for $F'(r,t:m,g_n(k))$

$$F'(r,t:m,g_n(k)) = \frac{1}{2\pi}\int_0^\infty \left(\frac{k^3}{g_n(k)^2}\right) e^{\left(-\frac{L^2k^2}{2}+img_n(k)t\right)} J_0(kr)dk. \tag{3.64}$$

Equation 3.63 may be written in a more compact, explicitly real form

$$\begin{aligned}
\frac{w_n(r,t)}{S_0} &= c_n^2\sigma_n\left(\Theta(t)-\Theta(t-T)\right)F''(r,t=0:g_n(k)) \\
&- c_n^2\sigma_n\Theta(t)F''(r,t:g_n(k)) \\
&+ c_n^2\sigma_n\Theta(t-T)F''(r,t-T:g_n(k)),
\end{aligned} \tag{3.65}$$

where

$$F''(r,t:g_n(k)) = \frac{1}{2\pi}\int_0^\infty \left(\frac{k^3}{g_n(k)^2} e^{-\frac{L^2k^2}{2}}\right)\cos(g_n(k)t)J_0(kr)dk. \tag{3.66}$$

Consider definition 3.66. The three factors of the integrand and their respective variation with integration variable, k, are considered in detail, in section 3.4, shortly. Here, we note that for $t = f = 0$ ($\implies g_n(k) \to c_n k$), equation 3.66 gives

$$\begin{aligned} \lim_{f,t\to 0}\left(F''(r,t:g_n(k))\right) &= \frac{1}{2\pi c_n^2}\int_0^\infty k e^{-\frac{L^2k^2}{2}} J_0(kr)dk, \qquad (3.67)\\ &\equiv \frac{1}{2\pi c_n^2}\mathbf{Ha}_0^{-1}\left(e^{-\frac{L^2k^2}{2}}\right),\\ &= \frac{1}{2\pi c_n^2 L^2}e^{-\frac{r^2}{2L^2}}, \end{aligned}$$

where we have used equation 3.62. Also, for $t \to \infty$, r finite, the integrand in definition (3.66) becomes an increasingly rapid oscillation, due to its cosine term, which is slowly modulated, due to the other terms. Then, the effective amplitude a single cycle of the cosine variation may be considered constant and so the positive and negative areas of the cosine cycle in the quadrature will cancel and

$$\lim_{t\to\infty}\left(F''(r,t:g_n(k))\right) = 0. \qquad (3.68)$$

Equations (3.67) and (3.68) confirm expected limits for equation (3.64) and hence adjustment $w_n(r,t)$ (equation (3.65)).

We have now determined a solution for the $w(r,z,t)$ adjustment to transient heating. That is, equations (3.18), (3.60), (3.63) determine the vertical flow response, $w(r,z,t)$.

Before proceeding, a few remarks are now appropriate. Whereas the equivalent 2D solution of equation 2.16 (see also Nicholls et al. (1991) and Parker et al. (2002)), is explicitly based upon non-dispersive waves of constant amplitude, propagating horizontally, with speed c_n, we will see in section 3.4 that 3D modal solution 3.65 contains only disturbances which propagate in the direction of r increasing, with diminishing amplitude. However, like equation 2.16, equation 3.65 holds for any buoyancy forcing for which the horizontal and vertical structure is separable, any stratification and, overall, its composition is similar i.e. it contains direct and time-shifted responses, determined by the form of the forcing. Again, a response to steady buoyancy forcing may be obtained on setting $T \to \infty$, when terms with factor $\Theta(t-T)$ disappear.

Proceeding, the potential temperature response is found by integrating equation 3.4, which we write

$$b(r,z,t) = \sum_n b_n(r,t)N(z)^2\phi_n(z), \quad b_n(r,t) \equiv \int_0^t \left(s_n(r,t') - w_n(r,t')\right)dt'. \qquad (3.69)$$

Substituting in the above with equations 3.60 and 3.63, we have

$$\begin{aligned} b_n(r,t) &= S_0 F(r)\sigma_n \int_0^t (\Theta(t') - \Theta(t'-T))\, dt' \qquad (3.70)\\ &- S_0\sigma_n c_n^2 \int_0^t (\Theta(t') - \Theta(t'-T))\, F'(r, t:0, g_n(k))dt' \\ &+ \frac{1}{2} S_0\sigma_n c_n^2 \int_0^t \Theta(t') F'(r, t':1, g_n(k))dt' \\ &+ \frac{1}{2} S_0\sigma_n c_n^2 \int_0^t \Theta(t') F'(r, t':-1, g_n(k))dt' \\ &- \frac{1}{2} S_0\sigma_n c_n^2 \int_0^t \Theta(t'-T) F'(r, (t'-T):1, g_n(k))dt' \\ &- \frac{1}{2} S_0\sigma_n c_n^2 \int_0^t \Theta(t'-T) F'(r, (t'-T):-1, g_n(k))dt'. \end{aligned}$$

Bearing in mind the definition of F', it is seen that a majority of terms in the above are repeated integrals with constant limits. For example, using the definitions of $\Theta(t')$ and F', from equation 3.64, we have, for the integral in the third term on the right hand side of equation 3.70

$$\begin{aligned} \int_0^t \Theta(t') F'(r, t':1, g_n(k))dt' &= \frac{1}{2\pi} \int_0^t \int_0^\infty \left(\frac{k^3}{g_n(k)^2}\right) e^{\left(-\frac{L^2k^2}{2} + img_n(k)t'\right)} J_0(kr)dkdt', \\ &= \frac{1}{2\pi} \int_0^\infty \left(\frac{k^3 e^{-\frac{L^2k^2}{2}}}{img_n(k)^3}\right) \left[e^{img_n(k)t'}\right]_o^t J_0(kr)dk, \\ &= \frac{1}{2\pi} \int_0^\infty \left(\frac{k^3 e^{-\frac{L^2k^2}{2}}}{img_n(k)^3}\right) \left(e^{img_n(k)t} - 1\right) J_0(kr)dk, \qquad (3.71) \end{aligned}$$

having reversed the order of t' and k integration. Recall, $m \in [-1, 0, 1]$. Return to equation 3.70 and integrate on time. After straightforward but extensive algebra, we obtain

$$\begin{aligned} b_n(r,t) &= S_0 F(r)\sigma_n \xi(t) - S_0\sigma_n c_n^2 F'(r, t:0, g_n(k))\xi(t) \qquad (3.72)\\ &+ \frac{1}{2} S_0\sigma_n c_n^2 \Theta(t) G(r, t:1, g_n(k)) \\ &+ \frac{1}{2} S_0\sigma_n c_n^2 \Theta(t) G(r, t:-1, g_n(k)) \\ &- \frac{1}{2} S_0\sigma_n c_n^2 \Theta(t-T) G(r, t-T:1, g_n(k)) \\ &- \frac{1}{2} S_0\sigma_n c_n^2 \Theta(t-T) G(r, t-T:-1, g_n(k)), \end{aligned}$$

with

$$\xi(t) = (\Theta(t) - \Theta(t-T))\, t + \Theta(t-T)T, \qquad (3.73)$$

and

$$G(r,t:m,g_n(k)) = \frac{1}{2\pi}\int_0^\infty \left(\frac{k^3 e^{-\frac{L^2k^2}{2}} \left(e^{img_n(k)t}-1\right)}{img_n(k)^3} \right) J_0(kr)dk, \quad m \in [-1,0,1]. \tag{3.74}$$

The b response may, like the w response, be conveniently transformed into a more computable, explicitly real form

$$\begin{aligned} b_n(r,t) &= S_0F(r)\sigma_n\xi(t) - S_0\sigma_n c_n^2 F''(r,t:g_n(k))\xi(t) \\ &+ S_0\sigma_n c_n^2 \Theta(t) G'(r,t:1,g_n(k)) \\ &- S_0\sigma_n c_n^2 \Theta(t-T) G'(r,t-T:g_n(k)), \end{aligned} \tag{3.75}$$

with

$$G'(r,t:g_n(k)) = \frac{1}{2\pi}\int_0^\infty \left(\frac{k^3 e^{-\frac{L^2k^2}{2}} \sin(g_n(k)t)}{g_n(k)^3} \right) J_0(kr)dk. \tag{3.76}$$

Following our treatment of the equivalent inversion integral in equation 3.66 above, it is possible to obtain, for $T < \infty$, the following limits for 3.76

$$\lim_{t\to 0}\left(G'(r,t:g_n(k))\right) = 0, \quad \lim_{t\to\infty}\left(G'(r,t:g_n(k))\right) = 0. \tag{3.77}$$

Note that for $T \to \infty$, the term in $\Theta(t-T)$ in equation 3.75 will ensure a finite b adjustment.

We have now determined a solution for the $b(r,z,t)$ adjustment to transient heating. That is, equations 3.69, 3.75, and 3.76 determine the buoyancy response, $b(r,z,t)$.

In this section, we have developed a 3D, axially symmetric, linear model of buoyancy-forced response in a rotating, stratified atmosphere. It holds for any vertical stratification and separable heat forcing (however, we choose to employ the same stratification and assumed heating structure as in our 2D model of Chapter 2). Physically, the 3D model solution of this section still relates to those of Nicholls et al. (1991), Holton et al. (2002) and Edman et al. (2017), in 2D, except that the factored, horizontal variation is now based upon zero-order Hankel functions (Arfken, 1966): a consequence of its 3D, axial character. The loss of translational physical symmetry in the domain's transverse direction means that it is not possible, as in the 2D case, to write contributions to the modally-expanded solution directly in terms of the assumed horizontal heating variation, F, which is uniformly translating. Mathematically, this is because the kernel of the Hankel integral transforms cannot be combined with time exponentials (even for $f = 0$) in the same way as in the corresponding 2D Fourier inversion. Numerical techniques will be necessary to determine and investigate modal horizontal variations, $w_n(r,t)$ (equation 3.65) and $b_n(r,t)$ (equation 3.69).

3.4 Implementation

For the sake of completeness, we shall continue, in this section, to allow rotation i.e. $f \neq 0$. Note, however, for meteorological applications, in section 3.5, $f \to 0$. All predicted responses clearly depend upon accurate estimates for $F''(r, t : g_n(k))$ (equation 3.66) and $G'(r, t : g_n(k))$ (equation 3.76), which must be carefully evaluated.

3.4.1 Properties of F''.

Consider equation 3.66. Its integrand has been expressed as a product of three factors. Consider these from left to right. As k increases, the first, envelope, factor does not oscillate, the second $(\cos(g_n(k)t))$ oscillates faster for larger times, t, and eigenvalues, c_n, (see equation 3.52). Figure 3.2 below shows how these variations combine in the overall variation of the integrand of F''. The properties of the integrand for $G'(r, t : k, g_n(k))$

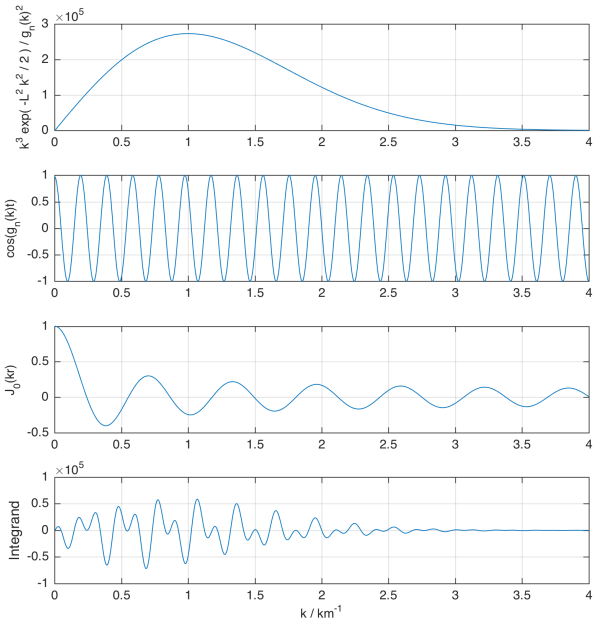

Figure 3.2: Composition of the integrand in equation 3.66. Data corresponds to $N_1 = 0.01$, $N_2 = 0.02$, $L = 1$, $H_L = 64H_t$, $f = 10^{-5}$, $t = 6 \times 60^2$s, The value of c_n chosen is the maximum for this paramterisation, $r = 10$km is also large. Hence, the second factor $(\cos(g_n(k)t))$ and the third factor $(J_0(kr))$ in the integrand of equation 3.66 oscillate rapidly, here.

(equation 3.76)) are similar.

3.4.2 Numerical Hankel Inversion

The inverse Hankel transform integrals for $F''(r,t:g_n(k))$ (equation 3.66) and $G'(r,t:k,g_n(k))$ (equation 3.76) are performed numerically, using Simpson's rule and Matlab. The transform space step, δk, used must be chosen carefully, to ensure uniform accuracy in the quadrature.

For $k \in [0, \frac{4}{L}]$, the common envelope factor, $e^{-\frac{L^2k^2}{2}}$, varies in the range $[1, e^{-8} \approx 3.3 \times 10^{-4}]$, i.e. the integrands will decay to 0.04% of their approximate maximum or minimum within conjugate space interval $k \in [0, \frac{4}{L}]$. Hence, a range for the Hankel inversion quadratures of equations 3.66 and 3.76 of $k \in [0, \frac{4}{L}]$ is chosen. Figure 3.2 shows the integrand oscillates, due to factors $\cos(g(k)t)$ and $J_0(kr)$ with respective conjugate space wavelengths

$$\lambda_c \approx \frac{2\pi}{c_n t}, \quad \lambda_{J0} \approx \frac{2\pi}{r}, \tag{3.78}$$

where we are neglecting the role of f, and, in the case of λ_{J0}, the first few zeros of $J_0(x)$ occur at $x \in [2.4048, 5.5201, 8.6537, 11.7915, 14.9309..]$, (Arfken, 1966) with a maximum interval (between the first and second zero) of 3.1153 admitting the approximation $3.1153 \approx \pi$.

Figure 3.3 shows a set of variations, in conjugate space, of the integrand for $F''(r,t:g_n(k))$ in equation 3.66. This data is parameterised as that in figure 3.2 and is plotted with quadrature step, $\delta k = 0.005$, constant. Variation of the integrand is plotted for $\max(c_n)$ and $\min(c_n)$ and small and large values of horizontal distance, r. A suitable choice of inversion quadrature step which places 20 quadrature points in each oscillation of the integrand, for a given c_n, is:

$$\delta k \equiv \frac{\min(\lambda_c, \lambda_{J0})}{20}. \tag{3.79}$$

We remark that for a majority of cases, $\delta k = \frac{2\pi}{c_n t}$, that the range of integration required to accurately evaluate these quadratures is conveniently restricted by the localized, Gaussian nature of the envelope of the integrand, that the computer execution time taken to evaluate an inversion integral decreases as c_n decreases and that the results from equation 3.79 compare well with a native but slower Matlab numerical integrator, which selects its own sampling rate.

3.4.3 Modal Propagation

In our 2D investigations of Chapter 2, each mode, $w_n(x,t)$, is characterised by a profile which is uniformly translating, at a phase speed c_n, without change of shape. In figure 3.4 we plot the behaviour of mode $w_{20}(r,t)$ ($n = 20$ chosen arbitrarily), for selected t, over a range of $r \in [0, 10]$km. This 3D model data show significant departures from the 2D counterpart, exhibiting both spreading and geometrical dissipation of the mode (due to geometry i.e. physical spreading of the wavefront).

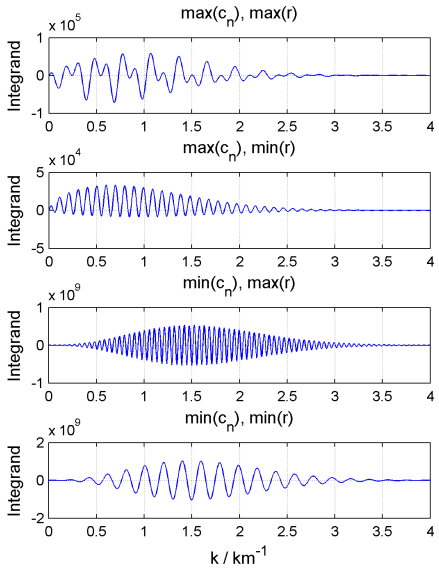

Figure 3.3: Behaviour of the integrand in the Hankel inversion integral, $F''(r, t : g_n(k))$ in equation 3.66. Data as figure 3.2. A quadrature step for Simpson's rule, δk, must be chosen adequately to resolve the oscillation of the integrand which originates from various sources. However, the period of oscillation varies between cases, which must be taken into account.

Plotting the approximate time position of the peak, r_{max} versus time, t, indicates a phase speed which is constant, in common with the 2D case (figure 3.5). We attribute the failure of the plot to intersect the origin to the lack of an identifiable propagating solution, for small r, which is not evident in the 2D counterpart. We return to the matter of propagation in section 3.5, when considering the horizontal propagation of adjustments.

It is appropriate to stress that solutions for w and b are based upon the numerical inversion process set-out in this section, and upon the eigenvalues, c_n, obtained from a numerical solution of the matching conditions applied to eigenfunctions $\phi_n(z)$ (section 2.4.1) and all data presented in the sequel was subject to convergence checks identical to those set-out for 2D, in section 2.4.2.

3.5 The Dynamics of Convective Adjustment

It is not our aim to replicate all the investigations in Chapter 2. The principal motivation for the present model is to assess the impact of the third dimension on e.g. the physical decay, of the propagating adjustments, which arise from purely geometrical considerations. Our main

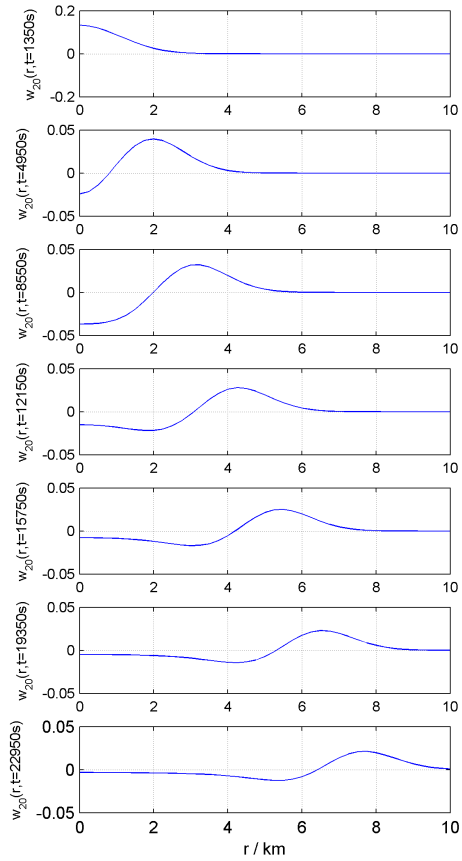

Figure 3.4: Propagation behaviour of the mode $w_{20}(r,t)$, which is equivalent to the Hankel inversion integral, $F''(r,t:g_{20}(k))$ in equation 3.66. Data as figure 3.2.

interest is to test the sensitivity of the gravity wave response in 3D, to different model configurations. Of particular interest is the structure and magnitude of the w and θ response in the troposphere.

We configure three simulations which complement our 2D solutions: (i) trapped regime with a rigid lid at the tropopause (3D_TRAP hereafter), (ii) a radiating regime with a high model lid and constant N (3D_RAD1 hereafter) and, (iii) a radiating regime with a high model lid and different values of N in the troposphere and stratosphere (3D_RAD2 hereafter). The high model lid height is identical to that used in Chapter 2 (namely, $H = 64H_t = 640\,\mathrm{km}$), as are the values of N_t ($= 0.01\mathrm{s}^{-1}$) and N_s ($= 0.02\mathrm{s}^{-1}$). The maximum heating rate is also the same ($Q_{max} = 0.001\,\mathrm{K\,s}^{-1}$). We now set $f = 0$.

For all data presented in this sub-section, equations 3.18, 3.60 and 3.63 together determine the vertical flow response, $w(r,z,t)$. Equations 3.18, 3.72 and 3.76 together determine the potential temperature re-

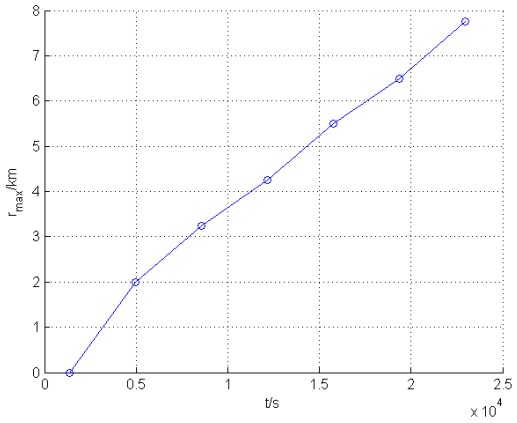

Figure 3.5: Propagation behaviour of the mode $w_n(r,t)$. The location in time of the local maximum, r_{max}, apparent in the data of figure 3.5. The solid line is a guide to the eye. Data as figure 3.4.

sponse, $b(r,z,t)$.

3.5.1 Trapped Solutions

We first characterise the convective adjustment to a prescribed heating in the simplest configuration of our model - the trapped case now nominated (3D_TRAP).

The top panels of figure 3.10 show the w and θ response at $t = 90$ mins when the lid is at $z = H_t$, thus trapping all energy in the troposphere. As in the 2D case, there is a steady response directly over the forced region until the forcing is truncated, at which time a rebound mode begins to propagate. Whilst this overall picture is consistent between the two geometries, there are a number of differences, which we shall discuss further in §3.6.

For now, our interest is in the propagating subsidence mode at the "head" of the w response. For a forcing with $L = 10$ km, and aspect ratio 1, the feature propagates at $33.3\,\mathrm{m\,s^{-1}}$. The mode of descending air precedes a tropospheric warming, with larger θ perturbations appearing closer to the head. The perturbations of both w and θ decay in time, as the response spreads over a larger radial area (seen in figure 3.11). We shall now characterise this decay.

We introduce a tropospheric average value for some property g as follows

$$g_z(r,t) = \frac{1}{H_t}\int_0^{H_t} g(r,z',t)dz'. \tag{3.80}$$

Given the axial symmetry of the problem, the total fluid kinetic energy, E_T, for the fluid contained in a cylindrical shell, height H_t, radius r, thickness δr, $\delta E_T(r,t) = 2\pi r H_t \bar{E}_z(r,t)\delta r$ (the total energy

density for our system is $\bar{E} + \bar{V} = \frac{\rho_0 w^2}{2} + \frac{\rho_0 b^2}{2N(z)^2}$.) Focusing attention on the response head, we characterise by positions $R_w(t)$ (centre of subsidence) and $R_b(t)$ (centre of warmth). Note, $R_w(t) \approx R_b(t)$ but $R_w(t) > R_b(t)$. Supposing, within the subsidence, $w \gg u_r, u_\theta$ and neglecting variation in the base state of density, ρ_0, we therefore have $\delta E_T(R_w(t)) \approx \pi r H_t \rho_0 w_z(R_w(t))^2 \delta r$. In the absence of radiation aloft, we expect this energy to be approximately conserved, $\delta E_T(R_w(r)) = \alpha$, a constant. Accordingly $w(R_w(t)) = \sqrt{\frac{k}{\pi H_t \rho_0 r \delta r}}$ and combining constants and setting $\delta r = 1$ we find

$$\bar{w_z}(R_w(t)) \sim \text{constant} \times r^{-\frac{1}{2}}, \tag{3.81}$$

at least for regions in which vertical flow is dominant. We expect a similar scaling to apply to the vertically averaged buoyancy response, $b_z(R_b(t))$. See also section 3.3.4.

In computation, we identify the position of the response head at a given time after heating onset, t, by the horizontal location of $\min(w_z(r,t))$ (for $R_w(t)$) and the horizontal location of $\max(b_z(r,t))$ (for $R_b(t)$). Figure 3.6 shows the time series of $R_w(t)$ and $R_b(t)$ in response to a 30 min forcing pulse. The head components propagate into the environment at very similar, constant speeds, $\frac{dR_w}{dt} \equiv c_w \approx 33\text{m}s^{-1}$ (based upon a value of $L = H_t = 10 \times 10^3$m, i.e. of 10km). In the 2D case of Chapter 2, the trapped response also propagates into its environment at constant speed.

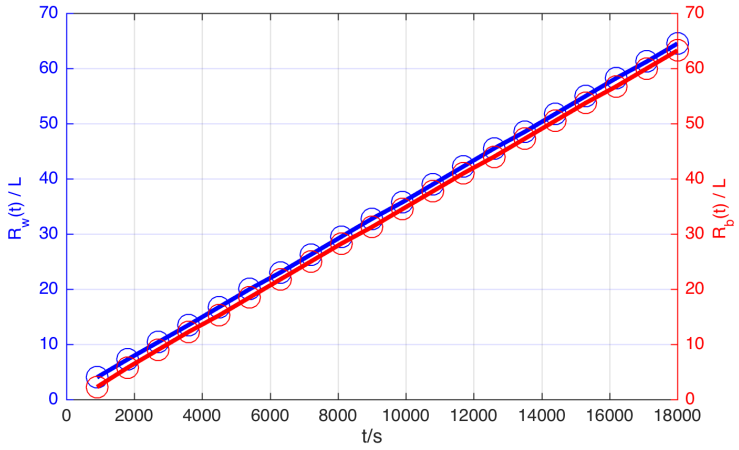

Figure 3.6: Time series of $R_w(t)$ (left) and $R_b(t)$ (right) (w and θ components of the subsidence mode) in 3D_TRAP. The propagation speed of the response head, $\frac{dR_w}{dt}$, is $c_w \approx 33.3\text{ms}^{-1}$. Note that the heating lags subsidence slightly.

Figure 3.7 shows computed values of descending subsidence, $w_z(R_w(t))$, and potential temperature, $b_z(R_b(t))$, as functions of $R_w(t)$ and $R_b(t)$ respectively, for the same range of times as figure 3.6. We see that the amplitude of both w and θ at the head of the response is dependent

upon the distance which the head has travelled, and obeys the scaling prediction 3.81 (figure 3.8).

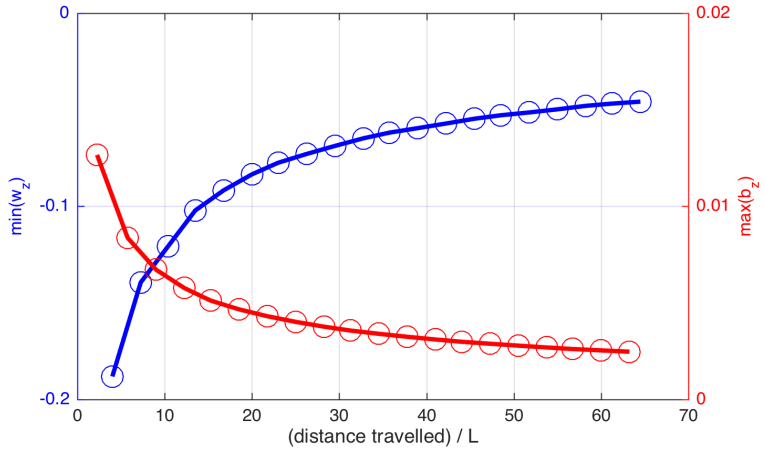

Figure 3.7: The variation in minimum w_z (left) and maximum b_z (right) with radial spreading of subsidence in 3D_TRAP.

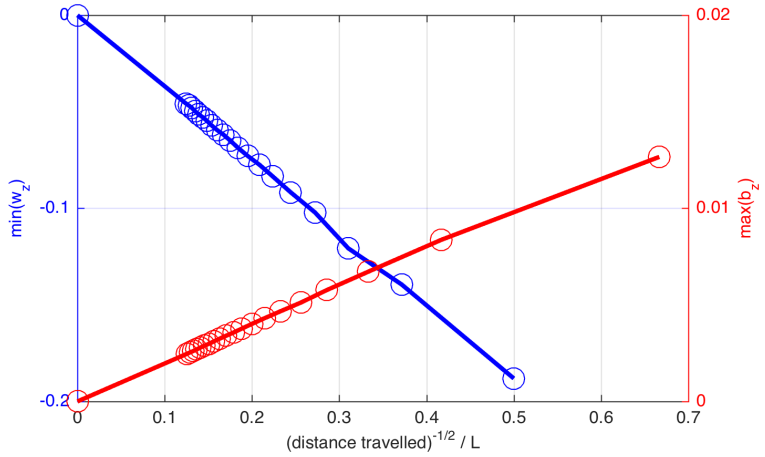

Figure 3.8: As in figure 3.7, but on a scaled x-axis.

Following our approach in 2D, we will next raise the upper lid aloft, to investigate how upward radiation affects the response in the troposphere.

3.5.2 Radiation and the Effect of Model Stratosphere

In Chapter 2, we saw that allowing for the upward radiation of energy reduces the amplitude of the tropospheric response and, less intuitively, communicates convective adjustment into the environment quicker as deeper gravity wave modes acquire significance. We expect the 3D case to display a similar pattern here, with the caveat that the 3D case will

also experience reduced amplitudes due to the radial spreading of its response, as the latter spreads into the environment.

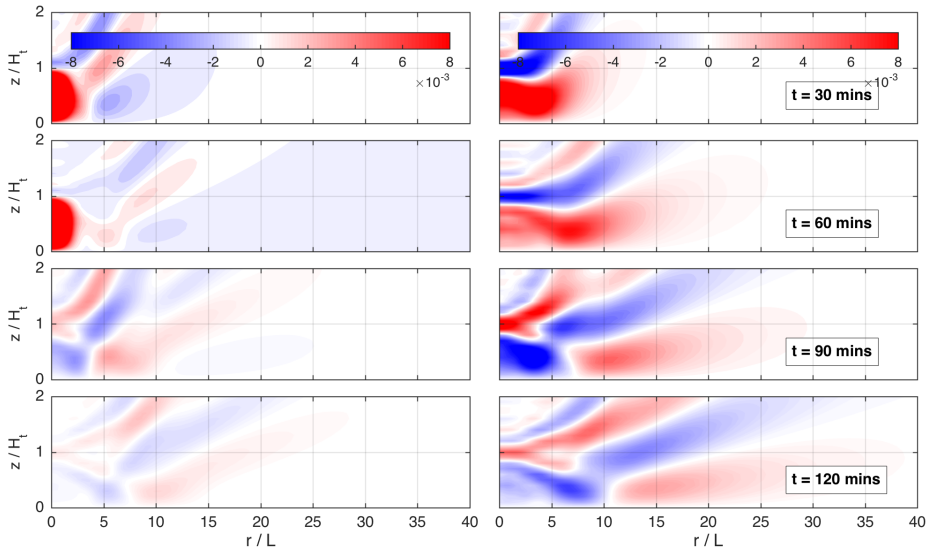

Figure 3.9: The time evolution of w ($\mathrm{m\,s^{-1}}$) (left) and θ ($\mathrm{K\,s^{-1}}$) (right) in response to to a transient, 1 hr pulse of heating with $L = 10\,\mathrm{km}$, uniform $N = 0.01\,\mathrm{s^{-1}}$, $H/H_t = 64$. Note that t increases down each column.

Figure 3.9 shows the time evolution of both the w and θ responses in 3D_RAD1 subject to a 1 hr pulse of forcing. As in the 2D case, having a high model lid allows a spectrum of gravity wave modes to be excited, which travel into the environment surrounding the forcing, thus communicating the convective adjustment. Another consistent feature is an immediate subsidence mode in the troposphere, leading to a spreading in θ. We observe a rebound mode following the truncation of heating. However, both w and θ both have a much richer structure in the troposphere compared with the 2D case, particularly after 1 hr.

The magnitudes of the response are clearly affected by radial decay (by factor $r^{-1/2}$), reducing from the 2D solutions by a factor 20. However, the speed of wave propagation appears consistent with that shown in figure 2.8.

Figure 3.10 shows the response in w and θ, for each of 3D_TRAP, 3D_RAD1 and 3D_RAD2. As in figure 2.10, we see that the trapped case (minimum upward radiation) has the largest magnitudes of w and θ, 3D_RAD1 (maximum upward radiation, since there is no interface at the tropopause) has the smallest magnitudes, and 3D_RAD2 lies between these two bounds. Further, the pattern of horizontal propagation of the dominant mode across the model configurations is similar to that in the 2D case, where the models with a deep atmosphere propagate slightly faster than the trapped mode. Finally, the θ response in 3D_RAD2 has

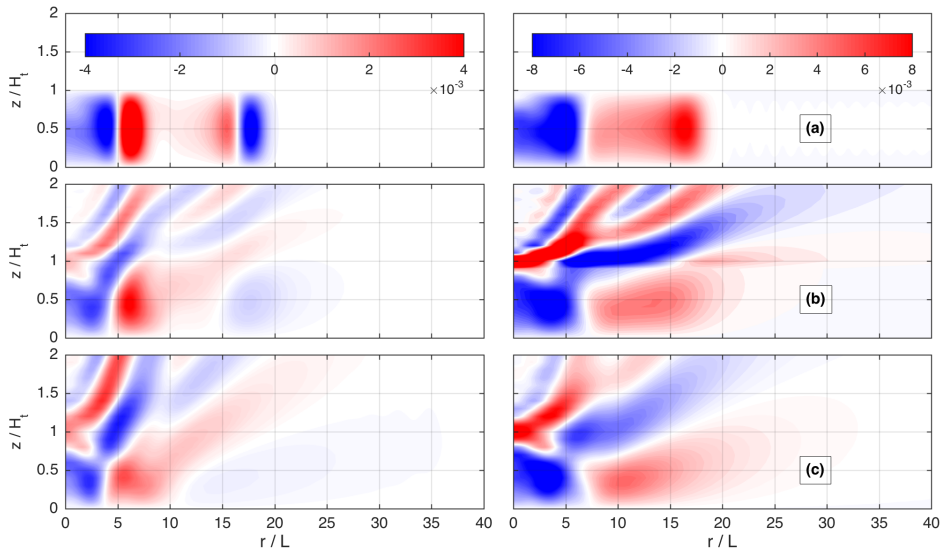

Figure 3.10: The w (left) and θ (right) response at $t = 90$ mins to a 1 hr pulse of forcing, with $L = 10$ km in 3D_TRAP (a), 3D_RAD2 (b) and 3D_RAD1 (c).

a noticeable discontinuity at the tropopause, for the same reasons as discussed in Chapter 2.

There are, however, a number of notable differences. First, the vertical velocities are much smaller in the 3D than in 2D (also seen in 3.9), as expected, given the growing volume of the adjusted atmosphere as r increases. Further, comparing the 3D models, the vertical velocities in 3D_RAD1 and 3D_RAD2 are much smaller than in 3D_TRAP, whereas the θ response is much more consistent across the regimes. These differences are quantified in figure 3.11. Second, the tropospheric response is much less homogenous than the 2D case. The reader is invited to compare the top panel in figures 3.10 and 2.10. The 3D geometry appears to introduce a head to the response, propagating radially from the forcing region with larger w and θ perturbations, followed by a tail with reduced perturbations. Following the truncation of heating, the rebound mode has the reverse characteristics.

3.6 Comparison to 2D

In 2D, we find trapped solutions which consist of two symmetric single gravity wave modes which propagate in opposite directions from the forcing. The situation becomes more complicated in a deep atmosphere, as the excitation of higher modes leads to a more dispersed tropospheric response, leading to a wider, weaker response (see figure 2.9). In 3D, this same effect is in play, with a key difference: a radial dispersion of

convective adjustment.

To compare data from the models of Chapter 2 and the present chapter, we must establish cross-calibrations which relate the heating rate amplitude, S_0 of the two models. Denote the heating rate amplitude of the 2D slab geometry model of chapter 2 S_0^s and the heating rate amplitude of the cylindrical geometry model of the present chapter S_0^c. We consider two cases, both based upon an equivalence of the total heat input into a finite region of space, in unit time.

First, match the total heat input rate for the model of Chapter 3 with $r \in [0, \infty)$, $z \in [0, H_t]$ to the model of Chapter 2 with $x \in (-\infty, \infty)$, $y \in [0, L]$, $z \in [0, H_t]$. Recall, L is the characteristic length scale of the buoyancy forcing, which is assumed identical in the both models. Balancing the heating rates we have

$$\begin{aligned} & S_0^s \int_{-\infty}^{\infty} e^{-\left(\frac{x^2}{2L^2}\right)} dx \int_0^{H_t} \sin\left(\frac{\pi z}{H_t}\right) dz \int_0^L dy \qquad (3.82) \\ = \; & S_0^c \int_0^{\infty} 2\pi r e^{-\left(\frac{x^2}{2L^2}\right)} dr \int_0^{H_t} \sin\left(\frac{\pi z}{H_t}\right) dz \end{aligned}$$

and, canceling the common vertical variation and using the standard integral $\int_{-\infty}^{\infty} e^{-\left(\frac{x^2}{2L^2}\right)} dx = \sqrt{2\pi} L$ we straightforwardly obtain the following relationship between buoyancy forcing rate amplitudes

$$S_0^c = \frac{1}{\sqrt{2\pi}} S_0^s. \qquad (3.83)$$

Alternatively, match the total heat input rate into finite, identical volumes. Now, for the model of Chapter 3 take the region $r \in [0, 10L]$, $z \in [0, H_t]$ with volume $100\pi L^2 H_t$ and for model of Chapter 2 take the equivalent volume $x \in [-10L, 10L]$, $y \in [0, 5\pi L]$, $z \in [0, H_t]$. Balancing the heating rates we now have

$$\begin{aligned} & S_0^s \int_{-10L}^{10L} e^{-\left(\frac{x^2}{2L^2}\right)} dx \int_0^{H_t} \sin\left(\frac{\pi z}{H_t}\right) dz \int_0^{5\pi L} dy \qquad (3.84) \\ = \; & S_0^c \int_0^{10L} 2\pi r e^{-\left(\frac{r^2}{2L^2}\right)} dr \int_0^{H_t} \sin\left(\frac{\pi z}{H_t}\right) dz. \end{aligned}$$

Canceling common factors, transforming variables and simplifying we obtain

$$5\pi L^2 S_0^s \int_{-10}^{10} e^{-\left(\frac{u^2}{2}\right)} du = -2\pi L^2 S_0^c \int_0^{10} -u e^{-\left(\frac{u^2}{2}\right)} du. \qquad (3.85)$$

Any standard normal distribution tabulation shows the integral on the left of the above to be very close to 1 whilst that on the right may be evaluated directly, to obtain $5\pi L^2 S_0^s = 2\pi L^2 S_0^c \left(1 - e^{-50}\right) \approx 2\pi L^2 S_0^c$, which yields an alternate relationship between buoyancy forcing rate amplitudes

$$S_0^c = \frac{5}{2} S_0^s. \qquad (3.86)$$

Between the calibrations in equations 3.83 and 3.86 there is almost an order of magnitude difference. For the data presented in this section, we use the calibration in equation 3.83. However, it is appropriate to note that the 3D adjustments could be all an order of magnitude larger than those shown in figure 3.12, below, if the alternative calibration is used.

Figure 3.12 shows the time series of maximum tropospheric w response for $r > 100\,\text{km}$ when forced with steady heating of width $L = 10\,\text{km}$. (Note, the equivalent for 2D is shown in figure 2.9).

First, as discussed in §3.5.1 we notice a stark difference in the trapped case. Unlike the trapped 2D solutions, 3D_TRAP no longer remains constant in time, but, rather, decays in time as the response spreads further into the environment.

Across the models, as in the 2D case, the amplitude of the response is much larger in the trapped case at all times. However, more unexpectedly, 3D_RAD1 and 3D_RAD2 produce very similar responses, despite the interface at the tropopause in the latter. Indeed, whereas there is a 50% difference in the amplitudes between RAD1 and RAD2, 3D_RAD1 and 3D_RAD2 are consistent after 1.5 hrs. It appears that increasing the dimensionality has a more significant influence on the response than the vertical stratification.

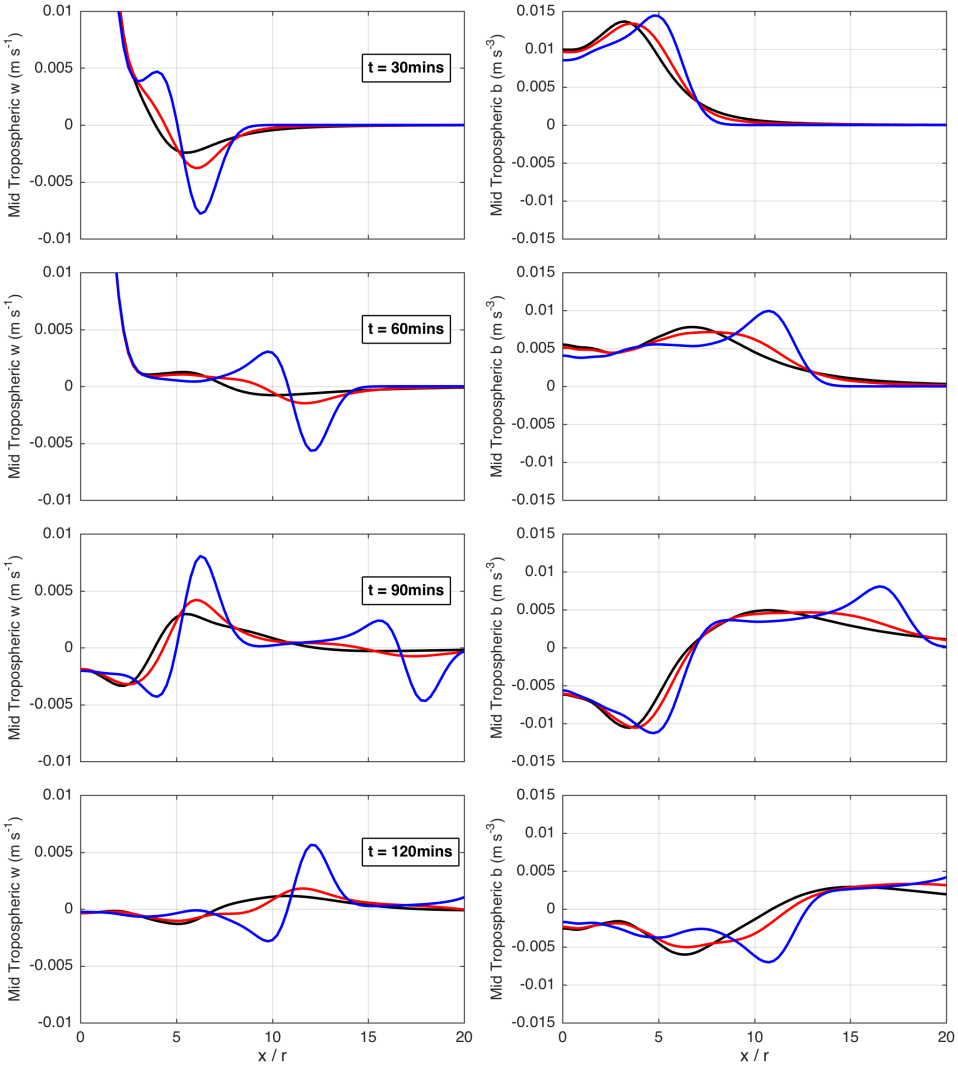

Figure 3.11: Mid-tropospheric w and θ response to a 1 hr pulse of heating, with $L = 10\,\text{km}$ in 3D_TRAP, 3D_RAD1 and 3D_RAD2. Here data is represented as follows. Blue line is 3D_TRAP, the black line is 3D_RAD1 and the red line is 3D_RAD1.

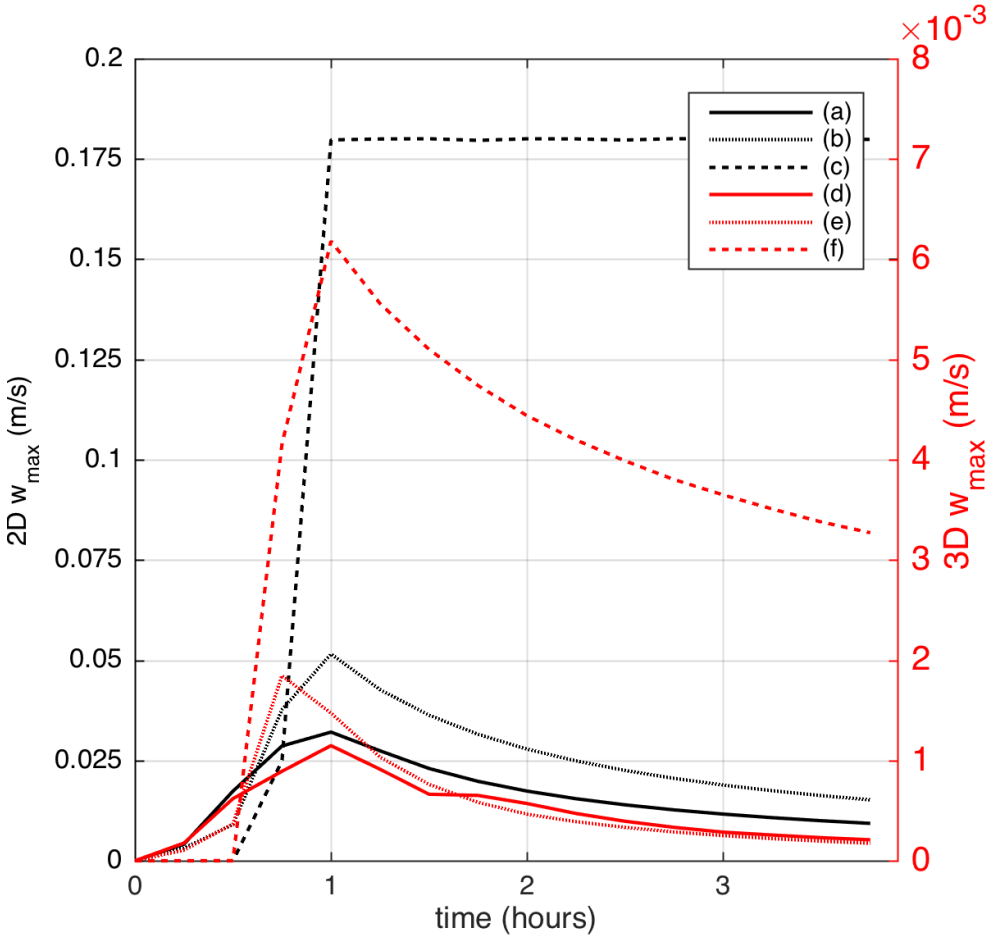

Figure 3.12: Time series of maximum tropospheric values of $|w|$ for $r >$ 100 km when forced with steady heating of width $L = 10$ km. (a,...,c) represent the 2D response, (d,...,f) represent the 3D response. Dashed lines refer to respective 3D_TRAP, solid refer to 3D_RAD1 and dotted refer to 3D_RAD2.

3.7 Summary and Discussion

We have extended the analytical model of Chapter 2 into a three-dimensional cylindrical geometry. Once again, the vertical velocity and potential temperature response to convective adjustment have been expressed in terms of convectively-forced gravity wave modes. We test the influence of the upper boundary condition and make comparisons with the 2D model.

A trapped solution, i.e. one with a rigid lid at the tropopause (allowing no radiation in the stratosphere), yields a single gravity wave subsidence mode (high intensity downward motion and warming in a localised region) which propagates into the environment and conditions the troposphere for further convection. This feature is broadly similar to 2D version, but differs in three ways: (i) a much reduced amplitude, as expected, since the response can now decay radially, (ii) a bore-like "head" pilots the response with larger perturbations at the leading edge of propagating feature (in 2D the response is much more homogeneous), and (iii) there is a time-dependent decay in the response as the feature spreads over a growing area. We characterise the decay, predicting a factor $r^{-\frac{1}{2}}$ in the trapped solutions, and confirm with model data.

When the altitude of the upper lid is raised high into the atmosphere (to approximate a semi-infinite solution), we see some very recognisable features: (i) a reduction in response amplitudes in the troposphere (since energy can now escape aloft), and (ii) the excitation of higher-order gravity wave modes, with a range of wave speeds which propagate into the immediate environment quicker. Further, the addition of a model stratosphere partially traps the response, thus producing a response with amplitudes which lie between the trapped and constant N case (see §2.5.3 for a detailed discussion). Note also, as in the 2D case, there is a discontinuity in the b response when a model stratosphere is included.

Qualitatively, the tropospheric response in 3D_RAD1 and 3D_RAD2 are similar (at least for $t = 90$ mins, as in figure 3.10). This is confirmed in figures 3.11 and 3.12.

In summary, in Chapter 3 we have have extended the essential physical content and regime of approximations of the 2D model of Chapter 2 into a 3D, cylindrically symmetric geometry. The treatment of Chapter 2 is found to extend transparently, with the caveat that use of Hankel rather than Fourier transforms, adds significant mathematical challenge to the solution of the horizontal part of the problem, thereby removing attractive analytic properties of the 2D solutions- specifically, its expression in terms of uniformly translating horizontal heating profile. As in Chapter 2, we have concentrated on investigating the effect of the pseudo-radiative, upper boundary condition at the tropopause (recall, we use a very high lid used to represent a radiating troposphere). Throughout, we take care to note the differences from 2D to 3D both in terms of i) the physical consequences of the extended dimensionality and ii) the mathematical structure of the solutions.

The work presented in Chapter 3 forms a clear basis for a benchmark study, but there are a number of possible avenues we leave unexplored. For instance, we have presented data for non-rotating ($f = 0$) cases only. Whilst this is consistent with our preceding treatment of 2D, in Chapter 2, it leaves the effect of rotation within our model of stratification unaddressed.

We raise this restriction in the next Chapter, where we will develop a new, steady state model which relies upon the same stratification.

L

Chapter 4

The Long Time Response to Convection in a Rotating Atmosphere

4.1 Introduction

In Chapter 2 we built a simple, analytic model of the non-rotating, radiating transient dynamics of convective adjustment in 2D. Two natural questions arise regarding i) the role of the third dimension and ii) rotation. In Chapter 3 we assessed the role of dimensionality, by extending our model's horizontal formulation whilst preserving all its other features, in particular its vertical, modal structure and stratification. In this chapter, we aim to address the second question.

In keeping with our central paradigm, we aim to use a predominantly analytic approach on a minimal formulation. This decision tends to rule-out further use of the 3D model of Chapter 3 which, whilst it was formulated with $f \neq 0$, relies heavily on numerics to invert from reciprocal space. To make meaningful comparisons, it is important to maintain as common a description and regime of physical approximations as possible. Accordingly, we shall here develop a new, predominantly analytic model of a rotating atmosphere from a slightly modified 2D description.

In Chapters 2 and 3 we have mainly examined the effect of an upper boundary at the tropopause, in three dynamic regimes- trapped, radiating, or a mixture of the two. In fact, the presence of rotation is manifest before dynamics, in the structure of the steady state of convective adjustment. Here we will examine what is, essentially, the same physical system and regime of approximations as previously, using an enhanced mathematical model capable of describing the steady state. Whilst such a model will not inform us on the transients of convective adjustment, but rather the final state of the atmosphere following convection, we deem that it does represent the simplest vehicle for an assessment of the effects of rotation, using our essential base physics and modelling assumptions.

The 2D, Boussinesq basic set of Chapter 2, i.e. equations 2.1 will

have to be modified to address rotation in what is termed 2.5 dimensions (a suitable basic set of equations for 2D must now contain both components of horizontal velocity). To retain the stratification of Chapter 2 and Chapter 3 (whilst formulating at least), it will be necessary to generalise our modal expansion methodology and to calibrate and interpret meteorological data, scalings and non-dimensionalisations will be developed.

Chapter 4 is organised as follows. We will begin with salient background physics and consideration of previous studies on rotating systems, in section 4.2, will then define and solve a steady-state model for a stratification identical to that used in Chapters 2, 3 in section 4.3. In section 4.4 we simplify the model to constant N and further simplify it in section 4.5 to constant N, ρ_0, in which limit we consider analytical solutions. Results are presented in section 4.6. Finally, we will end with discussion and a summary.

4.2 Background

The main motivation here is to understand the effect of Coriolis acceleration on the steady state of convective adjustment. Thus, we will now investigate a system with a non-zero f. Using a steady state model in 2.5D, with $\frac{d}{dy} = 0$, allows us to write simple, analytic solutions, even with a non-zero f, which is in keeping with the general paradigm of this thesis (thus far, at least).

In the Earth's mid-latitudes, a quasi-geostrophic balance is struck as Coriolis' force acts rapidly to restore equilibrium, in response to any changes in pressure gradient (Gill *et al.*, 1986; Hoskins *et al.*, 1985). Through latent heat release, deep cumulonimbus convection perturbs the pressure and buoyancy of the troposphere and forces a spectrum of gravity waves which mediate compensating subsidence in the environment (Bretherton and Smarlokwicz, 1989). In the mid-latitudes, gravity wave propagation is influenced by the Coriolis force and the subsidence is, as a consequence, confined to a finite distance (Bretherton, 1988, 1987; Chagnon & Bannon, 2001). Subsequently, the atmosphere develops a physical rotation or vorticity, visible in e.g. tropical cyclones or rotating mesoscale convective systems (MCSs). Such features generate anomalies in the potential vorticity (Liu & Moncrieff, 2004; Shutts & Gray, 1994), which, in the absence of diabatic heating and stratification, is a conserved quantity derived from the vorticity field and planetary rotation (Gill, 1982). Potential vorticity anomalies can persist long after convection terminates, advect and, indeed, they can trigger new convection (Raymond & Jiang, 1990).

We know gravity wave propagation facilitates convective adjustment and is influenced by many considerations, including atmospheric stratification, moist processes and vertical shear. When modelling, further complications are added through choice of boundary conditions (Edman

& Romps, 2017; Nicholls *et al.*, 1991), numerical resolution and parameterisations (Bretherton, 1988).This chapter focuses on the interaction of the two controllers of convective Rossby adjustment; (i) Coriolis force and (ii) upward radiation at the tropopause. The meteorology of these controls is immediately apparent in two ways. First, in gravity wave propagation, which is more restricted in the mid-latitudes than the tropics, where the Coriolis force is much weaker (Liu & Moncrieff, 2004). Second, the upward radiation of convectively forced waves through a leaky lid at the tropopause which alters the length-scale of tropospheric adjustment to convection (Edman et al. 2017 and Chapter 2 of this thesis). However, it is not clear how these processes work in tandem during convective adjustment and the sensitivity of Rossby deformation to upward radiation remains unexplored.

Numerical modelling of convective Rossby adjustment is problematic, due to the wide range of scales which demand consideration. For example, sub hour-long mesoscale convection interacts with day-long synoptic Rossby deformation. To circumvent this issue, we adopt, here, a theoretical approach and develop an analytical solution to linear, hydrostatic, steady-state equations, formulated in 2.5 dimensions. Initially we formulate a deep atmosphere, forced with a prescribed transient buoyancy source of finite duration. Our initial formulation allows for a stratified atmosphere but whilst vorticity dynamics in the atmosphere are influenced by stratification, we ultimately neglect variations in N^2, in order to attain exact solutions, assume that the important aspects of Rossby adjustment can be captured with a simpler equation set. Our analytical solutions reveal a balanced state of the atmosphere following convection and provide a direct way of investigating the sensitivity to both Coriolis force and upward radiation.

4.3 Mathematical Model

In this section we shall, for generality and consistency with Chapters 2, 3, formulate and solve a general mathematical description. Later, in section 4.4, we simplify our description, to uniform N and further, to uniform N and $\rho_0(z)$, in section 4.5. (The latter steps are not motivated by mathematical considerations only. Physically, in Chapter 2 we have shown that, within our formulation, energy radiation into the stratosphere is optimal for $N_t = N_s$).

We work throughout this chapter in 2.5 dimensions, with $\frac{d}{dy} = 0$, and consider the steady state atmospheric velocity, buoyancy (potential temperature) and potential vorticity (PV hereafter) adjustment to a prescribed tropospheric heating, or buoyancy forcing, of finite duration. The mathematics of the chapter follows that of Chapters 2, 3 but it is more complicated. For this reason, we now give an overview of subsections.

We define our system in sub-section 4.3.1 and proceed to derive and briefly discuss the basic physics of its energy and PV in sub-sections 4.3.2

and 4.3.3. Next we consider the system steady response, in sub-section 4.3.4. Much of the physical behaviour of the model will be deduced from the steady pressure field, $p(x)$: the equation which we solve for p is derived in sub-section 4.3.5. This equation is solved, for a stratification identical to that in Chapters 2, 3, using a generalised modal expansion of field variables p, v and b, from sub-section 4.3.6 onwards (where we derive heating expansion coefficients, eigenfunctions, normalisation, matching conditions etc. for a stratified atmosphere). We point-out in advance that the steady-state b adjustment is not determined, as in Chapters 2,3 from a time integration of the thermodynamic equation.

4.3.1 Governing Equations and System Geometry

We seek the steady-state atmospheric adjustment, in 2.5D, following heating of finite duration, T, modelled using a buoyancy forcing. The domain is a plane, $x-z$ slab. Initially, we allow an atmospheric stratification defined by (i) a variable base state density and (ii) a buoyancy frequency which changes at the tropopause. Our basic rationale and description are consistent with Chapter 2, where the corresponding dynamics were considered. Our basic set of equations are

$$\begin{aligned}
\frac{\partial u}{\partial t} - fv &= -\frac{1}{\rho_0(z)}\frac{\partial p}{\partial x}, \\
\frac{\partial v}{\partial t} + fu &= -\frac{1}{\rho_0(z)}\frac{\partial p}{\partial y}, \\
\frac{\partial w}{\partial t} - b &= -\frac{1}{\rho_0(z)}\frac{\partial p}{\partial z}, \\
\frac{\partial b}{\partial t} + N^2 w &= s, \\
\frac{\partial u}{\partial x} + \frac{\partial v}{\partial y} + \frac{\partial w}{\partial z} &= 0,
\end{aligned} \tag{4.1}$$

where

$$b \equiv g\frac{\theta'}{\theta_0}, \quad \bar{b} = g\frac{\bar{\theta}}{\theta_0}, \quad N^2 = \frac{d\bar{b}}{dz}. \tag{4.2}$$

Here, θ_0 is a reference potential temperature, which is constant and $\bar{b}(z)$ is the base state of potential temperature. The base state of the flow is rest and the base states of density, $\rho_0(z)$, and the buoyancy frequency, $N(z)$ have the altitude variation defined below. Heating is introduced in our thermodynamic equation essentially as a buoyancy forcing. The rationale underlying the above description is set-out in Chapter 2.

The geometry and assumed buoyancy forcing distribution we assume in this work is defined in Chapter 2. Rigid surface and lid boundaries are imposed at $z = 0, H$, well above the troposphere. The latter is assumed to occupy the range of altitude $0 \leq z \leq H_t$, with $H_t \ll H$.

4.3.2 System Energy

From an appropriately weighted combination of the first three momentum equations of equations 4.1 we obtain

$$u\frac{\partial u}{\partial t}+v\frac{\partial v}{\partial t}+w\frac{\partial w}{\partial t}-bw=-\frac{1}{\rho_0}\left(u\frac{\partial p}{\partial x}+v\frac{\partial p}{\partial y}+w\frac{\partial p}{\partial z}\right), \tag{4.3}$$

hence

$$\frac{\partial}{\partial t}\left(\frac{1}{2}\underline{v}\cdot\underline{v}\right)=-\frac{1}{\rho_0}\left(\underline{v}\cdot\underline{\nabla}\right)p+bw=-\frac{1}{\rho_0}\underline{\nabla}\cdot(p\underline{v})+\frac{p}{\rho_0}\underline{\nabla}\cdot\underline{v}+bw. \tag{4.4}$$

Finally, using the continuity equation and our thermodynamic equation, from equations 4.1, to replace w in the right hand side of the above, we obtain an energy equation

$$\frac{\partial}{\partial t}\left(\frac{1}{2}\rho_0\underline{v}\cdot\underline{v}+\frac{1}{2}\frac{\rho_0 b^2}{N^2}\right)+\underline{\nabla}\cdot(p\underline{v})=\frac{\rho_0 sb}{N^2}, \tag{4.5}$$

from which we infer an energy flux density $p\underline{v}$ and potential energy density $\frac{1}{2}\frac{\rho_0 b^2}{N^2}$. That is, from equation 4.5 we have a total scalar energy density, $\bar{E}$, and an energy flux density vector, $\underline{\bar{J}}$ as follows

$$\bar{E}=\frac{\rho_0}{2}\underline{v}\cdot\underline{v}+\frac{\rho_0 b^2}{2N^2},\qquad \underline{\bar{J}}=p\underline{v}. \tag{4.6}$$

Note that the right hand side of (4.5) vanishes when buoyancy forcing is removed, $s\to 0$.

Henceforth we take the hydrostatic approximation in the vertical momentum equation.

Equation (4.5) may be written $\frac{\partial E}{\partial t}+\underline{\nabla}\cdot\underline{J}=\frac{\rho_0 sb}{N^2}$. Using a time and domain integral of this equation, we can obtain an expression for the total energy.

$$\begin{aligned} E_{tot} &\equiv \int_\Omega\left(\int_0^t\frac{\partial E}{\partial t}dt\right)dV=\int_\Omega\left(\int_0^t\left(\frac{\rho_0 sb}{N^2}+\underline{\nabla}\cdot\underline{J}\right)dt\right)dV, \\ &= \frac{\rho_0}{N^2}\int_\Omega\left(\int_0^t(sb)\,dt\right)dV+\int_0^t\left(\int_{\partial\Omega}\underline{J}\cdot\underline{dA}\right)dt. \end{aligned} \tag{4.7}$$

In the above, the flux integral vanishes as follows: domain boundaries, $\partial\Omega$, located at $z=0,H$ have $\underline{dA}=-dxdy\hat{e}_z$, $\underline{dA}=dxdy\hat{e}_z$ respectively, so for $z=0$ (say), $\underline{J}\cdot\underline{dA}=-w(x,y,0)dxdy=0$, since $w(x,y,0)=0$ by the kinematic condition. Moreover, s is assumed zero outside the troposphere, $z>H_t$, and for all time $t>T$. Hence, for $t>T$

$$E_{tot} = \frac{\rho_0}{N^2}\int_0^{H_t}\int_0^L\left(\int_0^T(sb)\,dt\right)dxdz, \tag{4.8}$$

from which we note that a knowledge of the history of the buoyancy adjustment, $b(\underline{r},t)$ is necessary to compute E_{tot}.

4.3.3 Potential Vorticity

Potential Vorticity (PV hereafter) is the absolute circulation of an air parcel enclosed between two isentropic surfaces. The derivative following the motion of that parcel can only be changed by diabatic heating.

PV may be defined as follows

$$PV \equiv \frac{1}{\rho}\underline{\zeta}\cdot\underline{\nabla}\theta, \quad \underline{\zeta} = \underline{\nabla}\times\underline{v} + f\hat{e}_z \tag{4.9}$$

where $\underline{\zeta}$ is the absolute vorticity.

We seek an expression for the PV adjustment. We will require the following relations (Holton, (2012))

$$b \equiv \frac{g\theta}{\theta_0} = -g\frac{\rho}{\rho_0}, \quad \frac{\rho}{\rho_0} = -\frac{\theta}{\theta_0}. \tag{4.10}$$

Eventually, we will simplify the expression, using the Boussinesq approximation, however, we retain the density adjustment for the time being, as it will eventually assist us to recognise the significance of other terms. We note that buoyancy adjustment, b, is not to be neglected in the Boussinesq approximation (since it is associated with g) and that $\underline{\zeta}$ is already first-order in perturbation quantities (we write that it is $O(1)$) and make replacements in the definition above

$$\begin{aligned} PV &= \frac{1}{(\rho_0+\rho)}\underline{\zeta}\cdot\underline{\nabla}\left(\theta_0+\theta\right), \\ &= \frac{1}{\rho_0}\left(1-\frac{\rho}{\rho_0}\right)\underline{\zeta}\cdot\underline{\nabla}\left(\theta_0+\theta\right), \end{aligned} \tag{4.11}$$

where base states$=\theta_0$ is allowed z dependence. In particular, we take

$$N^2 \equiv g\frac{d}{dz}\log_e(\theta_0) = \frac{g}{\theta_0}\frac{d\theta_0}{dz}. \tag{4.12}$$

Expand about base states

$$\begin{aligned} PV \approx\ & \frac{1}{\rho_0}\left(1-\frac{\rho}{\rho_0}\right)\times \\ & \left(\frac{\partial w}{\partial y}-\frac{\partial v}{\partial z},\frac{\partial u}{\partial z}-\frac{\partial w}{\partial x},\frac{\partial v}{\partial x}-\frac{\partial u}{\partial y}+f\right)\cdot\left(\frac{\partial\theta}{\partial x},\frac{\partial\theta}{\partial y},\frac{d\theta_0}{dz}+\frac{\partial\theta}{\partial z}\right), \end{aligned} \tag{4.13}$$

and retain only terms of $O(1)$ or larger

$$PV = \frac{1}{\rho_0}\left(1-\frac{\rho}{\rho_0}\right)\left(\frac{\partial v}{\partial x}-\frac{\partial u}{\partial y}+f\right)\left(\frac{d\theta_0}{dz}+\frac{\partial\theta}{\partial z}\right)+O(2). \tag{4.14}$$

For the $O(1)$ PV adjustment, we have

$$PV' \approx \frac{1}{\rho_0}\left(\frac{\partial v}{\partial x}-\frac{\partial u}{\partial y}\right)\frac{d\theta_0}{dz}+\frac{f}{\rho_0}\frac{\partial\theta}{\partial z}-\frac{\rho}{\rho_0^2}f\frac{d\theta_0}{dz}, \tag{4.15}$$

where we have dropped the term $\frac{f}{\rho_0}\frac{d\theta_0}{dz}$, since it does not belong to the adjustment in PV. Appealing to our definition of buoyancy frequency, equation 4.12, we have $\frac{d\theta_0}{dz} = \frac{N^2\theta_0}{g}$, replacing θ in favour of b, using equations 4.10, and neglecting the fact that we have a $O(1)$ approximation

$$PV' = \frac{N^2\theta_0}{g\rho_0}\left(\frac{\partial v}{\partial x} - \frac{\partial u}{\partial y}\right) + \frac{f}{\rho_0}\frac{\partial}{\partial z}\left(\frac{b\theta_0}{g}\right) - \frac{N^2\theta_0\rho}{g\rho_0^2}f. \quad (4.16)$$

Recall, the last term in the above arises from density variation which will be negligible within the Boussinesq approximation. We now expand the second term on the right hand side using the product rule and again appeal to equations 4.12 and 4.10

$$PV' = \frac{N^2\theta_0}{g\rho_0}\left(\frac{\partial v}{\partial x} - \frac{\partial u}{\partial y}\right) + \frac{f\theta_0}{g\rho_0}\frac{\partial b}{\partial z} + \frac{fN^2\theta_0 b}{g^2\rho_0} - \frac{fN^2\theta_0\rho}{g\rho_0^2}. \quad (4.17)$$

Now, the third and fourth term on the right hand side of the above result for the potential vorticity adjustment are easily shown to be identical, using equation 4.10. Since the third term would be neglected within the Boussinesq approximation (recall, it arises from density variation in a term *not* coupled to gravity), one must also neglect the third term in that approximation. Hence, we arrive at the following non-Boussinesq and Boussinsesq approximations for a scaled potential vorticity adjustment within the system of Chapter 4, respectively

$$\frac{\rho_0 g}{\theta_0 N^2}(PV') = \left(\frac{\partial v}{\partial x} - \frac{\partial u}{\partial y}\right) + \frac{f}{N^2}\frac{\partial b}{\partial z} + \frac{2fb}{g}, \quad (4.18)$$

$$\frac{\rho_0 g}{\theta_0 N^2}(PV'_B) = \left(\frac{\partial v}{\partial x} - \frac{\partial u}{\partial y}\right) + \frac{f}{N^2}\frac{\partial b}{\partial z}.$$

Both the above allow variable ρ_0 and variable N^2, note.

Now, seek an alternative expression for the right hand side of equation 4.17, for our PV adjustment. By eliminating variables from the basic set (4.2) it is possible to obtain

$$\frac{\partial}{\partial t}\left(\frac{\partial v}{\partial x} - \frac{\partial u}{\partial y} + f\frac{\partial}{\partial z}\left(\frac{b}{N^2}\right)\right) = f\frac{\partial}{\partial z}\left(\frac{s}{N^2}\right). \quad (4.19)$$

Let us now assume a pulsed heating of finite duration, T. Integrating over a time $t > T$, and using quiescent initial conditions ($u = v = b = 0$, $t = 0$) gives

$$\frac{\partial v}{\partial x} - \frac{\partial u}{\partial y} + f\frac{\partial}{\partial z}\left(\frac{b}{N^2}\right) = \int_0^T f\frac{\partial}{\partial z}\left(\frac{s}{N^2}\right)dt, \quad (4.20)$$

The right hand side of equation 4.17 and the left hand side of equation 4.20 are similar. Eventually, a compact, analytic expression for PV will be obtained. To obtain such an expression however, N must be taken constant and s must be attitudinally integrable. We return to this matter in sections 4.4 and 4.5, when taking the constant N^2 and constant N^2, ρ_0 approximations respectively.

4.3.4 The Steady State Response

At steady state, $t \gg T$, with $\frac{d}{dy} = 0$ and $s = s(x, z)$, our basic set in equations (4.2) and equation (4.20) respectively simplify to

$$u = w = s = 0, \quad fv = \frac{1}{\rho_0}\frac{\partial p}{\partial x}, \quad b = \frac{1}{\rho_0}\frac{\partial p}{\partial z}, \tag{4.21}$$

$$\frac{\partial v}{\partial x} + f\frac{\partial}{\partial z}\left(\frac{b}{N^2}\right) = \int_0^T f\frac{\partial}{\partial z}\left(\frac{s}{N^2}\right) dt. \tag{4.22}$$

It is now possible to construct an equation in pressure only, which may be solved by modal expansion methods. Equations (4.21) will then be used to develop corresponding expansions for the other fields, v and b and (eventually) equation 4.18 will be used to compute PV'.

4.3.5 Master Equation for Pressure

Using (4.21) and (4.22), we can construct our principal equation for pressure

$$\frac{1}{\rho_0}\frac{\partial^2 p}{\partial x^2} + f^2\frac{\partial}{\partial z}\left(\frac{1}{\rho_0 N^2}\frac{\partial p}{\partial z}\right) = f^2\int_0^T \frac{\partial}{\partial z}\left(\frac{s}{N^2}\right) dt = f^2 T\frac{\partial}{\partial z}\left(\frac{s}{N^2}\right). \tag{4.23}$$

Solving equation (4.23) will allow us to derive equations for b, v and, eventually, PV. Careful choice of the x-dependence in the buoyancy forcing function, s, will yield analytic expressions for these diagnostics. After the method used in Chapter 2, we employ a Sturm-Loiuville eigenfunction expansion (Arfken, 1966). Our approach contains subtle differences to which will shall draw attention, as necessary. Let $Z_n(z)$ be a Sturm-Liouville eigenfunction, subject to boundary condition $\left[\frac{dZ_n}{dz}\right]_{0,H} = 0$, discussed in section 4.3.6 shortly. Multiply equation 4.23 by $Z_n(z)$, integrate on z over the interval $[0, H]$

$$\frac{\partial^2}{\partial x^2}\int_0^H \frac{1}{\rho_0} p Z_n dz + f^2\int_0^H \frac{\partial}{\partial z}\left(\frac{1}{\rho_0 N^2}\frac{\partial p}{\partial z}\right) Z_n dz = f^2 T\int_0^H \frac{\partial}{\partial z}\left(\frac{s}{N^2}\right) Z_n dz. \tag{4.24}$$

Use parts twice in the second term on the left hand side. The boundary terms are eliminated by the pressure boundary condition $\left[\frac{dp}{dz}\right]_{0,H} = 0$ and the condition $\left[\frac{dZ_n}{dz}\right]_{0,H} = 0$. Use parts in the right hand side, where the condition $s(0) = s(H) = 0$ was used to eliminate the boundary term. We obtain

$$\frac{\partial^2}{\partial x^2}\int_0^H \frac{1}{\rho_0} p Z_n dz + f^2\int_0^H \frac{\partial}{\partial z}\left(\frac{1}{\rho_0 N^2}\frac{\partial Z_n}{\partial z}\right) p dz = f^2 T\int_0^H \frac{s}{N^2}\frac{dZ_n}{dz} dz. \tag{4.25}$$

4.3.6 Modal Expansion

It is necessary to generalise the expansions used in Chapters 2 and 3 and to base the vertical variation of the different field variables on different sets of orthogonal eigenfunctions. Having established general expansions, we shall later simplify our description. We shall again use a modal expansion, now based upon Sturm-Liouville eigenfunctions, Z_n, satisfying

$$\frac{d}{dz}\left(\frac{1}{\rho_0 N^2(z)}\frac{dZ_n}{dz}\right)+\frac{1}{\rho_0 c_n^2}Z_n=0, \quad \left[\frac{dZ_n}{dz}\right]_{0,H}=0, \tag{4.26}$$

which, in the notation of Arfken (1966) corresponds to a choice of the usual polynomial coefficients in the self-adjoint operator as $p_0(z)=\frac{1}{\rho_0 N^2(z)}$, $p_1(z)=p_0'(z)$, $p_2(z)=0$, weighting function $\frac{1}{\rho_0(z)}$ and eigenvalue $\lambda=\frac{1}{c_n^2}$.

The Z_n will, of course, have appropriate orthogonality properties. However, in contrast to the analogous procedure in Chapters 2, 3, we now require a second set of orthogonal eigenfunctions. Re-define

$$\phi_n(z)=\int_0^z\left(\frac{Z_n(z')}{\rho_0(z')}\right)dz', \iff \frac{d\phi_n}{dz}=\frac{Z_n(z)}{\rho_0(z)}, \tag{4.27}$$

then it is possible to prove the following properties

$$\begin{aligned}\frac{dZ_n}{dz}+\frac{\rho_0 N^2}{c_n^2}\phi_n &= 0, \\ \phi_n(0)=\phi_n(H) &= 0,\end{aligned} \tag{4.28}$$

with the second a consequence of the first, using assumed boundary condition 4.26. Equations 4.28 then underwrite the following orthonormalities

$$\begin{aligned}\int_0^H\frac{1}{\rho_0}Z_nZ_m dz &= H\delta_{nm}, \\ \int_0^H\rho_0\frac{d\phi_n}{dz}\frac{d\phi_m}{dz}dz &= H\delta_{nm}, \\ \int_0^H\frac{1}{\rho_0 N^2}\frac{dZ_n}{dz}\frac{dZ_m}{dz}dz &= \frac{H}{c_n^2}\delta_{nm}.\end{aligned} \tag{4.29}$$

The second of the equations 4.29 is immediate from the first, using equation 4.27. The third follows from the first after using integration by parts and the second of equations 4.28.

It will now be possible to expand response functions in terms of the Z_n and their derivative functions, $\frac{dZ_n}{dz}$. We now take the following expan-

sions, which rely on both sets of eigenfunctions, note

$$\begin{aligned} p(x,z) &= \sum_j p_j(x) Z_j(z), \\ s(x,z) &= \frac{1}{\rho_0(z)} F(x) \sum_j \sigma_j \frac{dZ_j}{dz}, \\ v(x,z) &= \frac{1}{\rho_0(z)} \sum_j v_j(x) Z_j(z), \\ b(x,z) &= \frac{1}{\rho_0(z)} \sum_j b_j(x) \frac{dZ_j}{dz}. \end{aligned} \tag{4.30}$$

When substituted into equation (4.25) we obtain from the above an ordinary differential equation

$$\frac{d^2}{dx^2} p_n(x) - \frac{f^2}{c_n^2} p_n(x) = -\frac{f^2 T \sigma_n}{c_n^2} F(x), \tag{4.31}$$

where $F(x)$ is the horizontal structure of the heating and we have used the orthonormality properties in equations 4.29.

Before continuing, we return to the chosen boundary conditions on functions $\frac{dZ_n}{dz}$. We see above that the buoyancy or potential temperature vertical variation is expanded in terms of $\frac{dZ_n}{dz}$. Hence, the boundary condition in equation 4.26 imposes the physical condition that the temperature and hence the heat flux vanishes at the boundaries of our system.

We return to the solution for b and v shortly, and continue by considering steady pressure, p. To determine the particular integral of ordinary differential equation (4.31), take a Fourier transform

$$\hat{p}_n(k) = \frac{f^2 T \sigma_n}{c_n^2} \left(\frac{1}{k^2 + \frac{f^2}{c_n^2}} \right) \hat{F}(k). \tag{4.32}$$

To proceed, we must assume a particular horizontal variation. We consider a horizontal variation of heating

$$F(x) = e^{-\frac{|x|}{L}} \iff \hat{F}(k) = \sqrt{\frac{2}{\pi}} \left(\frac{1/L}{k^2 + 1/L^2} \right). \tag{4.33}$$

This choice represents a good approximation of a heating due to mesoscale cumulonimbus activity and is mathematically tractable. We obtain

$$\hat{p}_n(k) = \sqrt{\frac{2}{\pi}} \frac{f^2 T \sigma_n}{L c_n^2} \left(\frac{1}{k^2 + f^2/c_n^2} \right) \left(\frac{1}{k^2 + 1/L^2} \right), \tag{4.34}$$

and upon using partial fractions in the right hand side

$$\begin{aligned}\hat{p}_n(k) = &+ \alpha_n\left(\sqrt{\frac{1}{2\pi}}\frac{1}{ik - f/c_n}\right) \\ &- \alpha_n\left(\sqrt{\frac{1}{2\pi}}\frac{1}{ik + f/c_n}\right) \\ &- \beta_n\left(\sqrt{\frac{1}{2\pi}}\frac{1}{ik - 1/L}\right) \\ &+ \beta_n\left(\sqrt{\frac{1}{2\pi}}\frac{1}{ik + 1/L}\right),\end{aligned} \tag{4.35}$$

where we have defined

$$\alpha_n \equiv \frac{fT\sigma_n c_n L}{(L^2 f^2 - c_n^2)}, \quad \beta_n \equiv \frac{f^2 T\sigma_n L^2}{(L^2 f^2 - c_n^2)}. \tag{4.36}$$

We can now perform an inverse Fourier transform. Using the result

$$\mathbf{F}\left(\Theta(\mp x)e^{\frac{\pm x}{L}}\right) = \frac{1}{\sqrt{2\pi}}\left(\frac{\pm 1}{ik \pm 1/L}\right), \tag{4.37}$$

equation 4.35 yields

$$\begin{aligned}p_n(x) = &- \alpha_n\left(\Theta(x)e^{-\frac{f}{c_n}x} + \Theta(-x)e^{\frac{f}{c_n}x}\right) \\ &+ \beta_n\left(\Theta(x)e^{-\frac{1}{L}x} + \Theta(-x)e^{\frac{1}{L}x}\right),\end{aligned} \tag{4.38}$$

which simplifies to give the particular integral

$$p_n(x) = -\alpha_n e^{-\frac{f}{c_n}|x|} + \beta_n e^{-\frac{1}{L}|x|}, \tag{4.39}$$

provided $L \neq c_n/f$, when $\alpha_n$and β_n become infinite. It remains to determine the heating coefficient σ_n, the $Z_n(z)$ and the eigenvalues, or wave speeds, c_n.

4.3.7 Model Stratification

We assume that the vertical variation of Buoyancy frequency is that used previously, in Chapters 2, 3

$$N(z) = (\Theta(z) - \Theta(z - H_t))N_t + \Theta(z - H_t)N_s, \tag{4.40}$$

and the corresponding variation of the base state of density, likewise, is

$$\rho_0(z) = (\Theta(z) - \Theta(z - H_t))\rho_s e^{-\frac{z}{D_t}} + \Theta(z - H_t)\rho_s e^{-\frac{H_t}{D_t}} e^{-\frac{(z-H_t)}{D_s}}. \tag{4.41}$$

4.3.8 Eigenfunctions

Let us derive appropriate eigenfunctions for the representation of the response fields. With our choice of density and buoyancy frequency variation, equation (4.27) now gives for the $Z_n(z)$ the ordinary differential equations

$$\begin{aligned} \frac{d^2 Z_n^{(1)}}{dz^2} + \frac{1}{D_t}\frac{dZ_n^{(1)}}{dz} + \frac{N_t^2}{c_n^2} Z_n^{(1)} &= 0, z < H_t \\ \frac{d^2 Z_n^{(2)}}{dz^2} + \frac{1}{D_s}\frac{dZ_n^{(2)}}{dz} + \frac{N_t^2}{c_n^2} Z_n^{(2)} &= 0, z \geq H_t. \end{aligned} \tag{4.42}$$

To match the surface and lid boundary conditions, we require oscillatory solutions. Hence, to ensure complex roots to the auxiliary equations we assume

$$\frac{N_t^2}{c_n^2} > \frac{1}{4D_t^2}, \quad \frac{N_s^2}{c_n^2} > \frac{1}{4D_s^2}, \tag{4.43}$$

and accordingly

$$\begin{aligned} Z_n^{(1)}(z) &= e^{-\frac{1}{2D_t}z}\left(A_n^{(1)}\cos\left(k_n^{(1)}z\right) + B_n^{(1)}\sin\left(k_n^{(1)}z\right)\right), z < H_t \\ Z_n^{(2)}(z) &= e^{-\frac{1}{2D_s}z}\left(A_n^{(2)}\cos\left(k_n^{(2)}z\right) + B_n^{(2)}\sin\left(k_n^{(2)}z\right)\right), z \geq H_t, \end{aligned} \tag{4.44}$$

where $A_n^{(1)}..B_n^{(2)}$ are integration constants. Applying boundary conditions

$$\left[\frac{dZ_n^{(1)}}{dz}\right]_{z=0} = 0, \quad \left[\frac{dZ_n^{(2)}}{dz}\right]_{z=H} = 0, \tag{4.45}$$

we obtain for the model troposphere, $z < H_t$

$$Z_n^{(1)}(z) = A_n^{(1)} e^{-\frac{1}{2D_t}z}\sin\left(k_n^{(1)}z + \phi_n^{(1)}\right), \tag{4.46}$$

and for the model stratosphere $z \geq H_t$

$$Z_n^{(2)}(z) = A_n^{(2)} e^{-\frac{1}{2D_s}z}\sin\left(k_n^{(2)}z + \phi_n^{(2)}\right), \tag{4.47}$$

where we have defined

$$\begin{aligned} \phi_n^{(1)} &= \tan^{-1}(2D_t k_n^{(1)}), \\ \phi_n^{(2)} &= \tan^{-1}\left(\frac{2D_s k_n^{(2)} - \tan(k_n^{(2)}H)}{1 + 2D_s k_n^{(2)}\tan(k_n^{(2)}H)}\right), \\ &= \tan^{-1}\left(\tan\left(\tan^{-1}\left(2D_s k_n^{(2)}\right) - k_n^{(2)}H\right)\right), \\ &= \tan^{-1}\left(2D_s k_n^{(2)}\right) - k_n^{(2)}H, \\ k_n^{(1)} &= \sqrt{\frac{N_t^2}{c_n^2} - \frac{1}{4D_t^2}}, \\ k_n^{(2)} &= \sqrt{\frac{N_s^2}{c_n^2} - \frac{1}{4D_s^2}}. \end{aligned} \tag{4.48}$$

For completeness, we give the corresponding functions $\frac{dZ_n}{dz}$, obtained by differentiation of the Z_n. Using the product rule and a number of trigonometric identities we obtain, for the model troposphere, $z < H_t$

$$\frac{dZ_n^{(1)}}{dz}(z) = -A_n^{(1)} \left(k_n^{(1)2} + \frac{1}{4D_t^2} \right)^{1/2} e^{-\frac{1}{2D_t}z} \sin\left(k_n^{(1)} z\right), \tag{4.49}$$

and for the model stratosphere $z \geq H_t$

$$\frac{dZ_n^{(2)}}{dz}(z) = A_n^{(2)} \left(k_n^{(2)2} + \frac{1}{4D_s^2} \right)^{1/2} e^{-\frac{1}{2D_s}z} \sin\left(k_n^{(2)}(H - z)\right). \tag{4.50}$$

4.3.9 Matching Conditions and Secular Equation

Let us consider the matching conditions on $Z_n^{(1)}$ and $Z_n^{(2)}$ to be applied at $z = H_t$. Considering that pressure is expanded in the Z_n, continuity of pressure at the tropopause imposes the condition

$$Z_n^{(1)}(H_t) = Z_n^{(2)}(H_t). \tag{4.51}$$

To derive a second condition, we integrate equation (4.26) over a narrow range of z spanning the tropopause

$$\left[\frac{1}{\rho_0 N^2} \frac{dZ_n}{dz} \right]_{H_t^-}^{H_t^+} + \frac{1}{c_n^2} \int_{H_t^-}^{H_t^+} \frac{1}{\rho_0} Z_n = 0. \tag{4.52}$$

As $H_t^- \to H_t^+$ the integral vanishes (its integrand is bounded, by assumption) and so, from the evaluated term in the above we have $\left[\frac{1}{\rho_0 N_t^2}\frac{dZ_n^{(1)}}{dz}\right]_{H_t^-} - \left[\frac{1}{\rho_0 N_s^2}\frac{dZ_n^{(2)}}{dz}\right]_{H_t^+} = 0$, which, since ρ_0 is continuous, yields a second condition

$$\left[\frac{1}{N_t^2} \frac{dZ_n^{(1)}}{dz} \right]_{H_t} = \left[\frac{1}{N_s^2} \frac{dZ_n^{(2)}}{dz} \right]_{H_t}. \tag{4.53}$$

From equation (4.51) we therefore obtain

$$A_n^{(1)} e^{-\frac{H_t}{2D_t}} \sin(k_n^{(1)} H_t + \phi_n^{(1)}) - A_n^{(2)} e^{-\frac{H_t}{2D_s}} \sin(k_n^{(2)} H_t + \phi_n^{(2))}) = 0. \tag{4.54}$$

In passing, we note that the above equation allows us to write normalisation constant $A_n^{(2)}$ in terms of $A_n^{(1)}$. From (4.53) (and the product rule) we also obtain a second, lengthier condition

$$\begin{aligned} &A_n^{(1)} N_s^2 e^{-\frac{H_t}{2D_t}} \left(k_n^{(1)} \cos(k_n^{(1)} H_t + \phi_n^{(1)}) - \frac{1}{2D_t} \sin(k_n^{(1)} H_t + \phi_n^{(1)}) \right) \\ &- A_n^{(2)} N_t^2 e^{-\frac{H_t}{2D_s}} \left(k_n^{(2)} \cos(k_n^{(2)} H_t + \phi_n^{(2)}) - \frac{1}{2D_s} \sin(k_n^{(2)} H_t + \phi_n^{(2)}) \right) = 0. \end{aligned} \tag{4.55}$$

For a non-trivial solution to equations (4.54) and (4.55) (for $A_n^{(1)}$ and $A_n^{(2)}$), the determinant of the matrix of coefficients must vanish. Therefore

$$N_t^2 \sin(k_n^{(1)} H_t + \phi_n^{(1)}) \left(k_n^{(2)} \cos(k_n^{(2)} H_t + \phi_n^{(2)}) - \frac{1}{2D_s} \sin(k_n^{(2)} H_t + \phi_n^{(2)}) \right)$$
$$-N_s^2 \sin(k_n^{(2)} H_t + \phi_n^{(2)}) \left(k_n^{(1)} \cos(k_n^{(1)} H_t + \phi_n^{(1)}) - \frac{1}{2D_t} \sin(k_n^{(1)} H_t + \phi_n^{(1)}) \right) = 0, \tag{4.56}$$

in which we have canceled an exponential factor $e^{-H_t\left(\frac{1}{2D_t}+\frac{1}{2D_s}\right)}$. After some algebra, equation (4.56) may be written as

$$-N_t^2 k_n^{(2)} \cot(k_n^{(2)} H_t + \phi_n^{(2)}) + N_s^2 k_n^{(1)} \cot(k_n^{(1)} H_t + \phi_n^{(1)}) = \frac{N_s^2 D_s - N_t^2 D_t}{2 D_t D_s}. \tag{4.57}$$

The above equation must be solved numerically for the c_n's. Recall, $k_n^{(1)} = \sqrt{\frac{N_t^2}{c_n^2} - \frac{1}{4D_t^2}}$, $k_n^{(2)} = \sqrt{\frac{N_s^2}{c_n^2} - \frac{1}{4D_s^2}}$. Equation 4.57 is the secular equation for the general stratification.

4.3.10 Normalization of the $Z_n(z)$

Given that the Z_n is defined piecewise, our assumed normalisation condition (equation 4.29 i.e. $\int_0^H \frac{1}{\rho_0} Z_n Z_m dz = H\delta_{nm}$) requires

$$A_n^{(1)2} \int_0^{H_t} \frac{1}{\rho_s e^{-\frac{z}{D_t}}} \left(e^{-\frac{z}{2D_t}} \sin(k_n^{(1)} z + \phi_n^{(1)}) \right)^2 dz \tag{4.58}$$
$$+ \quad A_n^{(2)2} \int_{H_t}^{H} \frac{1}{\rho_s e^{-\frac{H_t}{D_t}} e^{-\frac{(z-H_t)}{D_s}}} \left(e^{-\frac{z}{2D_s}} \sin(k_n^{(2)} z + \phi_n^{(2)}) \right)^2 dz = H.$$

Noting the exponentials in both integrands cancel, we obtain

$$\frac{A_n^{(1)2}}{\rho_s} \int_0^{H_t} \sin^2(k_n^{(1)} z + \phi_n^{(1)}) dz + \frac{A_n^{(2)2}}{\rho_s e^{\frac{H_t}{D_s} - \frac{H_t}{D_t}}} \int_{H_t}^{H} \sin^2(k_n^{(2)} z + \phi_n^{(2)}) dz = H. \tag{4.59}$$

Using condition 4.54 to eliminate $A_n^{(2)}$ now

$$\frac{A_n^{(1)2}}{\rho_s} \left(\int_0^{H_t} \sin^2(k_n^{(1)} z + \phi_n^{(1)}) dz + \frac{\sin^2(k_n^{(1)} H_t + \phi_n^{(1)})}{\sin^2(k_n^{(2)} H_t + \phi_n^{(2)})} \int_{H_t}^{H} \sin^2(k_n^{(2)} z + \phi_n^{(2)}) dz \right) = H,$$

which we choose to write as follows

$$\frac{A_n^{(1)2}}{\rho_s} \left(\int_0^{H_t} \sin^2(k_n^{(1)} z + \phi_n^{(1)}) dz + g^2 \int_{H_t}^{H} \sin^2(k_n^{(2)} z + \phi_n^{(2)}) dz \right) = H,$$

where

$$g \equiv \frac{\sin(k_n^{(1)} H_t + \phi_n^{(1)})}{\sin(k_n^{(2)} H_t + \phi_n^{(2)})}. \tag{4.60}$$

Performing the integrals using the trigonometric substitution $\sin^2(x) = \frac{1}{2}(1 - \cos(2x))$ we have

$$\begin{aligned}
A_n^{(1)} &= \sqrt{\frac{2\rho_s H}{I_1 + g^2 I_2}}, \\
I_1 &\equiv H_t - \frac{\sin(2k_n^{(1)} H_t + 2\phi_n^{(1)})}{2k_n^{(1)}} + \frac{\sin(2\phi_n^{(1)})}{2k_n^{(1)}}, \\
I_2 &\equiv (H - H_t) - \frac{\sin(2k_n^{(2)} H + 2\phi_n^{(2)})}{2k_n^{(2)}} + \frac{\sin(2k_n^{(2)} H_t + 2\phi_n^{(2)})}{2k_n^{(2)}}, \\
A_n^{(2)} &= g e^{\frac{H_t}{2}\left(\frac{1}{D_s} - \frac{1}{D_t}\right)} A_n^{(1)},
\end{aligned}$$

where, to find $A_n^{(2)}$ in terms of $A^{(1)}$, we have used equation 4.54.

4.3.11 Heating coefficients σ_n

Now let us consider the heating coefficients, σ_n. Using equation 4.30 we have

$$s(x,z) \equiv F(x) \sin\left(\frac{\pi z}{H_t}\right)(\Theta(z) - \Theta(z - H_t)) = F(x)\frac{1}{\rho_0}\sum_j \sigma_j \frac{dZ_j}{dz},$$

Cancel $F(x)$, multiply by function $\frac{dZ_n}{dz}$, multiply by $\frac{1}{N^2}$ and integrate $\int_0^H$ to obtain

$$\int_0^H \frac{1}{N^2} \sin\left(\frac{\pi z}{H_t}\right)\frac{dZ_n}{dz}dz = \sum_j \sigma_j \int_0^H \frac{1}{\rho_0 N^2}\frac{dZ_j}{dz}\frac{dZ_j}{dz}dz = \frac{H}{c_n^2}\sigma_n.$$

Substituting for Z_n and noting $N = N_t$ over the range of integration used here, we obtain

$$\sigma_n = \frac{c_n^2 A_n^{(1)}}{H N_t^2}\int_0^{H_t} \sin\left(\frac{\pi z}{H_t}\right)\frac{d}{dz}\left(e^{-\frac{z}{2D_t}}\sin(k_n^{(1)} z + \phi_n^{(1)})\right)dz.$$

Using parts and replacing all trig functions using complex exponentials, we have

$$\sigma_n = \frac{c_n^2 A_n^{(1)}}{2H N_t^2}\left(k_n^{(1)}\left(\Im(\omega_1) + \Im(\omega_2)\right) + \frac{1}{2D_t}\left(\Re(\omega_1) + \Re(\omega_2)\right)\right), \tag{4.61}$$

where

$$\omega_1 = \frac{\left(e^{ik_n^{(1)} H_t - \frac{H_t}{2D_t}} + 1\right)e^{i\phi_n^{(1)}}}{\left(-i\frac{\pi}{H_t} + ik_n^{(1)} - \frac{1}{2D_t}\right)}, \quad \omega_2 = \frac{\left(e^{-ik_n^{(1)} H_t - \frac{H_t}{2D_t}} + 1\right)e^{-i\phi_n^{(1)}}}{\left(-i\frac{\pi}{H_t} - ik_n^{(1)} - \frac{1}{2D_t}\right)}. \tag{4.62}$$

4.3.12 Solutions for b and v

Having determined the solution for the steady pressure response, $p(x,z)$, we return to equations 4.2 and 4.30. In the first (third) of equations (4.2) we substitute the following modal expansions respectively

$$\begin{aligned} v(x,z) &= \frac{1}{\rho_0}\sum_j v_j(x)Z_j(z), \\ b(x,z) &= \frac{1}{\rho_0}\sum_j b_j(x)\frac{dZ_j}{dz}. \end{aligned} \tag{4.63}$$

In the case of v, multiply the first of equations (4.2) by Z_n, substitute for p, integrate on z over $[0,H]$ and apply the orthonormality of the Z_ns to obtain

$$\int_0^H vZ_n(z')dz' = \frac{1}{f}\sum_j \frac{d}{dx}p_j(x)\int_0^H \frac{1}{\rho_0}Z_jZ_ndz' = \frac{H}{f}\frac{d}{dx}p_n(x), \tag{4.64}$$

and using the second of equations (4.63) in the left and side expression and the orthonormality property we have

$$Hv_n(x) = \frac{H}{f}\frac{d}{dx}p_n(x) \implies v_n(x) = \frac{1}{f}p_n'(x). \tag{4.65}$$

In the case of b, first multiply the third of equations (4.2) by $\frac{1}{N^2}\frac{dZ_n}{dz}$, integrate on z over $[0,H]$ and use integration by parts to obtain

$$\int_0^H \frac{1}{N^2}b\frac{dZ_n}{dz'}dz' = \left[p\frac{1}{\rho_0N^2}\frac{dZ_n}{dz'}\right]_0^H - \int_0^H p\frac{d}{dz'}\left(\frac{1}{\rho_0N^2}\frac{dZ_n}{dz'}\right)dz', \tag{4.66}$$

and using the boundary condition on Z_n to eliminate the evaluated term and transforming the integrand on the right hand side using (4.26) we have

$$\int_0^H \frac{1}{N^2}b\frac{dZ_n}{dz'}dz' = \frac{1}{c_n^2}\int_0^H \frac{1}{\rho_0}pZ_ndz'. \tag{4.67}$$

Finally, substituting the modal expansions for p and b and using orthonormality we have

$$\frac{H}{c_n^2}b_n(x) = \frac{1}{c_n^2}Hp_n(x) \implies b_n(x) = p_n(x). \tag{4.68}$$

4.3.13 Summary of Solutions for p, v, b

Before continuing, we now summarise the steady atmospheric adjustments for p, v and b, for an atmosphere with variable buoyancy frequency and base density, $N(z)$, $\rho_0(z)$, subject to a buoyancy forcing

$s(x,z,t) = \sin\left(\frac{\pi z}{H_t}\right)(\Theta(z) - \Theta(z-H_t))\, e^{-\frac{1}{L}|x|}$

$$\begin{aligned} p(x,z) &= \sum_j p_j(x) Z_j(z), \\ v(x,z) &= \frac{1}{\rho_0(z) f} \sum_j p_j'(x) Z_j(z), \\ b(x,z) &= \frac{1}{\rho_0(z)} \sum_j p_j(x) \frac{dZ_j}{dz}, \end{aligned} \tag{4.69}$$

where $p_j(x)$ is (from equation 4.39)

$$p_j(x) = -\left(\frac{fT\sigma_j c_j L}{(L^2 f^2 - c_j^2)}\right) e^{-\frac{f}{c_j}|x|} + \left(\frac{f^2 T \sigma_j L^2}{(L^2 f^2 - c_j^2)}\right) e^{-\frac{1}{L}|x|}, \tag{4.70}$$

and heating co-efficient σ_j is given in equation 4.61, above. Above, eigenfunctions $Z_j(z)$ and $\frac{dZ_j}{dz}$ are given in section 4.3.8. Recall, the buoyancy forcing function was expanded as

$$s(x,z) = \frac{e^{-\frac{1}{L}|x|}}{\rho_0} \sum_j \sigma_j \frac{dZ_j}{dz}. \tag{4.71}$$

4.4 Constant N Approximation

Let us simplify by setting $N_t = N_s$. In doing so, the mathematics is simplified. The condition 4.53 is removed, along with the need to partition the solutions and the need to seek a numerical solution for the wave speeds, c_n, thereby producing a fully analytical model, as we shall shortly show. Following this simplification, it will be possible to consider non-dimensionalised, trapped solutions and to examine key limits of our model analytically to provide a benchmark for the discussions of section 4.6.

For the remainder of this section, the base state of density is determined by a single scale height

$$\rho_0(z) = \rho_s e^{-\frac{z}{D_t}}, \quad 0 < z < H, \tag{4.72}$$

but the lid will still be placed at a large height aloft, to allow for the effects of radiation.

By setting $N_t = N_s$ the physics is also simplified: as we showed in Chapter 2, radiative losses are a maximum for $N_t = N_s$.

4.4.1 Simplified Modal Expansion

The vertical variation in our modal expansion (the $Z_n(z)$) now satisfies a single equation over the whole vertical domain

$$\frac{d^2 Z_n}{dz^2} + \frac{1}{D_t}\frac{dZ_n}{dz} + \frac{N_t^2}{c_n^2} Z_n = 0, \quad z < H. \tag{4.73}$$

To match the surface and lid boundary conditions we still require oscillatory solutions, hence, to ensure complex roots to the auxiliary equation of the above ordinary differential equation, we again assume $\frac{N_t^2}{c_n} > \frac{1}{4D_t^2}$ and accordingly

$$Z_n(z) = e^{-\frac{1}{2D_t}z}\left(A'_n \cos\left(k_n z\right) + B'_n \sin\left(k_n z\right)\right), \quad k_n \equiv \sqrt{\frac{N_t^2}{c_n^2} - \frac{1}{4D_t^2}} \in R^+. \tag{4.74}$$

Note, no superscript now appears on k_n. Here A'_n, B'_n are integration constants. We choose to re-express $Z_n(z)$ as follows

$$Z_n(z) = A_n e^{-\frac{1}{2D_t}z} \cos\left(k_n z + \phi_n\right). \tag{4.75}$$

$A_n \neq A'_n$ and phase angle ϕ will be determined shortly. Hence, we can now obtain for our second set of functions, the following

$$\begin{aligned}\frac{dZ_n}{dz} &= A_n e^{-\frac{1}{2D_t}z}\left(-k_n \sin\left(k_n z + \phi_n\right) - \frac{1}{2D_t}\cos(k_n z + \phi_n)\right), \\ &= -A_n e^{-\frac{1}{2D_t}z}\sqrt{k_n^2 + \frac{1}{4D_t^2}}\sin\left(k_n z + \phi_n + \theta_n\right), \\ &= -A_n \frac{N_t}{c_n} e^{-\frac{1}{2D_t}z}\sin\left(k_n z + \phi_n + \theta_n\right),\end{aligned} \tag{4.76}$$

where

$$\theta_n \equiv \tan^{-1}\left(\frac{1}{2D_t k_n}\right), \tag{4.77}$$

and we have used the definition of the k_n in the third line. Applying boundary conditions

$$\left[\frac{dZ_n}{dz}\right]_{z=0} = \left[\frac{dZ_n}{dz}\right]_{z=H} = 0, \tag{4.78}$$

we straightforwardly obtain

$$\phi_n = -\theta_n = -\tan^{-1}\left(\frac{1}{2D_t k_n}\right), \qquad k_n = \frac{n\pi}{H}. \tag{4.79}$$

We can now summarise the full modal solution in the limit $N_t = N_s$

$$Z_n(z) = A_n e^{-\frac{1}{2D_t}z}\cos\left(k_n^{(1)} z - \theta_n\right), \tag{4.80}$$

$$\begin{aligned}\frac{dZ_n}{dz} &= -A_n e^{-\frac{1}{2D_t}z}\sin\left(k_n^{(1)} z\right), \\ k_n &= \frac{n\pi}{H}, \\ \theta_n &\equiv \tan^{-1}\left(\frac{1}{2D_t k_n}\right).\end{aligned} \tag{4.81}$$

It is now possible to write-down an analytical expression for the wave-speeds, c_n from the definition of k_n, which would otherwise require numerical solution of a secular equation derived from the matching condition. From equations 4.79 and 4.80 it is immediate that

$$\frac{n^2\pi^2}{H^2} = \frac{N_t^2}{c_n^2} - \frac{1}{4D_t^2} \iff c_n = \left(\frac{n^2\pi^2}{H^2N_t^2} + \frac{1}{4D_t^2N_t^2}\right)^{-1/2}. \tag{4.82}$$

The normalisation coefficient in this case A_n may be obtained from the orthogonality condition $\int_0^H \frac{1}{\rho_0} Z_n Z_m dz = H\delta_{nm}$ as follows. Exponentials cancel in the integrand to leave

$$\frac{A_n^2}{\rho_s}\int_0^H \cos^2\left(k_n^{(1)}z - \theta_n\right) dz = H, \tag{4.83}$$

and using the trigonometric identity $\cos(2x) = (2\cos^2(x) - 1)$, properties of trig functions and some straightforward algebra we easily obtain

$$A_n = \sqrt{2\rho_s}, \quad \forall n. \tag{4.84}$$

The heating expansion coefficient is again given by equation 4.61, with the simple replacement $A_n^{(1)} \to A_n$.

The revised expressions for eigenfunctions $Z_n(n)$ and $\frac{dZ_n}{dz}$ given in this sub-section may now be used, together with exact expressions for the wave-speeds, c_n, to evaluate modal solutions for the p, v and b adjustment. The PV adjustment warrants a little additional consideration.

4.4.2 Simplified PV Adjustment

Let us now assume constant N (but still retain ρ_0 variable) in equations 4.18 and consider the steady state of our system's PV adjustment, long after the application of a heat pulse of duration T. Hence, we take $s = u = w = 0$ and simplify the first of equations 4.18 to $\frac{\rho_0 g}{\theta_0 N^2}(PV') = \frac{\partial v}{\partial x} + \frac{f}{N^2}\frac{\partial b}{\partial z} + 2\frac{f}{g}b$, in which we may now use equation 4.20 (with N^2 taken constant) to simplify the first term on the right hand side. This yields

$$\begin{aligned} \frac{g\rho_0}{\theta_0 N^2}(PV') &= \frac{fT}{N^2}\frac{\partial s}{\partial z} + 2\frac{f}{g}b, \\ \frac{g\rho_0}{\theta_0 N^2}(PV'_B) &= \frac{fT}{N^2}\frac{\partial s}{\partial z}. \end{aligned} \tag{4.85}$$

Clearly, in the constant N limit, we need not seek a modal expansion for PV'- one can substitute for an assumed s (differentiated of course) and substitute for the b solution determined above. Put another way, equation 4.85 gives the scaled potential vorticity adjustment, at steady state, directly from the prescribed heating and b adjustment.

We observe the heating (and variables) in the first term of the right hand side of equation (4.85) is defined i.e. fixed, so changes to the PV

adjustment associated with system lid height, H_L, will arise only from the second term on the right hand side, through changes to the b solution. That term is absent in the Boussinesq approximation. To allow for PV adjustment with H_L, we therefore consider PV' in the sequel.

4.5 Constant N, ρ_0 Approximation

Within the constant N, constant ρ_0 approximation it will be possible to exact solutions for the trapped case, $H = H_t$, which exhibit the scaling of the solution with Rossby radius of deformation (see section 4.5.1).

If we return to section 4.3.4, in the present approximation equations 4.21 and 4.22 simplify to the following

$$u = w = s = 0, \quad fv = \frac{\partial \phi}{\partial x}, \quad b = \frac{\partial \phi}{\partial z}, \quad \phi \equiv \left(\frac{p}{\rho_0}\right), \tag{4.86}$$

$$N^2 \frac{\partial v}{\partial x} + f\frac{\partial b}{\partial z} = f\frac{\partial s_{tot}}{\partial z}, \quad s_{tot} \equiv \int_0^T s dt, \tag{4.87}$$

from which is straightforward to obtain a simplified equation for ϕ

$$\frac{\partial^2 \phi}{\partial x^2} + \frac{f^2}{N^2}\frac{\partial^2 \phi}{\partial z^2} = \frac{f^2}{N^2}\frac{\partial s_{tot}}{\partial z}. \tag{4.88}$$

4.5.1 Trapped Solutions

It is beneficial, now, to write the above in terms of dimensionless variables. This will allow us to investigate the role of length scales in limiting cases, in this section. These cases will provide guidance in our work in section 4.6, next.

We consider the gravest mode of heating here. Our total heat input is supposed to have magnitude $\bar{s}_{tot}$. Recall, the characteristic width of the diabatic heating profile is L and it extends to the tropopause, which is now coincident with the lid, implying a suitable vertical scale of $H = H_t$. Define dimensionless variables

$$\hat{x} = \frac{x}{L}, \quad \hat{z} = \frac{z}{H}, \quad \hat{\phi} = \frac{\phi}{H\bar{s}_{tot}}, \quad \hat{b} = \frac{b}{\bar{s}_{tot}}, \quad \hat{v} = \frac{Lfv}{H\bar{s}_{tot}}, \quad \hat{s}_{tot} = \frac{s_{tot}}{\bar{s}_{tot}}, \tag{4.89}$$

whereupon equation 4.88, for $\hat{\phi}$, may be written in dimensionless form

$$\frac{\partial^2 \hat{\phi}}{\partial \hat{x}^2} + \epsilon^2 \frac{\partial^2 \hat{\phi}}{\partial \hat{z}^2} = \epsilon^2 \frac{\partial \hat{s}_{tot}}{\partial \hat{z}}, \tag{4.90}$$

where we have defined dimensionless group

$$\epsilon \equiv \frac{fL}{NH_t}. \tag{4.91}$$

We also have the following, which may be used to determine $\hat{b}$ and $\hat{v}$

$$\hat{b} = \frac{\partial \hat{\phi}}{\partial \hat{z}}, \quad \hat{v} = \frac{\partial \hat{\phi}}{\partial \hat{x}}. \tag{4.92}$$

To estimate the value of parameter ϵ initially, we use the following data: $f \sim 10^{-4}\text{s}^{-1}$, $H \sim 5\text{km}$, $N = 0.01\text{s}^{-1}$, $L \sim 10\text{km}$, whereupon we find $\epsilon \approx 0.02$.

Formally, any constant horizontal scaling length could be used to achieve the non-dimensionalisations considered here. However, in the present problem, L, is the only physical scale available for the horizontal variation. Hence, dimensionless parameter ϵ is unambiguously representative of the horizontal scales: importantly, it corresponds to the physical length scale of the heating expressed as a fraction of the Rossby radius of deformation

$$\epsilon = \frac{fL}{NH_t} = \frac{L}{R_o}, \quad R_o \equiv \frac{NH_t}{f}. \tag{4.93}$$

Note that our non-dimensionalisation parameter ϵ, above, may also be identified with the Burger number, Bu, for a system in which the scaling length of the horizontal motion is L

$$\epsilon^{-1} = \frac{R_o}{L} \equiv Bu. \tag{4.94}$$

In general, Bu expresses the ratio between density stratification in the vertical and processes affected by terrestrial rotation in the horizontal. $Bu \sim$O(1) for many atmospheric phenomena, indicating a balance between stratification and rotation in governing vertical and other motions in the fluid- in the present case, motion forced by heating. In the sequel, we shall consider a larger range of ϵ. We return to this matter in section 4.5.3.

Continuing, we consider domain $0 < \hat{z} < \pi$ with an assumed diabatic heating which spans the vertical domain

$$\hat{s}_{tot}(\hat{x}, \hat{z}) \equiv X(\hat{x}) \sin(\hat{z}). \tag{4.95}$$

We seek a separable solution to equation 4.90 for $\hat{\phi}$

$$\hat{\phi}(\hat{x}, \hat{z}) = \Phi(\hat{x}) \cos(\hat{z}). \tag{4.96}$$

Fields $\hat{b}$ and $\hat{v}$ may be determined as follows:

$$\hat{b}(\hat{x}, \hat{z}) = -\Phi(\hat{x}) \sin(\hat{z}), \quad \hat{v}(\hat{x}, \hat{z}) = \frac{\partial \Phi}{\partial \hat{x}} \cos(\hat{z}), \tag{4.97}$$

once Φ has been determined from ODE equation 4.90

$$\frac{d^2\Phi(\hat{x})}{d\hat{x}^2} - \epsilon^2 \Phi(\hat{x}) = \epsilon^2 X(\hat{x}). \tag{4.98}$$

We proceed, to consider particular cases for horizontal heating distribution, $X(\hat{x})$.

4.5.2 Trapped Solutions for Narrow Heating: the Green Function

In this subsection we consider the limiting case heating which is formally narrow

$$X(\hat{x}) = \delta(\hat{x}), \tag{4.99}$$

corresponding to a horizontal distribution of heating which is highly localized relative to the lid height i.e. $\epsilon = \frac{fL}{NH_t} \to 0$ i.e. we assume a very small value of L. By definition, the solution to equation 4.98, $\Phi(\hat{x})$, is then the Green function.

Take the Fourier transform of equation 4.98 to obtain

$$(-ik)^2\hat{\Phi}(k) - \epsilon^2\hat{\Phi}(k) = \frac{\epsilon^2}{\sqrt{2\pi}}. \tag{4.100}$$

Here we have used the Fourier transform of derivatives theorem and the fact that the Fourier transform of $\delta(\hat{x})$ is $\frac{1}{\sqrt{2\pi}}\int_{-\infty}^{\infty}\delta(\hat{x})e^{ik\hat{x}}d\hat{x} = \frac{1}{\sqrt{2\pi}}e^0 = \frac{1}{\sqrt{2\pi}}$. Solving

$$\hat{\Phi}(k) = -\frac{\epsilon^2}{\sqrt{2\pi}}.\frac{1}{k^2+\epsilon^2} \iff \Phi(\hat{x}) = -\frac{\epsilon^2}{2\pi}\int_{-\infty}^{\infty}\frac{e^{-ik\hat{x}}}{k^2+\epsilon^2}dk. \tag{4.101}$$

Above, we have simply taken an inverse Fourier transform, which is to be performed using the calculus of residues (Arfken, 1966). Let us suppose $\hat{x} > 0$, then employ a clockwise contour (winding number -1) which returns in the lower half complex plane, to ensure integrand factor $e^{-ik\hat{x}}$ approaches zero. The chosen contour encircles the first order pole located at $k = -i\epsilon$ and we have $\Phi(\hat{x}) = -\frac{\epsilon^2}{2\pi}\int_{-\infty}^{\infty}\frac{e^{-ik\hat{x}}}{(k-i\epsilon)(k+i\epsilon)}dk = (-1)\times\left(-\frac{\epsilon^2}{2\pi}2\pi i\text{Res}(f(k),-i\epsilon)\right)$ where $f(k) = \frac{e^{-ik\hat{x}}}{(k-i\epsilon)(k+i\epsilon)}$, $k\in\mathbb{C}$ and we have multiplied by the winding number. Accordingly, we have $\Phi(\hat{x}) = \epsilon^2 i\lim_{k\to(-i\epsilon)}\left((k+i\epsilon)\frac{e^{-ik\hat{x}}}{(k-i\epsilon)(k+i\epsilon)}\right) = \left[\frac{i\epsilon^2e^{-ik\hat{x}}}{(k-i\epsilon)}\right]_{k=-i\epsilon} = -\frac{\epsilon}{2}e^{-\epsilon\hat{x}}$, for $\hat{x} > 0$ recall. Adapting the above approach to the case of $\hat{x} < 0$, we obtain $\Phi(\hat{x}) = -\frac{\epsilon}{2}e^{\epsilon\hat{x}}$. Hence, for any $\hat{x}$ we have

$$\Phi(\hat{x}) = -\frac{\epsilon}{2}e^{-\epsilon|\hat{x}|}, \tag{4.102}$$

which allows us to write the Green function for the trapped system as

$$G(\hat{x},\hat{x_0}) = -\frac{\epsilon}{2}e^{-\epsilon|\hat{x}-\hat{x}_0|}. \tag{4.103}$$

Parameter ϵ emerges as the parameter of the Green function. Shortly we will use it to develop other responses for the trapped case, corresponding to de-localised heating. For the case of $X(\hat{x}) = \delta(\hat{x})$ then, we find the

following solution to the trapped case, for small ϵ

$$\begin{aligned}\hat{\phi}(\hat{x},\hat{z}) &= -\frac{1}{2}\epsilon e^{-\epsilon|\hat{x}|}\cos(\hat{z}), \\ \hat{b}(\hat{x},\hat{z}) &= \frac{1}{2}\epsilon e^{-\epsilon|\hat{x}|}\sin(\hat{z}), \\ \hat{v}(\hat{x},\hat{z}) &= \frac{1}{2}\epsilon^2 e^{-\epsilon|\hat{x}|}\left(\Theta(\hat{x})-\Theta(\hat{x})\right)\cos(\hat{z}).\end{aligned} \tag{4.104}$$

From equations 4.104 it is clear that the only length scale characterising the non-dimensional response of all field variables is the non-dimensional length scale ϵ^{-1} (which is large, given ϵ is small). Recalling that physical length is related to non-dimensional length in our analysis by $\hat{x} = \frac{x}{L}$ we find that the corresponding physical scale of the responses to a very narrow heating is given by

$$L\hat{x} \to L\epsilon^{-1} = \frac{L}{\left(\frac{fL}{NH_t}\right)} = \frac{NH_t}{f}, \tag{4.105}$$

which is the Rossby radius, $R_o \equiv \frac{NH_t}{f}$.

In the case of narrow heating, as $L \to 0$ with $f \neq 0$, it follows $\epsilon \to 0$. From above, $\epsilon \to 0$ corresponds to the physical length scale of the trapped response tending to the Rossby radius, R_o. Put another way, for a steady, trapped, rotating solution, with any $f \neq 0$, as $\epsilon \to 0$, the physical scale of the response is R_o, irrespective of the value of f i.e. latitudinal location. Note that $\epsilon \to 0$ also when $f \to 0$ i.e. as the effects of rotation become negligible. In this limit, the length scale of the response is still, formally R_o, notwithstanding that fact that R_o diverges.

4.5.3 Trapped Solutions for Distributed Heating

In this subsection we consider a horizontally distributed heating with

$$X(\hat{x}) = \frac{1}{2}e^{-|\hat{x}|}. \tag{4.106}$$

Here the factor $\frac{1}{2}$ is included to ensure the domain average of X is unity.

Using the system Greens function developed above (equation 4.103), the solution to equation 4.98 for $X(\hat{x}) = e^{-|\hat{x}|}$ may be obtained as

$$\Phi(x) = \frac{1}{2}\int_{\infty}^{-\infty} e^{-|\hat{x}_0|}G(\hat{x},\hat{x}_0)d\hat{x}_0 = -\frac{\epsilon}{4}\int_{\infty}^{-\infty} e^{-|\hat{x}_0|}e^{-\epsilon|\hat{x}-\hat{x}_0|}d\hat{x}_0. \tag{4.107}$$

For definiteness, take $\hat{x} > 0$, then decompose the domain of integration

in the above in accord with the definition of the modulus function

$$\begin{aligned}\Phi(x) &= \left(-\frac{\epsilon}{4}\right)\int_{-\infty}^{0} e^{\hat{x}_0}e^{\epsilon(\hat{x}_0-\hat{x})}d\hat{x}_0 \\ &+ \left(-\frac{\epsilon}{4}\right)\int_{0}^{x} e^{-\hat{x}_0}e^{-\epsilon(\hat{x}-\hat{x}_0)}d\hat{x}_0 \\ &+ \left(-\frac{\epsilon}{4}\right)\int_{x}^{\infty} e^{-\hat{x}_0}e^{-\epsilon(\hat{x}_0-\hat{x})}d\hat{x}_0.\end{aligned} \tag{4.108}$$

Clearly, each integral in the above is straightforward to perform. After substituting limits and some algebra, we obtain $\Phi(\hat{x}) = \frac{\epsilon^2 e^{-\hat{x}} - \epsilon e^{-\epsilon\hat{x}}}{2(1-\epsilon^2)}$, for $\hat{x} > 0$, recall. After performing an equivalent calculation for $\hat{x} < 0$ we find for $X(\hat{x}) = \frac{1}{2}e^{-|\hat{x}|}$

$$\Phi(\hat{x}) = \frac{\epsilon^2 e^{-|\hat{x}|} - \epsilon e^{-\epsilon|\hat{x}|}}{2(1-\epsilon^2)}, \tag{4.109}$$

which is just the difference between two monotonic decays. For the case of $X(\hat{x}) = e^{-\hat{x}}$ then, we find the following solution, still for the trapped case

$$\begin{aligned}\hat{\phi}(\hat{x},\hat{z}) &= \left(\frac{\epsilon^2 e^{-|\hat{x}|} - \epsilon e^{-\epsilon|\hat{x}|}}{2(1-\epsilon^2)}\right)\cos(\hat{z}), \\ \hat{b}(\hat{x},\hat{z}) &= \left(\frac{\epsilon e^{-\epsilon|\hat{x}|} - \epsilon^2 e^{-|\hat{x}|}}{2(1-\epsilon^2)}\right)\sin(\hat{z}), \\ \hat{v}(\hat{x},\hat{z}) &= \epsilon^2\left(\frac{e^{-\epsilon|\hat{x}|} - e^{-|\hat{x}|}}{2(1-\epsilon^2)}\right)(\Theta(\hat{x}) - \Theta(\hat{x}))\cos(\hat{z}).\end{aligned} \tag{4.110}$$

Evidently, the above solution has two components, the first term is determined by the assumed length scale of the heating and the second is again determined by the Rossby radius. Note that for ϵ small, the above returns to the Green function. The solution in equation 4.109 provides us with a useful benchmark, as we shall see in the next section.

As in the case of narrow heating, is informative to examine the horizontal scale of the distributed heating solution in equation 4.109. Introduce $\hat{l}$, where, $\hat{l}$ is a non-dimensional length scale

$$\hat{l} = \frac{l}{L}. \tag{4.111}$$

$\Phi(\hat{x})$ is stationary at $\hat{x} = 0$, with value $\frac{-\epsilon}{2(1+\epsilon)}$, with $\frac{d^2\Phi}{d\hat{x}^2} = \frac{\epsilon^2}{2(1-\epsilon)}$, indicating a minimum (maximum) for $\epsilon < 1$ ($\epsilon > 1$). For $\epsilon < 1$, we therefore evaluate $\hat{l}$ from the e-folding length of Φ by solving the following

$$\Phi(\hat{l}) = \frac{\Phi(0)}{e} = -\frac{\epsilon}{2(1+\epsilon)e}. \tag{4.112}$$

Using equation 4.109, we obtain, after some algebra, the following equation to be solved for characteristic horizontal scale $\hat{l}$

$$\epsilon e^{-\hat{l}} - e^{-\epsilon\hat{l}} + \frac{(1-\epsilon)}{e} = 0. \tag{4.113}$$

Equation 4.113 requires a numerical solution (see below) however, its limiting solutions are obtained by straightforward analysis. We have $\epsilon e^{-\hat{l}} \approx \frac{\epsilon}{e}$, $\epsilon \gg 1$ and $e^{-\epsilon\hat{l}} \approx \frac{1}{e}$, $\epsilon \ll 1$, hence

$$\begin{aligned} \epsilon \ll 1 \quad &\Longrightarrow \quad \hat{l} \to \epsilon^{-1} \\ \epsilon \gg 1 \quad &\Longrightarrow \quad \hat{l} \to 1. \end{aligned} \tag{4.114}$$

In terms of the physical response length scale, $l = \hat{l}L$, the above limits are respectively equivalent to the following

$$\begin{aligned} L \ll R_o \quad &\Longrightarrow \quad l \to R_o \\ L \gg R_o \quad &\Longrightarrow \quad l \to L, \end{aligned} \tag{4.115}$$

Consider the scaling properties of our trapped solution $\Phi(\hat{x})$, obtained from equation 4.109. A characteristic length scale $\hat{l}$ is obtained from a numerical solution of equation 4.113 as follows. Observe that there is no solution for $\epsilon = 1$ and the $\hat{l}$-dependant terms in equation 4.113 reduce monotonically as $\hat{l}$ increases. Therefore, there is at most one root of equation 4.113, for any value of $\epsilon \neq 1$. Thus, the bisector method was used straightforwardly to obtain solutions for $\hat{l}$ over a range of ϵ such that $\epsilon^{-1} \in [0, 20]$ (which allows us to display the properties of $\hat{l}$ derived from equation 4.113). This data is plotted in figure 4.5. It represents the limiting case of data from the non-trapped solutions, to be considered in the next section. These non-trapped solutions will characterise the horizontal length scale of the response for systems with increased lid heights, H, with H_t, L (and N) all fixed. The range of ϵ considered in figure 4.5 was chosen as follows. $\epsilon = 0$ arises when $f = 0$, or when heating is very narrow relative to lid height. Terrestrially, $\max(f) \approx 2 \times 2\pi/24/60/60 \sin(\pi/2) = 1.45 \times 10^{-4}\text{rads}^{-1}$, $N = 0.01\text{s}^{-1}$, and we assume $L/H \leq 100$, hence $\max(\epsilon) = 1.45$ and, for Earth, we have $\epsilon \in [0, 1.45]$ or $\epsilon^{-1} \in [0.7, \infty)$. However, for both lidded or trapped solutions and un-lidded, non-trapped solutions of the next section, a range of ϵ such that $\epsilon^{-1} \in (0, 20]$ is seen to be sufficient, from figure 4.5.

4.5.4 Non-trapped Solutions

We continue to examine the limits of our steady-state model, now for a solution with a lid raised high aloft. In particular, in this section we are concerned with the effect of lid-height on the response's characteristic horizontal scale, $\hat{l}$. With the lid raised aloft, it is not possible to obtain an equivalent to equation 4.113, which applies to the trapped case and the description of vertical stratification is also complicated by the presence of

two parameters- H_t and H. Hence we will need temporarily to revise non-dimensional parameter ϵ. However, informative comparisons between the behaviour of trapped and non-trapped horizontal scales will be possible.

We proceed by defining an appropriate horizontal scale, $\hat{l}$, for the non-trapped case, then examining limits of the non-trapped model analytically and then presenting data for a non-trapped $\hat{l}$ as a function of parameter ϵ. This will facilitate comparison with the equivalent trapped data. See figure 4.5.

Using equations 4.69, 4.70 we obtain for the pressure response in the non-trapped regime

$$p(x,z) = -\sum_j \left(\frac{fT\sigma_j c_j L}{L^2 f^2 - c_j^2}\right) e^{-\frac{f}{c_j}|x|} Z_j(z) + \sum_j \left(\frac{f^2 T\sigma_j L^2}{L^2 f^2 - c_j^2}\right) e^{-\frac{1}{L}|x|} Z_j(z). \tag{4.116}$$

The limit of constant ρ_0 corresponds to $D_t \to \infty$ hence

$$c_n \to \frac{HN_t}{n\pi}, \tag{4.117}$$

and equation 4.116 therefore becomes, after some algebra

$$\begin{aligned} p(x,z) = \; & - \; \delta T \sum_j \left(\frac{j\pi}{\delta^2 j^2\pi^2 - 1}\right)\left(\frac{\sigma_j}{j\pi}\right) e^{-j\pi\delta\frac{|x|}{L}} Z_j(z) \\ & + \; \delta^2 T e^{-\frac{|x|}{L}} \sum_j \left(\frac{j^2\pi^2}{\delta^2 j^2\pi^2 - 1}\right) \sigma_j Z_j(z). \end{aligned} \tag{4.118}$$

Since $H \neq H_t$ in a non-trapped case, we re-introduce a dimensionless parameter to replace ϵ as follows

$$\delta \equiv \frac{fL}{N_t H} = \frac{H_t}{H}\frac{\epsilon}{\pi}, \tag{4.119}$$

which depends on two parameters of stratification- H_t and H. With this revision, scale parameter δ remains an effective Bu- it still characterises relative variation in f and stratification. The factor $\frac{1}{\pi}$ above is required because scale parameter ϵ is defined relative to a vertical domain $\hat{z} \in [0,\pi]$, corresponding to $z \in [0, \pi H_t]$ but the domain of equation 4.118 is $z \in [0, H_t]$. Note, we continue to consider the gravest mode of heating, so the tropopause location is still H_t.

Throughout this section we choose to define a horizontal scale for the steady response in the non-trapped case by sampling $p(x,z)$ in equation 4.118 at constant altitude z_0 where $z_0 \equiv 0.8 \times H_t$. At this location aloft, the variation produced by the two terms in the right hand side of equation 4.118 is straightforward over a wide range of parameter ϵ (see figure 4.1 and the discussions below). To be consistent with the trapped case, the e-folding length of the pressure response at z_0 is taken to define $\hat{l}$ for the non-trapped case: that is

$$\hat{l} : p(\hat{l}, z_0) = \frac{\max\left(|p(x,z_0)|\right)}{e}, \quad z_0 = 0.8 \times H_t. \tag{4.120}$$

Note, the maximum or minimum value of $p(x, z_0)$ is seen to always occur very close to the origin.

The overall x-variation in 4.118 allows only one solution for $\hat{l}$, defined in equation 4.120: see figure 4.1. Hence, solutions for $\hat{l}$ were obtained straightforwardly, using a bisector method on a horizontal mesh for a range of ϵ i.e. Coriolis' parameter f values chosen so as to show the properties of the scaling of $\hat{l}$ with ϵ (not necessarily terrestrial meteorology). We note that it is convenient to set the x-mesh horizontal spacing with interval $\Delta x \sim \frac{1}{f}$.

Before considering numerical data for the variation of $\hat{l}$ with ϵ, we pause to consider what can be deduced about it by analysis. We can identify dominant terms in equation 4.118 without writing heating expansion coefficients, σ_j, in terms of δ (since both terms would be affected by the substitution in the same way). We therefore proceed to examine limits of the pressure response.

For $\delta \gg 1$ (un-physically large f for Earth, note) the approximate response, obtained from the senior term in δ from equation 4.118 above, may be written

$$p(x, z) \approx \delta^2 T e^{-\frac{|x|}{L}} G(z), \quad G(z) \equiv \sum_j \left(\frac{j^2\pi^2}{\delta^2 j^2 \pi^2 - 1} \right) \sigma_j Z_j(z). \quad (4.121)$$

From the horizontal variation in the above we recognise an e-folding dimensionless distance $\hat{l} = 1$. This agrees with the limit obtained in the trapped case, equation 4.114. Of course, the above expression for p only provides the value of the ordinal intercept (of unity) in the plot of characteristic scale, $\hat{l}$ as a function of $\frac{1}{\epsilon}$, figure 4.5, with all other points shown there being obtained numerically, as previously discussed.

For $\delta \ll 1$ the approximate pressure response from equation 4.118 may be written

$$p(x, z) \approx -\delta T \sum_j \sigma_j e^{-j\pi\delta\frac{|x|}{L}} Z_j(z). \quad (4.122)$$

For small $|x|$, the exponential factors disappear and for the response close to the origin we may write

$$\lim_{x\to 0} (p(x, z)) = -\delta T \int s(x, z) dz, \quad (4.123)$$

whereas for large $|x|$ the horizontal variation, modelled on j^{th} series term $e^{-j\pi\delta\frac{|x|}{L}}$ has a dimensionless e-folding length $\hat{l}_j = \frac{1}{j\pi\delta} = \frac{H}{jH_t\epsilon}$, which decreases with increasing j. For small ϵ therefore, an overall e-folding length might be seen, from equation 4.122, as an arithmetic mean, weighted by the heating coefficient.

Figure 4.5 shows the variation of the characteristic scale, l/L (determined numerically from plots obtained using equation 4.116 as already

discussed) with ϵ^{-1}, parameterised by a range of lid-heights, H. H_t remains fixed in all the data and ϵ was varied using f alone. Data for values of ϵ outside the plotted range, in particular for $\epsilon^{-1} > 20$, continue in the trends shown in figure indefinitely. Note also that the variable H responses converges rapidly and there is no sensible change in the variation of $\hat{l}$ with ϵ after the lid $H \approx 32H_t$ is reached. Data for the non-trapped case is presented alongside the trapped solution, for reference. In light of the preceding discussions of this section, the data of figure 4.5 make sense- plotting numerical $\hat{l}$ as a function of $\frac{1}{\epsilon}$ for a range of H, we observe numerical data (discrete points) in figure 4.5 confirms (i) linear variation in $\hat{l}$ for small ϵ and (ii) an ordinal intercept of $\hat{l} = 1$, for all lid heights.

Figure 4.1 documents the relative horizontal variation of the two terms in equation 4.118 at a selected altitude of $z = 0.8H_t$. There, we show, for $H = 32H_t$, a set of responses, parameterised by ϵ, corresponding to the x-variation of adjustment $p(x/L, z = 0.8 \times H_t)$. As δ (or ϵ) increases, the x-variation of the first term changes (due to factors $e^{-j\pi\delta\frac{|x|}{L}}$) but that of the second term does not. Apparently two trends determine horizontal variation in the steady state pressure response: (i) the exponential factors in the first term, $e^{-j\pi\delta\frac{|x|}{L}}$, all decrease, except near $x = 0$, which has the effect of concentrating the contribution of the first term in equation 4.118 onto the origin, (ii) a reduction of the size of the first term in equation 4.118 relative to its second. To exhibit this behaviour we must allow ϵ to take values well outside the range characteristic of terrestrial meteorology. For the extremely large value of $\epsilon = 100\pi$, the contribution of the first term is restricted to the immediate region of the origin and, overall, the horizontal response may be described by the exponential decay $-e^{-\frac{x}{L}}$ of the second term. Note the detail very close to the origin- the maximum response is, in fact, slightly displaced in x. As ϵ decreases, the second term, with horizontal variation $e^{-\frac{x}{L}}$) diminishes in significance relative to the first term, which also spreads-out, in response to the reduction in ϵ. The smallest value of ϵ used in the data of figure 4.1 is large compared with any value characteristic of terrestrial meteorology.

Finally, we remark that, for a planet with rapid rotation (large f, $\epsilon \gg 1$) equation 4.122 may be written so as to make the connection to the heating profile explicitly clear. From equation 4.121 we have for all x

$$p(x, z) \approx T\rho_0 \int s(x, z)dz, \tag{4.124}$$

where we have used equation 4.71.

4.6 Results

Throughout this section we consider a steady state system, where u and w fields are zero, in the constant N, constant ρ_0 limit. We consider

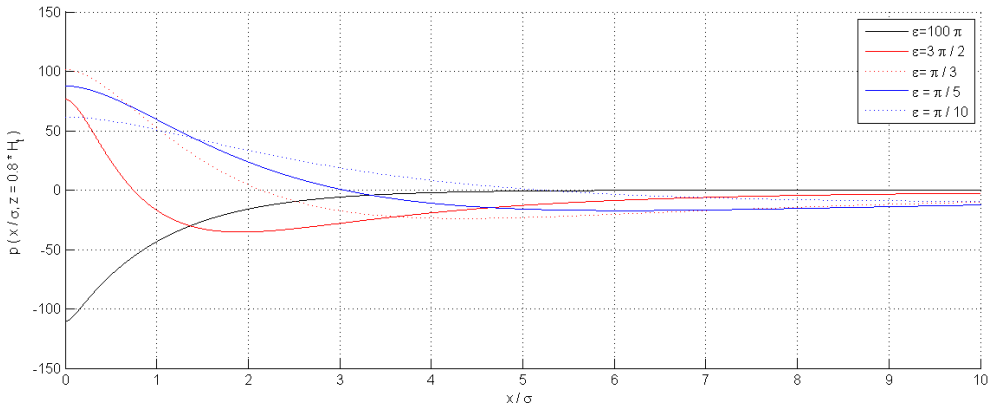

Figure 4.1: Horizontal cross section of steady state pressure adjustment $p(x/L, z = 0.8H_t)$ for large lid height $H = 32H_t$, for a range of f values chosen to illustrate the qualitative behaviour of the solution given in equation 4.118. The system has been forced with a heating pulse of duration 1 hr, $L = 10$ km and aspect ratio 1.

buoyancy, v-wind and pressure responses and focus on two processes known to affect the length-scale of convective adjustment: (i) the value of Coriolis parameter (i.e. latitude), and (ii) radiation of convectively forced gravity waves vertically into the stratosphere. Moving away from the equator, where $f = 0$, toward midlatitudes, where $f \approx 10^{-4}$, one observes an increase in rotational effects, which increase vorticity and constrain the horizontal range of dynamical perturbations. A higher upper lid invites upward propagation of gravity waves, tilting the group speed away from the horizontal, thereby also reducing the horizontal range of adjustment. How these two effects collaborate is the focus of our attention, here.

4.6.1 The f-dependence

In the absence of rotation, the atmospheric adjustment to buoyancy forcing is mediated by gravity wave propagation (as seen in Chapter 2 of this thesis). A finite heat source will induce transient alterations to the dynamical fields, but at steady state, all these effects will have propagated into the far field. The inclusion of rotation effects ($f \neq 0$) in the formulation generates vorticity, and introduces a Rossby adjustment aspect to the problem (see e.g. Gill 1982), which now has some local geostrophic equilibrium at steady state. In such cases, we are left with residual perturbations for certain fields, at steady state. Here, we quantify the effect that the value of Coriolis parameter, f, has on the steady state solutions, and consider how a leaky lid might alter Rossby adjustment.

Figures 4.2...4.4 show vertical cross sections of steady state b ($\mathrm{m\,s^{-3}}$), v ($\mathrm{m\,s^{-1}}$) and p (Pa) for a range of f ($\mathrm{s^{-1}}$) values in both the trapped case

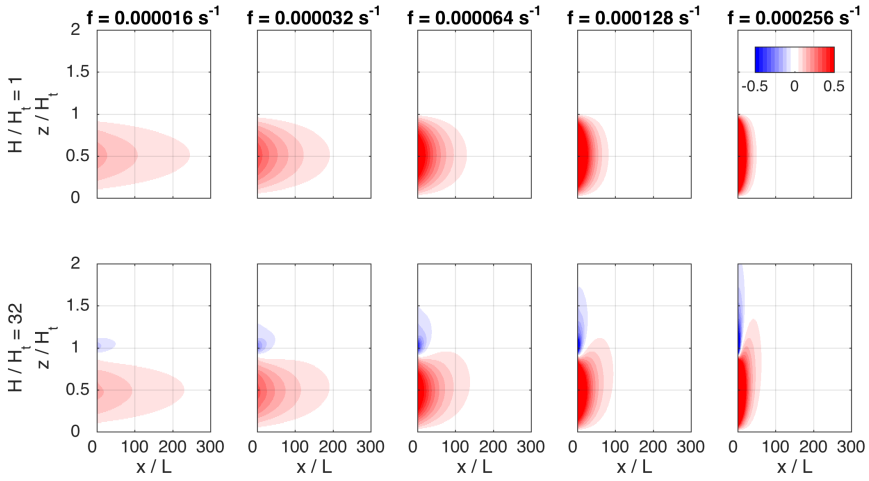

Figure 4.2: Vertical cross sections of steady state b ($\mathrm{m\,s^{-2}}$) for a range of f values, when the system is forced with a heating pulse of duration 1 hr, $L = 10\,\mathrm{km}$ and aspect ratio 1. The top row shows a trapped case with a rigid lid positioned at $H_L/H_t = 1$, i.e., directly above the heating. The bottom row shows a case in which the upper lid is located at $H_L/H_t = 32.$, i.e., well above heating.

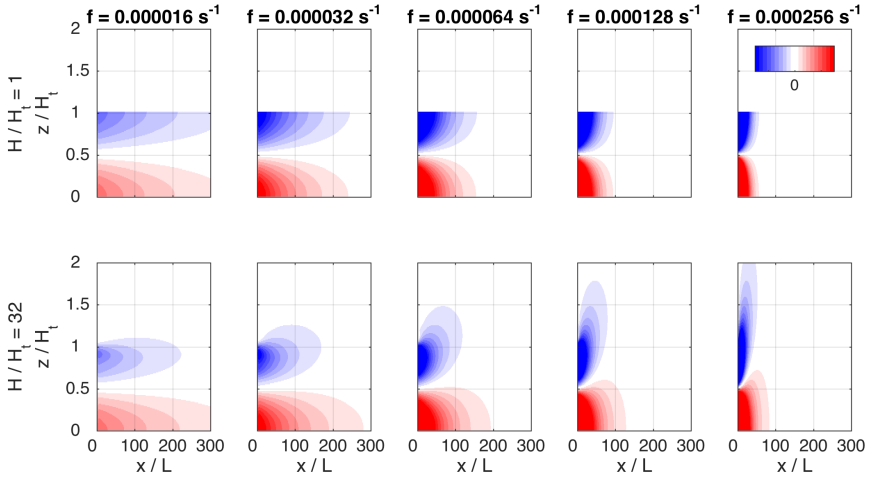

Figure 4.3: As in figure 4.2, but for v-wind response.

and high lid case. The responses are the adjustment to a 1 hr tropospheric buoyancy forcing pulse, of width 10 km, aspect ratio 1 and buoyancy forcing rate amplitude $S_0 = 0.01\,\mathrm{ms^{-3}}$. The values of f, from left to right, begin at $0.000016\,\mathrm{s^{-1}}$ and double in each panel, until we reach $f = 0.000256\,\mathrm{s^{-1}}$. Note, the largest value of f chosen here exceeds that at the Earth's poles and is included purely to provide context. A range of f values comparable to those observed on Earth is shown in figure 4.6, in which we non-dimensionalise on burger number. Again, for larger f

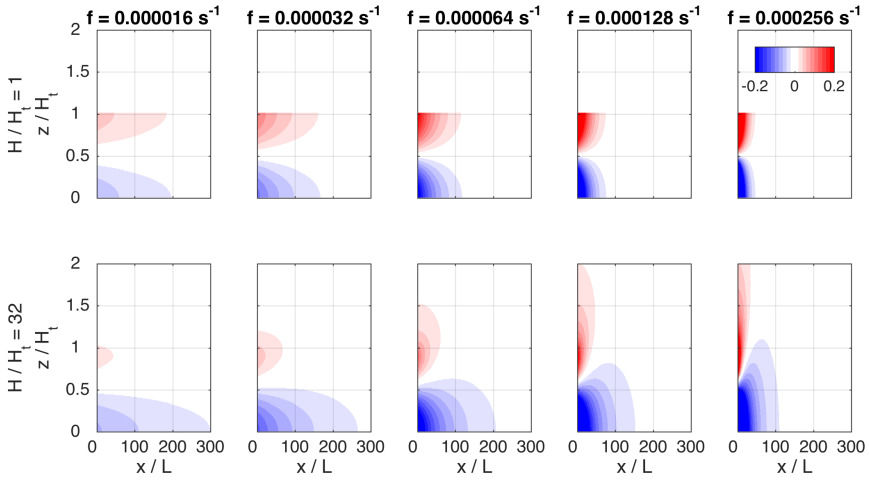

Figure 4.4: As in figure 4.2, but for pressure response.

we see larger amplitudes of pressure and buoyancy in the balanced state.

Clearly evident is the constraining effect of the Coriolis force. At small values of f, we see that the heating pulse has spread by gravity wave propagation, reaching a steady state with a fairly constant tropospheric distribution (see figure 4.2). However, as f ramps up, a cool anomaly persists directly over the forcing, and spreading is confined (also seen in figure 4.6). In the limiting case of $f = 0.000256\,\mathrm{s}^{-1}$, the gravity waves' propagation is presumably much more restricted. The effect of the lid is clear: wave modes propagating vertically transport perturbations and energy into the stratosphere, attenuating the tropospheric response. Further discussion of this effect is reserved for §4.6.3.

In order to quantify the extent to which the horizontal lengthscale of adjustment is altered by Coriolis effects and lid height, we define a characteristic length-scale, $< L >$, as the e-folding distance of upper level pressure perturbations (say). Note, maximum perturbations for all fields will be located at $x = 0$. The e-folding distance is evaluated at an altitude of $z = 0.8H_t$, as the effect of the lid is most apparent in the other levels. Figure 4.5 shows the $f-$dependence of the adjustment scale, for a range of lid heights. The x-axis is the reciprocal of Burger number (reference), or

$$\frac{1}{\epsilon} = \frac{fL}{NH_t} \tag{4.125}$$

where $L, N = 0.01$ and $H_t = 1$ are both fixed.

Let us consider the green set of points in figure 4.5, corresponding to the trapped case $H = H_t$. In this data we see that, at low values of f, scale $< L >$ is large. As f increases, $< L >$ reduces linearly with $\frac{1}{\epsilon}$, with unit gradient, until we reach very large values of f (see insert figure). For comparison, we include data for the theoretical trapped solutions, described in §4.5.1 (black dashed line). This data agrees very well with

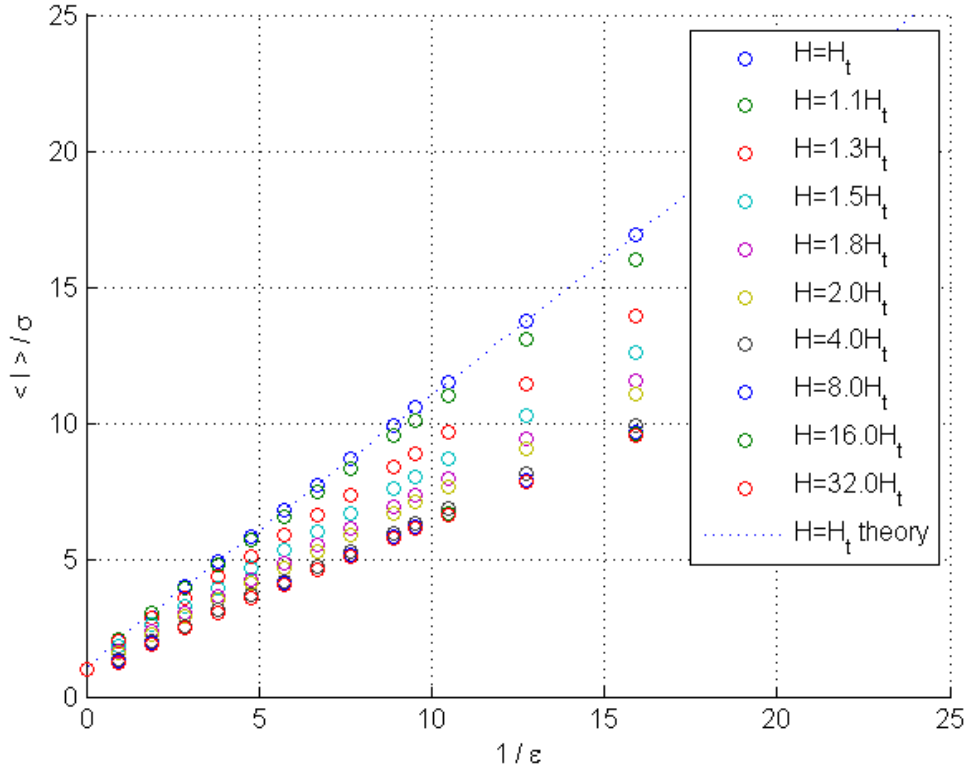

Figure 4.5: The effect of rotation and lid height on Rossby decay, for a heat source with $L = 10\,\text{km}$, aspect ratio 1, $N = 0.01\,\text{s}^{-1}$. We see a normalised characteristic horizontal length scale, defined as the e-folding distance of pressure perturbations at height $z = 0.8H_t$, against $1/\epsilon$, where $\epsilon = fL/NH_t$. The dotted line corresponds to the exact solution of the limiting case of trapped, narrow heating in equation 4.113 .

the full solution of the trapped case, until we reach very large values of f (small $\frac{1}{\epsilon}$), where the theoretical solutions depart.

4.6.2 Potential Vorticity

The inclusion of rotation, f, in our governing equations confers upon the system vorticity. In meteorology it is useful to consider the vorticity field, together with the Earth's rotation, to derive a conserved quantity known a potential vorticity, or PV (reference), which can be used a diagnostic of convective systems and meso-scale dynamics. Details of the derivation of PV for the system devised here was provided in §4.3.3.

The steady state PV for an isolated cloud is shown in the bottom panels of figure 4.7. The heating is the same as that shown in figure 4.2. The PV response peaks directly above the heated region, persists into the balanced state, and has the same length scale of the buoyancy

forcing. Note, the PV response is unaffected by lid height, as predicted in section §4.3.3.

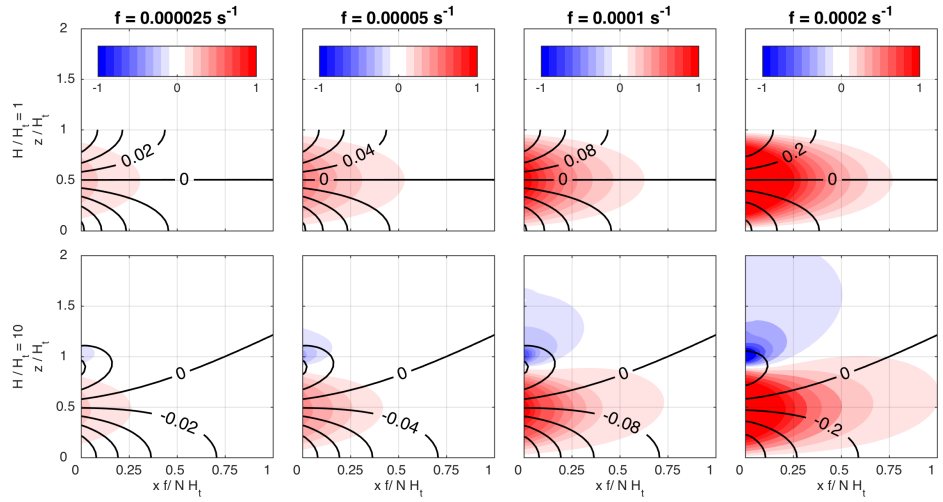

Figure 4.6: Vertical cross sections of the steady state b (ms^{-1}) (coloured contours) and pressure (Pa) (black contours), when the system is forced with a heating pulse of duration of 1 hr. The response for low and high lids for a range of f values is shown.

4.6.3 The Effect of Rigid Lid

We now switch our attention to the effect of lid height, H. A trapped solution is useful for understanding the effect variation in f has on the emergent steady state and it permits simple mathematical solutions. Further, cases of trapped wave propagation have been observed in the atmosphere (Monserrat & Thorpe, 1996). However, the atmosphere is unbounded aloft and waves forced in the troposphere can propagate vertically into the stratosphere, eventually to break high-up, in the mesosphere. The tropospheric meteorological response may be viewed as lying between the two regimes; the change in buoyancy frequency at the tropopause acts partially as a lid, to reflects some wave energy, but the deep structure of the atmosphere also permits transmission as well as refraction of wave energy at the tropopause. The effect of this "leaky lid" has been primary focus of recent theoretical studies by Edman and Romps (2017) and was discussed in Chapter 2. The numerical models used in weather prediction, which do not require any mesosphere dynamics, will simulate the essential situation addressed in these studies using a model stratosphere up to, typically, 35 km, with a thin sponge layer above that. However, this geometry does not always fully damp waves and some energy will be reflected into the troposphere, giving rise to spurious physical effects.

Here, we quantify the differences between the steady state of a trapped, convectively forced system, and a system with a high lid. We will simplify

matters by retaining N =constant.

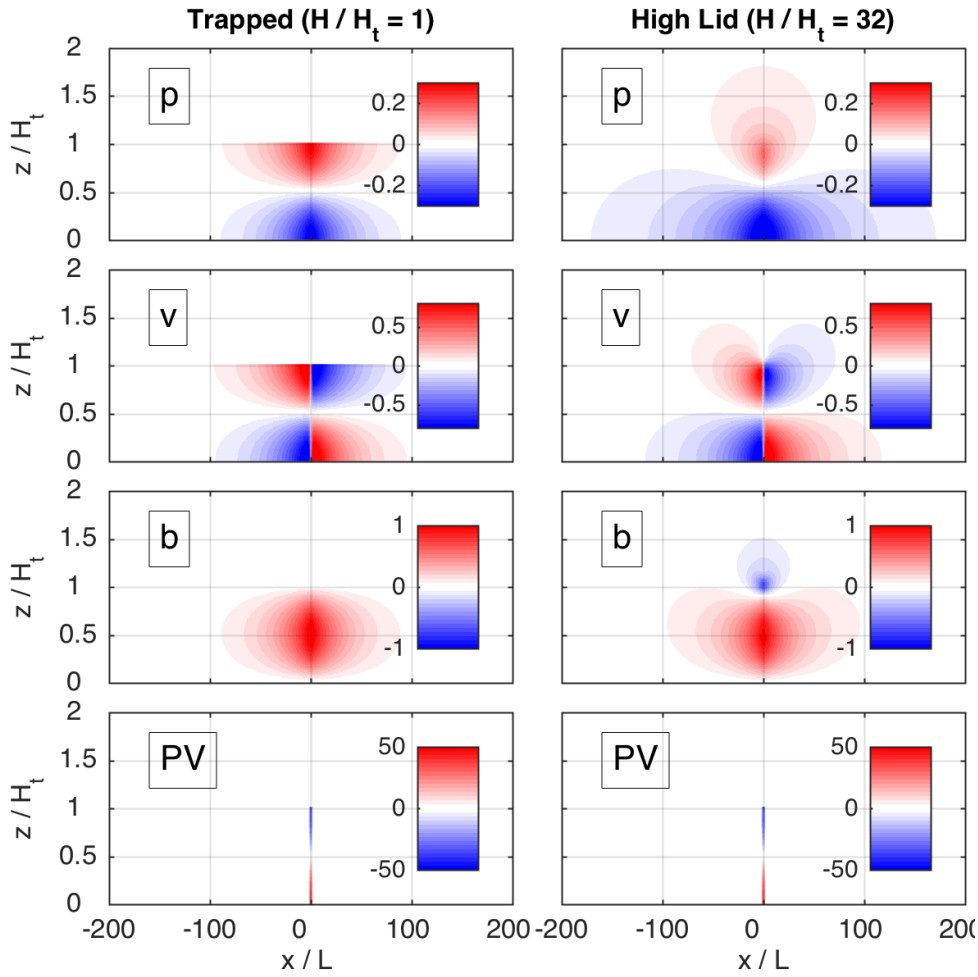

Figure 4.7: Vertical cross sections of p, u, v and PV for the case of rigid lid (left) and high lid (right). Shown is the steady state response to a 1 hr forcing of width 10 km and aspect ratio 1. $f = 10^{-4}$ for all data shown here.

Figure 4.7 shows vertical cross sections of p, v, b and PV for $f = 10^{-4}$. Pictured is the final steady state response to a 1 hr forcing of width 10 km and aspect ratio 1. The bottom left and right panels confirm that the PV response remains unchanged when allowing for upward radiation of gravity waves. However, clearly visible in the diagnostic variables is the effect of upward radiation. In all cases we see the response leaking out of the troposphere, as expected. The pressure field in particular shows a significant fractional reduction in amplitude in the upper troposphere when upward radiation is permitted. Here we also note a reduction in deformation radius. The v and b fields also display these features, albeit less dramatically.

The differences in the tropospheric solutions with and without the "leaky lid", for $f = 0.0001\,\mathrm{m\,s^{-1}}$ are quantified in figure 4.8. In the

top panel, the coloured contours show the buoyancy anomaly and the black contours pressure anomaly. In the bottom panel, we see the v-wind anomaly. In all fields, we observe a large anomaly (O(50%)). The cold anomaly in the buoyancy field will result in reduced stability. The pressure contours mirror this pattern, as expected, given pressure is a vertical integration of buoyancy. However, there are pressure anomalies of the order of 10% seen at the surface. The velocity field now has a reduced vorticity in the upper levels.

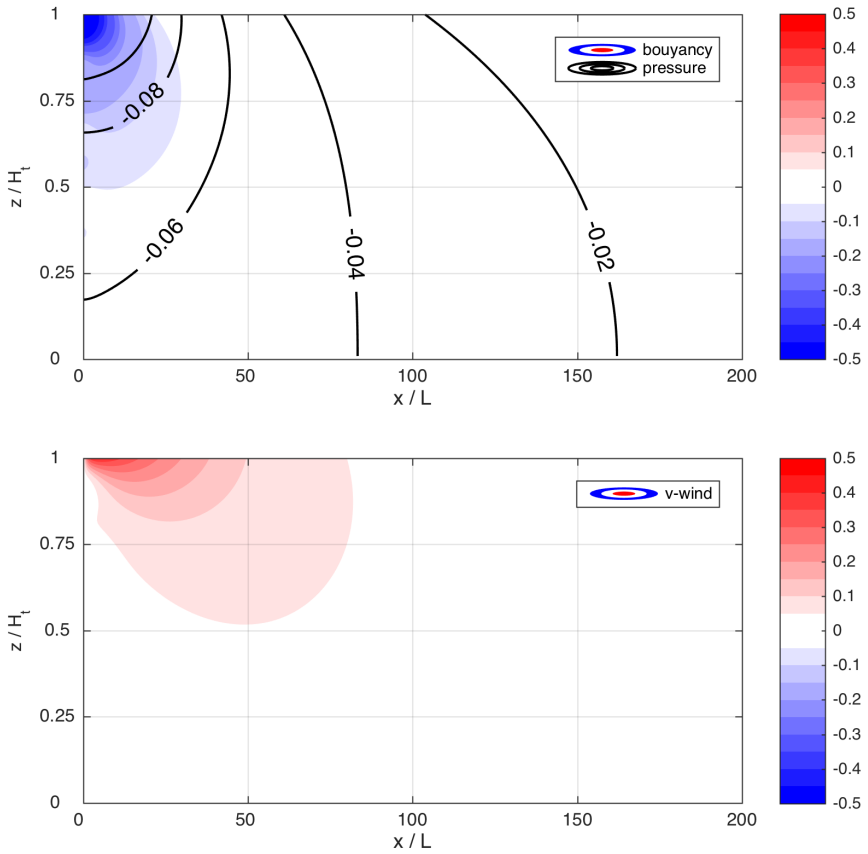

Figure 4.8: Anomaly plot for data shown in figure 4.7 (high lid - low lid). Top panel: coloured contours are buoyancy, black are pressure. Bottom panel: v-wind.

Figure 4.9 shows upper level ($z = 0.75H_t$) values of steady state b, v and p for trapped and high lid cases. In all variables we see smaller perturbations in the high lid case. The pressure field, in particular, experiences a significant fractional change, on the order of 40%, into the far field. Buoyancy differences are much smaller (O(10%)) and do not appear beyond $x/L = 50$. In the close neighbourhood to heating, the

v-wind sees no differences until $x/L = 5$. After this, the trapped and high lid solutions diverge, with fractional error growing very large in the far field.

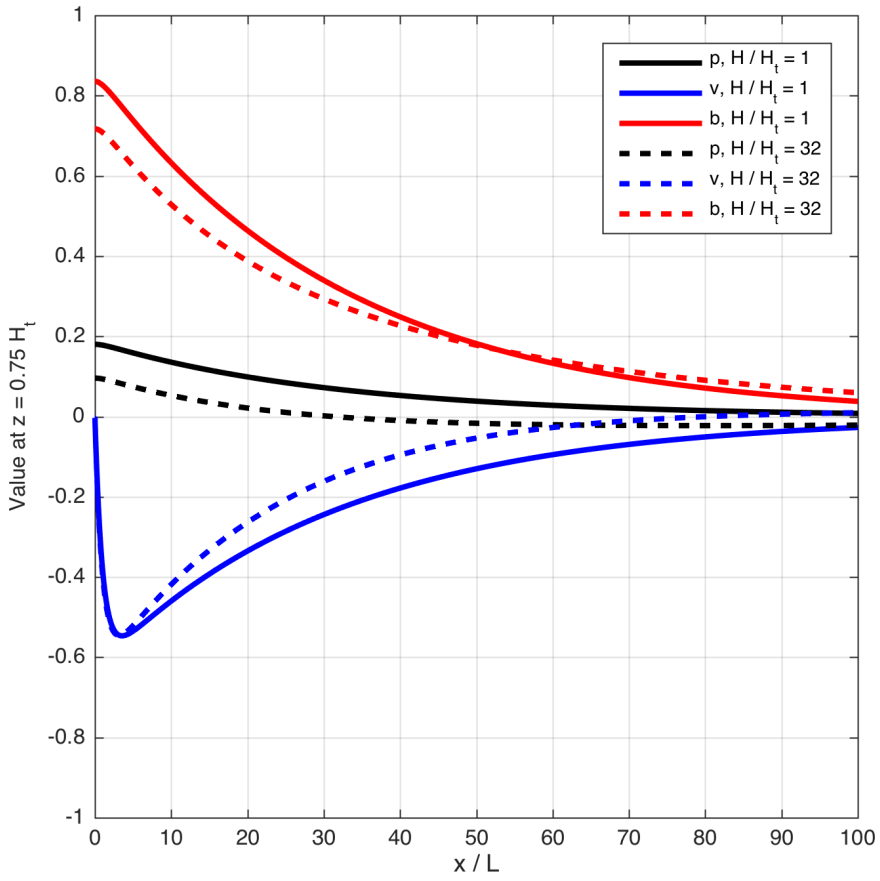

Figure 4.9: Values of steady state buoyancy (red), pressure (black) and v-wind (blue) at $z = 0.75H_t$, for trapped (solid) and high lid (dashed) solutions. The forcing is the same as that in figure 4.2.

4.7 Discussion

We have developed a semi-analytical steady state model of convective Rossby adjustment in order to investigate the ways in which Coriolis force affects the final state of the atmosphere following convective adjustment. The model geometry is 2.5D: we consider a slab, as in Chapter 2, which additionally experiences a v-wind and a horizontal rotation. Such a model permits solutions for pressure, buoyancy and horizontal velocity only, which can be used to derive an expression for potential

vorticity. As in Chapters 2 and 3, we test the influence of tropospheric boundary condition.

Without rotation, a pulsed buoyancy forcing will excite a range of transient gravity waves modes, which will propagate away from the forcing source, communicating the atmospheric adjustment. Such modes (an initial subsidence mode during forcing, followed by a rebound mode triggered by the truncation of heating - see Chapter 2 for details) leave the final state of the atmosphere unaltered. The inclusion of f, however, leads to an atmosphere in geostrophic balance at steady state, meaning perturbations in the dynamical fields persist for all time.

We find that the value of f restricts the length scale of convective adjustment: small f has a widespread response, large f has a confined response. The characteristic length scale is revealed in the limiting regimes of the trapped solutions, where very small f respond on a Rossby radius, and very large f have a response length scale which is determined by the lengthscale of the forcing.

As we saw in Chapter 2, taking a high upper lid (to simulate a radiative condition at the tropopause), reduces the horizontal distance at which the response has influence. We characterise the simultaneous interaction of f and lid height, finding that the growing f linearly reduces the lengthscale of the response. Having a higher lid further reduces the lengthscale.

Having a high lid leads to a cold anomaly in the upper tropopause (when compared to the trapped case). We have quantified this for a given value of f, $10^{-4}\mathrm{s}^{-1}$, a characteristic value for Earth. Anomalous values of p and v are of the order of 50% in the upper troposphere. Pressure anomalies are observed at the surface. The potential vorticity remains unchanged with lid height.

4.8 Summary

We have addressed rotation without which a period of transient buoyancy forcing does not lead to a local response at large time. With rotation, local pressure and buoyancy anomalies are in geostrophic balance with a transverse wind. This steady vortex state is fundamental.

In this Chapter, we have considered a steady state model, in 2.5D, again using an analytical approach. The model reveals the post-convection state of the atmosphere. We have found that the model lid and the value of Coriolis parameter restrict the lengthscale of the steady, balance response to transient convection, and have quantified how the two compete.

Here lies the end of our work with analytical models. We now depart, to examine a state-of-the-art numerical model to investigate the dynamics of fully coupled waves, like those seen in the real atmosphere.

Chapter 5

Convectively Coupled Waves in a General Circulation Model

5.1 Introduction

The tropical atmosphere and ocean are home to families of planetary waves, which propagate horizontally along the equator with meridional structures which, in the vicinity of the equator, are trapped. Tropical deep convection interacts with atmospheric waves through wave forcing, organisation or even coupling. On the synoptic scale, observed features include African easterly waves (Kiladis *et al.*, 2006; Parker, 2017), convectively coupled Kelvin and Rossby Waves (Wheeler & Kiladis, 1999) and the Madden-Julian oscillation (MJO), all of which have characteristic zonal scales, visible in cloudiness and precipitation fields, of thousands of kilometers (see Kiladis et al. (2009), or Gill (1982) for a review).

Additionally, case studies of specific regions reveal evidence for fast-moving (periods of 1-3 days) mesoscale, tropical wave-like disturbances. Inertia-gravity waves have been identified in satellite observations of the tropical western Pacific, Africa and South America (Haertel & Johnson, 1998; Haertel & Kiladis, 2004; Takayabu, 1994; Tulich & Kiladis, 2012) and, through high-resolution modelling, they have been characterised as westward-propagating convectively coupled gravity waves, with vertical wavelengths comparable to the depth of the troposphere (Tulich & Kiladis, 2012).

In a bench-mark experimental study, Wheeler and Kiladis (1999) produced a wavenumber-frequency spectral (Fourier) analysis of experimental, satellite-observed outgoing long-wave radiation (OLR hereafter), which is a good proxy for tropical deep convection. Wheeler and Kiladis were able to correlate statistically significant peaks in their experimental data to the dispersion relations of east-propagating Kelvin and certain equatorially-trapped wave modes of shallow water theory. More recently, Tulich & Kiladis (2012) moved this discussion onto the higher frequency

modes discussed in the earlier Chapters of this thesis. New, high resolution simulations of the whole pan-African continent have provided a database of predictions amenable to the methods of spectral analysis. In this chapter, we seek to quantify the extent to which similar correlations appear in one state-of-the-art convection-permitting model (CP4 hereafter) and how we might exploit that to improve understanding of the dynamics of convection coupling to gravity waves. Our research objectives are (i) seek evidence for gravity wave modes in a subset of dynamical and thermodynamical fields to illuminate the nature of particular modalities present in CP4, (ii) explore the extent to which gravity waves couple to rainfall and OLR and (iii) assess the potential of CP4 as research tool to illuminate convection coupling dynamics. Of course, understanding the nature and role of convectively coupled waves is intrinsically important, as they are a source of weather and climate predictability on a range of temporal and spatial scales.

To begin, we first outline the background, mathematically-predicted properties of convectively coupled, equatorial waves, since these properties provide our initial interpretative framework.

5.2 Background

As we hope to show, the work of Chapter 5 complements that of Chapters 2..4. However, it relies heavily on concepts not previously discussed in Chapter 1. We attempt to remedy this by producing in this section a reasonably self-contained account of convection, wave-convection coupling and the Fourier methods which we use to see if it is present in data.

5.2.1 Equatorial Wave Theory

The theory of equatorial waves is now very familiar to the tropical meteorologist (Gill, 1982; Matsuno, 1966). Families of tropical waves reveal themselves through solutions to linearised primitive equations of motion, which characterise each wave family via unique dispersion relations. Matsuno is generally credited with the first thorough study of large-scale atmospheric and oceanic waves in the equatorial area. In essence, he showed particular types of wave identified below, can, in the equatorial region, propagate eastward or westward along the "equatorial duct". These Matsuno modes may, perhaps, be most easily understood as quasi-horizontal planetary, Rossby, gravity and mixed small amplitude, long wave-length oscillatory disturbances (about a base state of rest) in a rotating, equatorial layer of homogeneous, incompressible fluid of constant depth, treated within beta-plane approximation (essentially a shallow water formulation). It is that formulation which we shall use as a background framework here, stating salient outcomes, in the form

of e.g. the wave dispersion relations for Matsuno modes. For the detail of all that follows in this section, refer to Matsuno (1966) or Gill (1982).

The solution for horizontal flow, on an equatorial beta plane, of the linearised, shallow-water equations yields:

1. An east-propagating Kelvin wave

$$\begin{pmatrix} u \\ v \end{pmatrix} = \begin{pmatrix} \sqrt{\frac{g}{H}} e^{-\frac{y^2}{2L^2}} \\ 0 \end{pmatrix} G(x-ct), \quad c = \sqrt{gH}, \tag{5.1}$$

   which is non-dispersive i.e. has dispersion relation

$$\omega = ck, \quad k > 0, \tag{5.2}$$

2. a set of equatorial wave modes

$$\begin{pmatrix} u \\ v \end{pmatrix} = \Re \left(\begin{pmatrix} -i\sqrt{\frac{c\beta}{2}} \left(\frac{D_{n+1}\left(\sqrt{\frac{2\beta}{c}} y\right)}{kc-\omega} - \frac{nD_{n-1}\left(\sqrt{\frac{2\beta}{c}} y\right)}{ck+\omega} \right) \\ D_n\left(\sqrt{\frac{2\beta}{c}} y\right) \end{pmatrix} e^{i(kx-\omega t)} \right), \tag{5.3}$$

   $n \in \mathbb{Z}^+$, $n \neq 0$,

3. and another wave mode

$$\begin{pmatrix} u \\ v \end{pmatrix} = \Re \left(\begin{pmatrix} -i\sqrt{\frac{c\beta}{2}} \left(\frac{D_1\left(\sqrt{\frac{2\beta}{c}} y\right)}{kc-\omega} \right) \\ D_0\left(\sqrt{\frac{2\beta}{c}} y\right) \end{pmatrix} e^{i(kx-\omega t)} \right), \tag{5.4}$$

   for $n = 0$, both of which follow the dispersion relation

$$\frac{\omega^2}{c^2} - k^2 - \frac{\beta k}{\omega} - \frac{\beta}{c}(2n+1) = 0, \quad n \in \mathbb{Z}^+. \tag{5.5}$$

Above, we have used the parabolic cylinder function

$$D_n(\alpha) \equiv 2^{-\frac{n}{2}} H_n\left(\frac{\alpha}{\sqrt{2}}\right) e^{-\frac{\alpha^2}{4}}, \tag{5.6}$$

where H_n denotes the n^{th} Hermite polynomial (Arfken 1966) and

$$L \equiv \sqrt{\frac{c}{\beta}}, \quad c = \sqrt{gH}, \quad \beta \equiv \frac{2\Omega}{a}, \tag{5.7}$$

with H the depth of the water (or equivalent depth of the atmospheric layer), $\Omega = 7.2729 \times 10^{-5}$rads $^{-1}$ is the angular velocity of the Earth and $a = 6371$km its radius. The dispersion relations in equation 5.5 are plotted in terms of dimensionless variables $k\sqrt{\frac{c}{2\beta}}$ and $\frac{\omega}{\sqrt{2\beta c}}$, for different values of n, in figure 5.1. The different branches, corresponding to e.g. large or small ω are discussed shortly. Note that parameter $\sqrt{\frac{c}{2\beta}}$ is the equatorial Rossby radius.

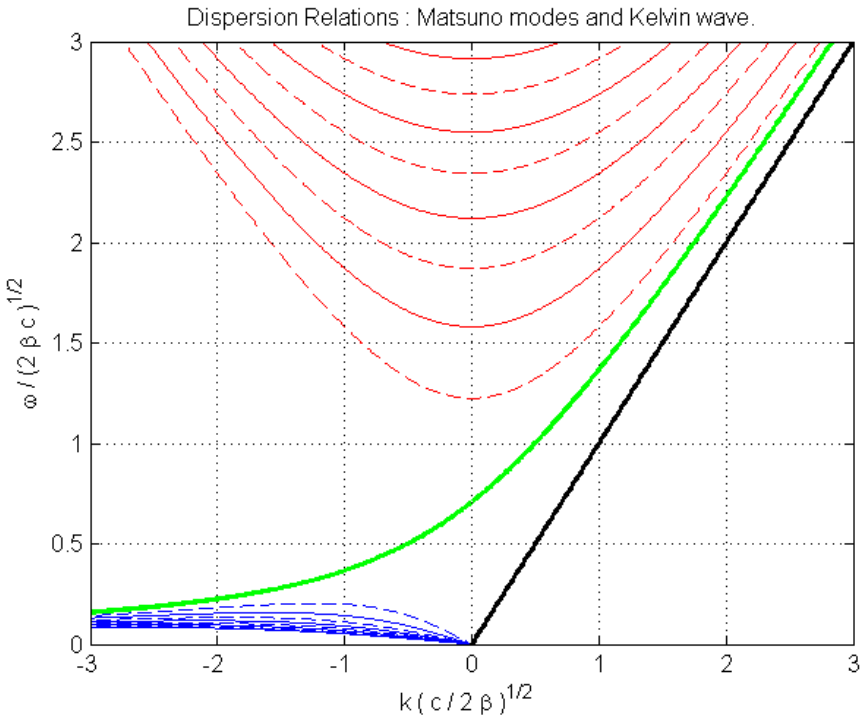

Figure 5.1: Dispersion relations of upper (red) and lower (blue) branch Matsuno modes, plotted with modes corresponding to even integer, n, displayed using solid lines, and odd integer n, displayed as broken lines. The solid black line is the Kelvin wave dispersion relation $\omega = kc$. The solid green line line is special solution $n = 0$.

5.2.2 Symmetric/Anti-Symmetric Spectral Decopo-sition

The meridional parity of the parabolic cylinder functions, D_n, is determined by the H_n, which are even for n even, and odd for n odd. From equation 5.3, horizontal velocity components u and v do not have the same meridional parity. However, since taking the x-derivative will not change the parity of u or v, the horizontal divergence field (which, note, we take to couple to convection) will always have definite, odd or even parity with respect to the y variable. (Recall, the derivative of an odd function is even, and vice versa). For the flow associated with the Kelvin wave defined in equation 5.1, the horizontal divergence

$$\underline{\nabla}_H \cdot \underline{v} = \frac{\partial u}{\partial x} + \frac{\partial v}{\partial y}, \tag{5.8}$$

will therefore be an even function of the zonal coordinate, y. However, the equatorial wave modes, classified by integer n, can exist in both odd

or even form. In equation 5.3 we have

$$\underline{\nabla}_H \cdot \underline{v} = \omega\sqrt{\frac{2\beta}{c}}\Re\left(e^{i(kx-\omega t)}\right) \times \left(\frac{1}{kc-\omega}D_{n+1}\left(\sqrt{\frac{2\beta}{c}}y\right) - \frac{n}{kc+\omega}D_{n-1}\left(\sqrt{\frac{2\beta}{c}}y\right)\right). \tag{5.9}$$

Note, to take the horizontal divergence of the disturbance flow in equation 5.3, we have used the recursion relation property of parabolic cylinder functions, namely

$$\frac{d}{d\alpha}D_n(\alpha) = \frac{1}{2}\left(nD_{n-1}(\alpha) - D_{n+1}(\alpha)\right). \tag{5.10}$$

Since $\underline{\nabla}_H \cdot \underline{v}$ will be an odd or even function of y, wave modes will decompose into symmetric and anti-symmetric parts. We will utilise this property later, to assist the identification of particular wave modes in African continent simulation data.

5.2.3 Branch Dispersion Relations

By imposing assumptions on the relative magnitude of zonal wavenumber, k or frequency, ω, one can write simplified dispersion relations for subsets of the equatorial wave spectrum.

For large, positive k, dispersion relation 5.5 approachs that of the Kelvin wave (equation 5.2) and also Poincaré waves (Gill 1982) and disturbances in this regime are designated equatorially-trapped gravity waves. High frequency modes (large ω) are known as "Matsuno, upper branch", for which the dispersion relation 5.3 may be approximated as

$$\omega \approx \sqrt{(2n+1)\beta c + k^2c^2}, \quad k \in \mathbb{R}, \tag{5.11}$$

where, importantly, speed c is a measure of the effective layer depth (recall $c = \sqrt{gH}$). For lower frequency modes (small ω), which are known as "Matsuno lower branch", the dispersion relation 5.3 is approximated as

$$\omega \approx \frac{-\beta k}{k^2 + \frac{(2n+1)\beta}{c}}, \quad k \in \mathbb{R}^-. \tag{5.12}$$

These waves are designated trapped planetary waves. For the special case $n = 0$ Matsuno mode, the dispersion relation in equation 5.3 may be factorised. After discarding unphysical spurious solutions we find

$$\omega = \begin{cases} \frac{ck}{2}\left(1 - \sqrt{1 + \frac{4\beta}{ck^2}}\right), & k \in \mathbb{R}^+, \\ \frac{ck}{2}\left(1 + \sqrt{1 + \frac{4\beta}{ck^2}}\right), & k \in \mathbb{R}^-. \end{cases} \tag{5.13}$$

The $n = 0$ mode is designated by Gill (1982) a mixed gravity-Rossby mode. See figure 5.1.

Mode	Branch	n	$\omega - k$ rel.	Physics	$\underline{\nabla}_H \cdot \underline{v}$ parity
Kelvin	-	-	Eq. 5.2	Gravity wave	Zonally even
Matsuno	upper	even	Eq. 5.11	Gravity wave	Zonally odd
Matsuno	upper	odd	Eq. 5.11	Gravity wave	Zonally even
Matsuno	lower	even	Eq. 5.12	Rossby wave	Zonally odd
Matsuno	lower	odd	Eq. 5.12	Rossby wave	Zonally even
Matsuno	-	$n = 0$	Eq. 5.13	Mixed wave	Zonally odd

Table 5.1: Classification and salient properties of equatorially trapped wave modes, with the dispersion relations such as those shown in figure 5.1.

As already discussed, evidence for all the wavenumber-frequency dispersion relations in equations 5.2, 5.11, 5.12 and 5.13 appears in observational i.e. experimental data, which must be transformed to Fourier space for any comparison. Generally, the value of the layer depth, H, is varied to optimise the correlation between data and the linear theory outlined above. Note that the effect of vertical shear can be modelled by varying effective depth H, so, in reality, authors generally compare experimental data with dispersion relations obtained for a range of H.

Let us summarise the dispersion relations in figure 5.1 in the light of the discussions of this section. Dispersion relations in figure 5.1 are plotted with modes corresponding to even integer, n, displayed using solid lines and odd integer n, displayed as broken lines. This decomposition corresponds to disturbances producing zonally odd or even divergence, respectively, which will therefore appear in zonally anti-symmetric or symmetric model data, respectively. We further summarise the discussions of this section in table 5.1.

5.2.4 Theory of Equatorial Wave Coupling to Convection

A number of quantitative hypotheses exist to describe the way in which convection couples to large scale circulations. In this brief summary we consider two theoretical, highly idealised dynamical feedback between convection and waves, namely i) Emmanuel's (1986) wind-induced surface heat exchange (WISHE) and ii) Lindzen's (1974) conditional instability of the second kind (wave-CISK). We examine these theories as (i) they provide a useful link between this Chapter and the theoretical work of Chapters 2...4, and (ii) wave-CISK in particular permits a wave dispersion relation similar to those described by Matsuno 1966.

Neither WISHE nor wave-CISK theory is without flaw, and in reality, there are a whole host of possibilities for ways in which convection couples to waves (e.g. convective downdraughts), so neither theory can be considered wholly responsible. Briefly, the WISHE mechanism involves

positive feedback between the circulation and heat fluxes from the sea surface, which are then quickly redistributed aloft by convection, in turn strengthening the circulation. In contrast, the wave-CISK mechanism involves low-level convergence in the wind field, which produces convection, which releases latent heat, which forces waves which enhances the convergence and further increases convection. For present purposes, we retain Lindzen's wave-CISK, since it uses mathematical techniques after those applied in Chapters 2, 3 and 4, and consequently it is positioned to link the forced waves considered there to the convectively coupled waves discussed here. We return to the generalities of wave-CISK at the end of this section and concentrate first on the emergence of the dispersion relations of convectively coupled waves.

Lindzen (1974) took a basic set of equations, linearised about a state of rest, used an equatorial β plane approximation, and introduced a heat forcing term of the right hand side of his thermodynamic equation. His system is similar to equations 2.2, indeed his model is, essentially, that of Chapter 2 but with a simplified stratification, in which the base state of density is $\rho_0(z) = \rho_0(0)e^{-z/D}$ but with constant N. The only effect of the Earth's sphericity in this model is to permit the vertical, z, component of Earth's rotation to vary linearly with y. All fields were assumed to have time and longitude dependancies $e^{i(\omega t+kx)}$. By straightforward elimination of variables, Lindzen formed an equation for the y-z dependance of variable $v' = \rho_0^{1/2}v$, a scaled eastward velocity. This equation is then separated after the methods of chapters 2,3 and 4, using a modal expansion

$$v'(x,y,z,t) = \sum_n V_{n,k,\omega}(z)\Psi_{n,k,\omega}(y)e^{i(kx+\omega t)} \tag{5.14}$$

which is based upon solutions to the eigenvalue equation

$$M_y\Psi_{n,k,w}(y) = \left(\frac{1}{gh_{n,k,w}} - \frac{k_2}{\omega^2}\right)\left((f+\beta y)^2 - \omega^2\right)\Psi_{n,k,\omega}, \tag{5.15}$$

where the operator

$$M_y = \frac{\partial^2}{\partial y^2} + \frac{k}{\omega}\left(\beta - \frac{k}{\omega}(f+\beta y)^2\right) \tag{5.16}$$

and eigenvalue $h_{n,k,\omega}$, to be discussed below, termed an effective depth, also appears in the equation for $V_{n,k,\omega}(z)$

$$\frac{d^2}{dz^2}V_n(z) + \left(\frac{\kappa}{Hh_{n,k,\omega}} - \frac{1}{4H^2}\right)V_n(z) = -\frac{\kappa}{H}S_n(z), \quad \kappa = \frac{\gamma-1}{\gamma}. \tag{5.17}$$

Above, the $S_n(z)$ are analogous to our heating expansion coefficients of Chapters 2..4. For an equatorial β plane (for which $f = 0$ locally) the equation 5.16 reduces to the Shroedinger equation for the quantum

linear harmonic oscillator (Dirac, 1981), with solutions determined by the Hermite polynomials (Morse & Feshbach, 1946).

$$\Psi_{n,k,\omega} = e^{-\frac{1}{2\xi^2}} H_n(\xi), \quad \xi \equiv \left(\frac{2\Omega}{a}\right)^{\frac{1}{2}} (gh_{n,k,\omega})^{-\frac{1}{4}}, \tag{5.18}$$

and the eigenvalue, $h_{n,k,\omega}$ is then determined by an equation which is effectively a dispersion relation for Lindzen's assumed horizontal wave motion

$$\left(\frac{k}{\omega}\frac{2\Omega}{a} - k^2 + \frac{\omega^2}{gh_{n,k,\omega}}\right) \frac{\sqrt{gh_{n,k,\omega}}}{\left(\frac{2\Omega}{a}\right)} = 2n + 1. \tag{5.19}$$

The horizontal variation in Lindzen's formulation is similar to Laplace's tidal theory and, in fact, Lindzen points-out that equation 5.17 is the isothermal case of the vertical structure equation of classical atmospheric tidal theory. Equation 5.19 corresponds to the dispersion relations predicted, about the same time, by Matsuno (1966), who used a similar basic set of equations, derived from the shallow water approximation. Lindzen therefore showed how tropical deep convection and long-wavelength motions in an atmosphere can couple. His framework is essentially that of wave-CISK (Lindzen, 1974) to which we now briefly return.

In wave-CISK, if surface air is sufficiently warm, moist and elevated it can become convectively unstable and give rise to convective hot towers, which span the troposphere vertically. In Lindzen's theory, a low-level convergence field associated with a large-scale meteorological system lifts air to that height, whereupon cumulonimbus convection initiates and, in turn, forces the large-scale motion whose low-level convergence gave rise to the convection. Lindzen investigated such an interaction by seeking to parameterise the relation between the cumulus heating and the low level convergence. Although the precise parameterisation of wave-CISK is disputed, it is reasonable to accept a coupling between convection and the known long wavelength modalities of shallow water theory.

5.3 CP4 Africa and the IMPALA Project

Here, we consider the capacity to recover coupled waves in one state-of-the-art model, which provides the data set used in this chapter. First, we digress slightly, to contextualise this data and the project which provides it. For a full account of this project's aims and a model description, see Stratton et al. (2018).

The Future Climate for Africa (FCFA hereafter) Improving Model Processes for African Climate (IMPALA hereafter) project aims to deliver a step change in global climate model capability for Africa, by delivering reductions in model systematic errors, through improved understanding and representation of the drivers of African climate, hence reducing uncertainty in future projections. IMPALA is a Met Office-led consortium of UK and African institutions, including the African Centre

of Meteorological Applications for Development, the Centre for Ecology and Hydrology, and the universities of Cape Town, Exeter, Leeds, Nairobi, Oxford, Reading and Yaounde. Its essential scientific aim is to improve understanding of Africa's climate and, hence, to provide support for decision making at the continental level. IMPALA is part of the £20M UK government-funded Future Climate for Africa (FCFA), which aims better to understand African climate change. FCFA is a joint programme of the Department for International Development and Natural Environment Research Council. Prior to IMPALA high-resolution climate model prediction capability had not been available across many parts of sub-Saharan Africa.

One of the key challenges to improve model performance is a better understanding of how the fundamentals of convective parameterisation impact on African climate variability and the Met Office Unified Model (UM hereafter) represents the key tool for that undertaking. Crucially for IMPALA, a set of high-resolution (4km), convection permitting UM simulations (CP4) over an Africa-wide domain, mean it is possible to represent individual convective cloud systems on the whole African continent for the first time. Within the project, two 10yr. (1997..2007) duration simulations will provide data for the present day and for an idealised future climate.

Here, we are interested in the present day runs, and subsets within that timeseries. The IMPALA initiative has provided a database of predictions amenable to the essential methods of spectral analysis used by Wheeler and Kiladis (Wheeler and Kiladis, 1999), who, in a bench-mark experimental study, produced a wavenumber-frequency spectral (Fourier) analysis of experimental, satellite-observed outgoing long-wave radiation (OLR hereafter), which is a good proxy for tropical deep convection. Wheeler and Kiladis were able to correlate statistically significant peaks in their experimental data quite well to the dispersion relations of east-propagating Kelvin and certain equatorially-trapped wave modes of shallow water theory. In the first instance, we aim, initially, to apply similar techniques to numerical model data derived from the CP4 runs to i) diagnose the planetary wave coupling model capability, discussed in section 5.3.1 and ii) characterise high frequency gravity waves found in the data.

5.3.1 IMPALA Perspectives and UM Description

The UM is a numerical model of the atmosphere used for both weather and climate applications, which is in continuous development by the Met Office and its partners. A single, coherent model family, which can be used for prediction across a range of timescales, has been a pillar of Met Office weather and climate prediction since 1990. In the UM, the same dynamical core and, where possible, the same parameterisation schemes are used across a broad range of spatial and temporal scales. The UM is suitable for numerical weather prediction, seasonal forecast-

ing, climate modelling (with forecast times ranging from a few days to hundreds of years) and for global and a regional modelling. We consider relevant scientific and mathematical content of the UM, in relation to CP4, in more detail, shortly. For present purposes, CP4 should be regarded as an high-resolution simulations of a pan-African domain, nested with a coarse global simulation. The model has been used to compile and archive extensive predictions of a wealth of dynamic and thermodynamic prognostic variables.

Our proposed analysis of model data is meaningful only in the context of the physics and mathematics of that model. In the usual oblate spheroidal system (r, φ, λ) (Gill, 1982), using its native symbols and notation (UM documentation) the zonal, meridional and vertical momentum equations solved in the UM are respectively

$$\begin{aligned}
\frac{Du}{Dt} &= -\frac{uw}{r} - 2\Omega w\cos(\varphi) + \frac{uv\tan(\varphi)}{r} - \frac{c_{pd}\theta_v}{r\cos(\phi)}\frac{\partial \Pi}{\partial \lambda} + S^u, \\
\frac{Dv}{Dt} &= -\frac{vw}{r} - \frac{u^2\tan(\varphi)}{r} - 2\Omega\sin(\varphi) - \frac{c_{pd}\theta_v}{r}\frac{\partial \Pi}{\partial \varphi} + S^v, \\
\frac{Dw}{Dt} &= \frac{u^2+v^2}{r} + 2\Omega u\cos(\varphi) - g - c_{pd}\theta_v\frac{\partial \Pi}{\partial r} + S^w,
\end{aligned} \tag{5.20}$$

(note, the vertical momentum equation is non-hydrostatic), with a continuity equation

$$\frac{D}{Dt}(\rho_y r^2\cos(\varphi)) + \rho_y r^2\cos(\varphi)\left(\frac{\partial}{\partial\lambda}\left[\frac{u}{r\cos(\phi)}\right] + \frac{\partial}{\partial\varphi}\left[\frac{v}{r}\right] + \frac{\partial w}{\partial r}\right) = 0, \tag{5.21}$$

and thermodynamic and state equations respectively

$$\frac{D\theta}{Dt} = \left(\frac{\theta}{T}\right)\frac{\dot{Q}}{c_{pd}}, \quad \Pi^{\frac{\kappa_d - 1}{\kappa_d}}\rho\theta_v = \frac{p_0}{\kappa_d c_{pd}}. \tag{5.22}$$

Here, S^u represents the u component of the dissipation, ρ_y is the density of dry air, $\theta = T\left(\frac{p_0}{p}\right)^{\frac{R_d}{c_{pd}}}$ is potential temperature, $\Pi = \left(\frac{p}{p_0}\right)^{\frac{R_d}{c_{pd}}}$ is the Exner function, $\kappa_d \equiv \frac{R_d}{c_{pd}}$, reference pressure is $p_0 = 1000h\text{Pa}$, horizontal material derivative $\frac{D}{Dt} \equiv \frac{\partial}{\partial t} + \frac{u}{r\cos(\varphi)}\frac{\partial}{\partial\lambda} + \frac{u}{r}\frac{\partial}{\partial\varphi} + w\frac{\partial}{\partial r}$ and:

$$\theta_v \equiv \frac{T}{\Pi}\left(\frac{1 + \frac{1}{\epsilon}m_v}{1 + m_v + m_{cl} + m_{cf}}\right). \tag{5.23}$$

Above, $m_v = \frac{\rho_v}{\rho_y}$ $(m_{cl} =\equiv \rho_{cl}\rho_y)$ $[m_{cf} = \frac{\rho_{cf}}{\rho_r}]$ is the mixing ratio of water vapour (cloud liquid water) [cloud frozen water], with $\rho = \rho_y(1 + m_v + m_{cl} + m_{cf})$. Moisture quantities m_v, m_{cl} and m_{cf} do not,of course, remain constant: the UM has dynamical equations which govern them:

$$\frac{Dm_v}{Dt} = S^{m_v}, \quad \frac{Dm_{cl}}{Dt} = S^{m_{cl}}, \quad \frac{Dm_{cf}}{Dt} = S^{m_{cf}}. \tag{5.24}$$

All other symbols have their usual meaning.

Since linear equatorial wave theory effectively derives from simplified forms of equations 5.20, 5.21 and 5.22, it is apparent form the above that the UM used to compile CP4 data sets will, in principle, be sufficient, to recover the phenomena of linear theory, such as Matsuno modes and Kelvin waves, once the UM is adapted to the appropriate geographical location.

5.4 Methodology

We consider an equatorial region of a convection permitting UM simulation of the whole pan-African continent (CP4). Specifically, we consider the region is bounded between -30 and 60 degrees longitude and $+/-10$N/S latitude. Such a region was chosen because: i) the equator is a known hot spot for planetary synoptic and mesoscale waves, ii) successful studies of convection-wave interactions have targeted this region (Wheeler and Kiladis 1999, Tulich and Kiladis 2012), and ii) this is the full longitudinal bound of the CP4 convection permitting runs. The domain is demonstrated in figure 5.2.

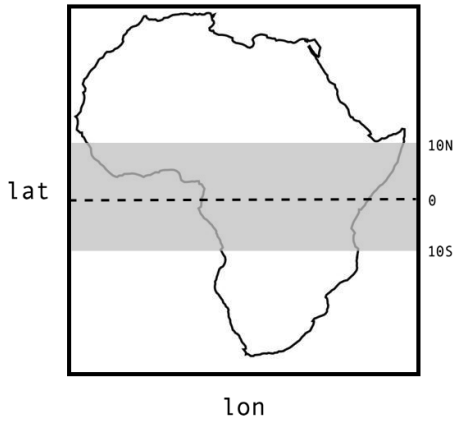

Figure 5.2: A schematic of the equatorial domain used in this work. The black box represents the full simulation domain, the grey shaded region shows how we have truncated output data to a region in which equatorial waves will be prevalent.

Our philosophy is first to inspect single-level model fields associated with moisture, i.e. rainfall and outgoing long wave radiation (OLR hereafter). Note, OLR, a measure of cloud cover, is an accepted proxy for convection. In such fields, we seek evidence for coupling between convection to long wavelength atmospheric waves. Specifically, we seek evidence for those wave modalities discussed in section 5.2, above. Subsequently, If such a coupling exists, we will look to the dynamical and thermodynamical fields of vertical velocity and potential temperature (those of our

analytical investigations, note), to characterise the nature of the convectively coupled waves. As one might expect, the raw model data is noisy to analyse with the unguided eye. We will therefore utilise well-known Fourier or spectral analysis methods to filter signal from the noise in a number of ways, to be discussed. Furthermore, such transformation to Fourier space facilitates comparison with wave modes (i.e. equations 5.2, 5.11, 5.12 and 5.13). Noting that high accuracy, "black box" code is readily available, verifiability argues for control of the computational algorithm used to process our CP4 data. Accordingly, all data presented here was processed using bespoke code, written in Matlab. We proceed now to detail our method.

5.4.1 Initial Data Processing

Before we begin spectral analysis, it is advantageous first to perform some spatial averaging, to produce data with definite zonal parity. This will aid in the identification of anticipated waves modalities with properties as summarised figure 5.1.

Let us denote the meridional, zonal and time coordinate of a certain gridded field, g, by discrete subscripts i, j and n respectively. Here $i, j, n \in \mathbb{Z}$ with $i \in [1, N]$, $j \in [-M, M]$ and $n \in [1, N_t]$. g denotes a single-level model output, such as OLR or rainfall. The equator corresponds to $j = 0$ on the mesh, with southern latitudes denoted by $j < 0$ and a range of j corresponding to a range of latitude of $\pm 10^0$. Mesh coordinate $i > 0$, with $i = 0$ corresponding to longitude -30 and 60 degrees. Of course time is positive, $n > 0$. Note that $g_{i,j,n} \in \mathbb{R}^+ \ \forall i, j, n$ considered. The temporal resolution varies with CP4 model variable, depending on how the runs are iterated. We return to this matter when we discuss specific field variables. for present purposes the spatial resolution is nominally 4.5 km. The number of data points in the meridional direction is denoted N_x.

For the reasons set-out in subsection 5.2, we consider g_{ijn} which are expressed in terms of their zonally-symmetric and anti-symmetric contributions defined as follows

$$g^{(s)}_{i,j,n} \equiv \frac{1}{2}\left(g_{i,j,n} + g_{i,-j,n}\right), \quad g^{(a)}_{i,j,n} \equiv \frac{1}{2}\left(g_{i,j,n} - g_{i,-j,n}\right), \tag{5.25}$$

where $g_{i,j,n} = g^{(s)}_{i,j,n} + g^{(a)}_{i,j,n}$.

We calculate the symmetric and anti-symmetric components of model rainfall and OLR from the full time series of the present day CP4A runs. Table 5.2 details the resultant data sets. For reference, it includes details of the TRMM data used by Wheeler and Kiladis (Wheeler and Kiladis, 1999) . We have ample data for time series analysis, which will contain the effects of seasonal variations. Note that table 5.2 contains certain, equivalent parameter values for the TRMM data of Wheeler and Kiladis. For a fuller comparison and the appropriate calculations, refer to Appendix A.

Prediction	Symmetry	T/ hr	L/km	N_t	N_x
OLR	even	1	4.5	69840	2000
OLR	odd	1	4.5	69840	2000
Rainfall	even	0.25	4.5	69840	2000
Rainfall	odd	0.25	4.5	69840	2000
Wheeler and Kiladis	even	12	280	13140	144
Wheeler and Kiladis	odd	12	280	13140	144

Table 5.2: Summary of the 4km resolution CP4 data used in the present chapter, with equivalent parameters for data of Wheeler and Kiladis (Wheeler and Kiladis, 1999). See also Appendix A.

We now define meridional averages as follows

$$g^{(s)}_{i,n} \equiv \frac{1}{2M}\sum_{j=1}^{M}\left(g_{i,j,n}+g_{i,-j,n}\right), \quad g^{(a)}_{i,n} \equiv \frac{1}{2M}\sum_{j=1}^{M}\left(g_{i,j,n}-g_{i,-j,n}\right). \quad (5.26)$$

Hovmöller plots of the now "$x-t$" data are shown in figure 5.3 (Note, $g^{(s)}_{i,n}$ may be distinguished from $g^{(s)}_{i,j,n}$ by the occurrence of the j subscript in the latter). A window of such a long time series is not useful in looking for features with frequency timescale smaller than the seasonal scale. In fact, it is hard to see anything propagating at all. However, anything masked by the contours in these plots will reveal itself in Fourier space. The seasonal signal, however, is reassuringly clear, note.

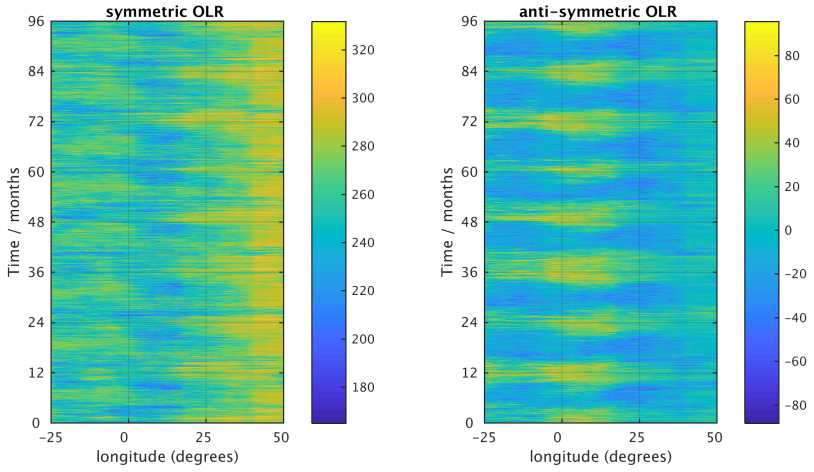

Figure 5.3: Hovmöller plots of the raw symmetric and anti-symmetric OLR, for a 10yr. period derived from CP4.

5.4.2 Windowing

Ideally, fast Fourier transforms (FFTs hereafter) should be applied to data which contains integer periods of the modalities it hypothesised to contain. With many possible modalities and relative phases, it is clearly impossible to ensure that the captured data is fully periodic e.g. by varying the spatial range over which measurement takes place. For even if the acquisition interval were adjusted to capture some wavelengths without abrupt cut-off, there would be other wavelengths that would be captured non-periodically. Spectral leakage (essentially, blurring of peaks in Fourier space) is the consequence of a failure to capture data periodically. Structures appear more diffuse than they might with more careful capturing- spectral power is said to have bled or leaked to other frequencies. The practice of *windowing* reduces this blurring of data. In the present context, windowing in x would involve multiplying data in the sampled interval by some window function, $h(x)$, which decays or tapers to zero at the limits of the domain, eliminating- or smoothing- its sharp spatial boundaries. There are a range of functions $h(x)$ designed to improve the appearance of data in Fourier space in different ways. We choose to avoid the use of windowing, and to make a retrospective assessment of its potential impact on IMPALA data, in our discussions, in section 5.7. We note that Wheeler and Kiladis report tapering their data's spatial window.

5.4.3 Data Analysis in Reciprocal or Fourier Space

We are now ready to transform the data into Reciprocal or Fourier space. We do this using the 2D FFT function in Matlab. Application of Matlab's native transform utility fft2 provides us wavenumber-frequency, "Fourier space" data. Let us denote discrete, complex data $\hat{g}^{(s)/(a)}_{f,k_x}$

$$\hat{g}^{(s)/(a)}_{f,k_x} \equiv \mathbb{F}_2\left(g^{(s)/(a)}_{i,n}\right), \quad \hat{g}^{(s)/(a)}_{f,k_x} \in \mathbb{C}. \tag{5.27}$$

Often, we will consider the modulus squared of this quantity, usually termed the spectral power

$$G^{(s)/a)}_{f,k_x} \equiv |\hat{g}^{(s)/(a)}_{f,k_x}|^2. \tag{5.28}$$

This quantity is usually expressed in decibels, dB. Specifically, plots of spectral power measure the latter as $20\log_{10}(|\hat{g}^{(s)/(a)}_{f,k_x}|)$ Above, discrete wavenumber is denoted k_x, with units km^{-1}, discrete frequency is denoted f, with units hr^{-1} and $f = \frac{n_f}{TN_t}$, with $n_f \in [0,(N_t-1)]$ and $k_x = \frac{2\pi n_x}{LN_x}$, with $n_x \in [0,(N_x-1)]$.

It will often be convenient to use dimensionless zonal, or planetary, wavenumber

$$s \equiv \frac{2\pi R_e \cos(\varphi)}{\lambda} = R_e k_x. \tag{5.29}$$

Here the disturbance has wavelength λ and we have adapted to the equator, $\varphi = 0$. The terrestrial radius is taken as $R_e = 6371$km.

Aliasing in the variable k_x (f), was eliminated by folding the power spectrum along the k_x axis. Aliasing in frequency was similarly removed from the data, however, only positive ω is displayed throughout this chapter. In summary, all data considered in the sequel correspond to the following ranges of discrete conjugate, Fourier, variable after aliasing has been removed

$$\begin{aligned} f &= \frac{n_f}{TN_t}, \quad n_f \in \mathbb{Z}^+, \quad n_f \in [0, \frac{N_t}{2}], \\ k_x &= \frac{2\pi n_x}{LN_x}, \quad n_x \in \mathbb{Z}, \quad n_x \in [-\frac{N_x}{2}, \frac{N_x}{2}], \\ s &= \frac{2\pi R_e n_x}{LN_x}, \quad n_x \in \mathbb{Z}, \quad n_x \in [-\frac{N_x}{2}, \frac{N_x}{2}]. \end{aligned} \tag{5.30}$$

It is immediate from the above that all our Fourier space data should be represented on a mesh with the following spacings:

$$\Delta f = \frac{1}{TN_t}, \quad \Delta k_x = \frac{2\pi}{LN_x}, \quad \Delta s = \frac{2\pi R_e}{LN_x}. \tag{5.31}$$

5.4.4 Red Background Filtration

Once aliasing has been removed, the broad nature of the resulting spectrum in Fourier space was observed to be red in both k_x and f. Accordingly, N_{121} cycles of $1-2-1$ filtration were applied in both k_x and f. A single step of this power-conserving filtration may be defined as

$$G_{f,k_x} \to \frac{1}{8}\left(G_{f+\Delta f,k_x} + 2G_{f,k_x+\Delta k_x} + 4G_{f,k_x} + 2G_{f-\Delta f,k_x} + G_{f,k_x-\Delta k_x}\right). \tag{5.32}$$

It is easy to show that the process of $1-2-1$ filtration conserves the total power (across all f, k_x) in the spectrum.

Denote the red spectrum corresponding to G_{f,k_x} by R_{f,k_x}. R_{f,k_x} for symmetric/anti-symmetric OLR and rainfall, expressed in dB, is shown in figure 5.4 for $N_{121} = 150$. For their experimental data, Wheeler and Kiladis effectively take $N_{121} = 10$. We note that the CP4 background spectra in figure 5.4 shows evidence of the diurnal variation, which is not visible in any data of Wheeler and Kiladis, though these authors do state that the first few harmonics of the diurnal variation were removed.

$1-2-1$ filtration is analogous to smoothing using a running average. It is therefore informative to consider the effective range, or smoothing length, corresponding to $N_{121} = 2n$, $n \in \mathbb{Z}^+$ cycles, or applications. Let us work in one dimension, say the variable f. For a single cycle, the weights applied at f, to data at $f-\Delta f$, f and $f+\Delta f$ are $1\times\frac{1}{4}, 2\times\frac{1}{4}, 1\times\frac{1}{4}$ respectively. For two cycles, the cumulative weights for combining data at f, with data at $f-2\Delta f$, $f-\Delta f$, f, $f+\Delta f$ and $f+2\Delta f$ are

$1 \times \frac{1}{16}, 4 \times \frac{1}{16}, 6 \times \frac{1}{16}, 4 \times \frac{1}{16}, 1 \times \frac{1}{16}$ respectively, which may be written $1 \times \frac{1}{2^4}, 4 \times \frac{1}{2^4}, 6 \times \frac{1}{2^4}, 4 \times \frac{1}{2^4}, 1 \times \frac{1}{2^4}$ and, in general, for $2n$ cycles, the "stencil" coefficients will be the binomial expansion coefficients of the expression $(1+p)^{2n}$ with $p = \frac{1}{2}$, namely:

$$\frac{2n!}{(2n-r)!r!} \times p^r (1-p)^{(2n-r)}, \quad p = \frac{1}{2}. \tag{5.33}$$

Let us use the standard deviation of the binomial distribution to characterise an effective smoothing length, or range, of the $1-2-1$ filtration:

$$\sigma = \sqrt{2n(1-p)p} = \sqrt{2n \times \frac{1}{2} \times \frac{1}{2}} = \sqrt{\frac{n}{2}} = \sqrt{\frac{N_{121}}{4}}. \tag{5.34}$$

The characteristic ranges, $[\Delta f]$, of the smoothing in Fourier space, for the following choices of N_{121} are therefore incremented by approximately equal amounts:

$$\begin{aligned} N_{121} &= 10, \qquad [\Delta f] = \sqrt{\frac{10}{4}} \approx 1.5, \\ N_{121} &= 50, \qquad [\Delta f] = \sqrt{\frac{50}{4}} \approx 3.5, \\ N_{121} &= 250, \qquad [\Delta f] = \sqrt{\frac{250}{4}} \approx 8. \end{aligned} \tag{5.35}$$

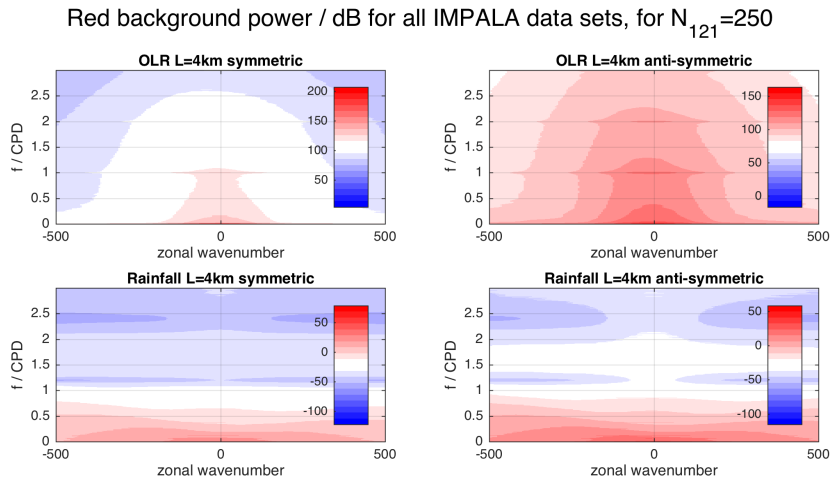

Figure 5.4: Red background spectra of all CP4 data shown in figure 5.3, displayed over a restricted region of Fourier (zonal wavenumber-frequency, $s-f$) space. Frequency is shown in cycles per day (CPD, day^{-1}). Left (right) panels show symmetric (antisymmetric) data. Top row $L = 4$km OLR, Bottom row, $L = 4$km rainfall. Power is expressed in decibels (dB). $N_{121} = 150$ for all data shown here.

Once a red background spectrum has been determined, it is possible to remove it from the original transform, by real division

$$G_{f,k_x} \to \frac{G_{f,k_x}}{R_{f,k_x}}, \quad \hat{g}_{f,k_x} \to \frac{\hat{g}_{f,k_x}}{R_{f,k_x}}, \tag{5.36}$$

which, in the case of the power, helps to identify significant peaks. Broadly, for the slow, long wavelength data close to the origin in Fourier space, when more $1-2-1$ smoothing has been applied (i.e. when a larger value of N_{121} has been used), the more signal remains, after removal of the background. Later, we choose the level of statistical significance in background-corrected spectra: this is done in relation to the chosen value of N_{121}. The key features of all our results (i.e. background and statistically filtered spectra) are robust: a range of values of the statistical cut-off and N_{121} all reproduce produce them.

Figure 5.4 shows the red background power, expressed in decibels (dB) for OLR and rainfall, for the region $s \in [-500, 500]\text{km}^{-1}$, $f \in [0, 3]$CPD. Consider the OLR red spectra spectra (top). These spectra exhibit qualitative similarity- all OLR spectral power lies in a similar interval. Consider the rainfall data (bottom two panels). These spectra clearly correspond more closely in shape to the experimental data of Wheeler and Kiladis.

5.4.5 Diurnal and Annual Cycle Filtration

Given the time span of all data sets considered, the signal associated with the diurnal cycle in CP4 may be regarded as periodic and coherent, with period $f_0 = 1$CPD, having a Fourier series expansion (Arfken, 1966)

$$g(x,t) = \sum_{n=-\infty}^{\infty} A_n(x) e^{in\omega_0 t}, \quad \omega_0 = 2\pi f_0, \tag{5.37}$$

where

$$A_n = A_{-n}^* = \frac{1}{2}\int_{-1}^{+1} g(x,t) e^{-i\omega_0 t} dt, \tag{5.38}$$

which, when Fourier transformed, gives a signal comprised of equi-spaced impulses

$$\begin{aligned} \hat{g}(t,k_x) &= \frac{1}{\sqrt{2\pi}}\int_{-\infty}^{\infty}\left(\sum_{n=\infty}^{\infty} A_n e^{-in\omega_0 t}\right) e^{in\omega t} dt, \\ &= \sum_{n=-\infty}^{\infty} A_n \left(\frac{1}{\sqrt{2\pi}}\int_{-\infty}^{\infty} e^{i(\omega - n\omega_0)t} dt\right), \\ &= \sum_{n=-\infty}^{\infty} A_n \delta(\omega - n\omega_0), \end{aligned} \tag{5.39}$$

where we have used a representation of the Dirac delta function (Arfken, 1966). Accordingly, we see in e.g. figure 5.4, a set of peaks, located

at $f = n$, $n \in \mathbb{Z}^+$ across the range of s, which we associate with the diurnal cycle. Once the red background was removed, the first ten Fourier coefficients of the diurnal cycle were identified and also removed manually from the all CP4 data sets, simply by removing data across the range of s at frequencies in a narrow interval $f = n \pm 0.05$CPD.

We estimate that the annual cycle in the CP4 sample corresponds to $\omega = \frac{2\pi}{365\times24\times60\times60} \approx 2 \times 10^{-7}$ rad s^{-1} or $f = \frac{1}{365}$CPD, which is too small to be resolved in any of the CP4 sets we shall shortly present. Hence, we take no steps to filter annual variation.

5.4.6 Statistical Significance

We calculate the mean, E, and standard deviation, σ, of the Fourier space rainfall and OLR. We retain statistically significant data only, according to the rule:

$$G_{f,k_x} < \left(E + \frac{5}{2}\sigma\right) \implies \left(G_{f,k_x} \to 0\right), \forall f, k_x. \tag{5.40}$$

As we have already outlined, any decision about the level of statistical significance used should be made in conjunction with the level of red background filtration applied i.e. the value of N_{121}. Here, $N_{121} = 50$, recall. As one would expect, applying larger levels of 121 filtration produces a smoother red background. Dividing-out smoother data leaves a larger level of residual signal, which should therefore be subject to screening for increased statistical significance. For example, data for $N_{121} = 250$ obtained with the rule $G_{f,k_x} < \left(E + \frac{5}{2}\sigma\right) \implies \left(G_{f,k_x} \to 0\right)$ and $N_{121} = 10$ using the rule $G_{f,k_x} < \left(E + \sigma\right) \implies \left(G_{f,k_x} \to 0\right)$ produces results which are very similar indeed.

Figure 5.5 shows statistically significant, Fourier space OLR and rainfall, after division by their respective red backgrounds. Note that the discretisation interval, Δs, is now particularly apparent in the data (as a granularity) as is the continued presence of a diurnal cycle.

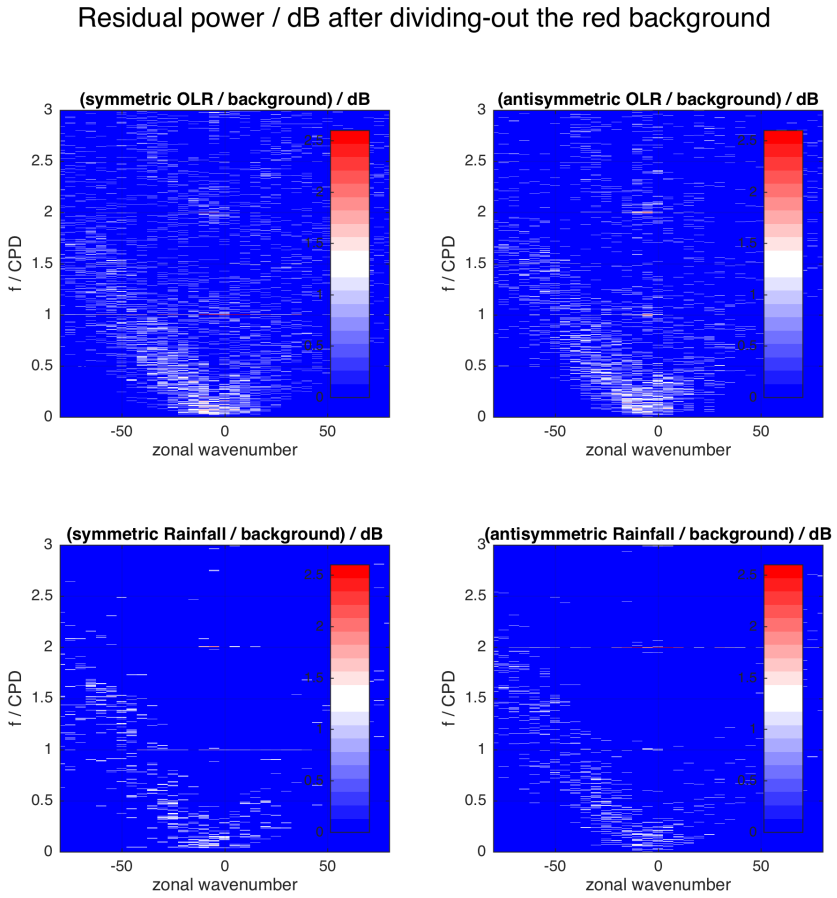

Figure 5.5: Statistically significant residual power, expressed in decibels (dB), after division by the respective red background of all CP4 data shown in figure 5.4, displayed over a restricted region of Fourier (zonal wavenumber-frequency, $s - f$) space. Left panels show symmetric data, right panels show anti-symmetric. Top row $L = 4$km OLR, bottom row $L = 4$km rainfall.

Figure 5.5 shows the restricted range of frequency $f < 3$CPD. This interval contains the maximum of the surviving power. This Fourier space data derives from approximately a decade of $x - t$ Hovmöller data we emphasise. Data is clearly skewed with a majority of wave power propagating west. Under closer examination (see below), over an extended range of $f \in [0, 10]$CPD a modality which we nominate a fast gravity wave may also be observed. We return to this matter in detail in section 5.6.

5.5 Results 1: Planetary Waves

In this section we principally address correlations with dispersion relations, based upon 10yrs of CP4 data, in the frequency range $f \in [0, 3]$CPD. However, it is necessary briefly to contextualise, by considering the larger interval $f \in [0, 10]$CPD. The latter interval will be considered in detail in the section 5.6, next. Henceforth, we use "low frequency" to refer to the interval $f \in [0, 10]$CPD.

5.5.1 Kelvin Waves and Matsuno Modes

Recall, the equatorial atmosphere, considered as a shallow layer of effective depth H, is widely believed to support long wavelength modalities which couple to convection. In figures 5.6 and 5.7, the certain modal dispersion relations for upper branch, lower branch Matsuno and Kelvin waves are superposed on the filtered, symmetric and anti-symmetric parts of the CP4 data for the OLR data, and rainfall, respectively.

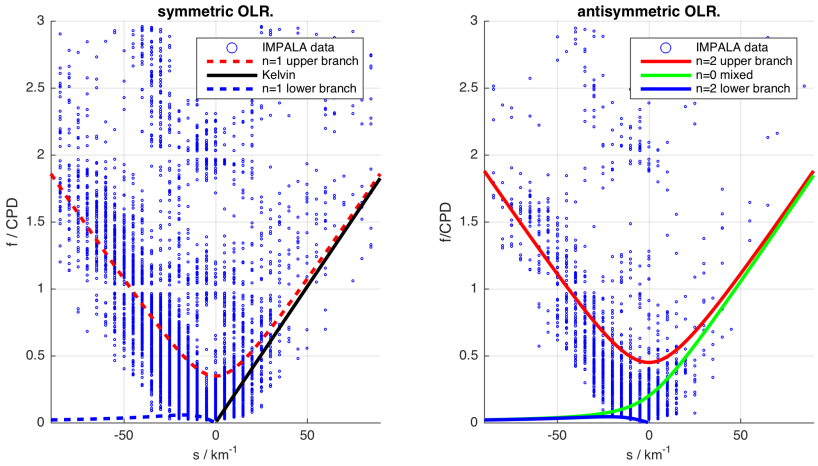

Figure 5.6: 4 km resolved, symmetric and antisymmetric OLR with Matsuno mode, Kelvin wave and fast gravity wave dispersion relations superposed. Following figure 5.1, broken lines indicate odd mode number, n, broken lines indicate even mode number, n. Red lines correspond to upper branch modalities, blue the lower branch, and the solid green line corresponds to the mixed gravity-Rossby mode. The solid black lines correspond to Kelvin wave modes. Odd n dispersion relations pair with zonally symmetric data, even pair with anti-symmetric. All dispersion relations correspond to $H = 9$m. Note, the domain has been truncated to reflect our interest in low-frequency, large scale planetary waves.

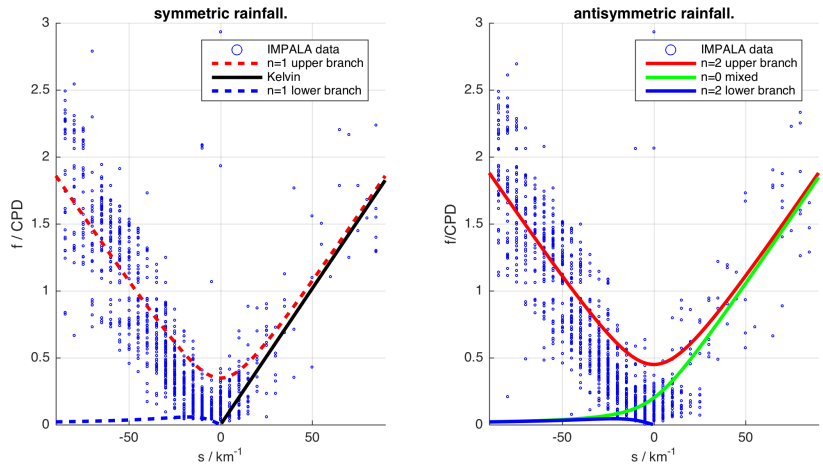

Figure 5.7: 4km resolved, symmetric and antisymmetric rainfall with Matsuno mode, Kelvin wave and fast gravity wave dispersion relations superposed. Following figure 5.1, broken lines indicate odd mode number, n, broken lines indicate even mode number, n. Red lines correspond to upper branch modalities, blue the lower branch, and the solid green line corresponds to the mixed gravity-Rossby mode. The solid black lines correspond to Kelvin wave modes. Odd n dispersion relations pair with zonally symmetric data, even pair with anti-symmetric. All dispersion relations correspond to $H = 9$m. Note, the domain has been truncated for interest in low-frequency, large scale planetary waves.

Broadly, the resolution in Fourier space of our CP4 data appears adequate to resolve east-propagating Kelvin, bi-directional upper branch, bi-directional lower branch Matsuno modes, which favour westward motion and an intriguing west propagating non-dispersive mode. For such disturbances, the dispersion relations are approximated by equations 5.2, 5.11 and 5.12 respectively. In each, H, the effective depth of the atmospheric layer, enters via parameter $c = \sqrt{gH}$.

In more detail now, figures 5.6 and 5.7 display a striking correlation, in the higher wavelength and frequencies, with $n = 1, 2$, westward-propagating upper branch Matsuno modes - also known as "Westward inertio gravity waves" (WIG, hereafter). There is a clear envelope of wave speeds, which appear in both the symmetric and anti-symmetric plots. Whilst there is some evidence for Kelvin wave modes in figures 5.6 and 5.7, the signal is weak compared to that of the WIG. There is also a large, non-dispersive signal in the low frequency, which cannot be explained by either the WIG (whose curves diverge from the model data at low s) or the Kelvin wave, whose curve sits below the data at low s. In the anti-symmetric plots, the $n = 0$ mixed Rossby-gravity (MRG, hereafter) does correlate well with the low frequencies, but does not satisfactorily explain all of the signal, as there is again a "wave dispersion

gap" in the westward propagating low frequencies. Notably, it appears there is no signal at all corresponding to the Rossby wave spectra. We hypothesise that we are filtering our these waves with our domain choice- see figure 5.2.

5.5.2 Fast Gravity Waves

At this stage, we have tentatively i) confirmed the existence of the Kelvin wave and WIG, in CP4, and ii) found some evidence for a MRG in OLR and rainfall data, at what we now designate low frequencies, $f \in [0, 3]$CPD. It is useful to estimate the speed of the low frequency, west propagating non-dispersive wave also observed

$$C_g^s \equiv \frac{d\omega}{dk} \rightarrow \frac{\Delta\omega}{\Delta k} = 2\pi R_e \frac{\delta f}{\delta s} \approx -13\text{ms}^{-1}. \tag{5.41}$$

Now, there is a second, large signal, in the lower frequencies, which does not appear to correlate to any expected wave dispersions. This signal emerges if we zoom out from figures 5.6 and 5.7, to the larger Fourier domain, $f \in [0, 10]$CPD: see figures 5.8 and 5.9. A remarkable, new, linear data correlation in the OLR appears at frequencies $f \in [0, 10]$CPD. Its dispersion relation seems linear and it appears in both the high and low frequencies bands. To guide the eye, we have superposed solid black lines of constant speed in figure 5.8, with corresponding legend "Fast gravity". The waves represented here propagate in both an easterly and a westerly direction, with approximately the same group speed. They therefore cannot be classified as Kelvin waves.

We estimate the group speed for the non-dispersive waves, fast gravity waves apparent in figure 5.8, which are presumably relatively fast-propagating gravity waves as

$$C_g^f \equiv \frac{d\omega}{dk} \rightarrow \frac{\Delta\omega}{\Delta k} = 2\pi R_e \frac{\delta f}{\delta s} \approx \pm 45\text{ms}^{-1}, \tag{5.42}$$

approximately three times greater than C_g^s. Importantly, there seems to no correlation to these waves in the rainfall spectra, suggesting that rainfall does not project onto such fast moving disturbances, which will be the crux of our investigations in §5.6. This is perhaps not surprising, as no know meteorological convective system propagates at so large a speed.

In summary, OLR and rainfall spectra both show clear correlation and cross-correlation with accepted dispersion relations, with values of $H \approx 9$m, and we infer the existence in CP4 of convectively-coupled Matsuno and Kelvin modes. We deem the predominance of data for $k < 0$ to rule-out a westward WIG as a cause and that OLR spectral plots (figures 5.8 actually show additional activity in the $45\text{m}s^{-1}$ and 13m^{-1} bands, which is consistent with the deepest tropospheric mode ($m = 1$) and tropospheric mode $m = 3$ respectively (recall, from Chapter

1, $c \sim N/m$ and $C_g^f \approx 3C_g^s$). Moreover, there is literature to support the relevance to convection of each of these two particular modalities (Lane & Reeder, 2001), note. Highly significantly is the fact that the rainfall spectral plots in figures 5.9 show activity at 13m^{-1} but none at 45m^{-1}.

On the basis of the spectra alone, then, we infer that two non-dispersive gravity wave modes exist in the CP4 data and influence OLR, that the fast, deeper mode may be a response to rainfall, whilst the slower mode 3 could be coupled with the rainfall. (However, alternative explanations for our fast spectral data exist, as we shall see.) The fast mode is bi-directional, the slower is west propagating. We devote our subsequent efforts to illuminating the properties of these two particular modalities, which we henceforth designate slow and fast gravity waves.

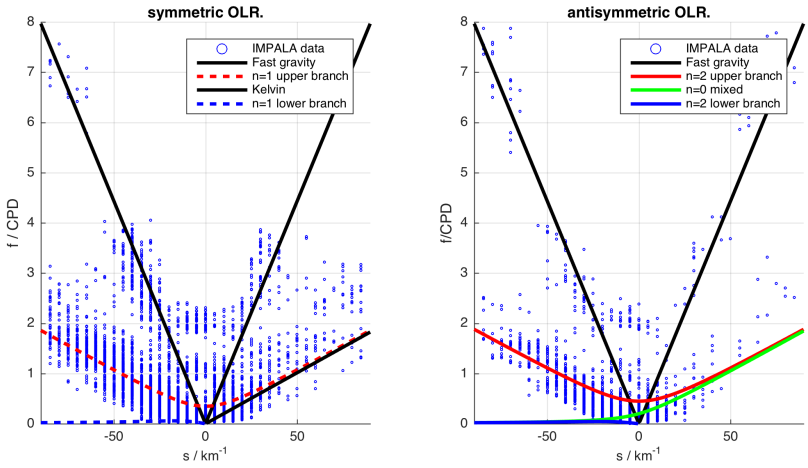

Figure 5.8: 4km resolved, symmetric and antisymmetric OLR with Matsuno mode, Kelvin wave and fast gravity wave dispersion relations superposed. Following figure 5.1, broken lines indicate odd mode number, n, broken lines indicate even mode number, n. Red lines correspond to upper branch modalities, blue the lower branch, and the solid green line corresponds to the mixed gravity-Rossby mode. The solid black lines correspond to Kelvin wave modes. Odd n dispersion relations pair with zonally symmetric data, even pair with anti-symmetric. All dispersion relations correspond to $H = 9\text{m}$. Note, the domain is now larger than that of figure 5.6.

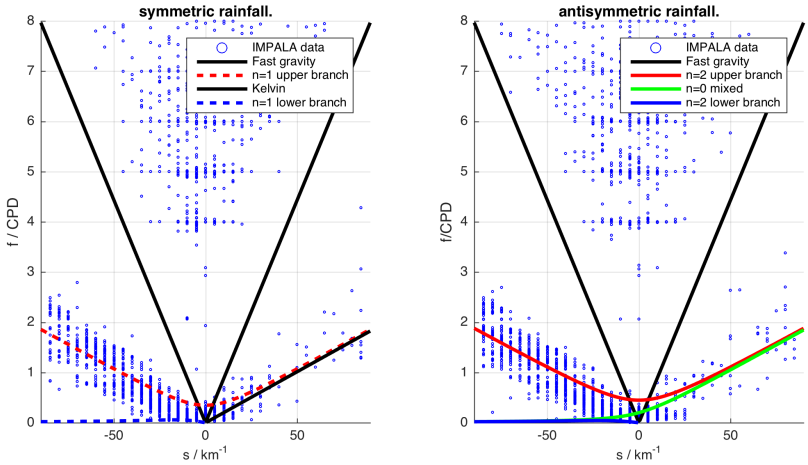

Figure 5.9: 4km resolved, symmetric and antisymmetric rainfall with Matsuno mode, Kelvin wave and fast gravity wave dispersion relations superposed. Following figure 5.1, broken lines indicate odd mode number, n, broken lines indicate even mode number, n. Red lines correspond to upper branch modalities, blue the lower branch, and the solid green line corresponds to the mixed gravity-Rossby mode. The solid black lines correspond to Kelvin wave modes. Odd n dispersion relations pair with zonally symmetric data, even pair with anti-symmetric. All dispersion relations correspond to $H = 9$m. Note, the domain is now larger than that of figure 5.7

5.6 Results 2: Fast Gravity Waves

Having diagnosed planetary waves in the high resolution CP4 runs, in §5.5, we now attempt to understand the dynamics of the fast waves revealed in the CP4 spectra. To interpret requires hypotheses: we also recognise our overall conclusions will rely heavily on the weight of confidence we attach to the competing data. Also, the nature of the slow wave provides valuable context for an understanding of the fast, so we shall need to continue to consider it.

In section 5.5, we only investigated two fields -rainfall and OLR- in spectral space, using accepted dispersion relations. The appearance of wave features in thermodynamic fields allows us to conclude that coupled waves exist in the model. However, to draw further conclusions on the dynamics we must investigate other dynamical fields. Certainly, investigation of the vertical velocity, w, and temperature, θ (the fields used to understand forced wave dynamics in chapters 2,..4, note), at multiple altitudes, will illuminate the spatial and temporal structure of the waves. Using multiple thermodynamic and dynamic fields, we now aim to extract fast gravity waves, aiming to construct a composite picture of

the waves, in physical space. In order to reduce computational demand, we truncate the full data set of section 5.5 for all fields, to a single year, arbitrarily chosen to be 2000. This choice was made on recommendation by colleagues at the University of Leeds experienced in processing and using CP4 data.

It is important to map-out and contextualise our strategy in this section, as a wealth of data will now appear rapidly. We will now proceed by inverting the Fourier transform of selectively filtered, west-propagating fields, to identify regions in physical space. Note that this filtration implicitly relies on an interpretation of the spectral data. Correlating the inverse FFT of filtered data with raw OLR and rainfall data in physical space-time allows us to locate candidate convection wave events in x-t. Additionally, we examine filtered dynamical fields of w and θ on two levels (mid and upper troposphere) in order assist our diagnosis of the dynamics of convectively coupled waves. For instance, correlated, coherent w and θ fields denote convection activity. In a nutshell, our approach is simple- identify candidate structures in Fourier space then try to pick-out and examine the corresponding fields in physical space. Time constraints limited the number of events which are analysed, but we nevertheless find some interesting results.

5.6.1 Processing

Guided by accepted dispersion relations, we have so far identified regions of Fourier space which contain features of interest. With reference to the spectra of the last section, regions of Fourier space containing signals tentatively arising from the activity of fast or slow, west-propagating (say) gravity waves of speed C_g are now identified as having the reciprocal space coordinates (k_x, ω) such that

$$\begin{aligned} C_g k_x + \Delta &\geq \omega \geq C_g k_x - \Delta, \\ \omega_{max} &\geq \omega \geq 7.2722 \times 10^{-5} \text{rads}^{-1}, \\ 0 &\geq k_x. \end{aligned} \tag{5.43}$$

Here, $\omega = 7.2722 \times 10^{-5}\text{rads}^{-1}$ corresponds to $f = 1$CPD, note. $\Delta = 1.0 \times 10^{-5}\text{rads}^{-1}$, note. For the fast, $m = 1$ mode, $C_g = C_g^f = 45\text{ms}^{-1}$, $\omega_{max} = 7.2722 \times 10^{-4}\text{rads}^{-1}$ corresponding to 10CPD. For the slow, $m = 3$ mode, $C_g = C_g^s = 15\text{ms}^{-1}$, $\omega_{max} = 2.18166 \times 10^{-4}\text{rads}^{-1}$ corresponding to 3CPD.

Unfiltered FFT data *without* its red background removed, lying within the region of Fourier space defined in equation 5.6.2 is multiplied by 1.0, and 0.0 outside, to generate filtered data in Fourier space, which is then reverse aliased and inverse transformed, using Matlab's native ifft2 function. This generates a subset of the original $x-t$ Hovmöller , presumably attributable to activity of the identified by the filtration in equation 5.6.2. A range of tests to e.g. check the influence of the Fourier convolution theorem (Arfken, 1966) etc. were performed on CP4 and benchmark special

cases. We assure the reader that the full process: Fourier transformation, feature filtering and inverse transformation, all work as expected.

The faster features of principal concern are present with equal strength in both symmetric and anti-symmetric data. We deem there is no longer an advantage in separating data into symmetric and anti-symmetric parts, to aid diagnosis: we therefore discard signal parity and work, arbitrarily, with symmetric data henceforth.

5.6.2 Convection-Wave Interaction

We wish to investigate the way in which the model convection dynamics interact with waves. To begin, we verify the moisture fields, namely OLR and rainfall for the *single* chosen year. Figure 5.10 shows the raw power spectrum of OLR (left) for model year 2000, a red background, calculated with 20 cycles of 1-2-1 filtration (middle) and the raw signal divided by the red background (red). This data is reassuringly consistent with that in section 5.5. Two waves are apparent in these spectra: (i) a westward-only propagating wave, with strength at a speed of $13\,\mathrm{ms}^{-1}$ (W_{slow}, hereafter), and (ii) a bi-directional wave with strength at a speed of $45\,\mathrm{ms}^{-1}$ (W_{fast}, hereafter). The strength of the signal is stronger in W_{slow}. However, in figure 5.11, which is equivalent of figure 5.10 but for rainfall, there is no power in W_{fast}, which is consistent with reality, as no known meteorological feature travels at $45\,\mathrm{ms}^{-1}$ - only waves can travel that fast. However, these speed estimates both agree with approximate values of group speeds, $C_g \sim \frac{N}{m}$, of the deepest ($m = 1$) and $m = 3$ modes, note. For example, for $N = 10^{-2}\,\mathrm{s}^{-1}$, $m = 2\pi \;/\; (2 \times 15\,\mathrm{km}$ (twice the height of the tropopause)), $c_g = 50\,\mathrm{ms}^{-1}$. The $m = 3$ mode, of course, simply reduces the speed by a factor 3.

In the w and θ spectra (figures 5.12 and 5.13), both W_{slow} and W_{fast} appear.

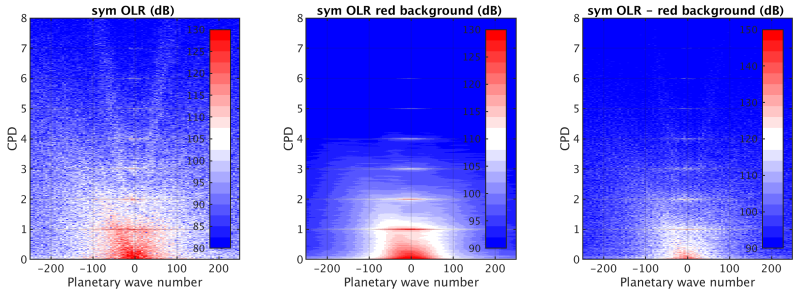

Figure 5.10: The symmetric OLR power spectra (dB) for UM model year 2000. Shown is the raw spectra (left), red background calculated with 20 cycles of 1-2-1 filtering (middle) and the raw spectra with red background removed (right).

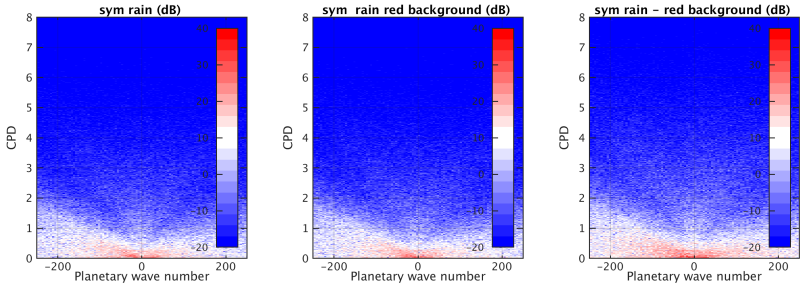

Figure 5.11: As in figure 5.10, but for rainfall.

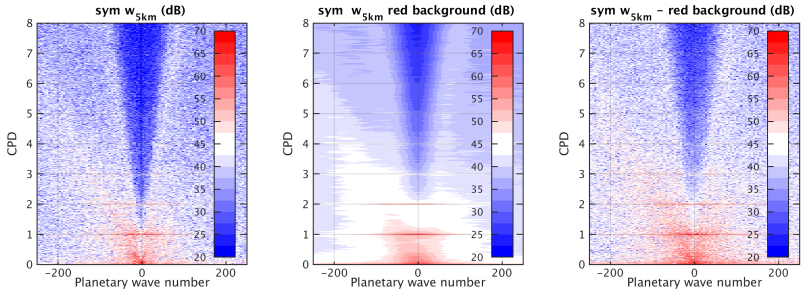

Figure 5.12: As in figure 5.10, but for w at 5 km.

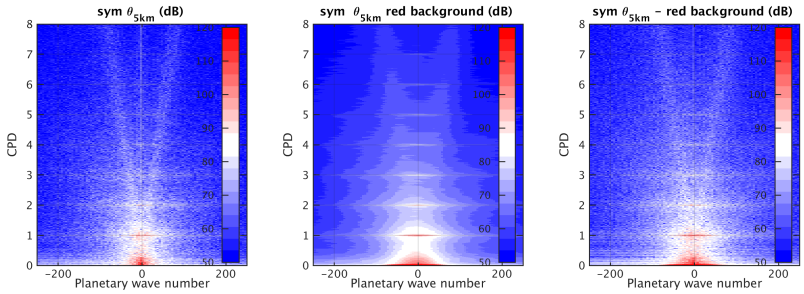

Figure 5.13: As in figure 5.10, but for θ at 5 km.

We now apply two filters to each field in spectral space, in order to isolate W_{slow} and W_{fast}, as shown in figure 5.14. Note, the filters used, defined in equation 5.6.2, take only westward-propagating features, for consistency, and take only faster features which have a frequency larger than 1CPD. The resulting filtered spectra are then inverted, as described previously.

Figure 5.15 shows the Hovmöller raw OLR field (with its diurnal cycle removed) for reference, alongside the corresponding OLR, after is has

been multiplied by the Fourier space filter functions. Figure 5.16 shows contours of the two filtered and Fourier-inverted functions, superposed on top of the raw field. The black solid and dashed lines correspond to $13\,\mathrm{ms}^{-1}$ and $45\,\mathrm{ms}^{-1}$. They are included to guide the eye only. We notice that W_{slow} have larger amplitude than W_{fast} in the filtered OLR, although the amplitude of W_{fast} is not insignificant. This observation suggests that OLR is projecting more strongly onto W_{slow} (as seen in figure 5.10 and in section 5.5). Indeed, when we inspect figure 5.16, it is easy to observe the correlation between the raw OLR and the OLR filtered for W_{slow}, particularly between -10 and 10 degrees longitude. Less easy to spot are $x-t$ regions principally controlled by W_{fast}. Whilst one can identify regions where there is W_{fast} activity only (e.g. at 20 degrees longitude, between days 143 and 145), it is hard to see well-defined wave patterns in the raw OLR. Qualitatively, this supports the hypothesis that the W_{slow} does couple to convection, but W_{fast} is moving too quickly to be interacting with convection.

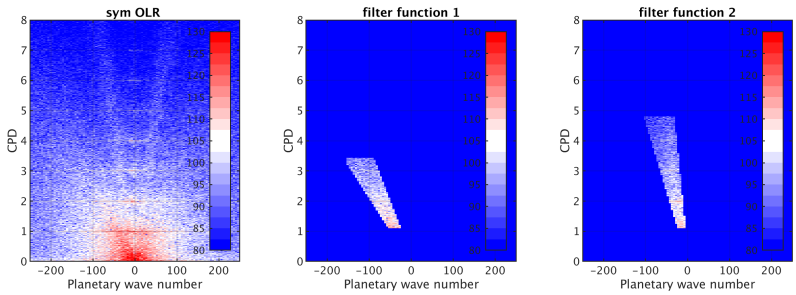

Figure 5.14: The symmetric OLR power spectra (dB) and filtered power after the filter function for W_{slow} and W_{fast} has been applied. Note the filters select in westward propagating Fourier space only and do not collect features with a frequency smaller than one cycle per day (see equation 5.6.2).

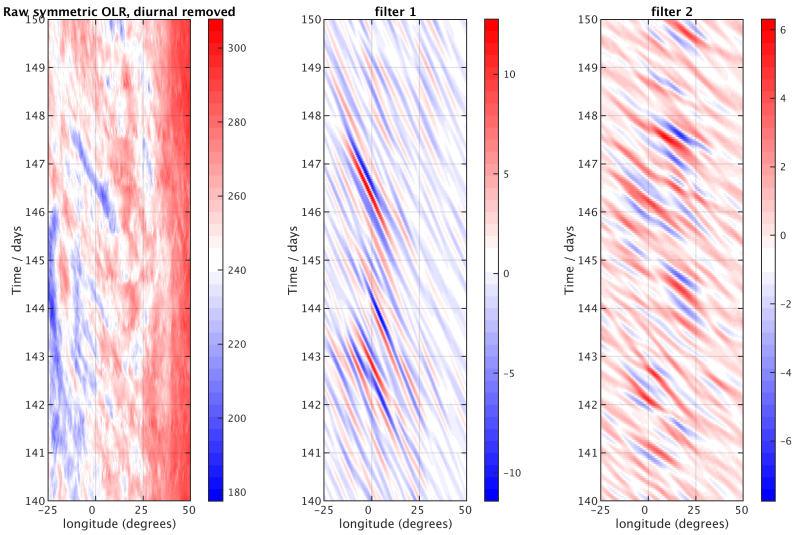

Figure 5.15: 10 day Hovmöller of raw OLR (K) with 8 harmonics of diurnal cycle removed (left) and the Fourier inverted OLR after it has been filtered with functions defined in figure 5.14.

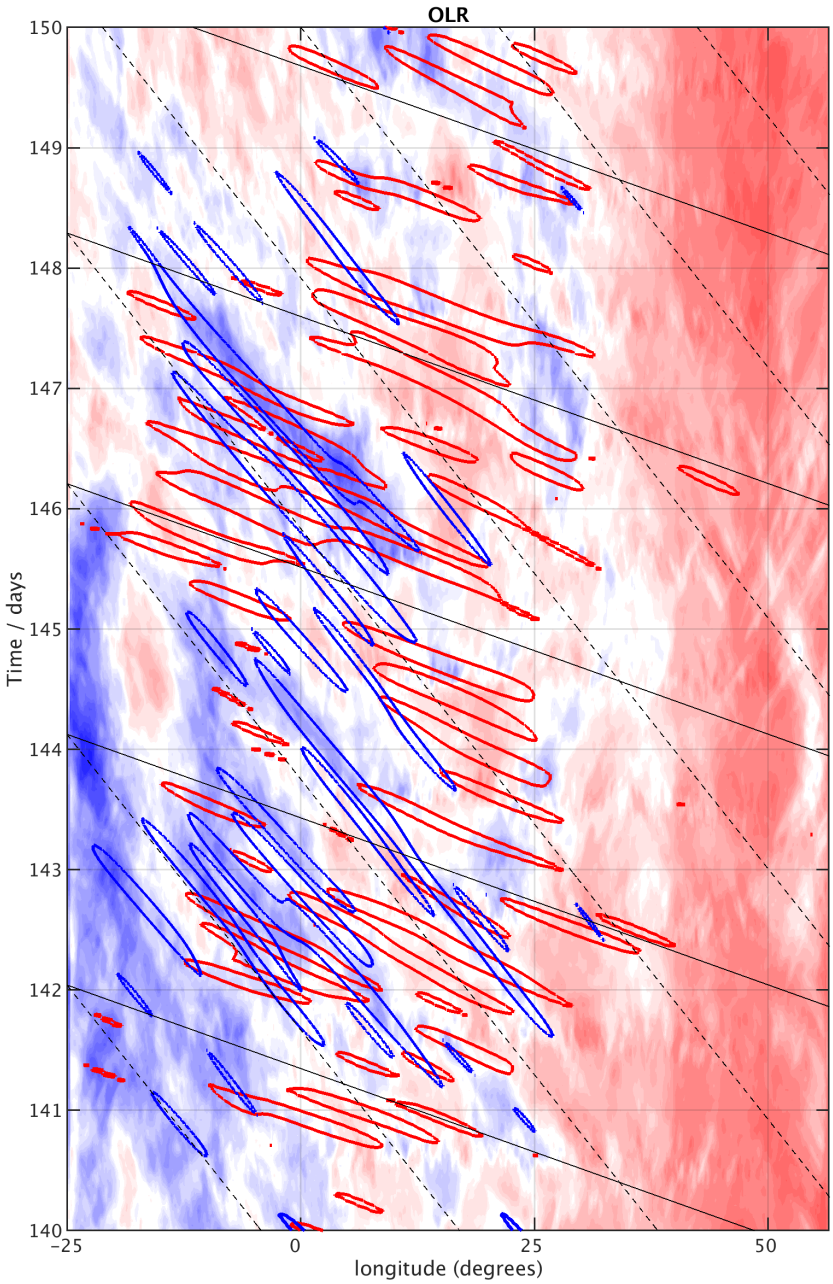

Figure 5.16: As figure 5.15, but the contours of the inverted, filtered W_{fast} and W_{slow} signals are superposed over the raw OLR Hovmöller data and displayed on a single panel. Filled/solid colour shows raw symmetric OLR with 8 harmonics of diurnal cycle removed, blue contours show activity in W_{slow} (filter 1) and red contours show activity in W_{fast} (filter 2). Solid black lines indicate a westward propagation speed of $13\,\mathrm{ms}^{-1}$, dashed black lines indicate a westward-propagation speed of $45\,\mathrm{ms}^{-1}$. The time series chosen corresponds to that of figure 5.15.

We apply the same filters as those depicted in figure 5.14 and defined in equation to rainfall and also to w and θ, now at sectioned mid (5 km) and upper (10 km) levels. Figures 5.17 and 5.18 show the fields filtered for W_{slow} and W_{fast}.

In figure 5.17 (W_{slow}) we see a good correlation between the OLR and the θ (on both levels). However, in the rainfall an w (on both levels), only a single event stands out, suggesting W_{slow} are shallower modes, which only propagate to upper levels in remarkable events.

In figure 5.18 (W_{fast}), the colour bar on the rainfall is an order a magnitude smaller than in figure 5.17, again confirming that rainfall does not couple to W_{fast}.

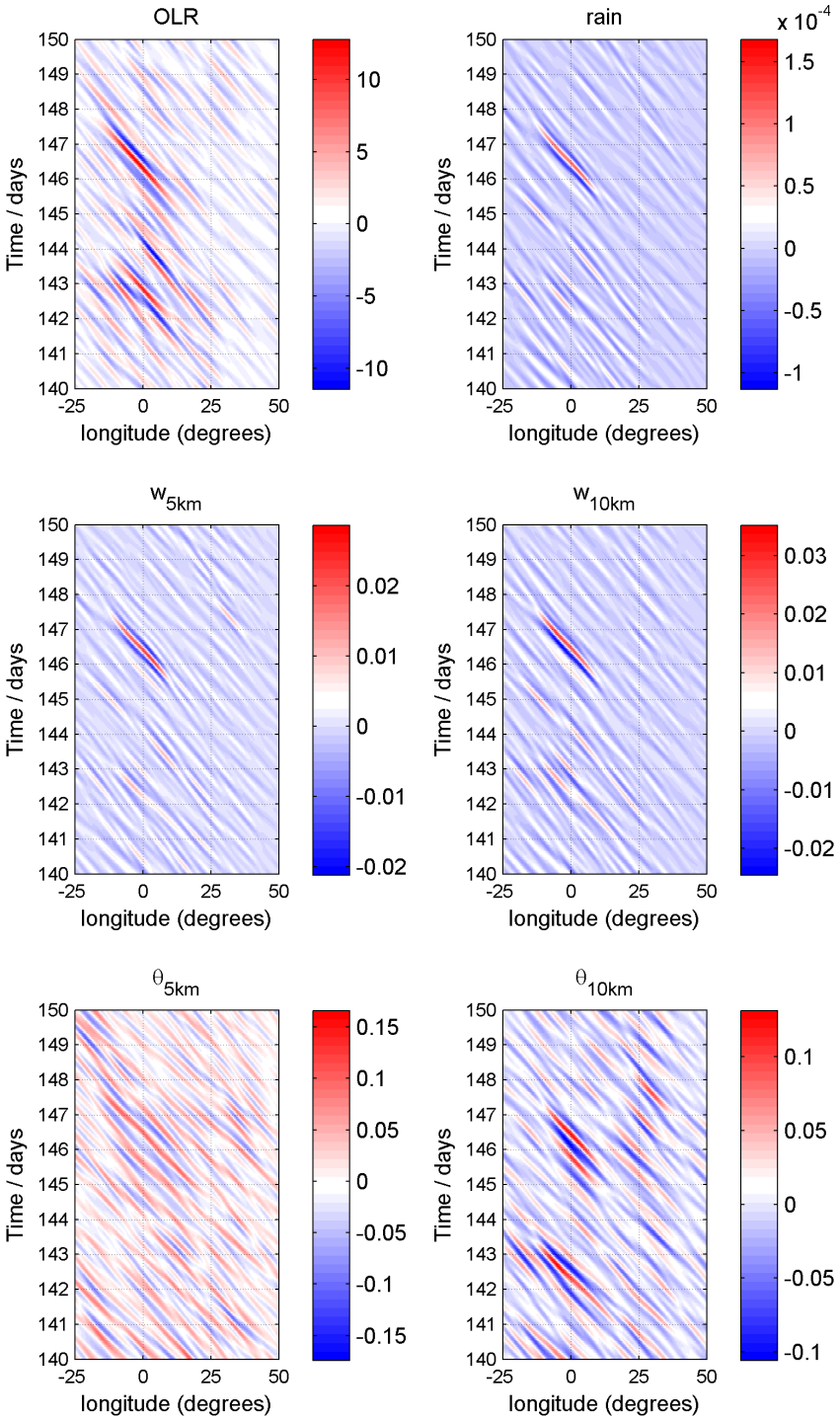

Figure 5.17: Hovmöller of W_{slow} filtered OLR (K), rainfall (mmhr^{-1}), w (ms^{-1}) for 5 km and 10 km and θ (K) for 5 km and 10 km. The filter applied to all fields is identical to filter 1 of figure 5.14. The time series chosen corresponds to that of figure 5.15.

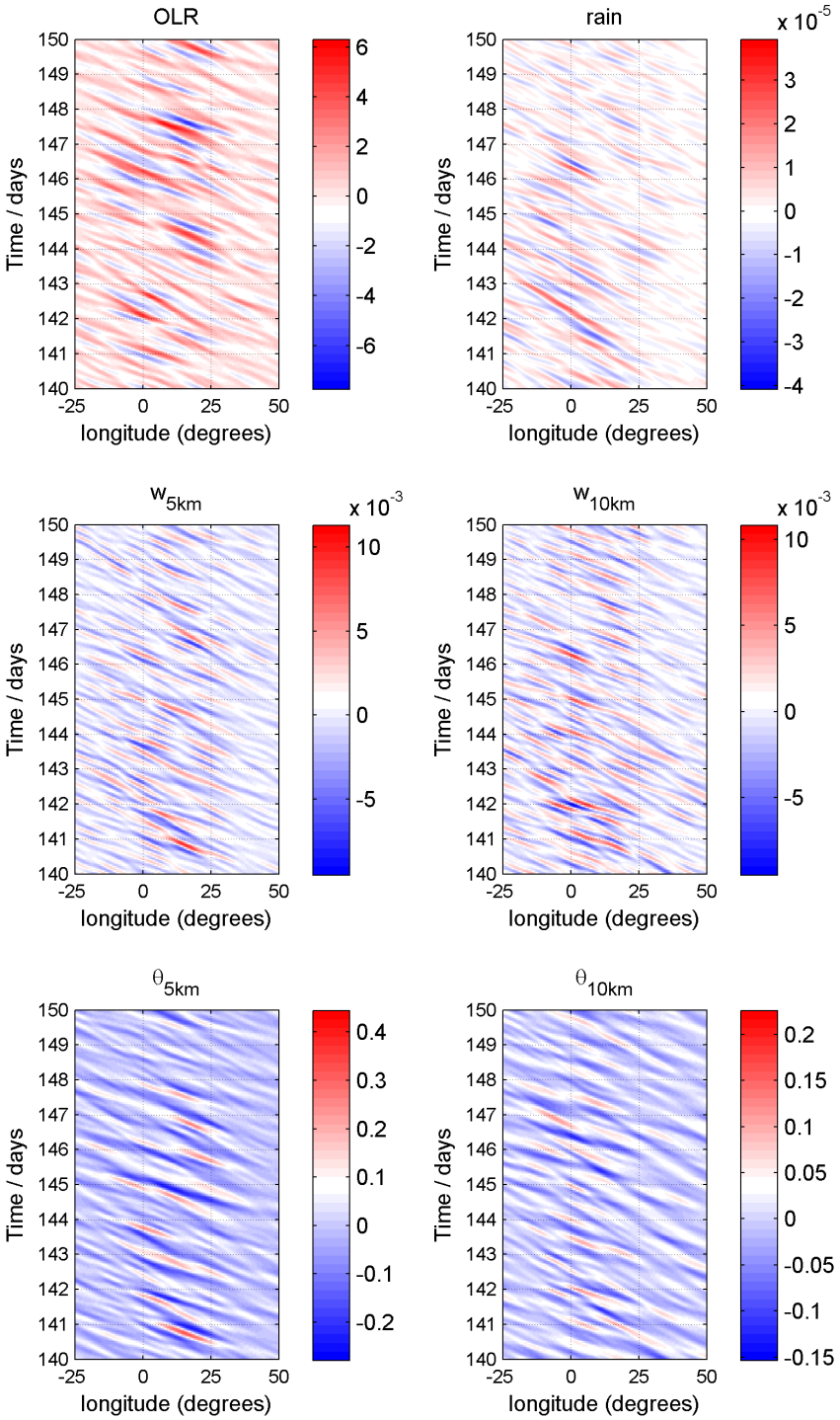

Figure 5.18: Hovmöller of W_{fast} filtered OLR (K), rainfall (mmhr^{-1}, w (ms^{-1}) for 5 km and 10 km and θ (K) for 5 km and 10 km. The filter applied to all fields is identical to filter 2 of figure 5.14. The time series chosen corresponds to that of figure 5.15.

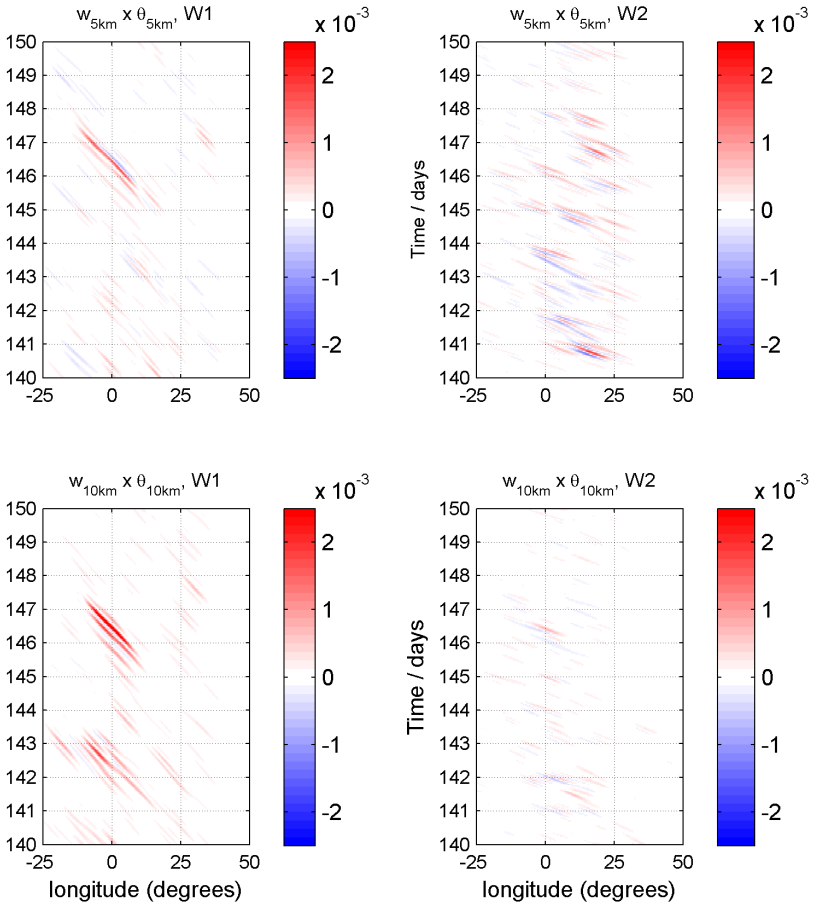

Figure 5.19: Hovmöller plots of the convecting regions of W_{slow} and W_{fast} at heights of 5 and 10 km associated with convection. A region is defined to be convecting if there is a strong coherence between w and θ, i.e. $w \times \theta$ large. The time series chosen corresponds to that of figure 5.15.

We now seek to correlate our dynamical fields, since a strong coherence between w and θ is indicative of convection. Figure 5.19 shows $w \times \theta$ (i.e. a convection field) for W_{slow} and W_{fast} on both levels. In the mid-levels, we see more activity in the faster, deeper mode, which is more distributed. A single event in W_{slow}, as seen in figure 5.17, dominates. This event lives longer than anything in W_{fast}. Generally, however, W_{slow} produces convection which is weaker and also more sparse, over the whole $x-t$ domain than W_{fast}. This observation is somewhat at odds with the stronger coupling of W_{slow} to moisture fields seen in spectra. In the upper levels, activity in W_{fast} is much reduced. In contrast, activity in W_{slow} intensifies in the upper levels.

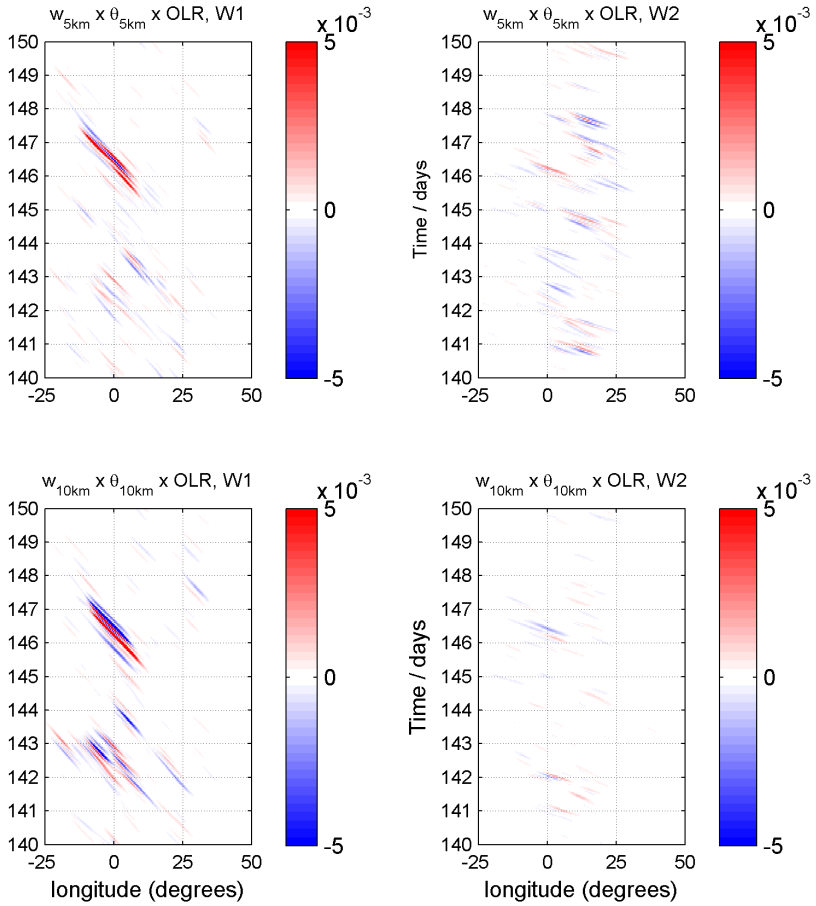

Figure 5.20: Hovmöller plots of the coherence between OLR and convecting (left) and non-convecting regions (right) at heights of 5 and 10 km (as shown in figure 5.19). The time series chosen corresponds to that of figure 5.15.

In figure 5.20, we correlate convection (as defined in figure 5.19) with OLR by considering the product $w \times \theta \times OLR$, to seek a coherence between cloud and convection. We see a strong coherence on both levels for W_{slow}, with a distribution which matches the convection field (figure 5.19). The shallower waves, W_{slow}, which are interacting with convection are producing cloud uniformly, i.e., for shallow waves, where there is convection, there is cloud. It is also clear that the strong event in W_{slow} is producing deep cloud. For W_{fast}, the pattern follows the convection fields; a much reduced signal aloft and a weaker signal in the mid-levels. Apparently, we confirm that the fast, deep wave, W_{fast}, is moving too quickly to interact with the moisture fields. Note, this finding is somewhat at odds with the view that W_{fast} is a deep tropospheric mode.

Further to defining a convection diagnostic field ($w \times \theta$), we can define

a wave-field diagnostic field $w \times \frac{d\theta}{dt}$. For each of W_{slow} and W_{fast}, on both vertical levels, we plot the wave-field figures 5.21 and 5.22. In the bottom panels of figures 5.21 and 5.22, we perform a running average, in the x-direction, on the convection and wave fields. The range of this running average filter was chosen to correspond to a wavelength which was calculated from the gravity wave dispersion relation, with C_g chosen from inspection of the OLR spectra- see discussions immediately after equation 5.6.2 in section 5.6.1.

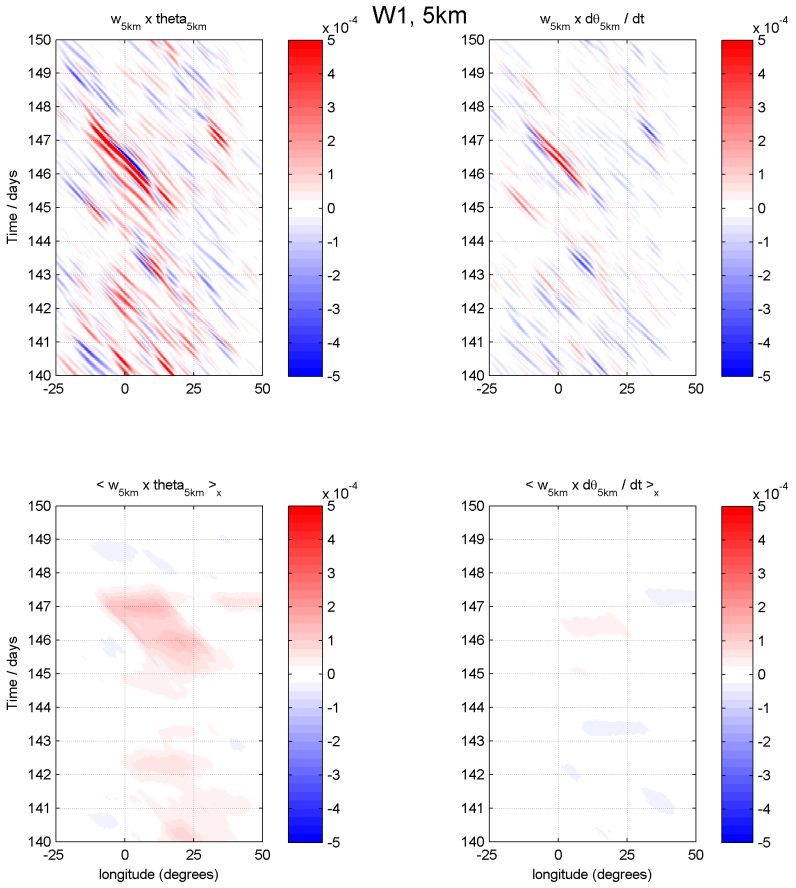

Figure 5.21: Hovmöller plots of the convecting regions ($w \times \theta$ - left) and non-convecting regions ($w \times \frac{d\theta}{dt}$ - right) of W_{slow}. The top panels show the filtered field, the bottom panels show the same field after application of a horizontal running average in x, with wavelength equal to the wavelength has been applied. The range of the running average was chosen to correspond to a characteristic wavelength of W_{slow}, determined using the gravity wave dispersion relation $c_p = \frac{\omega}{k}$ and a wavespeed c_p calculated from the wave signal in the OLR power spectra.

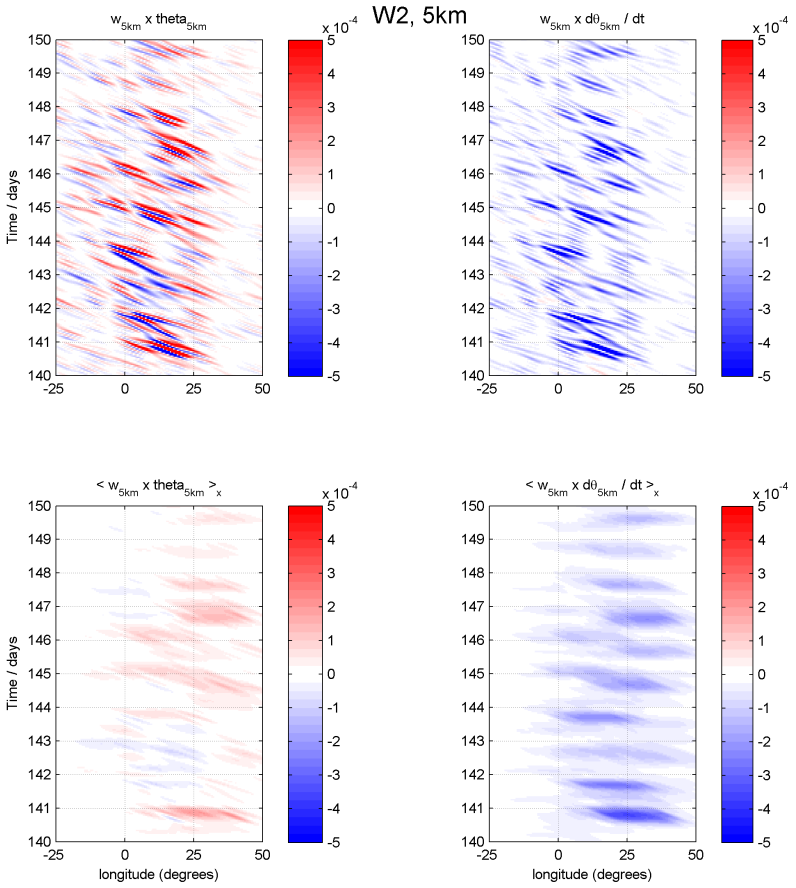

Figure 5.22: As in figure 5.22, but for W_{fast}.

In figures 5.23, 5.24 and 5.25, we show time series derived from the $x-t$ filtered Hovmöllers, as described below, for w, θ (top panels) and the corresponding moisture fields (bottom panels). This data was obtained by identifying, by eye, the x (longitude) coordinate of a dominant event in the data of figures 5.21.. 5.22, then taking a vertical (time slice) of that data, to obtain the time evolution of the event over a 3 day interval. The dominant event was chosen to be at longitude $x = 0$ degrees for $145 \leq t \leq 148$ for W_{slow} in figure 5.23. This region is populated by activity in both W_{fast} and W_{slow}. Whilst the fields are filtered, we obtain control data for $x = 0$ degrees for $143 \leq t \leq 146$ for W_{slow} in figure 5.24, where we assess only W_{slow} is active. The dominant event was chosen to be at longitude $x = 25$ degrees for $141 \leq t \leq 144$ for W_{fast} in figure 5.25.

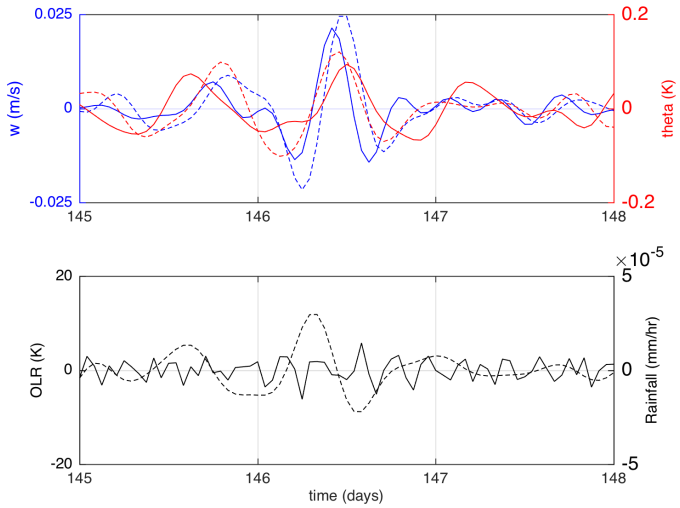

Figure 5.23: The data shown here represents a vertical (time) section of W_{slow} filtered fields, taken at a longitude of 0 degrees. In the top panel solid lines represent values at a height of 5 km, dashed represent values at a height of 10 km. In the bottom panel, where the moisture fields' covariance is recorded, the left ordinate measures the OLR (dashed), right measure the rainfall (solid).

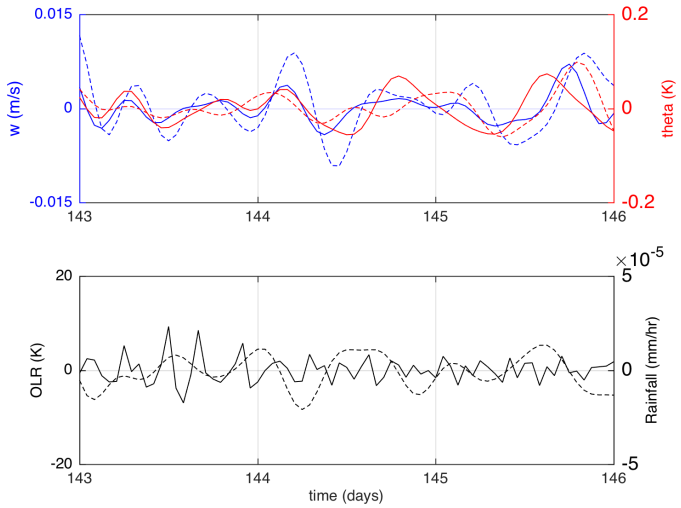

Figure 5.24: A control on data of figure 5.23. The filtered data of figure 5.23 was chosen a region of $x-t$ in which both W_{slow} and W_{fast} are active. The data above corresponds to a different time interval in which onW_{slow} only is judged to be active, at identical longitude. In the top panel solid lines represent values at a height of 5 km, dashed represent values at a height of 10 km. In the bottom panel the left ordinate measures the OLR (dashed), right measure the rainfall (solid).

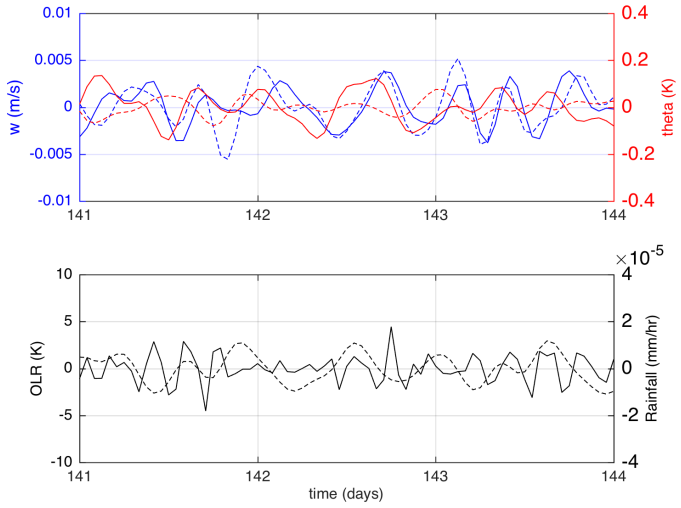

Figure 5.25: The data shown here represents a vertical (time) section of W_{fast} filtered fields, taken at a longitude of 25 degrees. In the top panel solid lines represent values at a height of 5 km, dashed represent values at a height of 10 km. In the bottom panel the left ordinate measures the OLR (dashed), right measure the rainfall (solid).

5.7 Discussion and Conclusions

We consider the results of our investigation of the dynamics of convection, contained in CP4. Whilst CP4 does not have the spatial extent or resolution of e.g. satellite observations, it is a highly sophisticated, fully coupled model, which allows for an in-depth study of many aspects of convection which could not be accessed with observations. Using spectral methods after Wheeler & Kiladis (1999), we investigate CP4 for the dynamics of convectively coupled gravity waves.

5.7.1 Estimating the Effect of Windowing

Here, we return to the influence of windowing on the appearance of IMPALA data structures in Fourier space. We choose to quantify its potential benefit by comparing two FTTs of IMPALA OLR, obtained with and without one form of windowing. The Hanning window was chosen as an all-purpose filter. Named after meteorologist Julius von Hann, it is realized here as filter spatial weighting function

$$h(x) = \sqrt{\sin\left(\frac{\pi x}{L}\right)}, \quad x \in [0, L], \tag{5.44}$$

which was used to multiply the x-variation of OLR data. Figure 5.26 shows the effect on an excerpt of raw OLR $x - t$ Hovmoller data, of the domain tapering produced by equation 5.44. An identical FFT process (as described above) was applied to both the raw data sets in figure 5.26 to produce the moisture spectra in figure 5.27. Specifically, both FFTs were smoothed in s and fCPD, with a 5-point running average filter, both had a red background corresponding to 50 cycles of $1 - 2 - 1$ filtration removed and both were subject to the same level of statistical significance (all data correspond to signal values 2σ greater than the mean). A comparison of the two data sets in figure 5.27 suggests that Hanning (and possibly other windowing) represents worthwhile pre-processing in a more extensive future study, as it has the potential to clarify the appearance of features in Fourier space. We note, for example, that there is a noticeable reduction in bleeding at small s, for $f > 5$CPD, and that features in the frequency interval $f \in [2, 5]$ are usefully sharper.

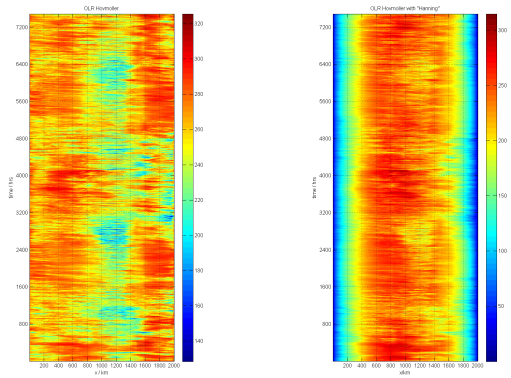

Figure 5.26: Symmetric $x-t$ data OLR Hovmoller data with (right) and without (left) application of the Hanning window defined in equation 5.44.

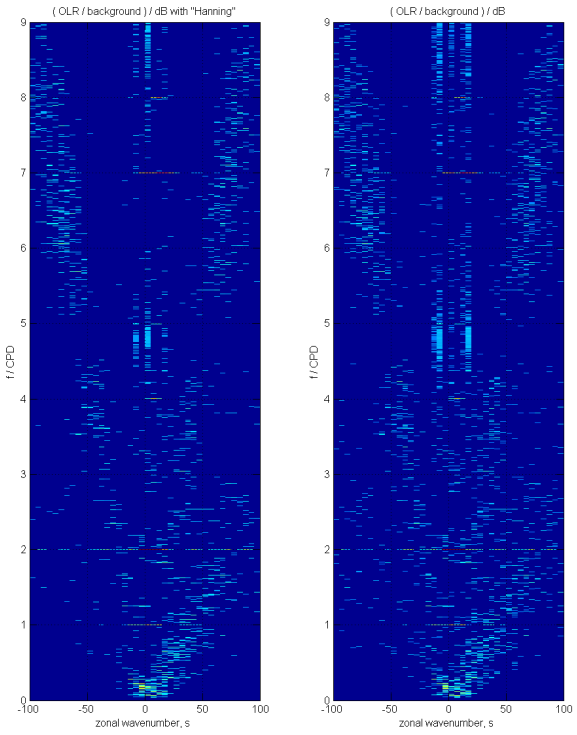

Figure 5.27: Symmetric $x-t$ filtered FFT from the OLR Hovmoller data shown in figure 5.26 with (left) and without (right) application of the Hanning window defined in equation 5.44.

5.7.2 Summary

Section 5.5 interprets a 10 year time series of CP4 OLR and rainfall in Fourier space, which we compare against well-known planetary dispersion relations. Note, the resolution of the CP4 in Fourier space is considerably lower than that achieved in the experimental studies of Wheeler & Kiladis (1999), but will contain sophisticated physics. As well as Matsuno modalities, we see non-dispersive waves of similar frequency, which project anomalously on moisture fields (OLR and rainfall). The westward branch of the fits to dispersion relations extends over a much larger range of planetary wavenumber that in corresponding experimental studies of Wheeler and Kiladis. We infer a relationship between these two waves, designated W_{slow} and W_{fast}, from spectra. W_{fast} is held to be a deep, fast mode, with $m = 1$, W_{slow} is a shallower, slower mode, with $m = 3$. Evidence for such modes arises in moisture fields' spectra, as the ratio and magnitudes of fitted group speeds (13 and $45\,\mathrm{ms}^{-1}$) is consistent with literature. There is also evidence for Kelvin wave activity in the spectra, which we do not investigate further here.

For a shorter time series (to avoid computational expense), we confirm the existence of W_{slow} and W_{fast} in an expanded number data fields (OLR, rainfall, w and θ). We apply a filtration in order to investigate the characteristics of W_{slow} and W_{fast} individually, and invert filtered Fourier fields into physical space. Our investigations in section 5.6 show filtration in Fourier space and subsequent inversion can point-out regions of the raw OLR space-time field associated waves: W_{slow} more readily than for W_{fast}. See the correlations in figure 5.16. Of course, this may simply mean W_{slow} projects more strongly on moisture fields, though not more frequently. This conclusion is supported by the spectra in section 5.5 and that W_{fast} is too fast. There are regions of the raw OLR Hovmöller where clusters of W_{slow} activity appear to match.

We proceed to explore the related issues of the inter-relationship of W_{fast} and W_{slow} and the individual dynamics of each. We need to address both together, as conclusions about one have implications for other.

5.7.3 Discussions

Initial correlations of filtered, reverse-transformed data, with raw moisture fields do support convection coupling in W_{slow}. They do not support convection coupling in W_{fast}. To explain this difference we confirm their nature, by verifying mode number, seeking the signature of convection (denoted e.g. by cross-correlation of e.g. smoothed $w \times \theta$) in other filtered dynamical fields and by examining 1D time series plots. A number of events were chosen by seeking peak activity in inverted, filtered fields.

Comparing time series plots of filtered w vs. t at 5km and at 10km (both locations are well within troposphere) for W_{fast}, we see a strong correlation between the w on both levels in figure 5.25. The simplest interpretation, supported by spectral data, is that W_{fast} indeed corre-

sponds to a deep mode. Correlation between w at 5km and 10km for W_{slow} is similar but less strong. To confirm that W_{slow} is an $m = 3$ mode, we might expect to see a change in sign of w between the levels. However, in figure 5.24, whilst the signals seems to be in phase, it is hard to infer the vertical structure of W_{fast}. However, taken with the ratio of groups speeds, this still seems likely. In figure 5.23, we inspect a convective event which has a signature in the dynamical fields (as seen in figure 5.18). Clear is the convective signal, and all dynamical fields and OLR align in phase and remain coherent for 3 days. In all cases, the rainfall is very noisy and cannot be attributed to interact with either W_{slow} or W_{fast}.

We turn to covariances. At 5km, Hovmöller plots of $w \times \theta$, when smoothed on x wavelength, show strong signal for W_{slow}, implying it is convecting at mid-level. At 5km, Hovmöller plots of smoothed $w \times \dot{\theta}$ show strong signal for W_{fast}, implying it is not convecting, at mid-level. Note, at 10km, both $w \times \theta$ and $w \times \dot{\theta}$ fields, when smoothed, show compatible activity for both W_{slow} and W_{fast} implying there in no convection aloft.

We rationalise observations from both moisture spectra, inverse filtration and covariances in the next section.

5.7.4 Conclusions

Ideally, one would use a statistical approach here, as we discuss in this final chapter. We advance hierarchical firm, tentative and speculative conclusions and hypotheses. The latter will then be considered further in the final chapter. We make the following firm conclusions

- CP4 can resolve wave spectra but the range of planetary wavenumber, s for the modes observed in this study is approaching an order of magnitude greater than the experimental study of Wheeler and Kiladis.
- CP4 is asymmetrically distributed, and skews to $s < 0$. This is consistent with Tulich & Kiladis (2012) who found a similar skew for observed coupled gravity waves.
- CP4 captures westward propagating features, some planetary wave modes and fast, and slow, bi-directional, non-dispersive waves. Both westward gravity waves, and the faster non-dispersive modes project onto OLR. The faster wave does not project onto rainfall, whereas the slower wave does.
- The speeds and structure of these modes are consistent with estimates of a deep mode ($m = 1$) and $m = 3$ mode.

We can also make some more tentative conclusions.

- There is some evidence of an east-propagating Kelvin mode in the moisture spectra which was not investigated further.

- At mid levels, the slower waves are interacting with convection, whereas the faster waves seem to be purely waves. We regard this as a tentative conclusion, as evidence for this is currently found only in a handful of events. If time permitted, we could apply a statistical approach here to firm up the conclusions.

Finally, we see evidence to make some speculative conclusions.

- From the 1-D time series data, derived from target events in $x - t$ one can pick-out sub-intervals where fields align.
- By inspection, co-spectra and covariances in the small number of test cases studied is consistent with the fast mode not being convectively coupled and the slow mode being convectively coupled.

s

Chapter 6

Conclusions and Further Work

In its final chapter, we will reflect upon work presented in this thesis: the inter-relationship of its different elements, its context, potential impact, pathways to impact and what opportunities exist to advance it.

In the bulk (Chapters 2, 3, 4) we have considered the mathematics and meteorology of three, related, essentially analytical models of buoyancy-forced, gravity-wave mediated adjustment to convection in a stratified atmosphere without feedback. However, Chapter 5 assesses, numerically, gravity wave coupling to predominantly equatorial convection in convection-permitting Unified Model data. Mathematically, our models all have a potentially radiating tropopause, all are based within linear theory, all are predominantly analytical, all separate horizontal and vertical variation (the latter being based upon a modal decomposition), all derive from a closed description based upon field variables u, w, b and p with prescribed $\rho_0(z)$ variation (necessitated by the deep nature of the convection we aim to address) and all use a potentially time-dependant heat or buoyancy forcing, S (mainly the first baroclinic mode).

In Chapter 2 we developed a non-rotating model in a 2D stratified atmosphere, with a radiating tropopause and a variable base state of density, after Nicholls et al. 1991 and Edman and Romps 2017. We used a prescribed tropospheric heat source to consider convective heating induced gravity wave response and its dependence on the length-scale of the forcing and the upward radiation of energy at the tropopause. It was used to examine the effects of radiation at the tropopause from a fundamental perspective, to assess its impacts in the context of numerical models' parametrisation and to assess secondary convection triggering.

Having established the credentials of our essential approach, we proceeded to quantify the impact of the third, spatial dimension in Chapter 3, developing an axially symmetric 3D model with otherwise equivalent physical and mathematical composition. Data obtained highlight a key difference in the forced gravity waves' decay as they move outward, broadly expected on geometrical and conservation grounds. Indeed, stud-

ies of gravity waves show concentric wave bands being emitted from a central storm (e.g. Lane & Reeder (2001); Piani *et al.* (2000)). Key mathematical innovations to facilitate this advance from Chapter 2 were (i) an extended basic set which includes v and (ii) Hankel-Laplace (rather than Fourier-Laplace) transform techniques and (iii) the development of a numerical inversion from reciprocal space.

In Chapter 4 we addressed rotation without which a period of transient buoyancy forcing does not lead to a local response at large time. With rotation, we predicted local pressure and buoyancy anomalies in geostrophic balance with a transverse wind. This steady vortex state is fundamental. Determination of its horizontal length-scale was regarded as a Rossby adjustment problem. Chapter 4 considers the post-convection steady state in 2.5D but has otherwise equivalent physics (stratification) as the models of Chapters 2, 3. However, another substantial Mathematical generalisation (vertical modal structure) was necessary and a non-dimensionalisation approach was applied to interpret our meteorologically relevant data.

Moving-on from prescribed thermal forcing, in Chapter 5, we considered, numerically, feedback between gravity waves and convection evident in data from high-resolution, convection permitting Met Office Unified Model simulations of the sub-Saharan African. We extract frequency-wavenumber spectra of moisture and dynamical fields (OLR, rainfall, vertical velocity and potential temperature) for gravity wave-like response. Tulich and Kiladis (2012) found evidence of coupling between convection and gravity waves in analysis of relatively low resolution TRMM data. We have used a dynamical model at much higher resolution and we were thus able to quantify fully coupled, grave wave-convective systems in terms of typical speeds of (coupled) gravity waves, coupling to equatorial modes e.g. Matsuno (1966) and to interrogate individual storm events, using a methodology adapted from that of Wheeler and Kiladis (1999).

The pursuit of relatively simple (semi-)analytical models has been fruitful and has illuminated some non-trivial aspects of convective adjustment and has opened many avenues for further research (see section 6.4 below). Analysis of high-resolution, fully coupled convection in a numerical modes gives insight into the nature of real systems and provides some context for our analytical results.

6.1 Contextual Review

Emphasis in the predominantly analytical work of Chapters 2...4 was laid on development of physically and mathematically coherent, tractable, benchmarks. All are based in linear theory and Sturm-Liouville eigenfunction expansions and all address heat forcing without consideration of coupling. We do not claim to originate this essential approach and we have drawn throughout on work originating in the 1990s, which enjoyed considerable success, (Mapes, 1993; Nicholls *et al.*, 1991) . These workers

pioneered an approach based, essentially, upon modal decomposition in the vertical coordinate. One could be forgiven for thinking that, after so long a time, linear theory in this area is exhausted. However, if not a renaissance, there is certainly a level of renewed interest (see e.g. Edman & Romps (2017)), motivated presumably by a need to *understand* issues with numerical models' paramterisation, such as those addressed in the applications considered in Chapter 2.

The analytical models we develop were intended transparently to furnish qualitative understanding of adjustment dynamics (Chapters 2, 3) and geostrophic adjustment (Chapter 4) to heat forcing, whilst considering for the effects of radiation at the tropopause.

In Chapter 3 our main objective was to take an opportunity to modify the horizontal variation, whilst transplanting a solved, base vertical variation from our 2D, non-rotating, model of Chapter 2, into 3D with axial symmetry, whilst also inserting rotation into the model. The result is ready to exploit immediately, we note. Our philosophy is also apparent in Chapter 4. Here, by extending the treatment of Chapter 2 (to 2.5D), to treat the steady-state response in a rotating atmosphere, we address the simplest, most fundamental part of the problem- a geostrophic adjustment. Again, the resulting model is ready to exploit immediately. The hierarchy of models developed across Chapters 2 and 4 further illustrate our guiding paradigm -simplicity, tractability and coherence- as follows. The non-rotating, dynamical 2D model of Chapter 2 applies to general horizontal variation of heat forcing, with minimal use of numerics (which allows us to consider different horizontal variations of heating and tendency within a single framework). The model of Chapter 3 represents the simplest evolution of the 2D model to treat 3D and rotation (albeit with increased reliance on numerics). The model of Chapter 4 is an extension of that in chapter 2, which facilitates an analytical solution.

There is also an element of feed-forward learning in effect in Chapters 2..4. For example, from the 2D models developed and used in Chapter 2, we determine that radiation effects are maximised when $N_t = N_s$. Hence, in considering the geostrophic adjustment in the rotating case, in Chapter 4, we can justify the mathematical simplification $N_t = N_s$ on physical grounds- this case corresponds a steady-state adjustment resulting from maximum loss of vertically-radiated gravity wave energy.

As we have stressed, our analytical work is limited principally in its neglect of feedbacks. The coupling between gravity waves and convection is clearly a large question and some account of it was judged essential- even in a thesis with a predominantly analytical ethos. The work of Chapter 5 is our attempt. Very broadly, it shows that the relevant couplings are present in the data of the Met Office Unified model.

6.1.1 Beneficiaries

Gravity wave energy radiation and reflection at the tropopause has important consequences. Numerical models, for all their physical sophistication and numerical accuracy, all must have finite meshes which terminate at a definite spatial location. That is, they must have some form of lid. The lid height is typically 40km aloft (corresponding to be that used for the comparison UM data presented in Chapter 2 of this thesis, note). Representation of the tropopause and the associated radiation effects are perhaps a predictable Achilles heel of numerical models. So, whilst the behaviour of trapped atmospheric layers is well understood, in both numerical and analytical models, what happens as the lid is raised aloft, to model deep atmospheric effects, is less clear. Numerical models address the problem of representing radiation at the tropopause typically by using damping layer, to e.g. restrict the lid reflection effects. Probably the most significant aim of the work in Chapters 2..4 is to include and, where appropriate, transparently quantify radiative effects of heating adjustment, within a tractable, predominantly analytical framework. With this in mind, the modelling community will benefit from access to a set of benchmark models, which are capable of addressing both the dynamics and the steady-state of adjustment, with and without rotation.

6.2 Summary of Findings

Here we summarise useful, case-specific findings from the individual work packages which comprise this work.

6.2.1 2D Model without Rotation

Our foundation, 2D model was formulated for generic horizontal variation of heating in Cartesian coordinates. This is made possible by neglecting rotation. The model has a tropopause (with buoyancy frequency N_t, for $0 \leq z \leq H_t$) and a stratosphere (with buoyancy frequency N_s, for $z > H_t$).

We first consider the case $N_t = N_s$, of no stratosphere or tropopause. Trapped solutions (with the lid placed at the tropopause, $z = H_t$) in a channel (well documented elsewhere, see e.g. Parker & Burton (2002)), for steady heating correspond to a single wave mode, which propagates away from forcing region at constant speed, and does not decay in time. As the lid is raised aloft, the solution becomes more complicated: a higher lid leads to excitation of higher order modes, with a range of wavespeeds. Faster (deep) modes communicate the adjustment into the neighbourhood of heat forcing more quickly. Furthermore, allowing upward radiation reduces the magnitude of tropospheric response. The maximum tropospheric vertical velocity, $|w|$, in fully radiating troposphere (with

$N_t = N_s$) has an amplitude that is 30% of those in a trapped troposphere.

Applying a transient, pulsed heat forcing produces a "rebound" mode (of ascent). Given the right conditions, this ascent may help further convection develop, since ascent will erode CIN. We identified in Chapter 2 regions of low-level ascent outside tropospheric subsidence zones (which will have reduced CAPE). The combination of larger CAPE and eroding CIN, communicated via gravity wave adjustment, may well lead to further convection.

Next, we summarise observations with a piecewise defined $N(z)$ (i,e. $N_t = 2N_s$). This stratification of our model (and by extension, the 3D model of Chapter 3) represents something closer to physical reality. In solutions for this case, gravity waves have both radiation and trapped characteristics, but the response in troposphere is only slightly modified. The maximum tropospheric vertical velocity, $|w|$, in this case has an amplitude that is 50% of those in a trapped troposphere.

We find that the characteristics of our forced gravity waves are influenced by the spatial and temporal dependence of the forcing function. Therefore the wave spectra is altered by the nature of the forcing function. We hypothesis that coarse models that do not resolve convective heating and instead smooth out the heating function onto their grid will not produce the correct wave spectra. Indeed, we find a error of 20% in the grid box mean tendency when a 10 km heating is smoothed out to a 100 km grid.

Finally, a set of comparisons, showed qualitative agreement with "full physics" iUM model runs, and find a spurious oscillation in the model due to the model lid.

Allowing for upward radiation of wave energy leads to solutions which decay with distance. In cylindrical geometry, we know a further decay is introduced due to geometrical restrictions. How do the length-scales of each decay compare? This question is considered in Chapter 3.

6.2.2 3D Model

A 3D model answers the need to contextualise preceding 2D investigations. The most obvious questions arise around the restricted dimensionality of the 2D model. In Chapter 3, we extend to 3D geometry, with rotational symmetry, for an axially symmetric system treated within cylindrical polar coordinates. Owing to use of identical stratification and heating temporal / spatial structure, the essential mathematical ideas of the 3D model of Chapter 3 are identical to those of 2D model, with one key proviso. The horizontal variation is more complicated. (However, the application of Sturm-Liouville theory proceeds identically). Specifically, for our 3D treatment of a deep, heat-forced atmosphere, the Fourier transform methodology of Chapter 2 must be replaced by a Hankel transform methodology (using a zero-order Bessel function), which compli-

cates the solution of the horizontal part of the separated problem. We are thus forced to perform a numerical inversion from reciprocal space, which clearly requires a defined (as opposed to generic) heating function. This makes it impossible to write-down results for general horizontal variation of heating and reliance on numerical inversion makes our 3D model less qualitatively informative than its 2d pre-cursor. Note that our analysis in Chapter 3 actually treats the case of $f \neq 0$ but data is obtained for $f = 0$, to maintain parity with between the physical regimes studied in Chapters 2 and 3.

The 3D model results follow a similar overall pattern to 2D- a single mode is observed in the extended, trapped case with a qualitatively similar, more geometrically complicated solution emerging as the lid is raised aloft. However, the single mode is now observed to decay as it propagates to greater r, due to transformed horizontal (radial) motion. (Physically, the wavefront is spreading over the area of a cylinder). Tentatively, we predicted spreading could be modelled by an amplitude decay factor $r^{\frac{-1}{2}}$ in the far field, which is confirmed in data. The trapped solution also now develops a "head" and "tails back" towards the heat forcing in sharp contrast to the 2D case, which has a constant amplitude i.e. no head and tail. In 3D, high lid solutions have, overall, a similar set of recognisable features.

We note that this model is ripe from further exploitation. For instance, one could straightforwardly investigate the role of rotation on the dynamics of adjustment, using the 3D model in its current form. However, the role of rotation would then have to inferred by, presumably, comparing data for equivalent cases, with $f = 0$ and $f \neq 0$. This empiricism was removed by choosing, instead, to develop a third, independent model of the geostrophic adjustment to an applied, transient heating of finite duration. A "non-zero" steady state is then entirely due to rotation- with $f = 0$ there is zero geostrophic adjustment to heating. In this sense, the structure of the geostrophic adjustment following a finite heat pulse provides the simplest measure of the role of rotation for the class of model under consideration. In Chapter 4, we build such a model.

6.2.3 Steady state (PV) Model with Rotation

In Chapter 4, we observe that the structure of the geostrophic adjustment to a finite-duration heat pulse, determined in 2.5 dimensions, provides a simple, *analytically tractable* assessment of the role of rotation. Counter-intuitively, the physical simplification resulting from setting $u = w = 0$ in the present formulation (our base set, stratification and heating in chapter 4 is still essentially that of Chapters 2, 3, note) does not offset the increase in challenge associated with the formulation, which results from integrating over the duration of the applied heating. The latter step impacts the treatment of stratification, making it necessary to extend

the Sturm-Liouville eigenfunction basis in use in Chapter 4. It is also appropriate to consider the PV of the geostrophic adjustment, so we also develop and identity PV in Chapter 4.

Key investigations of this Chapter 4 focus on the horizontal length-scale of geostrophic adjustment, allowed purely by inclusion of f, which leaves a residue at steady state (i.e. it introduces a geostrophic balance). Broadly, larger f restricts the range of influence of the convection. We chose to measure this length-scale control by e-folding length of steady p adjustment. Simple tests with a trapped case lead to surprising result, supported by a non-dimensional analysis, suggest that the length scale for small f tends towards a Rossby radius, whereas in large f the response's length scale is determined by the horizontal heating length scale.

An important message from Chapter 4 is that upward radiation only influences the lengthscale of the response when $\epsilon = \frac{NH_t}{fL}$ corresponds to a very large-scale heat source (larger than the Rossby radius), in which case the response lengthscale is that of the forcing. This does not apply to deep convection, which is much smaller-scale than L_R. Therefore, although there are subtleties in the Rossby adjustment problem, the Rossby radius remains the key scale of response for convection problems.

6.3 Coupled Waves in a High Resolution Numerical Model

In Chapter 5, we have examined a high resolution, convection-permitting, fully coupled numerical model (CP4) for convectively coupled gravity waves. Using Fourier techniques on fields of OLR, rainfall, w and θ, after Wheeler & Kiladis (1999), we have confirmed the existence of a bi-directional non-dispersive gravity wave moving at roughly $45\,\mathrm{ms}^{-1}$ (W_{fast}), and a westward-propagating gravity wave, moving at roughly $13\,\mathrm{ms}^{-1}$ (W_{slow}). These wave speeds are consistent with "back of the envelope" calculations for a deep tropospheric mode and a $m = 3$ mode, both of which have been shown to interact with convection (Lane & Reeder, 2001). We have also seen evidence for other planetary waves, such as the Kelvin wave.

There is no documented evidence for coherent storm systems moving at the speed of the fast modes shown here. Although the fast modes are projecting onto OLR, we do not see them coupling significantly with rainfall. Therefore, we interpret the fast mode being a dynamical response to convective forcing, and this fast wave forces a signature in OLR, but no significant feedback. In contrast, the slow mode exists at a speed which is common to observations of observed organised convection. It is tempting then to attribute this slow mode to a convectively coupled wave. However, there are other well-documented physical processes which can cause storms to move at these speeds in the atmosphere, most notably the interaction between a low level convective "cold pool" and the ambient

wind-shear. In other words, at these slower speeds, material advection of the air (in the cold pool) can be a propagation mechanism, as opposed to wave propagation. Untangling the real dynamical causes of the slow mode propagation would involve much deeper investigation: in practice storms of this nature do excite waves, and they do generate cold pools, so both phenomena are present in the observations and in the CP4 model. Attributing the storm propagation to one or the other mechanism (cold pool versus waves) would be difficult. A suitable modelling approach to tackle this might be to re-run the CP4 simulations with rainfall evaporation switched off in the model, to eliminate the cold pools, and see whether storm propagation still occurs according to the slow wave mode. This would be a substantial new study.

6.4 Further Work

Our work in Chapters 2..4 has been highly idealised. Longer term, we might consider softening, or even removing some restrictions in search of deeper understanding. This will likely come at computational expense, as analytical approaches will fail. We immediately see a handful of possible extensions, briefly categorised below, that could be applied generally to all three models.

1. Non-linearity.
   Inertial waves in the atmosphere can form solitary waves (e.g. the morning glory wave). Inclusion of non-linear terms in our models will steepen our waves whilst increasing the mathematical complexity of the description.

2. Dispersion
   Introducing dispersion, e.g. by raising hydrostatic balance would lead to dispersive waves, which, in-turn, leads to shallow waves. It would be interesting to examine how dispersion and non-linearity compete.

3. Vertical shear
   Inclusion of vertical shear would allow for investigations of Scorer parameter and dynamical trapping.

4. Boundary layer
   Introduction of a boundary layer, through extended, piecewise stratification.

We also foresee a number of research avenues which can be achieved with the models in their current state. We consider here how the analytical models we have developed might be used in future, the potential impact of such efforts and, importantly, we assess the deliverability of such projects. We consider only the most immediate possibilities.

In Chapter 2, one possible scenario is to push the iUM grid resolution, to a much more coarse level and then assess where iUM data loses a significant part of the wave spectrum predicted in the analytical model. The outcome of this work, which could be readily performed, would be of most value and of largest impact to Met Office modellers, who need to assess the capacity of their models. We assess that this work would directly impact a small community in the short term, however the provision of better software may benefit a larger community in time. Using the model in Chapter 2, we could also evaluate upwards momentum and energy fluxes, e.g. to provide estimates on the stratospheric / mesospheric wave drag.

The model of Chapter 3 has rotation formulated within it. The case of $f \neq 0$ is already facilitated in the Matlab codes generating the data of Chapter 3: in particular, the inversion from reciprocal space is already computing the inverse Hankel transform numerically. The presence of $f \neq 0$ in the numerical inversion integral should, if anything, facilitate (rather than obstruct) the computations and we assess that it will not add computational expense. We assess that the only data required to publish this result is qualitative: for example, images such as that in figure 6.1, which show the structure of the w-wind and the θ response. This data was not included previously in this thesis simply on logistic grounds- space had to be devoted to more significant results. Its presence here is intended purely to support our assertion that a good quality publication may be delivered almost immediately. An assessment of the impact upon the 3D dynamics of adjustment, of rotation, is, however, of limited significance. However, whilst limited in terms of impact, this effort would nicely bound and contextualise the work of Chapter 3. It is readily achievable and quickly publishable.

It would be interesting to investigate the temporal response to heating in the model developed in Chapter 4, as the included transverse wind would lead to dispersive waves ($w^2 = c^2k^2$ of Chapter 2 would modify to $w^2 = f^2 + c^2k^2$). A different remote response from that in Chapter 2 would develop.

The assessment of data in Chapter 5 clearly has significance for CP4. An immediate insight could be gathered by a tangential project comparing Kelvin waves in 4 km convection-permitting runs to the driving model at 25 km resolution, seeking to determine if their amplitude and/or phase correlate, using the filtration methods developed. The outcome of this investigation would be principally of interest to modellers, as another, timely check not only on Met Office tools but also on development trajectories.

More broadly, a statistical approach to fast wave diagnosis seems necessary but worthwhile, in order conclusively to characterise convection and wave dynamics in CP4. The nature of filtering and subsequent identification of individual, candidate events over longer data timespans (other years) is needed to calibrate models against physical reality, gain insights

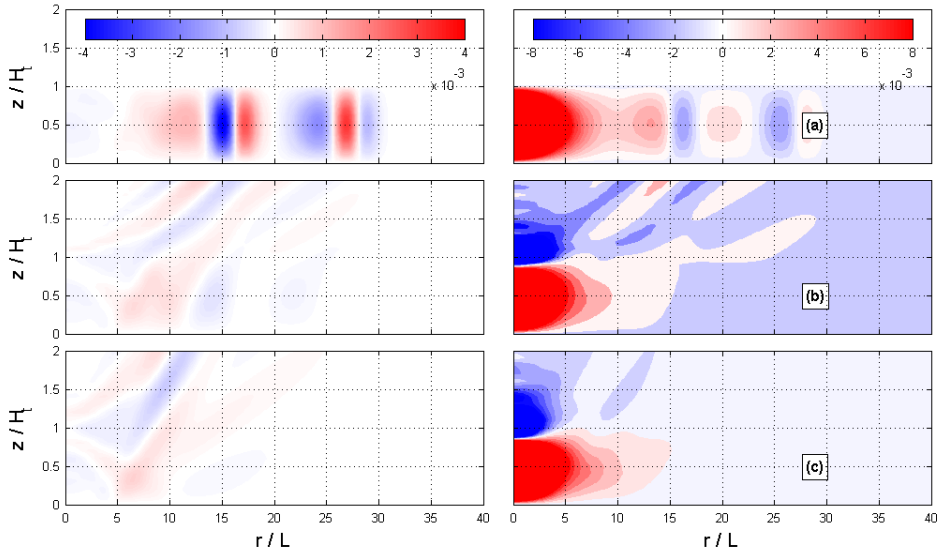

Figure 6.1: Output from the 3D model developed in Chapter 3 of this thesis with rotation: $f = 10^{-4}$. The left column corresponds to the w adjustments, the right column corresponds to θ adjustments. Rows (a)..(c) correspond to 2D models designated in Chapter 2 as TRAP, RAD1 and RAD2 respectively. (b) and (c) have their lid raised aloft, to $z = 64H_t$. That is, the row labelled (a) corresponds to a trapped case, (b) corresponds to $N_t = 2N_s$ and (c) corresponds to uniform N_z). The heads which develop on the 3D model adjustments are particularly apparent the top right image. For this data, time $t = 150$mins, for a heat pulse of duration 60mins.

for climate prediction and -not least- confirm model parameterisations. To add further incentive here, it may also be possible to calibrate model outputs against experimental data sets like TRMM.

There are technical problems to be overcome. For instance, how would one synchronise fields associated with a set of equivalent events, to reach well-defined averages? To obtain a statistical sample of (say) W_{fast} fields which are meaningfully averaged might require computationally intensive time-shifting of time-series data sets, relative to each other, *before* they are combined. Processing all correlations in this way generates a programming or even machine-learning project which is -presumably- long term and labour intensive. Even given this level of challenge, the task has to be worthwhile, given what it might reveal about the UM.

Finally, as we have already alluded, attributing storm propagation to one or the other mechanism (cold pool versus waves) would an interesting and worthwhile study. One could re-run CP4 simulations with rainfall evaporation switched off in the model, to eliminate the cold pools, and see whether storm propagation still occurs according to the W_{slow}. Possibly

an optimal outcome for Chapter 5 is that it serves to initiate a PhD programme, supported and part supervised by the Met Office.

6.5 Epilogue

Figure 6.2 is a snapshot of mid-level (5 km) w (ms^{-1}) from the fully coupled CP4 model, which contains the clear signature of waves: concentric circles radiate outward from strong up-draught regions. Since strong up-draughts are associated with deep convection, we speculate that the waves depicted here are, indeed, forced by convection- we have studied such waves in chapters 2 and 3. As the CP4 waves travel further from the equator, they will feel the influence of Coriolis force and our model in Chapter 3 is ready to investigate the influence of rotation on their transient dynamics. In Chapter 4, we do investigate the influence of Coriolis effects, but in the steady state limit (long time response to convection). In Chapter 5, we studied CP4 directly in an attempt to diagnose some characteristics of fully coupled gravity waves- which feeds back to the image in figure 6.2. If I have learned anything, it is that the coupled dynamics are formidable. This thesis represents my skilfully supervised attempts to toss a few smooth pebbles into a vast ocean of truth, hoping to create a few ripples.

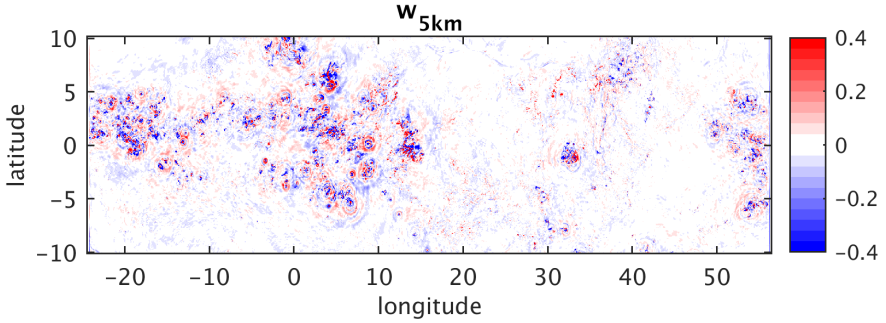

Figure 6.2: CP4 $w\,\mathrm{ms}^{-1}$ at 5 km.

Appendix A

CP4 : Resolution Comparisons and Processing

A.1 Comparison with Wheeler and Kiladis' Data Resolution

Wheeler and Kiladis' OLR experimental data was obtained with different spatial-temporal sampling, compared with IMPALA data sets. It is appropriate to quantify the difference, to understand the resolution limitations of the resolution of IMPALA at low frequency.

A.1.1 Spatial Resolution

Wheeler and Kiladis report using OLR satellite data on an grid with zonal spacing defined by the increment $\delta\varphi = 2.5^o$, corresponding to $360/2.5 = 144$ points in the meridional direction, with approximate linear spacing:

$$L^{(WK)} = 2\pi R_e/144 = 2 \times 3.149 \times 6371/144 = 280km. \tag{A.1}$$

This, and the total range of this data (equal to $2\pi R_e$) strongly selects for the small s, long wavelength processes of interest. In fact, these authors concentrate on data for zonal wavenumber $s \in [-15, 15]$. In comparison, certain of our IMPALA OLR data is resolved on a grid as fine as 4km, i.e. $L = 4$km, so that $280/4 = 70$ IMPALA gridded OLR data points correspond to the spatial region represented by a single datum of Wheeler and Kiladis. IMPALA, it seems, is resolving much shorter wavelength disturbances.

A.1.2 Temporal Resolution

Wheeler and Kiladis use approximately 18 consecutive years of satellite data, sampled twice daily corresponding to a sampling interval $T^{(WK)} =$ 12hr, which, they state, means that it is necessary to take steps to remove seasonal variations. In comparison, IMPALA model data is sampled

hourly (for OLR) or every 0.25hr (for rainfall) for $O(10^3)$ days. IMPALA data resolves much more high frequency phenomena.

A.1.3 Fourier Space Resolution

Since both the spatial and temporal span of Wheeler and Kiladis' experimental OLR data is greater than that available in the any of our IMPALA data, the resolution of their spectra in Fourier space is much finer. It is appropriate to quantify this difference in resolution to compare smoothing of data in Fourier space (see below).

Wheeler and Kiladis' OLR satellite data samples the whole of the equator, whereas that of the IMPALA data only spans a $\leq$ 8000km range, over tropical Africa. This means that Wheeler and Kiladis' resolution in discrete planetary wave-vector is always more than a factor 5 better than that for any of our IMPALA data sets, as follows. Let $\Delta s^{(WK)}$ ($\Delta s^{(IMP)}$) denote the increment in zonal wavenumber in Wheeler and Kiladis' (IMPALA) data, we have

$$\frac{\Delta s^{(IMP)}}{\Delta s^{(WK)}} \geq \frac{2\pi R_e}{8000} = \frac{2\pi \times 6371}{8000} = 5.0038 \tag{A.2}$$

The OLR satellite data of Wheeler and Kiladis is also better resolved in frequency. Wheeler and Kiladis' OLR data is of eighteen year duration. The longest duration IMPALA model rainfall data corresponds to about 10yr. Comparing the frequency step in Fourier space therefore

$$\frac{\Delta f}{\Delta f^{(WK)}} \geq \frac{18 \times 365}{60480} = 2.6087. \tag{A.3}$$

Clearly, their enhanced resolution makes it easier for Wheeler and Kiladis to examine the structure of their experimental OLR frequency spectrum over more restricted ranges of f, s than that available in the IMPALA data. However, this disadvantage is somewhat offset, for purposes of fitting at least. We shall see in the data of Chapter 5 that IMPALA moisture spectra sets all exhibit trends over larger ranges of f, s than the corresponding experimental data of Wheeler and Kiladis.

A.1.4 1-2-1 Filtration

We compare the number of cycles of $1-2-1$ filtration in Fourier space, N_{121}, to be used to obtain the IMAPLA data red background spectra. Wheeler and Kiladis state that they set $10 \leq N_{121} \leq 40$, to isolate their experimental red background spectra. Hence, their averaging takes place over an interval $[10 \times \Delta s^{(WK)}, 40 \times \Delta s^{(WK)}]$ in Fourier space. To average over a similar interval in Fourier space, the number of cycles of $1-2-1$ filtration necessary for IMPALA is

$$\frac{10 \times \Delta s^{(WK)}}{\Delta s^{(IMP)}} \leq N_{121} \leq \frac{40 \times \Delta s^{(WK)}}{\Delta s^{(IMP)}}, \tag{A.4}$$

which, using equation A.2 reduces to $\frac{10}{5} \leq N_{121} \leq \frac{40}{5}$. That is, to maintain parity with the approach of Wheeler and Kiladis $2 \leq N_{121} \leq 8$ i.e. Initially we set $N_{121} \approx 10$.

A.2 Discussion of DFT Data

Recall, the IMPALA data sets in of Chapter 5 were obtained directly from Matlab, using that software's native two-dimensional FFT algorithm. G_{f,k_x}, the residual power, expressed in dB, in typical IMPALA data sets is shown over the interval $s \in [-90, 90]$, $f \in [0, 3]$CPD, once the red background of figure has been divided-out. Clearly, the DFT IMPALA data span a much greater range of s but the clearest structures are apparent only in $s \in [-90, 90]$, as expected for long wavelength correlations characteristic of the convective coupling of interest in this study. We remark that this range is large compared with that used by Wheeler and Kiladis. Formally, truncating the range of s effectively filters for large wave-vector, small wavelengths from the data. The range of data in both f and s in spectra of Chapter 5 is necessary, honestly to show the full extent of the candidate structures revealed in the IMPALA data. The range of s is considerably greater that that used by Wheeler and Kiladis, whose experimental data reveals structures over the smaller interval $s \in [-15, 15]$. The fact that IMPALA data structures are characterised by a much larger range of s offsets IMPALA's increased value of $\Delta s^{(IMP)}$ (which is at least factor 5 larger than that found by Wheeler and Kiladis) for purposes of fitting spectra- but it is intrinsically puzzling. The ratio of interval to span typical of our data is $\frac{5}{2\times 80} = 0.0313$ is compatible to that in the experimental data of Wheeler and Kiladis' data, which is $\frac{1}{2\times 15} = 0.033$. Note that in all the IMPALA data considered, the power in spectrum decreases as distance from the origin in Fourier space increases. The discretisation in the IMPALA data is apparent throughout the spectra of Chapter 5. In particular, $\Delta s^{(IMP)}$ is very visible.

References

Alexander, M., Holton, J.R. & Durran, D.R. (1995). The gravity wave response above deep convection in a squall line simulation. *J. Atmos. Sci.*, **52**, 2212–2226. 22, 24

Alexander, M., Gille, J., Cavanaugh, C., Coffey, M., Craig, C., Eden, T., Francis, G., Halvorson, C., Hannigan, J., Khosravi, R. *et al.* (2008). Global estimates of gravity wave momentum flux from high resolution dynamics limb sounder observations. *Journal of Geophysical Research: Atmospheres*, **113**. 24

Andersen, J.A. & Kuang, Z. (2008). A toy model of the instability in the equatorially trapped convectively coupled waves on the equatorial beta plane. *J. Atmos. Sci.*, **65**, 3736–3757. 24

Arakawa, A. & Schubert, W.H. (1974). Interaction of a cumulus cloud ensemble with the large-scale environment, part i. *J. Atmos. Sci.*, **31**, 674–701. 58

Arfken, G.B. (1966). *Mathematical methods for physicists*. Academic press. 14, 26, 33, 79, 80, 87, 89, 111, 112, 125, 143, 157, 165

Baldwin, M., Gray, L., Dunkerton, T., Hamilton, K., Haynes, P., Randel, W., Holton, J., Alexander, M., Hirota, I., Horinouchi, T. *et al.* (2001). The quasi-biennial oscillation. *Reviews of Geophysics*, **39**, 179–229. 19

Bannon, P.R. (1995). Potential vorticity conservation, hydrostatic adjustment, and the anelastic approximation. *J. Atmos. Sci.*, **52**, 2302–2312. 20

Barnes, G. & Sieckman, K. (1984). The environment of fast- and slow-moving tropical mesoscale convective cloud lines. *Monthly Weather Review*, **112**, 1782–1794. 29

Beres, J.H. (2004). Gravity wave generation by a three-dimensional thermal forcing. *J. Atmos. Sci.*, **61**, 1805–1815. 24, 71

Beres, J.H., Alexander, M.J. & Holton, J.R. (2002). Effects of tropospheric wind shear on the spectrum of convectively generated gravity waves. *J. Atmos. Sci.*, **59**, 1805–1824. 24, 71

Birch, C., Parker, D., O'Leary, A., Marsham, J., Taylor, C., Harris, P. & Lister, G. (2013). Impact of soil moisture and convectively generated waves on the initiation of a West African mesoscale convective system. *Quart. J. Roy. Meteor. Soc.*, **139**, 1712–1730. 6, 23, 24, 54

Bracewell, R.N. & Bracewell, R.N. (1986). *The Fourier transform and its applications*, vol. 31999. McGraw-Hill New York. 84

Bretherton, C. (1988). Group velocity and the linear response of stratified fluids to internal heat or mass sources. *J. Atmos. Sci.*, **45**, 81–94. 22, 105, 106

Bretherton, C.S. (1987). A theory for nonprecipitating moist convection between two parallel plates. part i: Thermodynamics and ?linear? solutions. *J. Atmos. Sci.*, **44**, 1809–1827. 105

Bretherton, C.S. & Smolarkiewicz, P.K. (1989). Gravity waves, compensating subsidence and detrainment around cumulus clouds. *J. Atmos. Sci.*, **46**, 740–759. 21, 22, 24, 54, 105

Bushell, A.C., Butchart, N., Derbyshire, S.H., Jackson, D.R., Shutts, G.J., Vosper, S.B. & Webster, S. (2015). Parameterized gravity wave momentum fluxes from sources related to convection and large-scale precipitation processes in a global atmosphere model. *J. Atmos. Sci.*, **72**, 4349–4371. 7

Chagnon, J.M. & Bannon, P.R. (2001). Hydrostatic and geostrophic adjustment in a compressible atmosphere: Initial response and final equilibrium to an instantaneous localized heating. *J. Atmos. Sci.*, **58**, 3776–3792. 105

Chagnon, J.M. & Bannon, P.R. (2005). Wave response during hydrostatic and geostrophic adjustment. part i: Transient dynamics. *J. Atmos. Sci.*, **62**, 1311–1329. 20

Chimonas, G. (1972). The stability of a coupled wave-turbulence system in a parallel shear flow. *Boundary-Layer Meteorology*, **2**, 444–452. 10

Chumakova, L.G., Rosales, R.R. & Tabak, E.G. (2013). Leaky rigid lid: New dissipative modes in the troposphere. *J. Atmos. Sci.*, **70**, 3119–3127. 31

Clark, T. & Peltier, W. (1977). On the evolution and stability of finite-amplitude mountain waves. *J. Atmos. Sci.*, **34**, 1715–1730. 10

Clark, T.L., Hauf, T. & Kuettner, J.P. (1986). Convectively forced internal gravity waves: Results from two-dimensional numerical experiments. *Quart. J. Roy. Meteor. Soc.*, **112**, 899–925. 22, 24

Colby Jr, F.P. (1984). Convective inhibition as a predictor of convection during ave-sesame ii. *Monthly Weather Review*, **112**, 2239–2252. 5

Cullen, M. (1993). The unified forecast/climate model. *Meteorological Magazine*, **122**, 81–94. 63

Dewan, E., Picard, R., O'Neil, R., Gardiner, H., Gibson, J., Mill, J., Richards, E., Kendra, M. & Gallery, W. (1998). Msx satellite observations of thunderstorm-generated gravity waves in mid-wave infrared images of the upper stratosphere. *Geophysical Research Letters*, **25**, 939–942. 71

Dirac, P.A.M. (1981). *The principles of quantum mechanics*. 27, Oxford university press. 148

Durran, D.R. & Klemp, J.B. (1983). A compressible model for the simulation of moist mountain waves. *Monthly Weather Review*, **111**, 2341–2361. vii, 19

Edman, J.P. & Romps, D.M. (2017). Beyond the rigid lid: Baroclinic modes in a structured atmosphere. *J. Atmos. Sci.*, **74**, 3551–3566. 23, 25, 26, 29, 30, 87, 105, 106, 136, 186, 188

Emanuel, K.A. (1986). An air-sea interaction theory for tropical cyclones. Part I: Steady-state maintenance. *J. Atmos. Sci.*, **43**, 585–605. 25, 146

Emanuel, K.A., David Neelin, J. & Bretherton, C.S. (1994). On large-scale circulations in convecting atmospheres. *Quart. J. Roy. Meteor. Soc.*, **120**, 1111–1143. 23

Fovell, R., Durran, D. & Holton, J. (1992). Numerical simulations of convectively generated stratospheric gravity waves. *J. Atmos. Sci.*, **49**, 1427–1442. vii, 21, 22

Francis, S.H. (1975). Global propagation of atmospheric gravity waves: A review. *Journal of Atmospheric and terrestrial Physics*, **37**, 1011–1054. 18

Fritts, D.C. (1984). Gravity wave saturation in the middle atmosphere: A review of theory and observations. *Reviews of Geophysics*, **22**, 275–308. 10, 24

Fritts, D.C. & Alexander, M.J. (2003). Gravity wave dynamics and effects in the middle atmosphere. *Reviews of geophysics*, **41**. 18, 19

Fritts, D.C. & Luo, Z. (1992). Gravity wave excitation by geostrophic adjustment of the jet stream. part i: Two-dimensional forcing. *J. Atmos. Sci.*, **49**, 681–697. 71

Fritts, D.C. & Nastrom, G.D. (1992). Sources of mesoscale variability of gravity waves. part ii: Frontal, convective, and jet stream excitation. *J. Atmos. Sci.*, **49**, 111–127. 24

Fritts, D.C., Smith, R.B., Taylor, M.J., Doyle, J.D., Eckermann, S.D., Dörnbrack, A., Rapp, M., Williams, B.P., Pautet, P.D., Bossert, K. *et al.* (2016). The deep propagating gravity wave experiment (deepwave): An airborne and ground-based exploration of gravity wave propagation and effects from their sources throughout the lower and middle atmosphere. *Bulletin of the American Meteorological Society*, **97**, 425–453. 10

Gill, A. (1976). Adjustment under gravity in a rotating channel. *Journal of Fluid Mechanics*, **77**, 603–621. 20

Gill, A. (1980). Some simple solutions for heat-induced tropical circulation. *Quart. J. Roy. Meteor. Soc.*, **106**, 447–462. 6

Gill, A. (1984). On the behavior of internal waves in the wakes of storms. *Journal of Physical Oceanography*, **14**, 1129–1151. 20

Gill, A., Davey, M., Johnson, E. & Linden, P. (1986). Rossby adjustment over a step. *Journal of marine research*, **44**, 713–738. 20,

105

Gill, A.E. (1982). *Atmosphere-ocean dynamics*. Elsevier. 12, 13, 16, 20, 31, 105, 132, 141, 142, 143, 145, 150

Gregory, D. & Rowntree, P. (1990). A mass flux convection scheme with representation of cloud ensemble characteristics and stability-dependent closure. *Monthly Weather Review*, **118**, 1483–1506. 7

Haertel, P.T. & Johnson, R.H. (1998). Two-day disturbances in the equatorial western pacific. *Quart. J. Roy. Meteor. Soc.*, **124**, 615–636. 141

Haertel, P.T. & Kiladis, G.N. (2004). Dynamics of 2-day equatorial waves. *J. Atmos. Sci.*, **61**, 2707–2721. 141

Halliday, O.J., Griffiths, S.D., Parker, D.J., Stirling, A. & Vosper, S. (2017). Forced gravity waves and the tropospheric response to convection. *Quart. J. Roy. Meteor. Soc.*. 62

Hankinson, M.C., Reeder, M. & Lane, T. (2014). Gravity waves generated by convection during TWP-ICE: I. inertia-gravity waves. *J. Geophys. Research: Atmospheres*, **119**, 5269–5282. 23

Hauf, T. & Clark, T.L. (1989). Three-dimensional numerical experiments on convectively forced internal gravity waves. *Quart. J. Roy. Meteor. Soc.*, **115**, 309–333. 71

Hines, C.O. (1974). *The upper atmosphere in motion*. Wiley Online Library. vii, 9, 10

Holton, J., Beres, J. & Zhou, X. (2002). On the vertical scale of gravity waves excited by localized thermal forcing. *J. Atmos. Sci.*, **59**, 2019–2023. 23, 29, 72, 87

Holton, J.R. (1982). The role of gravity wave induced drag and diffusion in the momentum budget of the mesosphere. *J. Atmos. Sci.*, **39**, 791–799. 10

Holton, J.R. & Hakim, G.J. (2012). *An introduction to dynamic meteorology*, vol. 88. Academic press. 1, 3, 11, 16

Horinouchi, T., Nakamura, T. & Kosaka, J.i. (2002). Convectively generated mesoscale gravity waves simulated throughout the middle atmosphere. *Geophysical research letters*, **29**, 3–1. 71

Hoskins, B.J., McIntyre, M. & Robertson, A.W. (1985). On the use and significance of isentropic potential vorticity maps. *Quart. J. Roy. Meteor. Soc.*, **111**, 877–946. 105

Houze Jr, R.A. (2014). *Cloud dynamics*, vol. 104. Academic press. 2, 4

Jackson, J.D. (1999). Classical electrodynamics. 78

Kiladis, G.N., Thorncroft, C.D. & Hall, N.M. (2006). Three-dimensional structure and dynamics of african easterly waves. part i: Observations. *J. Atmos. Sci.*, **63**, 2212–2230. 141

Kiladis, G.N., Wheeler, M.C., Haertel, P.T., Straub, K.H. & Roundy, P.E. (2009). Convectively coupled equatorial waves. *Reviews of Geophysics*, **47**. 141

Kim, S.H., Chun, H.Y. & Jang, W. (2014). Horizontal divergence of typhoon-generated gravity waves in the upper troposphere and lower stratosphere (UTLS) and its influence on typhoon evolution. *Atmospheric Chemistry and Physics*, **14**, 3175–3182. 29

Kim, S.Y. & Chun, H.Y. (2011). Impact of typhoon-generated gravity waves in the typhoon development. *J. Geophys. Research: Letters*, **38**. 29

Kirshbaum, D.J. & Durran, D.R. (2005). Atmospheric factors governing banded orographic convection. *J. Atmos. Sci.*, **62**, 3758–3774. 5

Kittel, C. & Kroemer, H. (1970). *Thermal physics*, vol. 9690. Wiley New York. 4

Koch, S.E., Golus, R.E. & Dorian, P.B. (1988). A mesoscale gravity wave event observed during ccope. part ii: Interactions between mesoscale convective systems and the antecedent waves. *Monthly weather review*, **116**, 2545–2569. 10

Koster, R.D., Dirmeyer, P.A., Guo, Z., Bonan, G., Chan, E., Cox, P., Gordon, C., Kanae, S., Kowalczyk, E., Lawrence, D. *et al.* (2004). Regions of strong coupling between soil moisture and precipitation. *Science*, **305**, 1138–1140. 6

Lac, C., Lafore, J. & Redelsperger, J. (2002). Role of gravity waves in triggering deep convection during TOGA COARE. *J. Atmos. Sci.*, **59**, 1293–1316. 23

Landau, L.D. & Lifshitz, E.M. (1959). *Course of theoretical physics*. Elsevier. 13

Lane, T.P. & Reeder, M.J. (2001). Convectively generated gravity waves and their effect on the cloud environment. *J. Atmos. Sci.*, **58**, 2427–2440. 10, 22, 24, 26, 29, 71, 163, 187, 192

Lane, T.P. & Zhang, F. (2011). Coupling between gravity waves and tropical convection at mesoscales. *J. Atmos. Sci.*, **68**, 2582–2598. 23, 24

Lane, T.P., Reeder, M.J. & Clark, T.L. (2001). Numerical modeling of gravity wave generation by deep tropical convection. *J. Atmos. Sci.*, **58**, 1249–1274. 6, 24

Lindzen, R. & Tung, K. (1976). Banded convective activity and ducted gravity waves. *Monthly Weather Review*, **104**, 1602–1617. 18, 23

Lindzen, R.S. (1974). Wave-CISK in the tropics. *J. Atmos. Sci.*, **31**, 156–179. 25, 31, 146, 147, 148

Lindzen, R.S. (1981). Turbulence and stress owing to gravity wave and tidal breakdown. *Journal of Geophysical Research: Oceans*, **86**, 9707–9714. 10, 24

Liu, C. & Moncrieff, M.W. (2004). Effects of convectively generated gravity waves and rotation on the organization of convection. *J. Atmos. Sci.*, **61**, 2218–2227. 24, 105, 106

Mapes, B.E. (1993). Gregarious tropical convection. *J. Atmos. Sci.*, **50**, 2026–2037. 22, 25, 54, 187

Mapes, B.E. (1998). The large-scale part of tropical mesoscale convective system circulations. *J. Meteor. Soc. of Japan Series 2*, **76**, 29–55. 23

Mapes, B.E. (2000). Convective inhibition, subgrid-scale triggering energy, and stratiform instability in a toy tropical wave model. *J. Atmos. Sci.*, **57**, 1515–1535. 6, 54

Marsham, J. & Parker, D. (2006). Secondary initiation of multiple bands of cumulonimbus over southern Britain. II: Dynamics of secondary initiation. *Quart. J. Roy. Meteor. Soc.*, **132**, 1053–1072. 23, 24, 54

Matsuno, T. (1966). Quasi-geostrophic motions in the equatorial area. *J. of the Met. Soc. of Japan. Ser. II*, **44**, 25–43. 6, 27, 142, 143, 146, 187

Monserrat, S. & Thorpe, A.J. (1996). Use of ducting theory in an observed case of gravity waves. *J. Atmos. Sci.*, **53**, 1724–1736. 136

Morse, P.M. & Feshbach, H. (1946). *Methods of theoretical physics*. Technology Press. 148

Nappo, C.J. (2013). *An introduction to atmospheric gravity waves*. Academic press. 19

Nastrom, G.D. & Fritts, D.C. (1992). Sources of mesoscale variability of gravity waves. part i: Topographic excitation. *J. Atmos. Sci.*, **49**, 101–110. 6, 10

Nicholls, M.E. (1987). A comparison of the results of a two-dimensional numerical simulation of a tropical squall line with observations. *Monthly Weather Review*, **115**, 3055–3077. 29

Nicholls, M.E., Pielke, R.A. & Cotton, W.R. (1991). Thermally forced gravity waves in an atmosphere at rest. *J. Atmos. Sci.*, **48**, 1869–1884. 23, 25, 26, 29, 30, 33, 34, 36, 44, 47, 72, 85, 87, 106, 186, 187

Ong, H., Wu, C.M. & Kuo, H.C. (2017). Effects of artificial local compensation of convective mass flux in the cumulus parameterization. *J. Adv. Model. Earth Syst.*, **9**, 1811–1827. 29

Pandya, R.E., Durran, D.R. & Weisman, M.L. (2000). The influence of convective thermal forcing on the three-dimensional circulation around squall lines. *J. Atmos. Sci.*, **57**, 29–45. 22, 29

Parker, D.J. (2017). *Meteorology of tropical West Africa: The forecasters handbook*. John Wiley & Sons. 141

Parker, D.J. & Burton, R.R. (2002). The two-dimensional response of a tropical jet to propagating lines of convection. *J. Atmos. Sci.*, **59**, 1263–1273. 25, 33, 36, 44, 85, 189

Piani, C., Durran, D., Alexander, M. & Holton, J. (2000). A numerical study of three-dimensional gravity waves triggered by deep tropical convection and their role in the dynamics of the QBO. *J.*

Atmos. Sci., **57**, 3689–3702. 22, 26, 29, 71, 187

Ralph, F., Venkateswaran, V. & Crochet, M. (1993). Observations of a mesoscale ducted gravity wave. *J. Atmos. Sci.*, **50**, 3277–3291. 18

Raymond, D. & Jiang, H. (1990). A theory for long-lived mesoscale convective systems. *J. Atmos. Sci.*, **47**, 3067–3077. 105

Raymond, D.J. (1983). Wave-CISK in mass flux form. *J. Atmos. Sci.*, **40**, 2561–2574. 25

Reif, F. (2009). *Fundamentals of statistical and thermal physics*. Waveland Press. 4

Rotunno, R., Klemp, J.B. & Weisman, M.L. (1988). A theory for strong, long-lived squall lines. *J. Atmos. Sci.*, **45**, 463–485. 29

Schlemmer, L. & Hohenegger, C. (2014). The formation of wider and deeper clouds as a result of cold-pool dynamics. *J. Atmos. Sci.*, **71**, 2842–2858. 6

Schmidt, J.M. & Cotton, W.R. (1990). Interactions between upper and lower tropospheric gravity waves on squall line structure and maintenance. *J. Atmos. Sci.*, **47**, 1205–1222. 29

Scorer, R. (1949). Theory of waves in the lee of mountains. *Quart. J. Roy. Meteor. Soc.*, **75**, 41–56. 18, 19

Shige, S. & Satomura, T. (2000). The gravity wave response in the troposphere around deep convection. *J. Meteor. Soc. of Japan Series 2*, **78**, 789–801. 22

Shutts, G. & Gray, M. (1994). A numerical modelling study of the geostrophic adjustment process following deep convection. *Quart. J. Roy. Meteor. Soc.*, **120**, 1145–1178. 24, 105

Smagorinsky, J. (1963). General circulation experiments with the primitive equations: I. the basic experiment. *Monthly Weather Review*, **91**, 99–164. 63

Smith, R.B. (1979). The influence of mountains on the atmosphere. In *Advances in geophysics*, vol. 21, 87–230, Elsevier. 19

Smith, R.B., Doyle, J.D., Jiang, Q. & Smith, S.A. (2007). Alpine gravity waves: Lessons from map regarding mountain wave generation and breaking. *Quart. J. Roy. Meteor. Soc.*, **133**, 917–936. 10

Spiegel, E. & Veronis, G. (1960). On the boussinesq approximation for a compressible fluid. *The Astrophysical Journal*, **131**, 442. 12

Stensrud, D.J. (2009). *Parameterization schemes: keys to understanding numerical weather prediction models*. Cambridge University Press. 7

Stephens, G.L., L'Ecuyer, T., Forbes, R., Gettlemen, A., Golaz, J.C., Bodas-Salcedo, A., Suzuki, K., Gabriel, P. & Haynes, J. (2010). Dreary state of precipitation in global models. *J. Geophys. Research: Atmospheres*, **115**. 24

Stratton, R.A., Senior, C.A., Vosper, S.B., Folwell, S.S., Boutle, I.A., Earnshaw, P.D., Kendon, E., Lock, A.P., Mal-

COLM, A., MANNERS, J. *et al.* (2018). A pan-african convection-permitting regional climate simulation with the met office unified model: Cp4-africa. *Journal of Climate*, **31**, 3485–3508. 148

SUTHERLAND, B. (1996). Internal gravity wave radiation into weakly stratified fluid. *Physics of Fluids (1994-present)*, **8**, 430–441. 50, 54

SUTHERLAND, B.R. (2010). *Internal gravity waves*. Cambridge University Press. 54

TAKAYABU, Y.N. (1994). Large-scale cloud disturbances associated with equatorial waves. *Journal of the Meteorological Society of Japan. Ser. II*, **72**, 433–449. 141

THORPE, A., MILLER, M. & MONCRIEFF, M. (1982). Two-dimensional convection in non-constant shear: A model of mid-latitude squall lines. *Quart. J. Roy. Meteor. Soc.*, **108**, 739–762. 29

TOMPKINS, A.M. (2001). Organization of tropical convection in low vertical wind shears: The role of cold pools. *J. Atmos. Sci.*, **58**, 1650–1672. 6

TULICH, S.N. & KILADIS, G.N. (2012). Squall lines and convectively coupled gravity waves in the tropics: Why do most cloud systems propagate westward? *J. Atmos. Sci.*, **69**, 2995–3012. 24, 27, 141, 151, 183, 187

TULICH, S.N., RANDALL, D.A. & MAPES, B.E. (2007). Vertical-mode and cloud decomposition of large-scale convectively coupled gravity waves in a two-dimensional cloud-resolving model. *J. Atmos. Sci.*, **64**, 1210–1229. 22, 24

TULICH, S.N., KILADIS, G.N. & SUZUKI-PARKER, A. (2011). Convectively coupled Kelvin and easterly waves in a regional climate simulation of the tropics. *Climate Dynamics*, **36**, 185–203. 22

UCCELLINI, L.W. & KOCH, S.E. (1987). The synoptic setting and possible energy sources for mesoscale wave disturbances. *Monthly weather review*, **115**, 721–729. 10

VALLIS, G.K. (2006). *Atmospheric and oceanic fluid dynamics*. Cambridge University Press. 12, 13, 16

WALKER, J. & ROWNTREE, P. (1977). The effect of soil moisture on circulation and rainfall in a tropical model. *Quart. J. Roy. Meteor. Soc.*, **103**, 29–46. 6

WALTERS, D., BOUTLE, I., BROOKS, M., THOMAS, M., STRATTON, R., VOSPER, S., WELLS, H., WILLIAMS, K., WOOD, N., ALLEN, T. *et al.* (2017). The met office unified model global atmosphere 6.0/6.1 and jules global land 6.0/6.1 configurations. *Geoscientific Model Development*, **10**, 1487. 7

WEBSTER, P.J. & LUKAS, R. (1992). Toga coare: The coupled ocean-atmosphere response experiment. *Bulletin of the American Meteorological Society*, **73**, 1377–1416. 10

WEI, J. & ZHANG, F. (2014). Mesoscale gravity waves in moist baroclinic jet–front systems. *J. Atmos. Sci.*, **71**, 929–952. 10

Wheeler, M. & Kiladis, G.N. (1999). Convectively coupled equatorial waves: Analysis of clouds and temperature in the wavenumber-frequency domain. *J. Atmos. Sci.*, **56**, 374–399. 7, 22, 27, 141, 149, 151, 152, 153, 180, 182, 187, 192

Wood, N., Staniforth, A., White, A., Allen, T., Diamantakis, M., Gross, M., Melvin, T., Smith, C., Vosper, S., Zerroukat, M. *et al.* (2014). An inherently mass-conserving semi-implicit semi-lagrangian discretization of the deep-atmosphere global non-hydrostatic equations. *Quart. J. Roy. Meteor. Soc.*, **140**, 1505–1520. 63

Yanai, M., Esbensen, S. & Chu, J.H. (1973). Determination of bulk properties of tropical cloud clusters from large-scale heat and moisture budgets. *J. Atmos. Sci.*, **30**, 611–627. 7

Zhang, F. (2004). Generation of mesoscale gravity waves in upper-tropospheric jet–front systems. *J. Atmos. Sci.*, **61**, 440–457. 24

Zhang, F., Davis, C.A., Kaplan, M.L. & Koch, S.E. (2001). Wavelet analysis and the governing dynamics of a large-amplitude mesoscale gravity-wave event along the East Coast of the United States. *Quart. J. Roy. Meteor. Soc.*, **127**, 2209–2245. 23

Zhu, X. & Holton, J.R. (1987). Mean fields induced by local gravity-wave forcing in the middle atmosphere. *J. Atmos. Sci.*, **44**, 620–630. 71